HEINRICH HEINE
UNIVERSITÄT DÜSSELDORF

Max Planck Institute
for Metabolism Research

Positron Emission Tomography in the Context of Metabolism

Inaugural-Dissertation

zur Erlangung des Doktorgrades
der Mathematisch-Naturwissenschaftlichen Fakultät
der Heinrich-Heine-Universität Düsseldorf

vorgelegt von

Anna Lena Cremer
aus Köln

Köln, Mai 2020

Angefertigt am Max-Planck-Institut für Stoffwechselforschung in Köln

Gedruckt mit der Genehmigung der
Mathematisch-Naturwissenschaftlichen Fakultät der
Heinrich-Heine-Universität Düsseldorf

Berichterstatter:

1. Prof. Dr. Jens Mittag

2. Prof. Dr. Thomas Heinzel

Tag der mündlichen Prüfung:

Eidesstattliche Erklärung

Ich versichere an Eides Statt, dass die Dissertation „Positron Emission Tomography in the Context of Metabolism“ von mir selbständig und ohne unzulässige fremde Hilfe unter Beachtung der „Grundsätze zur Sicherung guter wissenschaftlicher Praxis an der Heinrich-Heine-Universität Düsseldorf“ erstellt worden ist. Ich erkläre weiterhin, dass die vorliegende Arbeit noch nicht im Rahmen eines anderen Prüfungsverfahrens eingereicht wurde.

Köln, den

Zusammenfassung

Im Kontext der globalen Adipositasepidemie besteht ein großes Interesse an Methoden, welche helfen können Mechanismen, die für ein Versagen der Energiehomeostase verantwortlich sind, zu entschlüsseln. Das Belohungssystem des Gehirns, welches vorwiegend durch den Neurotransmitter Dopamin reguliert wird, ist eine entscheidene Stellschraube im Zusammenhang mit übermäßiger Nahrungsaufnahme. Untersuchungen von Dopaminausschüttungen als Reaktion auf Essen, sowie ein potentieller Zusammenhang mit der konsumierten Nahrung oder dem Körpergewicht sind daher interessante wissenschaftliche Fragestellungen. Bisher gibt es jedoch keine Methode, mit welcher physiologische Dopaminauschüttungen im menschlichen Gehirn über einen bestimmten Zeitraum gemessen werden können.
Im Rahmen dieser Arbeit wurde eine neue Methode für [11C]Raclopride Positronen Emissions Tomographie (PET) entwickelt, mit welcher zeitlich und räumlich aufgelöste Dopaminausschüttungen detektiert werden können. Die neue Methode wird anhand von Kompartmentmodellen, welche die Interaktion von dem Radiotracer [11C]Raclopride und Dopamin einbeziehen, eingeführt und mittels experimenteller Daten validiert. Neben PET Experimenten schließt die Validierung der Methode direkte Messungen von Dopamin im Maushirn mittels Voltammetrie ein. Die neue Methode wurde darüber hinaus erfolgreich zur Detektion von Dopaminauschüttungen als Reaktion auf Nahrungsaufnahme im Rahmen einer Probandenstudie angewendet. Fundamentale Prozesse, wie Diffusion und Entnahme von Dopamin im Extrazellulärraum, sind die Basis des eingefühten Models. Diese Prozesse finden auch für andere Neurotransmitter statt. Dementsprechend wurden Modellrechungen für die Neurotransmitter Serotonin, Acetylcholin und Glutamat durchgeführt. Die Ergebnisse zeigen, dass die Methode mit jeweils geeigneten Radiotracern potenziell zur Detektion von Auschüttungen dieser Neurotransmitter angewendet werden kann. Zukünftige Messungen müssen dies jedoch erst bestätigen.

Grundlage für die Entwicklung von Adipositas ist die Fehlregulation des Stoffwechsels. Mittels [18F]FDG PET kann der Glukosestoffwechsel in Menschen und Tieren untersucht werden, wobei die Anwendung bisher hauptsächlich auf Gehirndaten beschränkt war. Die Analyse von weiteren Organen und Geweben im Hinblick auf einen veränderten Glukosestoffwechsel mit [18F]FDG PET könnte jedoch wichtige Einblicke in Bezug auf systemische metabolische Veränderungen geben. Im zweiten Teil dieser Arbeit werden Methoden eingeführt, mit welchen der Glukosemetabolismus im ganzen Körper an Hand von [18F]FDG PET und CT analysiert werden kann. Dadurch wird das gesamte Potential von [18F]FDG PET/CT in der Stoffwechselforschung in Mäusen dargelegt. Die entwickelten Methoden können auch zur Untersuchung von Menschen angewendet werden.

Summary

In light of the global obesity epidemic there is an overall interest in methods that can help to unravel the basic mechanisms responsible for the failure of energy homeostasis. One important driver of increased food intake is the brain's reward system. The so-called hedonic system is predominantly regulated by the neurotransmitter dopamine. Therefore, the analysis of dopamine release in response to food intake and potential correlations with the consumed food or body weight is an interesting research objective. Methods to assess dopamine release within the human brain over time are lacking, especially for physiological release events like in response to food intake.

Within the framework of this thesis a novel method using [11C]raclopride Positron Emission Tomography (PET) was developed to detect spatiotemporal dopamine release in the human brain. The novel method is introduced on basis of model calculations using compartment models that take into account the interaction between the PET tracer [11C]raclopride and dopamine, and is validated by mouse experiments as well as a clinical study. Apart from PET experiments, the validation includes direct assessment of dopamine concentrations in the mouse brain with the help of fast-scan cyclic voltammetry. Application of the method to detect dopamine release during food intake in humans demonstrates the power of the novel approach.

The introduced method is based on fundamental processes, such as diffusion and removal, that in principle apply to any neurotransmitter system. Accordingly, the applicability of the method to the neurotransmitter systems of serotonin, acetylcholine, and glutamate is analyzed on basis of theoretical considerations and model calculations. The results indicate potential applicability to any of the systems, which needs to be confirmed in future applications.

A second important research field with regard to increasing rates of overweight and obesity is the metabolic health, since accumulation of adipose tissue leads to various diseases. A common problem is an impaired glucose metabolism. Using [18F]FDG PET glucose metabolism in humans and mice can be assessed *in vivo*. However, peripheral tissue analysis using dynamic [18F]FDG PET data including kinetic modeling is no standard approach in clinical routine, especially with regard to metabolic diseases. Within this thesis, whole-body [18F]FDG PET and CT data of mice were used for combined analysis to exploit its full potential in metabolism research in rodents, as well as introducing ways of data analysis which can be applied to human data.

Abbreviations

[11C]ABP688	3-(6-methyl-pyridin-2-ylethynyl)-cyclohex-2-enone-O-[11C]-methyl-oxime
[11C]CUMI-101	[O-methyl-11C]2-(4-(4-(2-methoxyphenyl)6 piperazin-1-yl)butyl)-4-methyl-1,2,4-triazine-3, 5(2H,4H)dione
[11C]WAY-100635	[*carbonyl*-11C]-(N-(2-(4-(2-methoxyphenyl)-1-piperazinyl)ethyl)-N-(2-pyridyl) cyclohexane-carboxamide
[11C]raclopride	(S)-3,5-dichloro-N-((1-ethylpyrrolidin-2-yl)methyl)-2-hydroxy-6-methoxybenzamide
[18F]AZAN	[18F]JHU87522/(-)-2-(6-([18F]-fluoro-2,3'-bipyridin-5'-yl)-7-methyl-7-azabicyclo[2.2.1]heptane
[18F]DMFP	[18F]desmethoxyfallypride/(S)-N-((1-Allyl-2-pyrrolidinyl)methyl)-5-(3-[18F]fluoropropyl)-2-methoxybenzamide)
[18F]FDG	[18F]2-fluoro-2-deoxy-D-glucose
[18F]FTHA	[18F]-fluro-heptadonic acid
[18F]MPPF	4-[18F]fluoro-N-[2-[1-(2-methoxyphenyl)-1-piperazinyl]ethyl-N-2-pyridinyl-benzamide
[18F]SP203	3-fluoro-5-(2-(2-18F-(fluoromethyl)-thiazol-4-yl)ethynyl)benzonitrile
[18F]XTRA	[18F](-)-JHU86428/(-)-2-(2'-[18F]fluoro-3,3'-bipyridin-5-yl)-7-methyl-7-aza-bicyclo[2.2.1]heptane
[18F]fallypride	(S)-N-[(1-allyl-2-pyrrolidinyl)methyl]-5-(3'-18F-fluoropropyl)-2,3-dimethoxy-benzamide
[18F]flubatine	[18F]NCFHEB/[18F](-)-norchloro-fluorohomoepibatidine
[18F]nifene	2-[18F]Fluoro-3-[2-((S)-3-pyrrolinyl)methoxy]pyridine
5-HT	5-hydroxytryptamine/Serotonin
AgRP	agouti-related peptide
AMPA	α-amino-3-hydroxy-5-methyl-4-isoxazolepropionic acid
ATP	adenosine triphosphate
BAT	brown adipose tissue
BBB	blood-brain barrier
BMI	body mass index
BP	binding potential
cAMP	cyclic adenosine monophosphate
CMR_{glc}	cerebral metabolic rate of glucose
CNO	clozapine-n-oxide
CNS	central nervous system
CP	caudate putamen/striatum

CT	Computer Tomography
DAT	dopamine transporter
DG	2-deoxy-d-glucose
DREADD	Designer Receptors Exclusively Activated by Designer Drugs
DVR	distribution volume ratio
EAATs	excitatory amino acid transporters
ECS	extracellular space
fMRI	functional Magnetic Resonance Imaging
FOV	field of view
FRTC	full reference tissue compartment model
FSCV	fast-scan cyclic voltammetry
GABA	γ-Aminobutyric acid
GluT	glucose transporters
GluT4	glucose transporter 4
HFD	high fat diet
hM3D$_{Gq}$^{DAT}	chemogenetic mouse model
HU	hounsfield units
i.p.	intraperitoneal
i.v.	intravenous
LC	lumped constant
LSRRM	linearized simplified reference region method
MAT	monoamine transporters
mGluRs	metabotropic glutamate receptors
MNI	Montreal Neurological Institute
MPFC	medial prefrontal cortex
MR$_{glc}$	metabolic rate of glucose
MRI	Magnetic Resonance Imaging
MRS	Magnetic Resonance Spectroscopy
NAc	nucleus accumbens core
nAChRs	nicotinic acetylcholine receptors
NCD	normal chow diet
NeuroPET	Neurotransmitter PET
NMDA	N-methyl-D-aspartate
PET	Positron Emission Tomography
POMC	pro-opiomelanocortin
ROI	region of interest
SERT	serotonin transporter
SN	substantia nigra
SPECT	single photon emission computed tomography
SRTM	simplified reference tissue model
SSRI	selective serotonin reuptake inhibitor
SUV	standardized uptake value
SUVR	standardized uptake value ratio
TAC	time activity curve

TCA	tricarboxylic acid cycle
UCP-1	uncoupling protein 1
VOI	volume of interest
VTA	ventral tegmental area
WAT	white adipose tissue
WHO	World Health Organization

Nomenclature

$B_{\mathbf{avail}}$	available concentration of binding sites
$B_{\mathbf{max}}$	total concentration of binding sites
D	diffusion constant of dopamine in the ECS
$N_{\mathbf{b}}$	concentration of bound neurotransmitter in the ECS
$N_{\mathbf{e}}$	free neurotransmitter concentration in the ECS
$N_{\mathbf{s}}$	neurotransmitter concentration in the synaptic cleft
R	total radiotracer concentration
$R_{\mathbf{b}}$	concentration of bound radiotracer
$R_{\mathbf{e}}$	concentration of free radiotracer
$R_{\mathbf{p}}$	concentration of radiotracer in the plasma
$R_{\mathbf{sb}}$	concentration of bound radiotracer in the synapse
$R_{\mathbf{s}}$	concentration of free radiotracer in the synapse
$V_{\mathbf{e}}$	volume of the extrasynaptic extracellular space
$V_{\mathbf{s}}$	volume of the synapse
α	the fraction of extracellular volume
$k_{\mathbf{d}}$	dissociation rate constant of the radiotracer
$l_{\mathbf{s}}$	synaptic leakage
$n_{\mathbf{D}}$	dissociation rate constant of the neurotransmitter
$n_{\mathbf{be}}$	unbinding rate of neurotransmitter from receptor/binding site
$n_{\mathbf{eb,max}}$	maximal binding rate of neurotransmitter in the case that the total amount of binding sites is available
$n_{\mathbf{eb}}$	effective binding rate of neurotransmitter from ECS to receptor/binding site
$n_{\mathbf{on}}$	binding rate of neurotransmitter from ECS to receptor/binding site
$r_{\mathbf{D}}$	dissociation rate constant of the radiotracer
$r_{\mathbf{be}}$	unbinding rate of radiotracer from receptor/binding site
$r_{\mathbf{diff}}$	diffusion rate constant of radiotracer in the ECS
$r_{\mathbf{eb,max}}$	maximal binding rate of radiotracer in the case that the total amount of binding sites is available
$r_{\mathbf{eb}}$	effective binding rate of radiotracer from ECS to receptor/binding site
$r_{\mathbf{ep}}$	transport rate of radiotracer from ECS to plasma
$r_{\mathbf{on}}$	binding rate of radiotracer from ECS to receptor/binding site
$r_{\mathbf{pe}}$	transport rate of radiotracer from plasma to ECS
rDA	parameter of temporal variations in the PET signal for the dopamine system

rN	parameter of temporal variations in the PET signal for neurotransmitter systems different from dopamine

List of Figures

List of Tables

Table of Contents

1 Introduction

In the recent decades the fractions of overweight and obesity in the worldwide population are rapidly increasing. While in 1980 28.8% of men and 29.8% of women were overweight or obese, in 2016 more than 39% (1.9 billion) adults were overweight and 13% (650 million) obese[1]. According to the World Health Organization (WHO) worldwide obesity has nearly tripled since 1975, with a further uptrend[1]. The increase in overweight and obesity is not only restricted to certain populations like inhabitants of industrialized countries, but is observed globally even in developing countries and also among all ages[1].

Obesity and overweight are defined as the abnormal or excessive accumulation of adipose tissue that might impair health[1]. The WHO classifies overweight and obesity by the body mass index (BMI), which is defined as body weight in kg divided by the square of the body height in meters ($\frac{kg}{m^2}$). With a BMI equal or greater than 25 an adult is defined as overweight, with a BMI equal or greater than 30 as obese[1]. Obesity is a very complex condition with major risks for lots of serious physiological diseases like diabetes, cardiovascular diseases and cancer, and moreover has various social and psychological consequences. It has even been suggested that, due to the increase in obesity, future life expectancy may even decrease[2].

In normal conditions the body is able to maintain a stable body weight over long times by the use of different homeostatic signaling pathways that keep energy intake (i.e. food intake) and expenditure (i.e. the basal metabolic rate, physical activity and adaptive thermogenesis) balanced[3,4]. Homeostasis is a complex interplay between the central nervous system (CNS), particularly the hypothalamus, and peripheral storage and mobilization of fat stores[3]. Note that adipose tissue does not just act as energy storage, but also as endocrine organ that produces adipokines (e.g. leptin, resistin, etc.) which modulate metabolic processes in the body[3].

In the recent decades enormous progress has been made in deciphering the homeostatic system in the hypothalamus – predominantly regulated by pro-opiomelanocortin (POMC) and agouti-related peptide (AgRP) neurons – and its modulation of metabolism related to energy stores and intestinal tract activity[5]. However, the development of the obesity pandemic indicates that homeostatic regulation is prone to failure in environments which offer easily accessible, cheap and palatable food with high caloric density.

Apart from homeostatic mechanisms, food intake appears to be driven by another important factor: the reward system of the brain, also referred to as hedonic system. The reward system responds to factors as visual appearance, smell and taste of food and can override homeostatic signals in environments with excess accessibility to food[5,6]. In this context the dopamine system has been studied, with dopamine being the most prominent neurotransmitter of the reward system. Dopamine signaling

from ventral tegmental area (VTA) neurons to the nucleus accumbens core (NAc), hippocampus, amygdala and pre-frontal cortex promotes reward-related activities like food intake and is also postulated to promote learning associations between food rewards and environmental factors [5]. Moreover, there is increasing evidence that hormones like insulin, leptin and ghrelin – which are hormonal inputs to the homeostatic system – directly affect the dopamine system [5].
Taken together, the control of food intake consists of a mixture of homeostatic, hedonic/reward-related and cognitive mechanisms. Research efforts addressing the obesity pandemic from different perspectives are being made by various scientific fields, including genetics, medicine, neurology/neurobiology, endocrinology and psychology.
Studies are performed on population or individual level in humans and animals. To answer the different research questions arising, more and more elaborate techniques have been and are being developed. Today, it is possible to activate and analyze single neurons *in vivo* in animals. Furthermore, single genes can be knocked out or modified and the behavior of the transgenic animal can be investigated.
For humans the methods are restricted, as in clinical studies only non-invasive techniques are feasible. At that point, non-invasive imaging techniques – which in animals might not necessarily be the method of choice – come into play. The field of "metabolic imaging" grew over the recent decades and various new methods have been developed.
The imaging techniques Magnetic Resonance Spectroscopy (MRS) and Positron Emission Tomography (PET) allow for visualization and quantification of metabolites. By the use of Computer Tomography (CT) or Magnetic Resonance Imaging (MRI) the distribution of adipose tissue can be analyzed. Moreover, MRI is used for diagnosis and investigation of obesity-related disease progression like fatty liver disease, cardiovascular diseases, cancer and a lot more. Functional MRI (fMRI) can provide information on cognitive control of food intake and PET provides a tool to quantify physiological processes depending on the used radiotracer.
One objective of this thesis is the analysis of [11C]raclopride PET data to assess dopamine release in response to food intake in the human brain. While most of the knowledge on dopamine signaling in the context of food intake behavior is based on data from studies in rodents, methods for the assessment of dopamine release in humans are lacking. Up to now, only pharmacological induced robust and long-lasting dopamine release events could be detected by [11C]raclopride PET. However, PET applications are thought to be insensitive to fast and more subtle changes in dopamine concentrations. To be able to detect dopamine release in response to a relatively subtle stimulus like food intake, a novel method was developed within the framework of this thesis. The novel method is based on [11C]raclopride PET data and relates temporal variations in the [11C]raclopride PET signal to changes in dopamine concentrations in the extracellular space. To validate the method direct *in situ* measurements of dopamine levels were performed in a chemogenetic mouse model. Moreover, a theoretical framework including model calculations is introduced substantiating the experimental results. Successful application of the novel method to

human [11C]raclopride PET data reveals the power of the approach. While common analysis methods fail to detect dopaminergic release events in these data, the novel method produced reliable results.
A second objective of this thesis is the whole-body analysis of glucose metabolism using [18F]FDG PET and CT data of mice. [18F]FDG is widely used to assess the cerebral metabolic rate of glucose, but can also be applied to assess glucose uptake and metabolism in peripheral metabolic tissues. Methods for tissue analysis exist, but the full dynamics of spatiotemporal [18F]FDG distribution within the whole body is usually not taken into account in clinical data. This is due to a lack of whole-body scanners for humans. As a consequence the subject is either step-wise moved through the scanner and no full time course of data is obtained, or only tissues inside of the field of view (FOV) can be analyzed. Recently, a whole-body PET for humans was developed [7,8], so that methods for peripheral tissue data analysis need to be validated, refined or newly developed. Using [18F]FDG PET and CT data whole-body glucose metabolism in mice is investigated within the framework of this thesis and the influence of the nutritional state on the results is examined. Moreover, a method to synergetically analyze combined [18F]FDG PET and CT is developed.

This thesis is divided into three chapters. The first chapter "Principles of Positron Emission Tomography" gives an introduction on PET and compartment modeling with a focus on the state-of-the art of Neurotransmitter PET (NeuroPET). The second chapter "Spatiotemporal Assessment of Neurotransmitter Release using PET" addresses the first objective of the thesis by introducing a novel method for the assessment of neurotransmitter release. The underlying theoretical model will be elaborated followed by results from experimental studies in mice and humans. The third chapter "Advancements in the Application of [18F]FDG PET and CT for Whole-Body Analyses" focuses on the investigation of whole-body glucose metabolism using an integrative approach of [18F]FDG PET and CT data in mice.

2 Principles of Positron Emission Tomography

2.1 Introduction on Positron Emission Tomography

Positron Emission Tomography (PET) is a non-invasive nuclear medicine imaging technique, which is widely used in standard medical care as well as in preclinical and basic research. The technique enables the measurement of physiological processes *in vivo* by injecting a pharmacologically or biochemically active compound labeled with a short-lived positron-emitting radionuclide. Typically fluorine-18 ($T_{1/2}$=109.77 min) or carbon-11 ($T_{1/2}$=20.33 min) are used to label the molecule of interest. The labeled and biologically active molecule, the so-called radiotracer, takes part in metabolism and will eventually decay. The emitted positrons annihilate through collision with electrons in tissue. This process releases two γ-rays with 511 keV in opposite directions, which can be detected as coincident events by surrounding PET detectors. Emission of two oppositely directed γ-rays instead of a single γ-ray supersedes the usage of collimators, that limit the angular field of the detectors. This explains the much higher sensitivity of PET in comparison to gamma cameras or single photon emission computed tomography (SPECT). Using the detected signal three-dimensional images can be reconstructed, which show the quantitative distribution of the tracer of interest (Figure 2.1).[9,10,11]

PET provides a tool for the analysis of complex biological processes in their natural environment, the investigation of signaling pathways and the examination of drug delivery and pharmacokinetics[9,10,12]. So far a wide range of biologically active molecules have been labeled including sugars, amino acids, nucleic acids, water, molecular oxygen, receptor-binding peptides and antibodies. Depending on the used molecule different measures like blood flow, biodistribution, transport rates, binding properties, etc. can be obtained.[9,12,13] The most commonly used radiotracer is the glucose analog [18F]FDG. Measurements with [18F]FDG provide, amongst others, information on neuronal metabolism, glucose uptake in tumors, glucose transport and inflammatory processes.[10,11,12,14,15]

Since the radiotracer is the essential component for imaging and quantifying the desired molecular process, it needs to fulfill different requirements. First of all the tracer should not be toxic, induce an immune reaction or other significant biological response within the body. In general, the radiotracer should be given in so called "tracer doses", i.e. sub-pharmacological doses, such that no physiological effects by the radiotracer itself are induced. Therefore, a high specific activity of the radioligand, i.e. the ratio of the number of radioactive atoms to the total number of atoms, is of advantage. Moreover, the tracer needs to be sensitive and specific for the metabolic

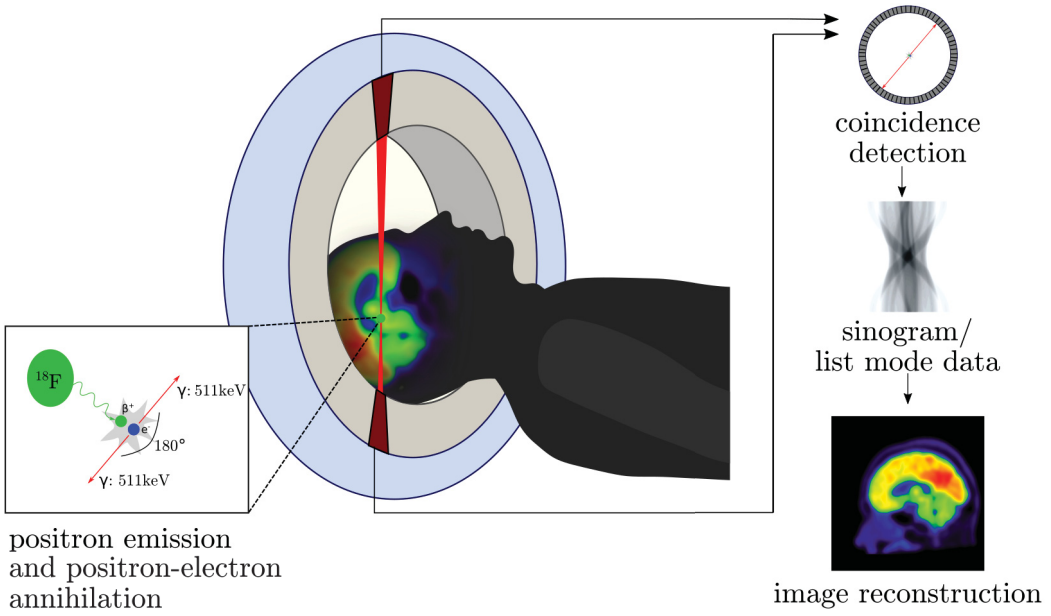

Figure 2.1: Basic principle of PET. Radioisotopes suitable for PET imaging decay via positron (β^+) emission. The emitted positrons travel through space and lose velocity until they eventually annihilate through collision with an electron. Thereby two γ-rays with 511 keV each are released in opposite directions. The surrounding PET detectors recognize coincidence photons. From the "lines of response" (LOR) the point of origin can be reconstructed. From the integrated decay events three-dimensional images can be reconstructed showing the quantitative distribution of the tracer throughout the imaged tissue.

process to be analyzed. If needed, anatomical barriers like cell membranes or the blood-brain barrier (BBB) must be overcome.[9,10,11,16]
The major advantage of PET is its high sensitivity and its quantitative nature[9,13]. The later is due to the fact that in contrast to SPECT or gamma cameras exact attenuation correction can be applied by measuring the attenuation along each line of response with the help of an external radioactive source such as a CT X-ray source. Furthermore, PET enables whole-body imaging (in animals and recently also in humans[7,8]) and insight into different physiological processes. The main limitation is its rather low spatial resolution, which is in the order of 4-8 mm for clinical systems and 1-2 mm for preclinical systems[9,17]. Since the spatial resolution is restricted by fundamental physics as the mean distance from the emitted positron to annihilation is around 0.1 to 1 mm dependent on the initial energy, there is not much space for improvement[10,18]. Moreover the costs and complexity of tracer synthesis, transport and the needed infrastructure are quite expensive[10].

Anyway, PET has added diagnostic value for many diseases, foremost for tumor detection, delineation, monitoring of disease progression and assessment of treatment response[9,19]. PET can provide an increasing understanding of normal brain function and pathophysiological processes in medical research and gained a central role in drug discovery and development in pharmacology[9,11,13,20]. Regarding neurology, the role of brain metabolism and neurotransmitter systems in psychiatric disorders, for example the dopamine system in schizophrenia and the serotonin system in depressive disorders or anxiety, were analyzed using PET[11,12,13]. Dopamine metabolism was studied in patients with Parkinson's disease using different PET tracers ([18F]FDG, [18F]DOPA, [18F]FP-CIT, [11C]PE2I) addressing specific metabolic patterns, dopamine synthesis and storage in the presynaptic terminals, as well as, the dopamine transporter[12,13]. Various studies using [11C]raclopride, a dopamine D2 receptor antagonist, were performed in patients[21,22,23,24]. Also in the field of Alzheimer's disease or other neurodegenerative diseases PET plays an important role in diagnosis, monitoring and the assessment of treatment response[12,13,15].
State-of-the-art systems combine PET and CT[10,11] or PET and MRI[25,26]. Recently, the first whole-body human PET/CT system has been developed[7,8]. For preclinical and basic research dedicated small-animal PET scanners ("microPET" scanners) are available for measurements of rodents[16,20,27]. Rats and mice are widely used in basic and preclinical research: rats are primarily used as surgical and interventional models, while mice can be easily genetically modified and therefore provide a valuable tool to examine many different research questions[16,20]. One key advantage of *in vivo* imaging is that animals can be used for longitudinal studies and therefore multiple types of studies can be performed in one individual animal[16,20].

2.2 Compartment Models

From PET scans quantitative radioactivity measurements throughout a target structure or organ are obtained, either as a single static image covering one time interval post-injection or as multiple images by dividing the measurement into different time intervals [28]. By analyzing the kinetic of the radiotracer in tissue different parameters of interest can be derived. With the use of appropriate models one can for example quantify neuroreceptor binding [29], the cerebral metabolic rate of glucose (CMR_{glc}) [30,31] or blood flow [32,13].
After intravenous (i.v.) injection of the radiotracer, it crosses the capillary membranes and enters the tissues. In tissue it may be bound irreversibly or reversibly to intra- or extracellular sites or it may be metabolized into one or more chemical forms. Therefore the concentration of radioactivity in a given tissue region at a particular time post-injection depends on the local tissue physiology (blood flow, metabolism, etc.), the properties of the tracer, and the time-course of tracer radioactivity concentration in the blood or plasma that defines the availability of tracer to the target organ. Usually, the radiotracer is designed to provide information about a specific physiological function of interest and is a radiolabeled version of a naturally occurring compound, an analog of a natural compound, or an unique compound with specific chemical properties. [28]
Compartment models, in which each compartment defines one possible "state" of the radiotracer, are used to obtain specific and quantitative information on the physiological process of interest. The "states" can either be physical spaces like the extracellular space or chemical states like the current metabolic form or the binding state. In general it is assumed that within each compartment the tracer is homogeneously distributed. [28,33,13] Transport of radiotracer from one compartment to another in a certain time interval is assumed to be proportional to the total amount of tracer in the source compartment and can be described by a rate constant k of dimension $1/time$ [28,33,13]. Premises for the models are the conservation of mass and that the underlying physiological processes are in steady-state, i.e. rate constants do not change with time during the study [28]. The compartmental states and transitions between compartments can be described by a set of ordinary differential equations, which mathematically describe the behavior of the tracer in the tissue over time. To obtain estimates for the rate constants of the model, the time course of the radiotracer in tissue, i.e. the data obtained from a dynamic PET scan, and the input function, i.e. the time course of activity in the plasma, need to be measured. The input function is then used to fit a model to the time activity course in the tissue measured by PET. [28,33,11,13]
Compartment models can be illustrated in form of box-diagrams, in which each box represents a compartment. Box-diagrams for the most common model types are shown in Figure 2.2. With the help of these diagrams the set of differential equations for each model can be easily formulated. Note that although the models include a blood compartment, i.e. the input function, it is not counted as a tissue compartment. [13,28,33,11].

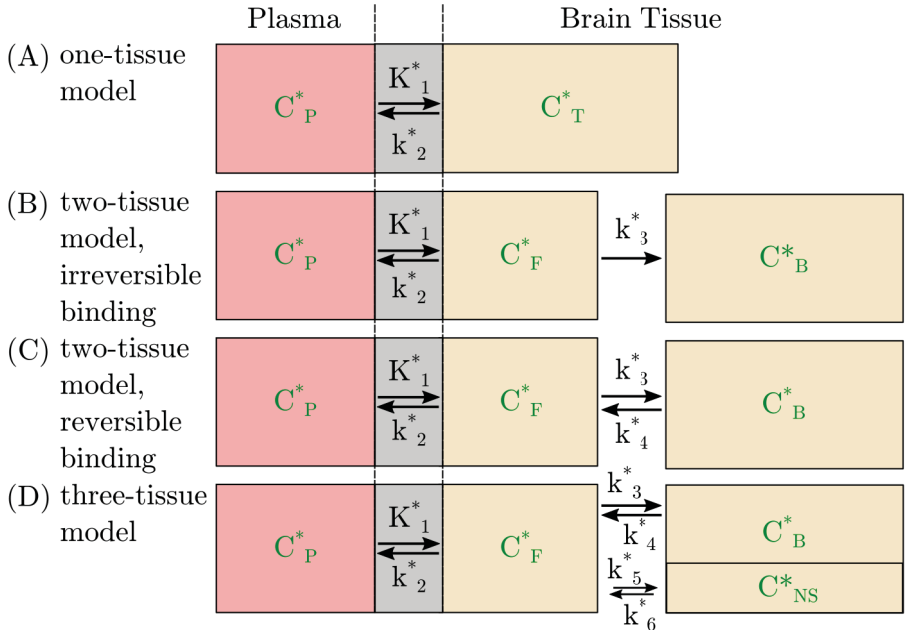

Figure 2.2: Exemplary box-diagrams for common compartment models. (A) One-tissue model for the determination of blood flow. (B) Two-tissue model for irreversible binding of the tracer. (C) Two-tissue model for reversible binding of the tracer. (D) Three-tissue model including non-specific binding of the tracer. C^* denotes the radiotracer concentration, the indices indicate the respective compartments (P: Plasma, T: Tissue, F: free/unbound, B: bound and NS: non-specifically bound), and the rate constants for transport between the compartments are labeled by k^*.

Detailed description of the application of a two-tissue compartment model to quantify cerebral glucose metabolism by [18F]FDG will be given in section 2.3.
While compartment models provide valuable information for various parameters of interest, they also require measurement of the input function and are computationally relatively time consuming due to the procedure of fitting the parameters [13]. Therefore, alternative approaches to estimate parameters of interest have been developed, including graphical analyses, reference region methods or semi-quantitative estimates. Those methods will be shortly described in section 2.4.

2.3 Kinetic Modeling of [18F]FDG PET Data

The most prominent application of PET is the measurement with [18F]FDG to assess glucose metabolism. From dynamic [18F]FDG PET data and knowledge of the input function one can quantify the cerebral metabolic rate (CMR_{glc}), i.e. glucose consumption in the central nervous system in units of μmoles/min/g tissue.
The original "deoxyglucose model", which was applied to measure the glucose consumption in the functional units of the central nervous system, goes back to Sokoloff et al. from 1977[30,11]. Originally it was applied to autoradiography and [14C] labeled 2-deoxy-d-glucose (DG) resulting in a compartmental model to mathematically describe the behavior of DG in cerebral tissue[11]. The method was then modified and applied to SPECT and [18F]FDG PET data[34,31,33].
The two-tissue compartment model for glucose and [18F]FDG underlying the method is shown in Figure 2.3. The following premises and assumptions for the model as well as the derivation of model equations are based on Phelps et al., 1979[31] and more recent developments are introduced based on Backes et al., 2011[35].
[18F]2-fluoro-2-deoxy-D-glucose ([18F]FDG) differs from glucose only in the replacement of the hydroxyl group at the second position by fluorine[11]. In the body [18F]FDG is taken up by the same transporters as glucose and is phosphorylated by hexokinase, the enzyme which also phosphorylates glucose. That means that [18F]FDG and glucose compete for the same carriers and enzymes, and occupy the same physical spaces. Note that transport of [18F]FDG and enzyme-mediated reactions have different efficiencies for glucose and [18F]FDG[11]. While glucose will be converted to pyruvate by glycolysis, the anomalous structure of [18F]FDG prevents metabolism after phosphorylation in the glycolytic pathway (Figure 2.4)[11,33,30,9]. This so-called "trapping" of [18F]FDG in metabolically active cells is the basis for the quantification of glucose metabolism and will be further elaborated in the following.
For [18F]FDG PET experiments [18F]FDG is injected intravenously into the subject to be investigated. [18F]FDG will then be distributed via the blood, more precisely the plasma, throughout the body. The concentration of [18F]FDG in plasma, C_P^*, is displayed on the left in Figure 2.3. For transport from plasma to brain [18F]FDG and glucose share and compete for glucose transporters (GluT) in the blood-brain barrier. Once in tissue, [18F]FDG and glucose enter a common precursor pool, where they are phosphorylated to [18F]FDG-6-phosphate and glucose-6-phosphate by the enzyme hexokinase (Figures 2.3 and 2.4)[31,11] . Note that, since transport of glucose and [18F]FDG from the interstitium into the cells is much faster than the transport from blood to interstitium as well as the phosphorylation reaction, the interstitium is effectively in equilibrium with the cellular compartment and they can be approximated as one common compartment (precursor pool)[31,11]. In the compartment model [18F]FDG and [18F]FDG-6-phosphate are therefore represented as two compartments with concentrations C_E^* (precursor pool) and C_M^* (metabolic products). Accordingly, glucose and glucose-6-phosphate concentrations are given in the compartment model and are labeled with C_E and C_M. The plasma glucose concentration is labeled by C_P. Since hydrolysis from [18F]FDG-6-phosphate back to free [18F]FDG is slow ($k_4^* \to 0$)

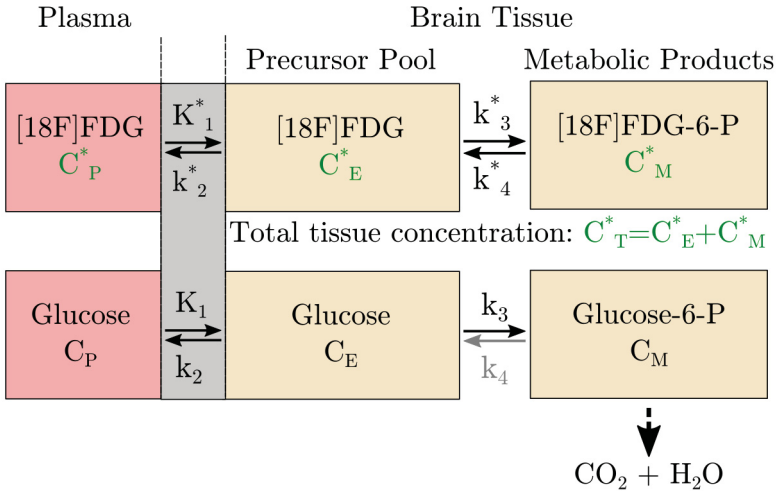

Figure 2.3: Two-tissue compartment model for glucose and [18F]FDG. Glucose and [18F]FDG are transported from plasma into the interstitium and into the cells (precursor pool) with rate constants K_1 and K_1^*. Transport from the precursor pool back to plasma is given by the rate constants k_2 for [18F]FDG and k_2^* for glucose. In the cytoplasm hexokinase phosphorylates glucose and [18F]FDG to glucose-6-phosphate and [18F]FDG-6-phosphate with the rate constants k_3 and k_3^*, respectively. The reactions from glucose-6-phosphate and [18F]FDG-6-phosphate back to glucose and [18F]FDG are described by k_4 and k_4^*. Glucose-6-phosphate is further metabolized, while [18F]FDG-6-phosphate is trapped within metabolically cells for the duration of the measurement. Compartments for glucose and [18F]FDG are drawn separately to emphasize that transport of [18F]FDG and enzyme-mediated reactions are distinct from those for glucose, even though [18F]FDG does compete for the same carriers and enzymes and occupies the same physical spaces as glucose [11].

and [18F]FDG-6-phosphate is not a suitable substrate for any other enzymes known to be present, [18F]FDG-6-phosphate is trapped and accumulates in metabolically active cells for the time of the measurement in proportion to the glucose metabolic rate [11,36]. Glucose-6-phosphate on the other hand is metabolized further via the tricarboxylic acid cycle (TCA) pathway producing adenosine triphosphate (ATP) as cellular energy substrate [11,9]. Alternatively glucose-6-phosphate can be a substrate for the pentose phosphate pathway [11,37].

The application of the model for quantification of local cerebral glucose utilization depends on the validity of the following assumptions and conditions [36]: (i) The model is only applicable to a localized region of tissue that is homogeneous with respect to blood flow, rates of transport of [18F]FDG and glucose between plasma and tissue, the concentrations of [18F]FDG, glucose, [18F]FDG-6-phosphate, glucose-6-phosphate and the rate of glucose utilization [36,30,33]. (ii) Throughout the time of measurement the glucose metabolism in the brain is assumed to be in a steady-state, i.e. the plasma glucose concentration, the rate of local cerebral glucose utilization, and the concentrations of the intermediates of the glycolytic pathway remain constant [36,30,31,11]. (iii) Moreover [18F]FDG and [18F]FDG-6-phosphate are

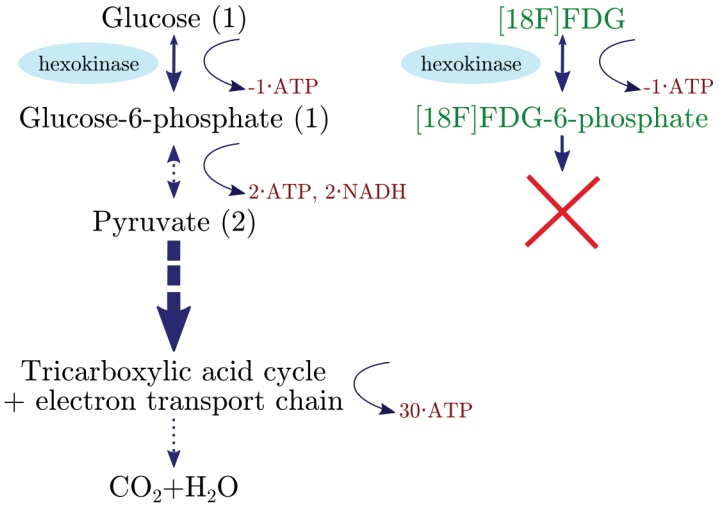

Figure 2.4: Metabolic pathways of glucose and [18F]FDG. Glucose in the cytoplasm will first be phosphorylated to glucose-6-phosphate by the enzyme hexokinase. From there it is further metabolized to two molecules of pyruvate. If oxygen is present pyruvate oxidation in the mitochondria takes place via the TCA cycle yielding ∼30 molecules of ATP (up to a theoretical maximum of 38 molecules). If no oxygen is available lactate will be produced yielding only 2 ATP molecules. [18F]FDG is taken up by the cells just as glucose and will also be phosphorylated, but in contrast to glucose, [18F]FDG-6-phosphate can not be further metabolized. The de-phosphorylation to [18F]FDG is slow, so that [18F]FDG-6-phosphate is trapped within the cytoplasm on the time scale of measurement.

only allowed to be present in tracer amounts, i.e. their molecular concentrations in blood and/or tissue are quantitatively and pharmacologically negligible[36,30,33]. (iv) Additionally, capillary plasma concentrations of [18F]FDG and glucose are assumed to be approximately equal to or bear a constant relationship to their arterial plasma concentrations[36,30].

Derivation of model equations for [18F]FDG and glucose

Following the injection of [18F]FDG into the blood the total content of [18F]FDG per unit mass of any tissue, C_T^*, is equal to the sum of the concentrations of the free [18F]FDG in the precursor pool, C_E^*, and its metabolic product [18F]FDG-6-phosphate, C_M^*, in that tissue (Figure 2.3):

$$C_T^*(t) = C_E^*(t) + C_M^*(t) \tag{2.1}$$

The concentrations are usually given in activity per tissue mass or volume.

The rate of change of tissue [18F]FDG concentration is given by the derivate of equation 2.1 with respect to time:

$$\frac{dC_T^*(t)}{dt} = \frac{dC_E^*(t)}{dt} + \frac{dC_M^*(t)}{dt}. \tag{2.2}$$

The rate of change of the free [18F]FDG concentration in tissue, $dC_E^*(t)/dt$, is equal to the difference between the rates of its transport into tissue from plasma (K_1^*) and its loss from tissue by transport back to plasma (k_2^*) and loss by hexokinase-catalyzed phosphorylation to [18F]FDG-6-phosphate (k_3^*) plus its increase from the back reaction to [18F]FDG (k_4^*):

$$\frac{dC_E^*(t)}{dt} = K_1^* C_P^*(t) - (k_2^* + k_3^*) C_E^*(t) + k_4^* C_M^*(t). \tag{2.3}$$

K_1^* is given in units of mL blood/min/mL tissue, while k_2^*, k_3^* and k_4^* are in units of min^{-1}. The unit of K_1^* is different, because K_1^* takes into account the different fractional volume of the plasma and the extracellular compartment.
Temporal accumulation of [18F]FDG-6-phosphate depends on the concentration of [18F]FDG in the precursor pool:

$$\frac{dC_M^*(t)}{dt} = k_3^* C_E^*(t) - k_4^* C_M^*(t). \tag{2.4}$$

Note that k_3^* is a function of hexokinase concentration.
Equations 2.3 and 2.4 can be integrated and solved for C_E^* and C_M^* as described elsewhere (see[11,31,36]), which yields:

$$C_E^*(t) = \frac{K_1^*}{\alpha_+ - \alpha_-}[(k_4^* - \alpha_-)\int_0^t C_P^*(t')e^{-\alpha_-(t-t')}dt' + (\alpha_+ - k_4^*)\cdot \int_0^t C_P^*(t')e^{-\alpha_+(t-t')}dt'] \quad \text{and} \tag{2.5}$$

$$C_M^*(t) = \frac{K_1^* k_3^*}{\alpha_+ - \alpha_-}[\int_0^t C_P^*(t')e^{-\alpha_-(t-t')}dt' - \int_0^t C_P^*(t')e^{-\alpha_+(t-t')}dt'] \tag{2.6}$$

where t is any given time following the injection of the [18F]FDG into the circulation and with,

$$\alpha_\pm = \frac{1}{2}(k_2^* + k_3^* + k_4^*) \pm \frac{1}{2}\sqrt{(k_2^* + k_3^* + k_4^*)^2 - 4k_2^* k_4^*}. \tag{2.7}$$

The functions for C_E^* and C_M^* defined in equations 2.5 and 2.6, can now be substituted for these variables in equations 2.1 to obtain the following equation[35]:

$$C_T^*(t) = A_- \int_0^t C_P^*(t')e^{-\alpha_-(t-t')}dt' - A_+ \int_0^t C_P^*(t')e^{-\alpha_+(t-t')}dt' \tag{2.8}$$

$$\text{with, } A_\pm = \frac{K_1^*}{\alpha_+ - \alpha_-}(k_3^* + k_4^* - \alpha_\pm). \tag{2.9}$$

Equation 2.8 defines the total tissue concentration of [18F]FDG as a function of time. C_T^* only depends on the tissue course of [18F]FDG in the plasma, C_P^*, and the kinetic rate constants K_1^*, k_2^*, k_3^* and k_4^*. Note, that the activity in blood also contributes to the PET signal. The average blood volume in a brain compartment is in the order of $\sim 3\%$ [31]. The PET signal can then be written as:

$$C_{PET}^*(t) = V_B C_B^* + (1 - V_B) C_T^*(t). \tag{2.10}$$

V_B is the blood volume in a compartment and C_B^* the activity of the blood.

The behavior of glucose is similar to that of [18F]FDG, but its mathematical description is simpler since a constant arterial plasma glucose concentration as well as steady-state of glucose uptake and metabolism in the brain can be assumed [11,30,31]. The rate constants K_1, k_2 and k_3 describe the transport from plasma to tissue (mL plasma/min/g tissue), transport from tissue to plasma (min^{-1}) and phosphorlyation of glucose to glucose-6-phosphate (min^{-1}) [11,30,31]. Hydrolysis from glucose-6-phosphate back to free glucose is negligible (k_4=0). The rate of changes of the free glucose concentration in the tissue, $dC_E(t)/dt$, is given by:

$$\frac{dC_E(t)}{dt} = K_1 C_P(t) - (k_2 + k_3) C_E(t). \tag{2.11}$$

Assuming steady-state conditions, i.e. $dC_E(t)/dt$=0, this yields the relation:

$$C_E = \frac{K_1 C_P}{k_2 + k_3}. \tag{2.12}$$

The rate of changes for the glucose-6-phosphate compartment C_M are:

$$\frac{dC_M(t)}{dt} = k_3 C_E(t) - CMR_{glc}, \tag{2.13}$$

with the parameter CMR_{glc} of interest.
Therefore, at steady-state, i.e. $dC_M(t)/dt$=0, the metabolic rate of glucose is given by:

$$CMR_{glc} = k_3 C_E. \tag{2.14}$$

Combining equations 2.14 and 2.12 results in:

$$CMR_{glc} = \frac{K_1 k_3}{k_2 + k_3} C_P. \tag{2.15}$$

$C_E/C_P = \frac{K_1}{k_2+k_3}$ is the so-called distribution volume of glucose.
Since the aim of the model is to calculate the CMR_{glc} from the [18F]FDG PET data, the differences between the rate constants of glucose (K_1, k_2 and k_3) and the rate constants of [18F]FDG (K_1^*, k_2^* and k_3^*) need to be taken into account.

Lumped constant

The so-called "lumped constant" converts rates of [18F]FDG uptake and phosphorylation into rates of glucose[31,11,36,33].
The classical derivation for the lumped constant (LC) can be found in Phelps et al. (1979)[31]. By taking the different rate constants of [18F]FDG and glucose into account in terms of the lumped constant, $\mathrm{CMR_{glc}}$ can be calculated as:

$$\begin{aligned} CMR_{glc} &= \frac{K_1^* k_3^*}{k_2^* + k_3^*} \frac{C_P}{LC} \\ &= K_i^* \frac{C_P}{LC}. \end{aligned} \tag{2.16}$$

C_P is the plasma glucose concentration. K_i^* is the combination of the rate constants K_1^*, k_2^* and k_3^* for [18F]FDG. LC can be measured directly by different methods and it has been shown that it is relatively stable under various physiological conditions[11]. In 1985 Reivich et al. reported a directly measured value of LC for [18F]FDG in the whole brain in humans under normal physiological conditions to be 0.52[36,33]. The range of reported values for LC ranges between 0.42 and 0.89 for the human brain[31,38,36]. Therefore, to make $\mathrm{CMR_{glc}}$ values obtained by this method comparable between studies the applied LC should always be given[36]. The use of LC as described above goes back to autoradiography data, where only a single time point of tissue activity is measured, and it was not possible to fit equation 2.10 to obtain the rate constants K_1^*, k_2^*, k_3^* and k_4^* separately.
Since in contrast to autoradiography PET provides the complete time course of the tissue activity, $C_T^*(t)$, equation 2.10 can be fitted to the data to obtain K_1^*, k_2^*, k_3^* and k_4^*, so that the differences in transport and phosphorylation can be disentangled. The differences in transport and phosphorylation of [18F]FDG and glucose are more likely to remain constant even in pathologic conditions, since they are based on the chemical properties of glucose and [18F]FDG. LC on the contrary, is affected by the ratio of glucose transporter to hexokinase concentration changes.
The ratios of the kinetic rate constants of [18F]FDG and glucose are:

$$\begin{aligned} L_1 &= K_1^*/K_1 \\ L_2 &= k_2^*/k_2 \\ L_3 &= k_3^*/k_3. \end{aligned} \tag{2.17}$$

Transport in and out of the cells are both mediated by glucose transporters (GluTs). Therefore, the differences between efficiencies for [18F]FDG and glucose of in- and outward transport are the same, i.e. $L_1{=}L_2$. This is equivalent with the (often used) assumption that K_1/k_2 equals K_1^*/k_2^*. L_3 describes the different efficiency of hexokinase for phosphorylating [18F]FDG and glucose. The values for L_1 and L_3/L_2 were determined by Hasselbach and colleagues to 1.48 and 0.26, respectively[39,40,35]. No species difference for L_1 was found[39], underpinning the fact that differences in efficiencies are based only on chemical different efficiencies of [18F]FDG and glucose to GluTs. The value of $L_3{=}0.38$ reported by Hasselbach et al. is in accordance with

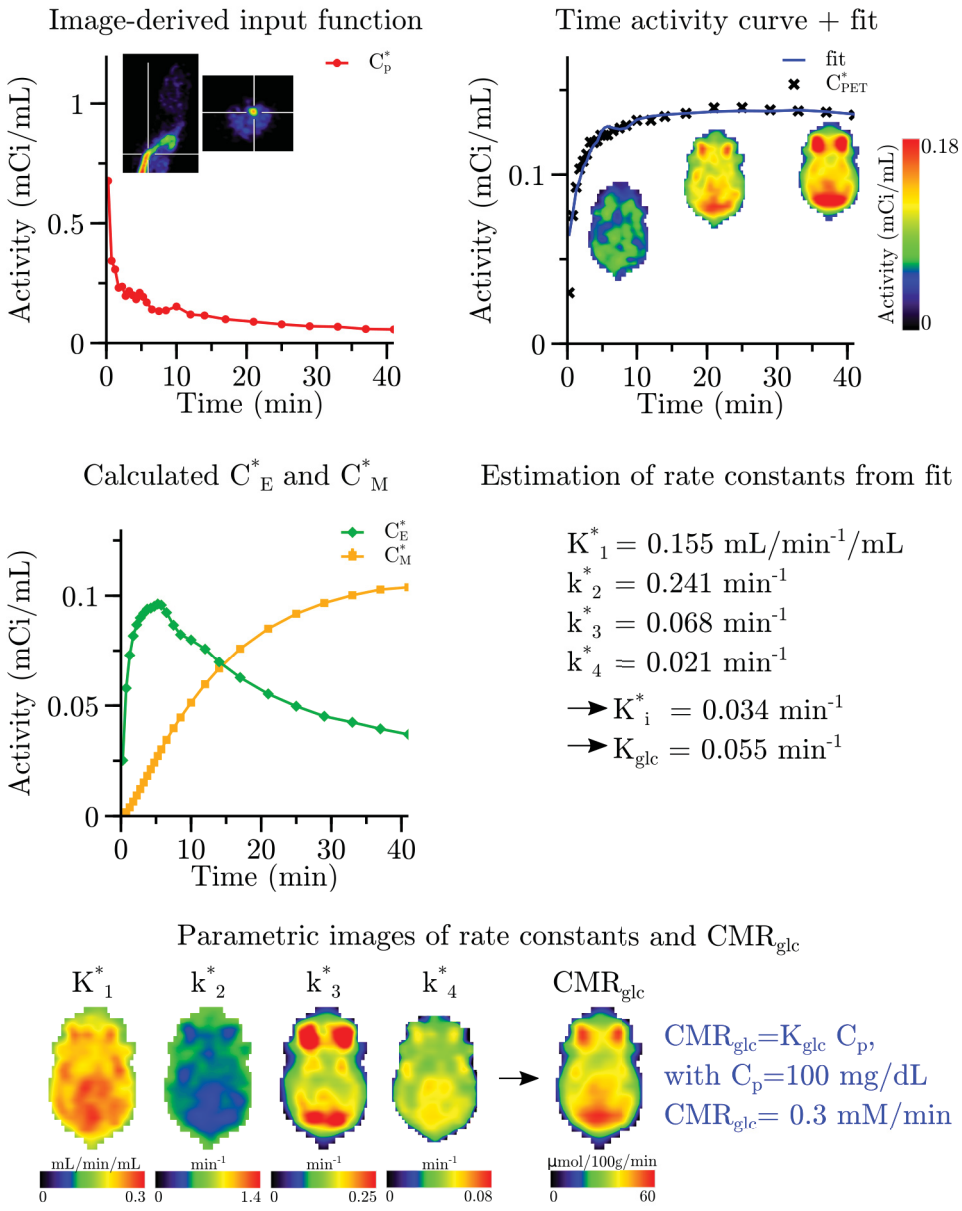

Figure 2.5: Procedure to fit [18F]FDG PET data and parametric image calculation. In the first time frames of [18F]FDG PET data the aorta can be located and an image-derived input function can be obtained. The [18F]FDG time activity data is used to fit equation 2.10 and thereby determining the rate constants K_1^*, k_2^*, k_3^* and k_4^*. The concentrations of [18F]FDG in the two compartments C_E^* and C_M^* can be calculated over time. For each rate constant voxelwise parametric images can be calculated. From that, a parametric image of CMR_{glc} is obtained and the absolute consumption of glucose in a region of interest can be analyzed. Data shown here is from a mouse brain.

the value reported by Cunningham and Cremer[41] of 0.37 in rats.
Using the relations in 2.17 the glucose consumption rate constant K_{glc} can be expressed as[35]:

$$K_{glc} = K_i^* \frac{1}{LC} = \frac{1}{L_1} \frac{K_i^*}{L_3/L_2 + (1 - L_3/L_2)K_i^*/K_1^*}. \tag{2.18}$$

The local glucose consumption is then given by:

$$CMR_{glc} = K_{glc} C_P. \tag{2.19}$$

The parameters K_i^* (i.e. K_1^*, k_2^* and k_3^*) and K_1^* can be obtained by fitting equation 2.10 to the [18F]FDG PET data with knowledge of the input function $C_P^*(t)$. The input function can either be obtained by arterial blood sampling or under certain conditions from the image data (image-derived input function) (see[42,43,44,35]). The blood glucose level C_P can simply be measured by a commercially available glucometer.
Parametric images of the rate constants as well as of $\mathrm{CMR_{glc}}$ can be calculated by the voxelwise fitting procedure. The procedure for calculation $\mathrm{CMR_{glc}}$ in a mouse brain is illustrated in Figure 2.5.

2.4 Further Methods for [18F]FDG PET Data Analysis

Other approaches than compartment models exist to analyze parameters of interest from PET data. Some methods were introduced since fitting of parameters is computationally relatively time consuming or was not possible at that time. An other reason was that the need of an input function was to be avoided. A short overview on some common methods is given here.

Graphical analyses

Graphical methods are based on the differential equations of the compartmental models. The model equations are converted into linear plots, in which the slopes represent measures of tracer binding/metabolic rates [28]. For graphical analysis radiotracer uptake data from a region of interest over time and the input function (either plasma measurements or uptake data from a reference region) are needed [45,28]. There are two types of graphical methods: (i) for irreversible binding (first described by Patlak et al. [46]) and (ii) reversible binding (first described by Logan et al. [47]) radiotracers. The so-called Patlak plot is the most frequently used method of graphical analysis with the outcome measure of K_i^* (the "effective net influx rate") and can be applied to [18F]FDG PET data. The so-called Logan method is typically applied to PET measurements with radioligands binding to neuroreceptors, and the outcome measure is the distribution volume (V_T) or distribution volume ratio (DVR) in the case of reference region input [48]. The main advantage of graphical analyses is that they are easy and quick to compute (also by hand) [45,28]. On the other hand they are relatively sensitive to noise and not every parameter of interest can be assessed by graphical analysis [45,28,13].

Reference regions

Reference region methods are mainly used for radiotracers binding to neuroreceptors with the aim to determine the binding potential (BP) of the radiotracer. The BP is related to the receptor density (see also below) and therefore a measure of interest. The underlying assumption for reference region models is that some regions in the brain are devoid of a specific receptor type, so that this region can be used as a so-called "reference region". The reference region can be described by a one-tissue model, while regions with a high density of receptors are described by a two-tissue model [13,28]. The most commonly used approach is the simplified reference tissue model (SRTM) developed by Lammertsma and Hume [49], which is shortly introduced here. Note, that the gold standard of reference tissue models is the full reference tissue compartment model (FRTC) by Cunningham et al. from 1991 [50]. For the SRTM the underlying assumption is that the ratio between the rate of transport from plasma to tissue and back is equal in all regions: $K_1^*/k_2^* = K_1^{*\prime}/k_2^{*\prime}$. Using $R_1 = K_1^*/K_1^{*\prime}$ and $BP = k_3^*/k_4^*$ results in a description of total tissue concentrations dependent on the three parameters R_1, k_2^* and BP (Figure 2.6) [49]. The equation for the tissue concentration can be solved by nonlinear fitting or further approaches in order to obtain parametric images of the model parameters [48]. The main advantage of reference region methods is that blood sampling is not necessary [13,28].

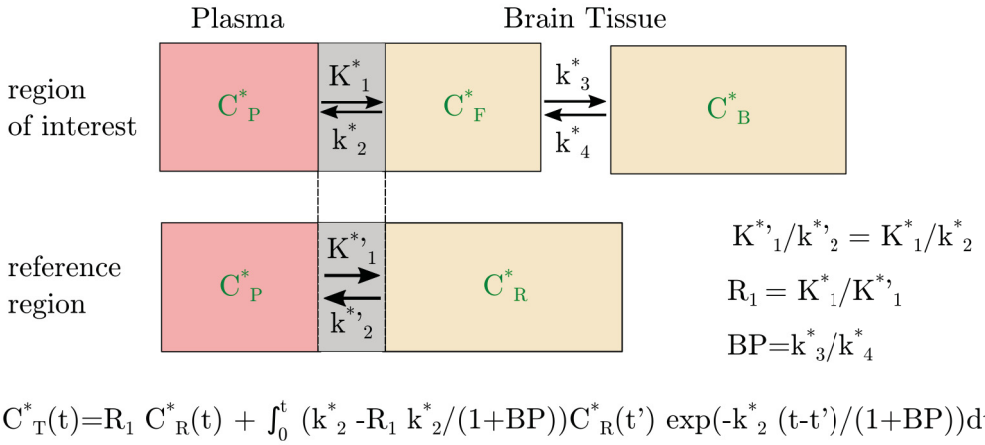

Figure 2.6: Simplified reference region model. The tracer is exchanged between tissue and plasma with the rate constants K_1^* and k_2^* in the region of interest and in the reference region with $K_1^*/k_2^* = K_1^{*\prime}/k_2^{*\prime}$. R_1 is introduced as $R_1 = K_1^*/K_1^{*\prime}$. In the region of interest the tracer binds to reversibly to the available binding sites and the binding potential BP is given by k_3^*/k_4^*. The total tissue concentration can finally be described by the three parameters k_2^*, R_1 and BP.

Semiquantitative estimates

The standardized uptake value (SUV) is calculated as the measured radioactivity normalized to the bodyweight of the subject and to the administered amount of radioactivity[51]. The normalization can be applied frame-by-frame or to a sum of time frames for a specific time-window resulting in a static image. The SUV is a unit-less value estimating tracer uptake. The advantage of SUV's is that they enable comparisons between different scans and subjects. Moreover no arterial blood sampling and long scan durations are needed. Due to its simplicity SUV's are used in clinical routine applications, most commonly applied in oncology to identify tumor tissue. However, it is not suitable for quantitative analysis.
The standardized uptake value ratio (SUVR) relates the measured tissue radioactivity to that of a reference region and is rather used in neurological studies. Here, the SUVR is a measure for the relative contribution of specific and non-specific binding.[13]

2.5 NeuroPET: Principles and Methods

PET brain imaging enables the visualization and analysis of neurotransmitter systems *in vivo* by using tracers that bind to different locations in the neurotransmitter pathway. Three common locations of radiotracer binding are pre-synaptic neurons (e.g. transporters), post-synaptic neurons (e.g. receptors) or intra-neuronal binding sites[52,12]. Measures of NeuroPET applications are the receptor/transporter density, the binding affinity by which the radiotracer binds to the receptors/transporters of interest, or enzyme synthesis rates[12,11]. Moreover distribution, concentration and occupancy of drug targets can be studied, for example in the process of medical drug development[53].
NeuroPET applications are usually based on two- or three-tissue reversible or irreversible compartment models depending on the used radiotracer. For the analysis most commonly graphical methods like the Logan or Patlak plot[47,46] or reference tissue models[50,49,54] are applied. Within this section, relevant parameters and assumptions for radiotracers binding to receptors or transporters are introduced.
The binding potential (BP) of a radiotracer is defined as[29,55,56]:

$$BP = \frac{B_{max}}{k_D} = \text{receptor density} \cdot \text{affinity}. \tag{2.20}$$

$B_{\max}$ is the total receptor density in a region of interest and k_D is the equilibrium dissociation constant of the radiotracer both given in units of "concentration", e.g. nM[55,56]. The binding affinity is given by the inverse of k_D, which equals the ratio of the dissociation (k_{off} in time^{-1}) and the equilibrium association (k_{on}, concentration^{-1}time^{-1}) rate of the tracer[56]:

$$k_D = \frac{k_{off}}{k_{on}}. \tag{2.21}$$

The dissociation rate k_{off} equals k_4^* in the compartment model representation introduced before.
Due to occupancy of binding sites by the endogenous ligand, i.e. the neurotransmitter, not all receptors ($B_{\max}$) are available for binding for the radiotracer. The term B_{avail} describes the receptor density that is available for binding of the tracer[55]. For the BP the quantity BP_F was introduced, which takes into account only the fraction of free binding sites[55]:

$$BP_F = \frac{B_{avail}}{k_D}. \tag{2.22}$$

In the case that all binding sites $B_{\max}$ would be available for binding, the binding rate constant k_3^* in the compartment model representation equals $k_{on}B_{\max}$.
In the presence of an endogenous ligand it is:

$$k_3^* = k_{on}B_{avail} = k_{on}(B_{max} - C_B - C_B^*). \tag{2.23}$$

C_B is the concentration of the endogenous ligand that is bound to the target binding site and C_B^* the concentration of bound radiotracer. Due to the tracer principle, i.e.

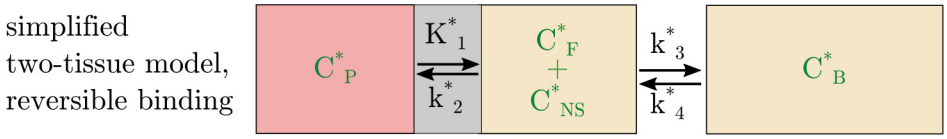

Figure 2.7: Two-tissue reversible compartment model including non-specific binding. The fractions of free C_F^* and non-specifically bound C_{NS}^* concentrations are kinetically indistinguishable after (rapid) equilibrium is reached between them. Therefore they are combined in a single compartment. This simplifies the three-tissue compartment model that takes into account the free (C_F^*), the non-specifically (C_{NS}^*) and the specifically (C_B^*) bound compartments to a two-tissue model. This also reduces the parameters to be estimated.

low injected concentrations of the radiotracer, C_B^* can be neglected in most cases ($C_B^* << C_B$).
Usually one is interested in the specific binding of the radiotracer, meaning the binding to the target receptor/transporter. However, often non-specific binding of the radiotracer is observed. This means that the radiotracer binds not only to the target receptor/transporter, but also to other binding sites. The term non-displaceable uptake is the sum of non-specific and free radiotracer concentrations in tissue. It is called non-displaceable since this fraction can not be removed by adding large amounts of non-labeled ("cold") tracer [57,48]. The non-displaceable binding potential BP_{ND} is defined as [55]:

$$BP_{ND} = f_{ND}\frac{B_{avail}}{k_D} = \frac{V_T}{V_{ND}} - 1. \tag{2.24}$$

f_{ND} is the fraction of non-displaceable binding and V_{ND} is the non-displaceable volume of distribution [55]. V_T is volume of distribution of the radiotracer and equals $K_1^*/k_2^*(1 + k_3^*/k_4^*)$ for a two-tissue compartment model [57]. Note, that the term "volume of distribution" in the PET field refers to the ratio of radiotracer concentration in tissue to the radiotracer concentration in plasma with units of mL/cm^3 [55]. V_T therefore equals $V_T = C_T^*/C_P^*$. Since a tissue compartment contains specifically bound (C_B^*), free (C_F^*) and non-specifically bound (C_{NS}^*) radiotracer, the total radiotracer concentration, C_T^*, is the sum of those concentrations [55,57]. Furthermore, the non-displaceable radiotracer concentration, C_{ND}^*, is the sum of non-specific and free concentration as indicated in Figure 2.7 [55]:

$$C_{ND}^* = C_F^* + C_{NS}^*. \tag{2.25}$$

The ratio of V_T to V_{ND} is referred to as distribution volume ratio (DVR) [57]. V_T and V_{ND} can be obtained for example with the Logan method including a reference tissue that only contains non-specific binding.
The DVR can be estimated for example by the (simplified) reference tissue compartment model or the Logan plot including a reference tissue.

To understand the brain under physiological and disease conditions not only the receptor density or distribution volumes, which are static measures, but also the dynamic of neurotransmitter systems (e.g. the assessment of release events) is of great interest. Tools that are able to image and quantify neurotransmitter concentration changes, which are for example induced by a certain drug, are therefore needed.
Several reports demonstrate that PET, using a radiotracer with a low to moderate affinity for a receptor of interest, is able to evaluate neurotransmitter release after pharmacological manipulation[58,13]. In 1989 Seeman et al. observed that endogenous dopamine lowers the dopamine D2 receptor density measured by [3H]raclopride in vitro[59]. Based on that observation, the theory emerged that endogenous neurotransmitter and radiotracer compete for the same binding sites. Therefore, an increasing endogenous neurotransmitter concentration leads to displacement of the radiotracer and vice versa. This principle is referred to as "competition model" or "occupancy model" (Figure 2.8).
Today, [11C]raclopride is available as PET radiotracer, which is as [3H]raclopride, a dopamine D2 receptor antagonist with a relative low to moderate affinity. Over the last decades [11C]raclopride was used in various studies for the assessment of changes in dopamine levels in animals and humans[60,23,61,62,63,64,65,66,67,68,69,70,71,72]. Usually, the outcome measure of these applications is the BP, and changes in BP are interpreted according to the competition model. Either "blocking" or "displacement" studies were performed[58,73]. In "blocking" studies radiotracer binding is measured under control conditions and *after* pharmacological intervention, which is supposed to induced changes in receptor occupancy. In "displacement" studies the pharmacological intervention occurs *during* the scan, so that only one scan session needs to be performed[58,73]. For displacement experiments a bolus-plus-constant infusion radiotracer injection protocol to reach steady-state conditions before the intervention has been shown to be useful. Once equilibrium is reached the BP can be calculated as the ratio of the radiotracer concentration in a region of interest (ROI) to its concentration in a reference region: $BP_{ND} = (C_{ROI} - C_{REF})/C_{REF}$[73]. The change in specific binding of the tracer after the "stimulus", e.g. the pharmacological intervention, is then monitored[74]. Importantly, several studies showed release-dependent changes in [11C]raclopride binding that were proportional to drug-induced increases in dopamine concentrations as measured by direct methods like microdialysis[23,65,53].
Originally, [11C]raclopride PET data analysis methods were based on kinetic three-tissue compartment models including an arterial input function[64], the graphical Logan plot method[62,63,75], two-compartment models with the cerebellum as input function (e.g the SRTM)[76,58,73] or the peak equilibrium method[61,77]. Using the Logan plot method distribution volume ratios between striatum and cerebellum at baseline and after pharmacological intervention of amphetamine, methylphenidate or other drugs that increase dopamine levels, were calculated ($DVR = BP_{ND} + 1$)[62,75,23]. The striatum is the region in the brain with the highest D2 receptor density, while the cerebellum is assumed to be devoid of D2 receptors and therefore serves as reference region (no specific binding). An overview and description of nomenclature and model approaches for those early methods can be found by Slifstein and Laruelle (2001)[56].

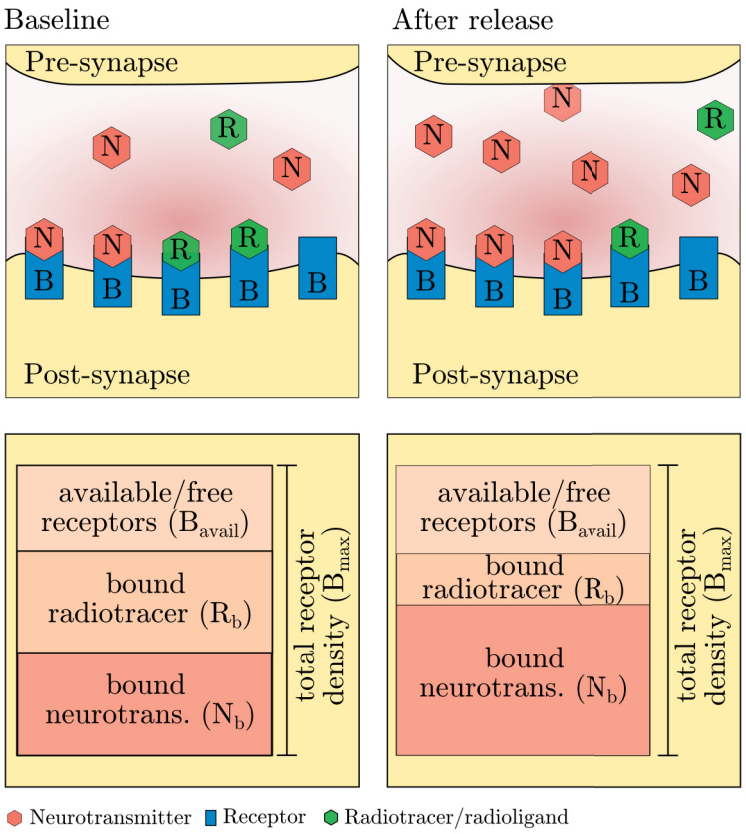

Figure 2.8: Classical competition model. In steady-state part of the total available receptors are occupied by the neurotransmitter (N_b) and a small fraction (tracer principle) by the radiotracer (R_b). After release of endogenous neurotransmitter a higher fraction of receptors are bound by the neurotransmitter and part of the radiotracer is displaced, since both compounds compete for binding. A radiotracer with a moderate to low affinity for the receptor is more sensitive to neurotransmitter concentration changes. High affinity radiotracers are less sensitive for displacement by the endogenous neurotransmitter.

With time more advanced methods were developed that take into account the temporal varying dopamine concentration and the interaction between dopamine and the radiotracer. These approaches are not based on steady-state conditions anymore and allow for a temporal component. The first reported method including a temporal component by Alpert et al.[68] is a linear extension of the simplified reference tissue model by Lammertsma and Hume[49]. In that approach the model includes a time-dependent component, which is fitted to the data to measure time-dependent changes in dopamine release. The method is sensitive enough to detect changes in dopamine concentrations in individuals and has been applied to measure release during motor tasks[67,73]. Criticism about this approach occurred due to the fact that the tasks lead to changes in blood flow, which might elicit alterations in the dynamic PET

data that are not distinguishable from the effect of dopamine release [73]. Further methods are developed by Morris, Constantinescu, Normandin and colleagues termed "ntPET" (neurotransmitter PET) and are either model-based/ "parametric" ("p-ntPET") [78] or data-driven/"non-parametric" ("np-ntPET") [79]. The newest method called "lp-ntPET" is based on the model by Alpert et al. [71,72] by extending the linearized simplified reference region method (LSRRM) using a set of basis functions to characterize the time course of neurotransmitter activation [71]. With the use of these methods temporal patterns of dopamine fluctuations can be extracted [80]. Overall, methods to assess dopamine release using PET have provided various information on the role of dopamine – amongst others – in the healthy brain as well as in the pathophysiology of addiction, Parkinson's disease and schizophrenia [53].
However, the measurement of endogenous neurotransmitter release, especially under physiological conditions (i.e. without pharmacological intervention) is still challenging [13]. First of all, suitable radiotracers that are sensitive to small changes in neurotransmitter concentration are required, because physiological release events are thought to lead to much smaller concentration changes as induced by drugs [13]. Moreover, radiotracer kinetics are rather slow compared to neurotransmitter actions, which limits the interaction time scale. A further limitation is that the methods referred above are restricted to the analysis of the striatum, because of low extrastriatal [11C]raclopride binding as consequence of small extrastriatal D2 receptor densities. Therefore, studies using higher affinity radiotracers to investigate extrastriatal dopamine release were conducted and are reviewed in Finnema et al. (2015) in Table 1 [53]. Furthermore, attempts have been made to apply the methodologies, developed to assess dopamine release using PET, to other systems with suitable radiotracers. An overview on the investigation of serotonin, noradrenaline, GABA, glutamate and acetylcholine is given in Finnema et al. (2015) [53].
Within the framework of this thesis a novel method to analyze PET data for the detection of neurotransmitter release was developed and is introduced in the next chapter. In contrast to the approaches referred to in this section, which analyze net reductions in regional tracer binding, the novel methods takes into account temporal fluctuations of the radiotracer signal. The method will be validated by experimental studies and is substantiated by a theoretical model. Taken together, it will be demonstrated that the novel approach allows spatiotemporal assessment of neurotransmitter release at physiological levels.

3 Spatiotemporal Assessment of Neurotransmitter Release using PET

Neurotransmission is a fundamental principle of signal transfer in the brain. In general a neurotransmitter is characterized by the following criteria: (i) it is synthesized in neurons or is otherwise present within it, (ii) it must be released when the neuron is active (upon depolarization) and lead to a response in its target cell mediated by neurotransmitter-specific receptors and (iii) it is removed from the site of action after transmission (e.g. by re-uptake or metabolic inactivation by specific enzymes)[81,82,83,84]. The various different neurotransmitters existing in the CNS can be classified by their chemical class. An overview of the different classes of neurotransmitters is given in Figure 3.1. Glutamate and γ-Aminobutyric acid (GABA) are for example neurotransmitters of the class of amino acids. To the class of monoamines belong – amongst others – the three catecholamines dopamine, norepinephrine and epinephrine as well as 5-hydroxytryptamine/Serotonin (5-HT), histamine, and melatonin.[83,81,85] The first neurotransmitter to be discovered was acetylcholine, which is a cholinergic agonist and does not belong to any of the groups[83,81]. So far more than 50 peptide "neurotransmitters" have been discovered, examples are oxytocin and the opioid peptides. The neuropeptides are often referred to as neurotransmitters, but actually belong to the class of "neuromodulators" as they differ from "classical" neurotransmitters[81]. Sometimes also gases, like nitric oxide, are categorized as neurotransmitters and are referred to as "gasotransmitters". Gasotransmitters are produced in the neural cytoplasm from where they immediately diffuse through the cell membrane into the extracellular fluid and into nearby cells to stimulate production of second messengers[85,81].

Each neurotransmitter system is composed of the neurotransmitter, a set of receptors and different re-uptake or removal mechanisms. Furthermore, specific neuron groups can be concentrated, or widely spread within the CNS so that their projections form so-called neural pathways. Therefore each neurotransmitter system has its own characteristics and, importantly, its specific function within the body. Neurotransmitter signaling regulates almost all physiological and psychological functions of the body and malfunctions can lead to various diseases. Therefore, understanding neurotransmitter signaling under physiological and pathophysiological conditions is important. However, as neurotransmitter signaling includes a vast range of temporal and spatial scales, its investigation is challenging: In response to perception of a macroscopic stimulus, the neurotransmitter is released into only $\sim$20-30 nm broad synapses, binds within milliseconds to intrasynaptic receptors and diffuses into the extracellular space, where it binds to extrasynaptic receptors and thereby triggers secondary processes, which eventually cause changes in macroscopic behavior[86].

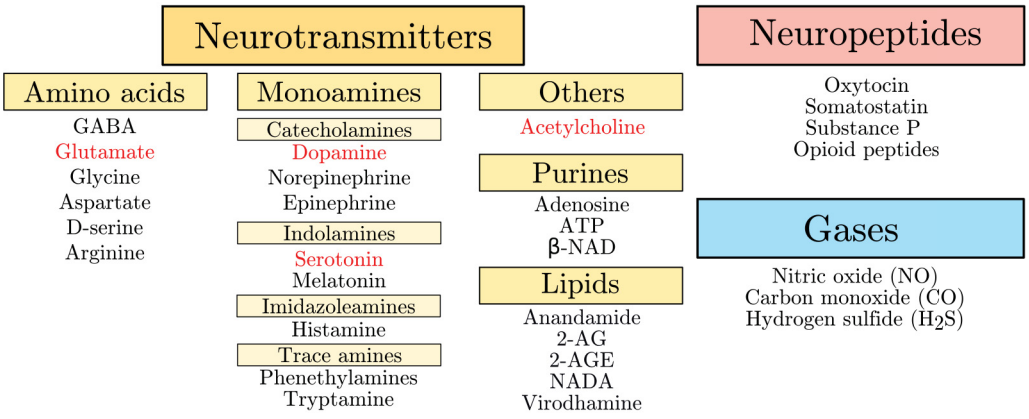

Figure 3.1: Classification of neurotransmitters. Neurotransmitters can be classified by their chemical structure. The major classes are given by amino acids, including the main excitatory and inhibitory neurotransmitters within the CNS glutamate and GABA, and the monoamines with neurotransmitters like dopamine, serotonin, epinephrine and norepinephrine. Another important neurotransmitter is acetylcholine, which does not belong to any of the classes. Furthermore some purines and lipids are known to play a role in neurotransmission. Neuropeptides are no classical neurotransmitters and are often referred to as neuromodulators [81]. The same applies to gasotransmitters. Neurotransmitters which are analyzed further within the thesis are highlighted in red. Abbreviations are: GABA - γ-Aminobutyric acid, ATP - adenosine triphosphate, β-NAD - nicotinamide adenine dinucleotide, 2-AG - 2-arachidonoylglycerol, 2-AGE - 2-arachidonyl glyceryl ether and NADA - N-arachidonoyl dopamine.

Available methods to analyze these processes can only address single aspects of this complex cascade (see also Lippert and Cremer et al. (2019) [86]).
Even though PET enables for the visualization and quantification of neuroreceptor binding and – under certain conditions – changes in neurotransmitter concentrations, to date, the spatiotemporal release of specific neurotransmitters at physiological levels in the human brain cannot be detected (see section 2.5) [86]. Within this thesis a method is presented that uses PET to time-dependently monitor stimulus-evoked neurotransmitter release at physiological levels.
In the chapter "Theoretical Framework and Experimental Data" the underlying assumptions for the novel approach are elaborated by deriving differential equations describing the kinetics of the neurotransmitter, the radiotracer and their interaction on basis of a compartment model (section 3.1.1). The resulting model is used to theoretically analyze PET signal variations under different conditions, and to analyze the influence of different parameters (section 3.1.2). Further model calculations for the dopamine system and common radiotracers, using realistic parameters from literature, are performed (section 3.1.3), followed by experimental application of the novel method to [11C]raclopride PET data from mice and humans (sections 3.1.4 and 3.1.5). The results of a first pilot study with [18F]DMFP in mice are shown in section 3.1.6. To validate the kinetic behavior of neurotransmitters in the extracellular

space that is assumed for the model continuous fast-scan cyclic voltammetry (FSCV) data were acquired. Using the data, a connection between fast synaptic release events and longer lasting concentration increases in the extracellular space could be demonstrated. The relation is further substantiated by theoretical model calculations taking into account diffusion and transport of the neurotransmitter (section 3.1.7). In the last section of "Theoretical Framework and Experimental Data" characteristics of further (other than dopamine) neurotransmitter systems and common radiotracers for the respective systems are introduced and the systems are analyzed using the theoretical model with regard to applicability of the novel method (section 3.1.8). Methodological details and experimental protocols can be found in section 3.2. The theoretical and experimental results will be discussed in section 3.3 and a short conclusion will be given in section 3.4.

Note that the underlying principle of the method as well as data and results of the [11C]raclopride PET studies in mice and humans, such as the dopamine FSCV measurements are published in the manuscripts by Lippert and Cremer et al. (2019) and Thanarajah and Backes et al. (2018) [86,87]. The novel method for PET data analysis and the underlying theoretical model were developed by Heiko Backes and me. The PET data in mice were acquired by Rachel Lippert, Heiko Backes and me. Human [11C]raclopride PET data were acquired at the Max Planck Institute for Metabolism Research in collaboration with the group of Marc Tittgemeyer by Sharmili Edwin Thanarajah. Dopamine FSCV recordings were performed at the University of Oxford by Clio Korn and Lauren Burgeno of Marc Walton's group and the transient template analysis was programmed by Thomas Jahans-Price. The serotonin FSCV recordings were performed by Alyssa West of Parastoo Hashemi's group at the University of South Carolina. All model calculations and data analyses – unless otherwise noted – were done by me.

3.1 Theoretical Framework and Experimental Data

3.1.1 Compartment Model: Kinetics of Neurotransmitter and Radiotracer

Derivation of model equations

A full compartment model of endogenous neurotransmitter release into the synapse and extracellular space (ECS), as well as, of radiotracer delivery and binding is visualized in Figure 3.2.

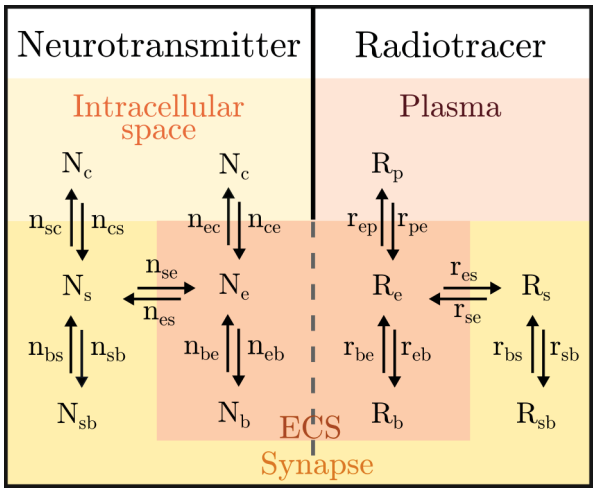

Figure 3.2: Full compartment model for the interaction between endogenous neurotransmitter and radiotracer. (A) Synaptic and extracellular compartments are shared by the endogenous neurotransmitter and the radiotracer. The neurotransmitter is supplied from and cleared into the intracellular space, the radiotracer from the blood. Compartments of the neurotransmitter are labeled with N, transfer rate constants of the neurotransmitter with n, radiotracer compartments with R and transfer rate constants with r. Subscripts are c: intracellular space, p: plasma, s: synapse, e: extracellular (extrasynaptic) space, b: bound to receptor in the extracellular space, sb: bound to receptor in synapse. The Figure (modified) is part of Figure 1 in the manuscript by Lippert and Cremer et al. [86].

Synaptic release events lead to neurotransmitter concentration increases in the synaptic cleft with the fractional volume V_s. Due to the high concentration gradient at the borders of the synapse part of the released neurotransmitter diffuses into the extrasynaptic ECS with volume V_e. In the synaptic cleft, as well as, in the ECS the neurotransmitter binds to certain binding sites, e.g. special receptors or enzymes. While the neurotransmitter is supplied from and cleared into the intracellular space, the radiotracer is transported to the brain after intravenous injection and crosses the blood brain barrier (BBB), where the concentration in the extracellular fluid will equilibrate by passive diffusion. Passive diffusion of the radiotracer between plasma and brain tissue is described by the rate constants r_{pe} and r_{ep}. The radiotracer is then distributed throughout the ECS, where it can be found as free compound with

concentration R_{e}. From here the radiotracer can also reach the extracellular synaptic space with the fractional volume V_{s}. Within these compartments, R_{e} and R_{s}, the radiotracer reversibly binds to the binding sites of interest.
The total radiotracer concentration and therefore PET signal, R, in a certain tissue volume ($\vec{x}$) is the sum of all compartments:

$$R(\vec{x},t) = V_p R_p(\vec{x},t) + V_e(R_e(\vec{x},t) + R_b(\vec{x},t)) + V_s(R_s(\vec{x},t) + R_{sb}(\vec{x},t)). \qquad (3.1)$$

Here, R_{p} is the radiotracer concentration in plasma with fractional volume V_p, R_{e} the free concentration in the extrasynaptic ECS, R_{b} is the concentration of bound radiotracer in the extrasynaptic ECS, R_{s} the free concentration in the synapses, and R_{sb} the concentration of intrasynaptic bound radiotracer (see Figure 3.2, right side: "Radiotracer"). Given that the free concentrations of the radiotracer in tissue are equilibrated, i.e. R_{e}=R_{s} and that the amount of bound radiotracer, R_{b}, is in the order of magnitude of free radiotracer, R_{e}, the contributions of the synaptic radiotracer to the volume signal can be neglected due to the small volume of synapses relative to the ECS volume ($V_{\mathrm{s}} \ll V_{\mathrm{e}}$). If we further assume the contribution of radiotracer in the blood to be negligible due to the small fractional volume of this compartment ($\sim 3\%$), the total radiotracer signal in a tissue volume is $R(\vec{x},t) = R_e(\vec{x},t) + R_b(\vec{x},t)$. Since the PET signal is dominated by the extrasynaptic ECS compartment, it is modulated effectively only by neurotransmitter concentrations in the extrasynaptic ECS. The simplified compartment model for the extrasynaptic ECS is shown in Figure 3.3.
The neurotransmitter can be found in the extrasynaptic ECS as free compound with the concentration $N_{\mathrm{e}}(\vec{x},t)$ and as bound to available binding sites with the concentration $N_{\mathrm{b}}(\vec{x},t)$. Temporal variations of the free neurotransmitter concentration $N_{\mathrm{e}}(\vec{x},t)$ are given by release events, which increase the neurotransmitter concentration, and removal mechanisms (e.g. transport back into the cell). Within the model a source (release event) and removal term is used for simulation of the free neurotransmitter concentration, as will be explained later in more detail. The rate of change in neurotransmitter concentration within the bound tissue compartment is given by the ordinary differential equation that describes the flux of neurotransmitter in and out of the respective compartments, i.e. binding and unbinding to the binding sites (Figure 3.3):

$$\frac{dN_b(\vec{x},t)}{dt} = n_{eb}(\vec{x},t)N_e(\vec{x},t) - n_{be}N_b(\vec{x},t). \qquad (3.2)$$

Note that the rate constant $n_{\mathrm{eb}}(\vec{x},t)$ depends on the available binding sites B_{avail}, i.e. $n_{\mathrm{eb}}(\vec{x},t)$=$n_{\mathrm{on}}B_{\mathrm{avail}}(\vec{x},t)$. The maximal binding rate in the case that all binding sites are available for binding is $n_{\mathrm{eb,max}}$ with $n_{\mathrm{eb,max}}$=$n_{\mathrm{on}}B_{\mathrm{max}}$. B_{max} is the total (bound plus free) amount of binding sites accessible for neurotransmitter and radiotracer. n_{on} is the association rate constant given in units of concentration^{-1}time^{-1} and is a chemical property of the neurotransmitter/receptor interaction. n_{be} equals n_{off} and describes the dissociation from the binding site. The ratio n_{D}=$n_{\mathrm{be}}/n_{\mathrm{on}}$ is known as

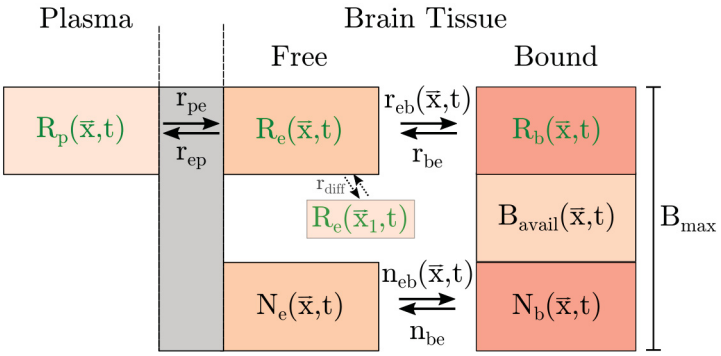

Figure 3.3: Simplified compartment model for the interaction between endogenous neurotransmitter and radiotracer in the ECS. The radiotracer is transported from plasma into the ECS of the tissue with a rate constant r_{pe}. The transport from tissue back to plasma is given by r_{ep}. In tissue the radiotracer can be found as free compound or bound to binding sites. The rate of binding to receptors is given by r_{eb}, unbinding by r_{be}. The neurotransmitter is present in the ECS due to diffusion from the synaptic space. Binding and unbinding to receptors is described by the rate constants n_{eb} and n_{be}. A total concentration of binding sites B_{max} are available for the radiotracer and neurotransmitter. The available fraction of binding sites B_{avail} influences the binding rates r_{eb} and n_{eb}.

dissociation constant and its inverse is called binding affinity.
Assuming that the free concentration of the neurotransmitter in the ECS, $N_{\mathrm{e}}(\vec{x},t)$, varies in time due to release events and removal mechanisms, the amount of bound neurotransmitter in the ECS, $N_{\mathrm{b}}(\vec{x},t)$, varies as well according to equation 3.2, leading to a change in the number of available binding sites, B_{avail}, and the binding rate constant, $n_{\mathrm{eb}}(\vec{x},t)$:

$$\begin{aligned} n_{eb}(\vec{x},t) &= n_{on} B_{avail}(\vec{x},t) \\ &= n_{eb,max}(\vec{x})(1 - \frac{N_b(\vec{x},t)}{B_{max}(\vec{x})} - \frac{R_b(\vec{x},t)}{B_{max}(\vec{x})}). \end{aligned} \tag{3.3}$$

Note, that the fraction of binding sites blocked by the radiotracer is negligible in comparison to the total amount of binding sites ($R_{\mathrm{b}}(\vec{x},t)/B_{\mathrm{max}} \rightarrow 0$) since the tracer is injected in "tracer doses". Thus the binding rate, $n_{\mathrm{eb}}(\vec{x},t)$, effectively varies according to:

$$n_{eb}(\vec{x},t) = n_{eb,max}(\vec{x})(1 - \frac{N_b(\vec{x},t)}{B_{max}(\vec{x})}). \tag{3.4}$$

The time-dependent changes in the free and bound radiotracer concentration within the ECS compartment are given by the following two differential equations (Figure 3.3):

$$\frac{dR_e(\vec{x},t)}{dt} = r_{pe}R_p(\vec{x},t) - (r_{ep} + r_{eb}(\vec{x},t))R_e(\vec{x},t) + r_{be}R_b(\vec{x},t) + D_R \triangle R_e(\vec{x},t) \tag{3.5}$$

$$\frac{dR_b(\vec{x},t)}{dt} = r_{eb}(\vec{x},t)R_e(\vec{x},t) - r_{be}R_b(\vec{x},t). \tag{3.6}$$

Here, it is further assumed that the free radiotracer fraction can diffuse within the ECS. D_R is the diffusion constant of the radiotracer in the ECS and $\triangle$ the Laplace operator. The binding rate constant $r_{\mathrm{eb}}(\vec{x},t)$ depends, as for the neurotransmitter, on the available binding sites $B_{\mathrm{avail}}(\vec{x},t)$ and is therefore dependent on $N_{\mathrm{b}}(\vec{x},t)$:

$$r_{eb}(\vec{x},t) = r_{eb,max}(\vec{x})(1 - \frac{N_b(\vec{x},t)}{B_{max}(\vec{x})} - \frac{R_b(\vec{x},t)}{B_{max}(\vec{x})}). \tag{3.7}$$

The same relations as for the binding constant of the neurotransmitter apply. r_{on} is the association rate of the radiotracer to the binding site, $r_{\mathrm{eb}}(\vec{x},t)$=$r_{\mathrm{on}}B_{\mathrm{avail}}(\vec{x},t)$ and the maximal binding rate is $r_{\mathrm{eb,max}}$=$r_{\mathrm{on}}B_{\mathrm{max}}$. As the concentration of blocked binding sites by the radiotracer can be neglected ($R_{\mathrm{b}}/B_{\mathrm{max}} \to 0$) the effective binding rate is:

$$r_{eb}(\vec{x},t) = r_{eb,max}(\vec{x})(1 - \frac{N_b(\vec{x},t)}{B_{max}(\vec{x})}). \tag{3.8}$$

The free and bound radiotracer concentrations $R_{\mathrm{e}}(\vec{x},t)$ and $R_{\mathrm{b}}(\vec{x},t)$ will therefore predominantly be influenced by changes in the extrasynaptic ECS bound neurotransmitter concentration, $N_{\mathrm{b}}(\vec{x},t)$, via the binding rate $r_{\mathrm{eb}}(\vec{x},t)$.
Since we use a bolus-plus-constant infusion protocol for radiotracer injection, we can assume steady-state conditions. This means that at baseline conditions the rates of changes of free and bound radiotracer concentrations equal zero.

Numerical model details

To analyze the influence of the neurotransmitter concentration on the PET signal the equations derived above are used for numerically simulations with the finite difference method. The used model equations and algorithms are explained in detail in the "Material and Methods" chapter (section 3.2.1).
The model calculations are based on parameters for an exemplary neurotransmitter system and exemplary radiotracer: B_{max}=20 nM, n_{D}=10 nM, r_{D}=10 nM, r_{pe}=0.20 min^{-1}, r_{ep}=0.20 min^{-1}, $r_{\mathrm{eb,max}}$=0.30 min^{-1} and r_{be}=0.15 min^{-1} (see "Material and Methods" section 3.2.2).
For the numerical calculations time and space domains were replaced by a set of mesh points. The time is discretized into time points in steps of Δt from 0 to T, i.e. $t_n = n\Delta t$ (n=0,...,$\mathrm{N_t}$). Within the space domain, a box of 343 uniformly distributed and equally spaced elements is simulated, with each element representing a tissue volume element at position [x_i, y_j, z_k], here denoted for simplicity by $\vec{I}$=[i,j,k]. Only a inner box of 125 elements is analyzed to exclude border effects. The expression $R([i,j,k],t_n)$, or in short $R(\vec{I},t_n)$, denotes the mesh function that approximates the radiotracer concentration at element $\vec{I}$=[i,j,k] and time t_n. The same applies for the free and bound radiotracer concentrations R_e and R_b. Within the numerical model the diffusion term for the radiotracer in equation 3.5 for an element $\vec{I}$=[i,j,k] at time t_n is approximated by linear transport and the diffusion parameter r_{diff} is introduced. r_{diff} is a rate constant with unit min^{-1} and its order of magnitude is estimated by assuming that diffusion of the radiotracer in the ECS has the same order of magnitude as the neurotransmitter. For dopamine a diffusion constant of

$D_{DA} \approx 7{\cdot}10^{-6}$ cm^{2}s^{-1} is reported [88]. Using the Einstein-Smoluchowski-Equation the average diffusion velocity can be calculated by [89,90,91]:

$$\frac{\Delta x}{t_{\Delta x}} = \frac{2D}{\Delta x} \tag{3.9}$$

Resolving equation 3.9 for Δx results in a diffusion distance of $\sim$0.004 cm within 1 s for dopamine ($\frac{\Delta x}{t_{\Delta x}} \approx 0.04\,\mathrm{mm\,s^{-1}} = 2.4\,\mathrm{mm\,min^{-1}}$). The size of an element in our model is supposed to reflect the typical resolution of a voxel from a PET measurement. Within the model diffusion of free radiotracer concentration from element i, j, k to one neighboring element i+1, j, k is given by $r_{diff}(R_e([i+1,j,k],t_n) - R_e([i,j,k],t_n))$. Therefore, a diffusion rate of r_{diff}=2.4 min^{-1} with a voxel size of 1 mm reflects diffusion in the order of dopamine. If not noted differently a r_{diff}=2 min^{-1} is used.

For the model calculations two different approaches are followed: (I) in the first approach a periodically varying binding rate $r_{\mathrm{eb}}(\vec{I},t)$ is simulated indirectly mimicking a periodically varying neurotransmitter concentration, (II) in the second approach the free neurotransmitter concentration is simulated directly in order to mimic more realistic conditions.

Approach I: periodically changing binding rate

For the first approach temporal variations of the radiotracer binding rate are simulated, which indirectly mimic a periodical changing neurotransmitter concentration. Periodical variations of the binding rate, r_{eb}, take place within the single element i=j=k=0 ($\vec{I_0} = [0,0,0]$) according to:

$$r_{eb}(\vec{I_0},t_n) = r_{eb}(0)(1 + A_I \sin(2\pi f_I t_n)). \tag{3.10}$$

In equation 3.10 the binding rate, r_{eb}, in the element $\vec{I_0}$ oscillates around $r_{eb}(0)$, which was chosen to be 0.3 min^{-1}. Within all other elements the binding rate remains constant at $r_{eb}(0)$. f_I is the frequency and A_I the relative amplitude of the changes of the binding rate at position $\vec{I_0}$.
Using a step-wise procedure free and bound radiotracer concentrations, $R_e(\vec{I},t_n)$ and $R_b(\vec{I},t_n)$, are calculated for each time step whereby the temporal variations of $r_{\mathrm{eb}}(\vec{I_0},t_n)$ according to equation 3.10 are inserted (see section 3.2.1 for more details). The resulting temporal variations in the total radiotracer signal, $R(\vec{I},t_n) = R_e(\vec{I},t_n) + R_b(\vec{I},t_n)$, are analyzed by the parameter rN_{f} as:

$$rN_f(\vec{I}) = \frac{\Delta R_f(\vec{I})}{R_{baseline,f}(\vec{I})} = \frac{R_{max,f}(\vec{I}) - R_{min,f}(\vec{I})}{R_{baseline,f}(\vec{I})}. \tag{3.11}$$

$R_{baseline,f}(\vec{I})$ is the mean radiotracer concentration given by $\frac{1}{2}(R_{max,f}(\vec{I}) + R_{min,f}(\vec{I}))$, $R_{max,f}(\vec{I})$ is the maximal signal over time and $R_{min,f}(\vec{I})$ the minimal signal.
Note that for approach (I) only a single value of $rN_{\mathrm{f}}(\vec{I})$ for the element of interest, $\vec{I_0}$, is calculated, which reflects the amplitude of induced signal changes over time.

Therefore, $rN_{\mathrm{f}}(\vec{I}_0)$ is denoted by rN_{f} in the following. Approach (I) is used to analyze the reaction of the radiotracer on temporal neurotransmitter changes with different frequencies and amplitudes (section 3.1.2).

Approach II: variation of free neurotransmitter concentration

To mimic more realistic conditions, i.e. release events and removal mechanisms, the neurotransmitter concentration is simulated directly. The simulated temporal variations of the free neurotransmitter concentration consist of baseline release events and intervals with increased neurotransmitter release according to data measured by voltammetry (see below).
For approach (II) release events and removal mechanisms are incorporated by increasing the neurotransmitter concentration to a defined amplitude, which then decreases exponentially. Release events and the according removal are referred to as pulses within the model calculations. A baseline neurotransmitter concentration is modeled by pseudo-randomly distributed pulses with an average frequency of 1 pulse per minute and a variance of 0.2 per minute (pseudo-random Gaussian-distribution). Each pulse has an amplitude of 100 nM and an exponential decay constant of 2 s (typical transient duration, see below). So-called stimulation intervals, i.e. phasic neurotransmitter release events, are chosen to occur at 20 minutes and 45 minutes for 5 minutes each. During stimulation intervals an increased frequency of pulses with the same amplitude and decay time as for the baseline concentration are assumed. The free neurotransmitter concentration is modeled for each element, $\vec{I}$, for a time of 60 minutes. The changes in the radiotracer binding rate, r_{eb}, as well as in free and bound radiotracer concentrations, $R_e(\vec{I}, t_n)$ and $R_b(\vec{I}, t_n)$, which are induced by the neurotransmitter concentration variations are calculated as a function of time (see "Material and Methods" section 3.2.1). Temporal total radiotracer concentration variations, i.e. PET signal variations, are analyzed by the parameter rN for approach (II) according to:

$$rN(\vec{I}, t_f) = \frac{\Delta R(\vec{I}, t_f)}{R_{baseline}}$$
$$= \frac{1}{R_{baseline}} \sqrt{\frac{1}{I_{sum}} \sum_{u=i-d_i}^{i+d_i} \sum_{v=j-d_j}^{j+d_j} \sum_{w=k-d_k}^{k+d_k} (R([u,v,w], t_f) - R([u,v,w], t_{f-1})^2} \quad (3.12)$$
$$\text{with, } R_{baseline} = \frac{1}{N_f - fs} \frac{1}{I_{sum}} \sum_{f=fs}^{N_f} \sum_{u=i-d_i}^{i+d_i} \sum_{v=j-d_j}^{j+d_j} \sum_{w=k-d_k}^{k+d_k} R([u,v,w], t_f).$$

The parameter rN is calculated as the average of the absolute difference between the signal at time t_f and t_{f-1} in a region that includes the elements in the box $i-d_i, i+d_i, j-d_j, j+d_j, k-d_k, k+d_k$. The temporal difference between Δt_f=t_f-t_{f-1} reflects the duration of a time frame of the reconstructed PET data. For the model calculations a Δt_f of 5 min was used.

The square root term is a measure for $\Delta R(t_f)$, the average signal change from time t_{f-1} to time t_f in the box centered at element $\vec{I}$. I_{sum} is the number of elements in the box. Within this thesis a box size of 125 with d_i=d_j=d_k=2 was used. R_{baseline} is calculated as the average signal in the box after steady-state has been reached at t_{fs}. In the model fs is zero, since the time point t=0 is defined as a point in time at which steady-state conditions are given. N_f is given by the total simulation time T. For a total time of T=60 minuntes and a Δt_f of 5 minutes N_f is 12. For PET data fs would be the number of the frame at time t_{fs}, when steady-state conditions are achieved and N_f the total number of time frames.
Calculating rN by the expression given in 3.12 is a way to estimate the temporal signal variations despite the low temporal resolution of PET: instead of calculating the temporal variation in a single elements as the difference between time t_f and t_{f-1}, which is very noisy, the average temporal variations are calculated for a box containing multiple elements. By that, noise is reduced without loosing time resolution, but at the cost of spatial resolution. [86]
PET signal responses to changes of neurotransmitter concentration as simulated in approach (II) provide a more realistic model to analyze the interaction between neurotransmitter and radiotracer and the analysis of temporal variations as introduced here can directly be applied to PET data.
Approach (II) is used to analyze the impact of stimulation parameters like the frequency of stimulation pulses and the size of stimulation volume as well as the strength of diffusion r_{diff} on the amplitude of temporal variations in the PET signal. Moreover the influence of the rate constants of the radiotracer (r_{pe}, r_{ep}, r_{on} and r_{be}) as well as of the neurotransmitter system inert parameters B_{max} and n_{D} is analyzed (section 3.1.2). Additionally, parameters for radiotracers of interest were taken from literature to analyze their feasibility to detect PET signal changes as response to neurotransmitter release events for different neurotransmitter systems (sections 3.1.3 and 3.1.8).

3.1.2 Model Results: Temporal Variations in the PET Signal

Approach I: periodically changing binding rate

The impact of a periodically changing radiotracer binding rate, r_{eb}, on temporal PET signal variations is analyzed using approach (I) as explained in section 3.1.1. Figure 3.4A+B shows the modeled temporal variation of the binding rate, $r_{\mathrm{eb}}(\vec{I_0}, t_n)$, normalized to its initial value, $r_{\mathrm{eb}}(0)$, for the frequencies f_I=0.2 Hz and f_I=0.01 Hz with a relative amplitude A_I=1. The effect of the periodically changing binding rate on the free radiotracer concentration, $R_{\mathrm{e}}(\vec{I_0}, t_n)$, is displayed in Figure 3.4C+D and the resulting PET signal, $R(\vec{I_0}, t_n)$, in Figure 3.4E+F. Analyzing the induced temporal variations in the total radiotracer signal by the parameter rN_{f} in the case of a periodically changing binding rate with a frequency of 0.2 Hz yields a rN_{f} lower than 0.1 %, while for a frequency of 0.01 Hz it is rN_{f}=4.7 %. This indicates that "slower" changes in the system can better be picked up by a typical radiotracer.
To analyze the impact of the frequency of the variations, rN_{f} was calculated for different frequencies f_I of the periodically changing binding rate, $r_{\mathrm{eb}}(\vec{I_0}, t_n)$, between 0 and 0.2 Hz (Figure 3.5A). For frequencies above 0.011 Hz temporal signal variations are below 4 % and become negligible with increasing frequencies. With decreasing frequencies (slower variations) rN_{f} increases rapidly, suggesting that longer lasting concentration changes of the neurotransmitter in the ECS can induce more pronounced changes in the PET signal via the binding rate r_{eb}.
The amplitude of changes in the PET signal assessed by rN_{f} is directly proportional to the amplitude of changes of $r_{\mathrm{eb}}(\vec{I_0}, t_n)$ as displayed in Figure 3.5B.
The phase shift visible between the binding rate, free radiotracer concentration and total radiotracer signal in Figure 3.4 is a result of the diffusion included in the model. In Figure 3.6 the free, bound and total radiotracer concentrations over time are shown for the cases that no diffusion, low diffusion (r_{diff}=0.2 min^{-1}) or a realistic diffusion (r_{diff}=2 min^{-1}) is included in the model with a periodically changing binding rate $r_{\mathrm{eb}}(\vec{I_0}, t_n)$ at a frequency of f_I=0.01 Hz. Without diffusion the free and bound radiotracer have a phase shift of ∼167°. This means that free and bound concentrations are alternating in accordance with the mass conservation law, i.e. free and bound concentrations are interchanging without loss of total radiotracer. The slight shift in contrast to the expected 180° is a result of the exchange with the blood pool, i.e. the rate constants r_{pe} and r_{ep}. Including diffusion leads to smaller phase shifts between free and bound radiotracer concentrations, i.e. 137° for r_{diff}=0.2 min^{-1} and 50° for r_{diff}=2 min^{-1}. In those cases a decrease in bound radiotracer concentration leads to an increase in the free concentration, which then leads to diffusion of radiotracer into the neighboring elements so that the resulting maximal free concentration within the element is achieved earlier as in the case without diffusion. The change of phase shift between free and bound radiotracer concentration induced by diffusion results in stronger signal variations in the total radiotracer signal (Figure 3.6F), compared to the case without diffusion where the total concentration stays more or less constant.

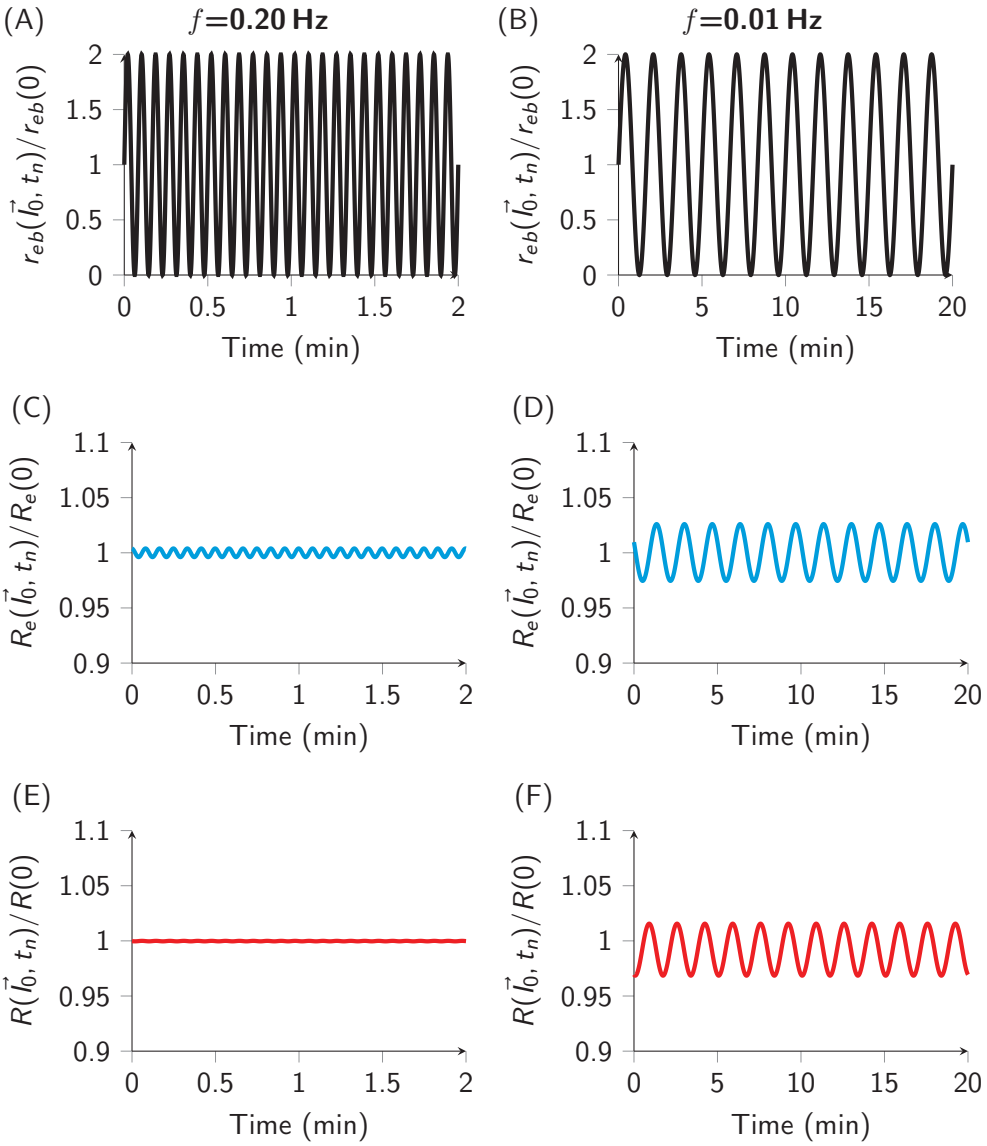

Figure 3.4: Periodically changing binding rate and its impact on the free and total radiotracer concentration. (A-B) Periodical changing binding rate, $r_{\mathrm{eb}}(\vec{I}_0, t_n)/r_{\mathrm{eb}}(0)$, for the frequencies f_I=0.2 Hz and f_I=0.01 Hz over time. (C-D) Free radiotracer concentration, $R_{\mathrm{e}}(\vec{I}_0, t_n)$, over time calculated via equation 3.5 normalized to the steady-state concentration of $R_{\mathrm{e}}(0)$. (E-F) Radiotracer signal, $R(\vec{I}_0, t_n)$, over time normalized to its steady-state radiotracer concentration $R(0)$.

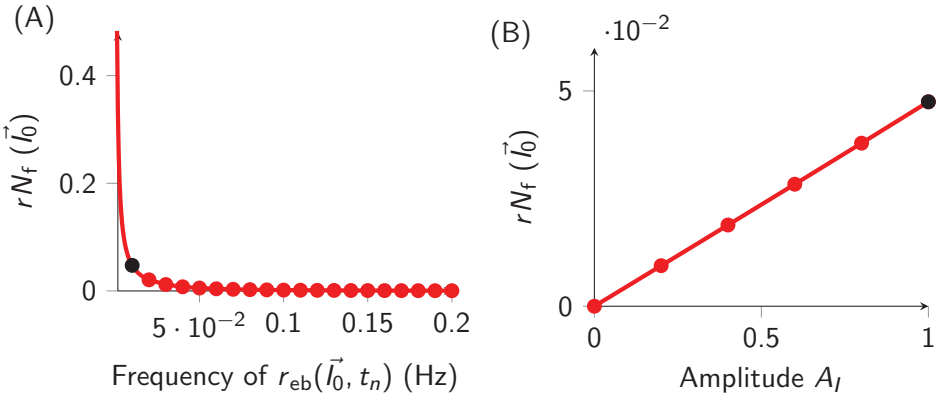

Figure 3.5: Frequency and amplitude dependency of temporal variations in the radiotracer signal. (A) Parameter rN_f for frequencies of $r_{eb}(\vec{I}_0, t_n)$ from 0.0005 Hz to 0.2 Hz. (B) rN_f for amplitudes of $r_{eb}(\vec{I}_0, t_n)/r_{eb}(0)$ A_I from 0 to 1. The black dots indicate a frequency of 0.01 Hz and an amplitude of 1 as used for the calculations above.

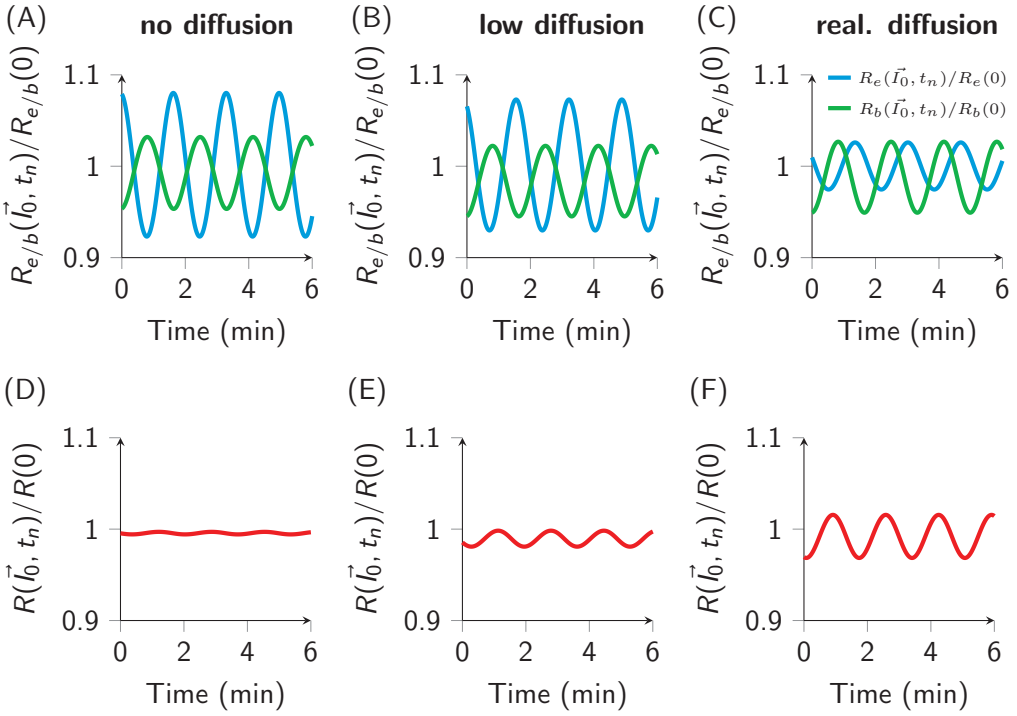

Figure 3.6: Influence of different diffusion rates. Free $R_e(\vec{I}_0, t_n)$ (cyan) and bound $R_b(\vec{I}_0, t_n)$ (green) radiotracer concentration over time calculated via equations 3.5 and 3.6 normalized to their steady-state concentrations of $R_{e/b}(0)$ for a diffusion rate (A) r_{diff}=0 (no diffusion), (B) r_{diff}=0.2 (low diffusion) and (C) r_{diff}=2 (realistic diffusion). The total radiotracer signal $R(\vec{I}_0, t_n)$ over time normalized to its steady-state radiotracer concentration for (D) r_{diff}=0 (no diffusion), (E) r_{diff}=0.2 (low diffusion) and (F) r_{diff}=2 (realistic diffusion).

Approach II: variations of free neurotransmitter concentration

A typical trace of simulated free neurotransmitter concentration within one element is shown in Figure 3.7A. At stimulation intervals at 20 minutes and 45 minutes the pulse frequency is increased from 1 pulse per minute to 10 pulses per minute for a duration of 5 minutes. The increase in pulse frequency leads to an increase of bound neurotransmitter concentration and therefore a reduction in the effective binding rates for neurotransmitter and radiotracer (Figure 3.7A+B). This leads to a displacement of part of the bound radiotracer concentration from the binding sites and increases the free radiotracer concentration (Figure 3.7C). The free radiotracer can diffuse to neighboring elements and can be cleared to blood (r_{ep}), which leads to a reduction in the total amount of radiotracer. Note, that the curves in Figure 3.7 only reflect the data from one single element, $\vec{I_0}$.
The influence of the neurotransmitter concentration variations on the radiotracer signal is analyzed within a box of 125 elements centered at $\vec{I_0}$ by the parameter rN as explained in section 3.1.1. For simplicity $rN(\vec{I_0})$ is in the following denoted by rN. The parameter rN as a function of time is shown in Figure 3.8B. The stimulation time points can clearly be identified by the analysis of the temporal variations by rN, while in the average time activity curve of the 125 elements the effect of changes in the free neurotransmitter concentration is not visible (Figure 3.8A).
The influence of the following parameters on the amplitude of the signal variations at the time of stimulation (t_s) as assessed by rN was further analyzed: the size of the diffusion rate of the radiotracer r_{diff}, the frequency of stimulation pulses, and the number of stimulated elements within the box of interest. The results are summarized in Figure 3.9. Summarizing, a larger diffusion rate, a higher stimulation pulses frequency as well as a larger stimulated volume increase $rN(\mathrm{t_s})$. Temporal signal variations of up to $\sim$25 % were achieved with the used set of parameters.
Furthermore, the impact of the parameters for the neurotransmitter system B_{max} and n_{D}, as well as the rate constants of the radiotracer (r_{pe}, r_{ep}, r_{on}, r_{be}) on the signal variations were analyzed, see Figure 3.10. For the calculations the exemplary parameters given above were taken and only the parameter of interest was varied. Note that 27 elements are stimulated with a pulse rate of 10 pulses/minute. While a larger total receptor density, B_{max}, is advantageous, there seems to be an optimal dissociation constant, n_{D}, for the used set of parameters. For the calculation of the dissociation constant, which is the ratio of $n_{\mathrm{eb}}/n_{\mathrm{on}}$, a fixed n_{on} was used. The radiotracer rate constants, r_{pe} and r_{ep}, which determine exchange of the radiotracer with the blood, don't have an impact on the temporal signal variations. This can be explained by the bolus-plus-constant infusion approach that is used to remain steady-state conditions. For the binding and unbinding rate constants of the radiotracer, r_{on} and r_{be}, an optimal value to achieve maximal signal variations is found. For the set of parameters used, the optimal values are $r_{\mathrm{on,opt.}}$=0.1 $\mathrm{min^{-1}nM^{-1}}$ and $r_{\mathrm{be,opt.}}$=0.26 $\mathrm{min^{-1}}$ ($k_{\mathrm{d,opt.}}$=2.6 nM).

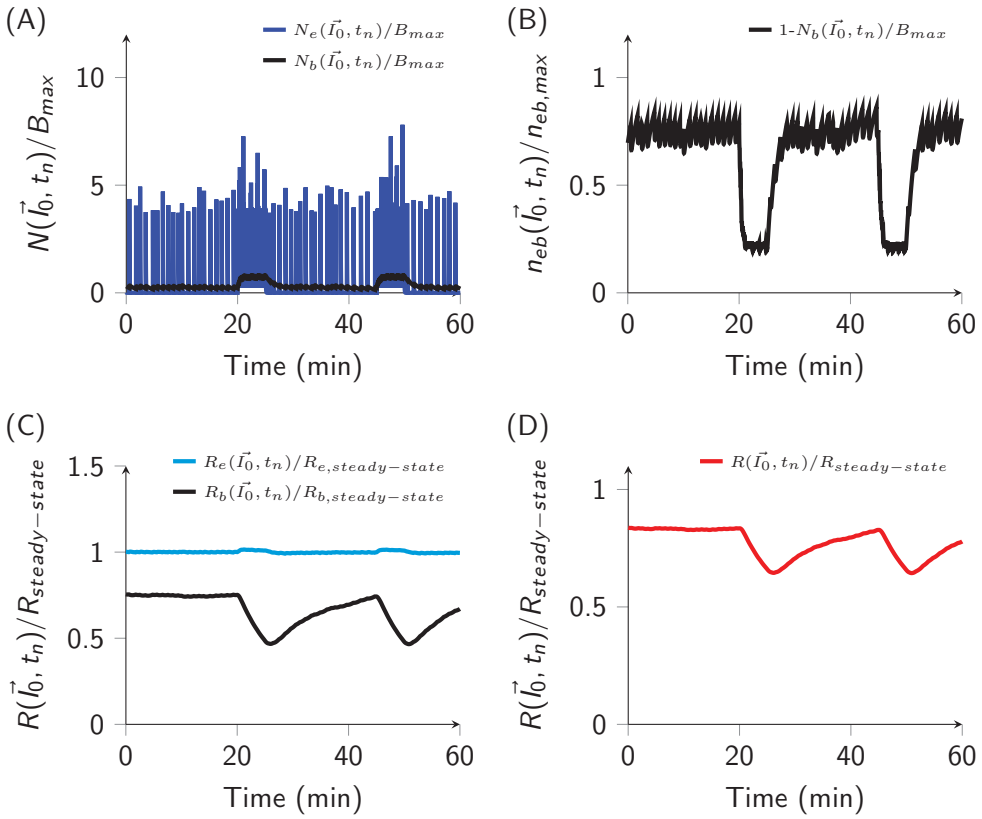

Figure 3.7: Simulated free neurotransmitter concentration. (A) Simulated free neurotransmitter concentration, $N_{\mathrm{e}}(\vec{I_0}, t_n)$, consisting of pseudo-random baseline pulses and stimulation intervals at 20-25 minutes and 45-50 minutes (blue). The resulting fraction of bound neurotransmitter, $N_{\mathrm{b}}(\vec{I_0}, t_n)$, is shown in black. The concentrations are normalized to the receptor density B_{max}, respectively. (B) The binding rate of the neurotransmitter, $n_{\mathrm{eb}}(\vec{I_0}, t_n)$, is influenced by the changes in bound neurotransmitter concentration. Note, that the binding rate of the radiotracer is influenced in the same manner. (C) The variations in the binding rate lead to changes in the free, $R_{\mathrm{e}}(\vec{I_0}, t_n)$, (cyan) and bound, $R_{\mathrm{e}}(\vec{I_0}, t_n)$, (black) radiotracer concentrations. The concentrations are normalized to their steady-state conditions, which were calculated for N_e=0, respectively. (D) The total radiotracer signal, $R(\vec{I_0}, t_n)$, is influenced by the increases in free neurotransmitter concentration. The total radiotracer signal is normalized to its steady-state concentration.

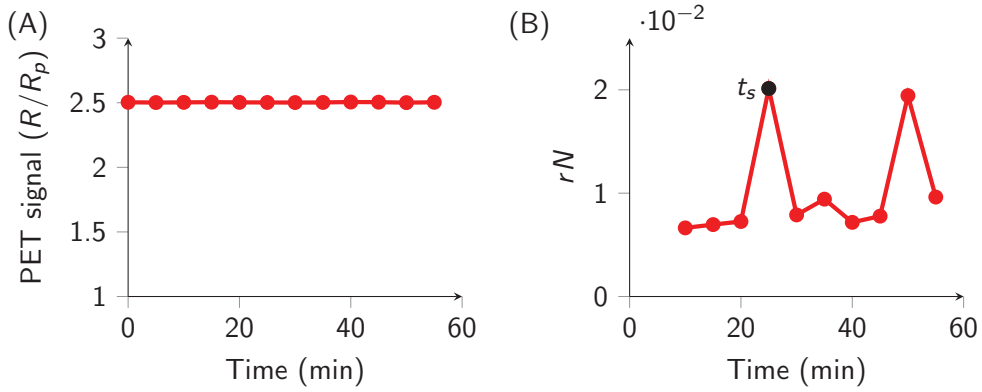

Figure 3.8: Comparison of the time activity curve and the parameter of temporal signal variations rN. (A) Time activity curve of the box of interest (125 elements) assuming a free neurotransmitter concentration in one element with stimulation intervals at 20-25 minutes and 45-50 minutes. (B) Temporal variations of the total radiotracer concentration analyzed by rN for the same free neurotransmitter concentration as in (A). In black the time point t_s of the first stimulation interval, which is used for further analysis, is highlighted.

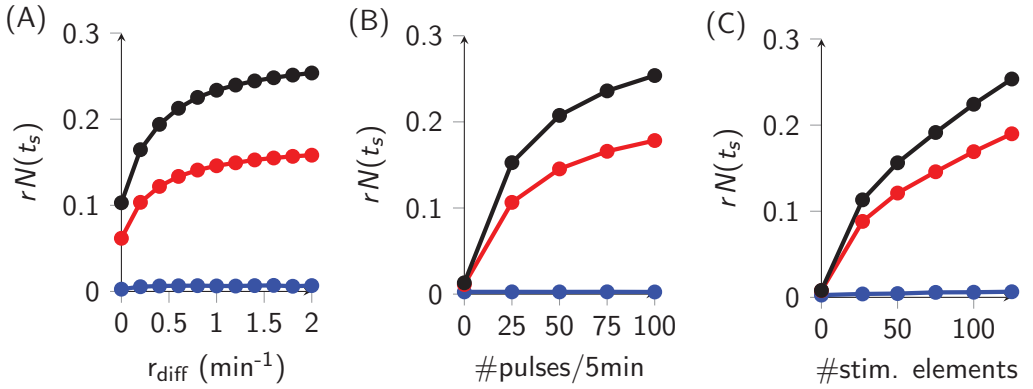

Figure 3.9: Influence of different parameters on the amplitude of signal variations. (A) Influence of the diffusion rate, r_{diff}, on temporal signal variations assessed by rN at the time of stimulation t_s. For the analysis three different sets of parameters are used: (blue) no stimulation (only baseline pulses), (red) 75 stimulated elements with 10 pulses/min, and (black) 125 stimulated elements with 20 pulses/min. (B) Influence of the stimulation pulse frequency on rN. For the analysis three different sets of parameters are used: (blue) no diffusion and one stimulated element, (red) a diffusion factor of 0.6 and 75 stimulated elements, and (black) a diffusion factor of 1 and 125 stimulated elements. (C) Influence of the number of stimulated elements on rN. The influence of the number of stimulated elements is shown for (blue) no diffusion and no stimulation pulses, (red) a diffusion factor of 0.6 and 10 pulses/min, and (black) a diffusion factor of 1 and 20 pulses/min.

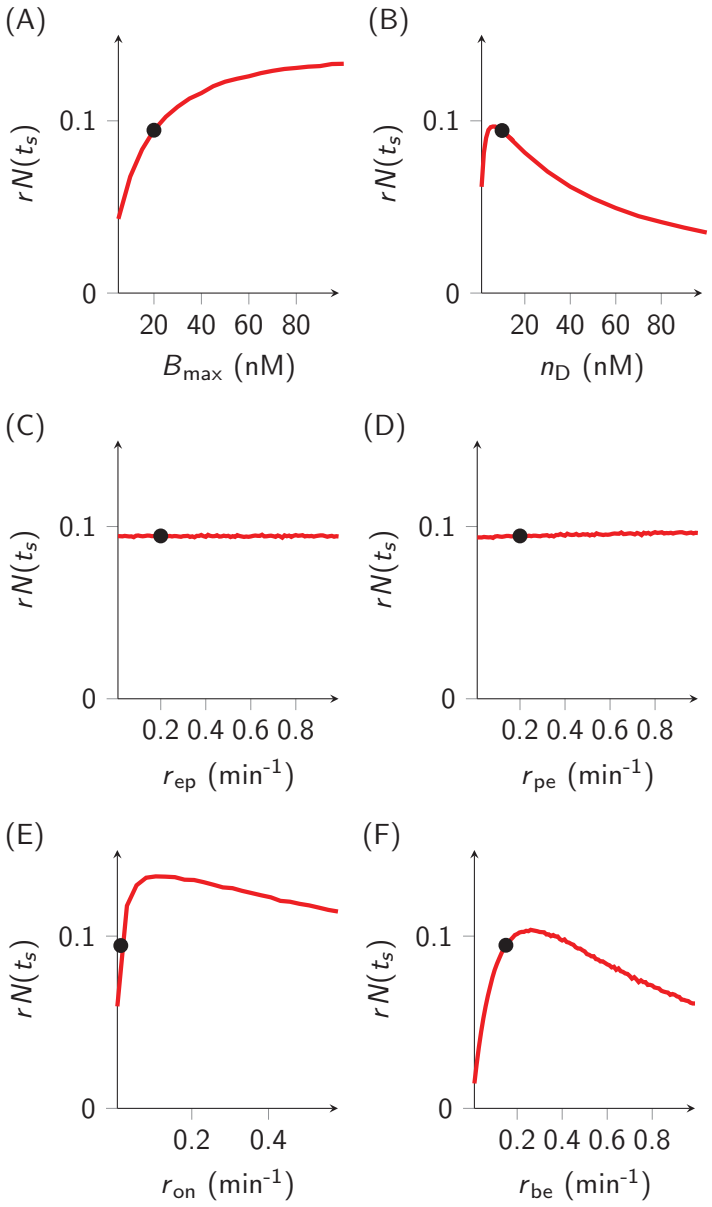

Figure 3.10: Influence of neurotransmitter and radiotracer parameters on the amplitude of signal variations. Influence of (A) the total receptor density, $B_{\max}$, (B) the dissociation rate constant, n_{D}, of the neurotransmitter, (C) the transport rate from plasma to ECS, r_{pe}, for the radiotracer, (D) the transport rate from ECS to plasma, r_{ep}, (D) the binding rate, r_{on}, (E) the unbinding rate, r_{be}, on temporal signal variations rN at the stimulation time t_s. The parameters, which were fixed for the calculations of the other plots are marked by black dots, respectively.

3.1.3 The Dopamine System: Parameters, Scales and Radiotracers

The dopamine system is one of the best studied neurotransmitter system. Therefore explicit description of temporal and spatial scales are known. Moreover the radiotracer [11C]raclopride is well studied and kinetic rate constants are available from literature. Within this thesis the developed model was applied and validated for the dopamine system. In this section a short introduction on the functions and pathways of the dopamine system is given, followed by a summary of known temporal and spatial scales of dopamine signaling. Furthermore, the behavior of [11C]raclopride and its interaction with dopamine is elaborated. The radiotracers [18F]DMFP and [18F]fallypride, which are like [11C]raclopride dopamine D2 receptor antagonists, are introduced and analyzed.

Functions, pathways and neurotransmission

The neurotransmitter dopamine belongs to the group of monoamines and can be further categorized as a catecholamine (see also Figure 3.1) [84,92,81].
The dopamine system is known to be involved in the regulation of reward-motivated behavior, addiction and motor control [84,81,93]. Dopamine can not cross the blood-brain barrier and is synthesized within the CNS from tyrosine via L-DOPA [84,81]. In total, dopaminergic neurons only account for less than 1% of the total neuronal population of the brain and their cell bodies are grouped within few distinct brain areas including the substantia nigra (SN), the ventral tegmental area (VTA), the posterior hypothalamus, the arcuate nucleus, the zona incerta and the periventricular nucleus [93,94]. However, dopaminergic axons project to many brain regions forming pathways that are related to different functions, e.g. the nigrostriatal pathway, in which substantia nigra pars compacta cells project to the dorsal striatum, that is important for motor function (Figure 3.11) [94,93,84]. Further dopaminergic pathways are the mesocortical and mesolimbic pathways – together referred to as mesocorticolimbic projections –, which play a central role in reward and motivation [93,84].
Five subtypes of dopamine receptors (D1 to D5) have been identified [84,81]. The receptors are all metabotropic, G protein-coupled receptors and can be divided into two classes: D1-like (D1 and D5) and D2-like (D2, D3 and D4) receptors [84,81]. The effect of dopamine on a target neuron can be inhibitory or excitatory dependent on the type of receptors and their response to the second messenger cAMP [84]. D1 receptors exhibit low affinity for dopamine, while D2 receptors are mainly found in a high affinity state (EC50 $\sim$1 μM and $\sim$10 nM, respectively) [84]. D2 receptors are configured in states of high or low affinity for agonists, with approximately 50% of the receptors contributing to each state in vitro [58,95]. Note, that antagonist bind to both affinity states with the same affinity [95,58]. Excess released dopamine is absorbed back into the presynaptic neuron. This occurs via re-uptake into the cell by the dopamine transporter (DAT) or plasma membrane monoamine transporters (MAT), where it can be chemically degraded or repackaged into vesicles for future release [84].

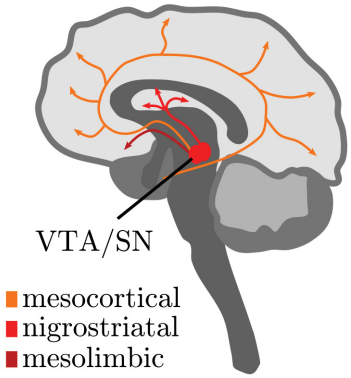

Figure 3.11: Pathways of the dopamine system. The major dopamine-containing area is the dorsal striatum (caudate nucleus and putamen), which receives major input from the substantia nigra (SN)/ substantia nigra pars compacta (SNc) via the so-called nigrostriatal pathway. The mesocortical pathway describes dopamine neurons, which project from the ventral tegmental area (VTA) to the prefrontal cortex. Dopamine projections from the VTA to the ventral striatum, including the nucleus accumbens and olfactory tubercle, are referred to as the mesolimbic pathway.

Temporal and spatial scales

Two different firing modes exist for dopamine signaling: tonic and phasic firing. Tonic firing is characterized by low frequency (1-9 Hz) irregular firing, while phasic firing consists of high frequency bursts of 2-5 spikes with a typical burst frequency of 20 Hz up to 100 Hz [96,97,98]. During release events, dopamine concentrations are elevated 10^4-fold within the synapse for $\sim$1 ms [88]. After phasic release and due to diffusion extracellular dopamine concentrations increases are in the order of 10-100-fold and last for $\sim$2 s [99]. This was robustly shown by fast-scan cyclic voltammetry (FSCV) measurements (see section 3.1.7 for a description on FSCV) [88,100]. Extracellular changes in dopamine concentration measured with this technique show a fast concentration increase followed by a slower exponential decrease of the signal. Dopamine is removed from the extracellular space by dopamine transporters (DATs) with the effective removal rate constant of k, which reflects the local density of DATs. Reported values for the removal rate k range from k=0.01 s^{-1} to 20 s^{-1}, which corresponds to effective lifetimes of 100 s to 0.05 s (see section 3.1.7) [88,101].

PET signal variations induced by dopamine release assessed with dopamine D2 receptor radiotracers

[11C]raclopride is a well known dopamine D2 receptor antagonist with a relatively moderate affinity (reported k_i's of 1-10 nM[102]) and with a lower affinity to dopamine D3 receptors[103,58,102]. [11C]raclopride has been and still is widely used to assess changes in its binding potential in response to variations in endogenous dopamine concentrations (see section 2.5). The radiotracer [18F]DMFP is reported to have similar kinetics as [11C]raclopride, but is labeled with 18F-fluorine instead of 11C-carbonyl. Its longer half-life makes [18F]DMFP easier to handle[104]. The radiotracer [18F]fallypride has a high affinity to D2 receptors, which is thought to limit its capability to capture signal variations in response to dopamine release and is rather used for extrastriatal analyses[73].

To analyze temporal PET signal variations as introduced in sections 3.1.1 and 3.1.2 by the parameter rN for the dopamine system and the named radiotracers, typical parameters were taken from literature. The parameters applied for the dopamine system are summarized in Table 3.1 in the "Material and Methods" section 3.2.2. The used kinetic rate constants for [11C]raclopride, [18F]DMFP and [18F]fallypride are given in Table 3.2 (section 3.2.2).

For the analysis approach (II) was applied by simulating a trace of free dopamine concentration. Baseline pulses are simulated as in the general model: 1 pulse per minute of 100 nM with a decay constant of 2 s. During the stimulation intervals 27 elements were "stimulated" with 50 pulses within 5 minutes.

The resulting temporal signal variations for the different radiotracers are displayed in 3.12A+C. Note, that for the dopamine system the parameter to assess temporal signal variations, rN, is renamed to rDA.

The influence of noise in the radiotracer signal on rDA was further analyzed. Therefore, 5 and 10 % noise was added to the signal (Gaussian distributed pseudo-random noise) within the model, rDA was calculated and normalized to the time interval before the first stimulus (rDA_{baseline}). The temporal signal variations for the different radiotracers in the case that noise is added to the signal are shown in Figure 3.12B+D.

Taken together, signal variations in the order of 6-8% are yielded for [11C]raclopride. Those signal variations are still visible when 5% noise were added to the signal. With 10% noise the stimulation events cannot be seen clearly anymore. With [18F]DMFP signal variations in the order of 13% are theoretically achievable. In the cases with 5% and 10% noise added to the signal, the temporal signal variations increases due to increased dopamine concentration can still be observed. With the radiotracer [18F]fallypride signal variations up to 5% were yielded, but including noise in the model leads to a loss of the temporal signal variations.

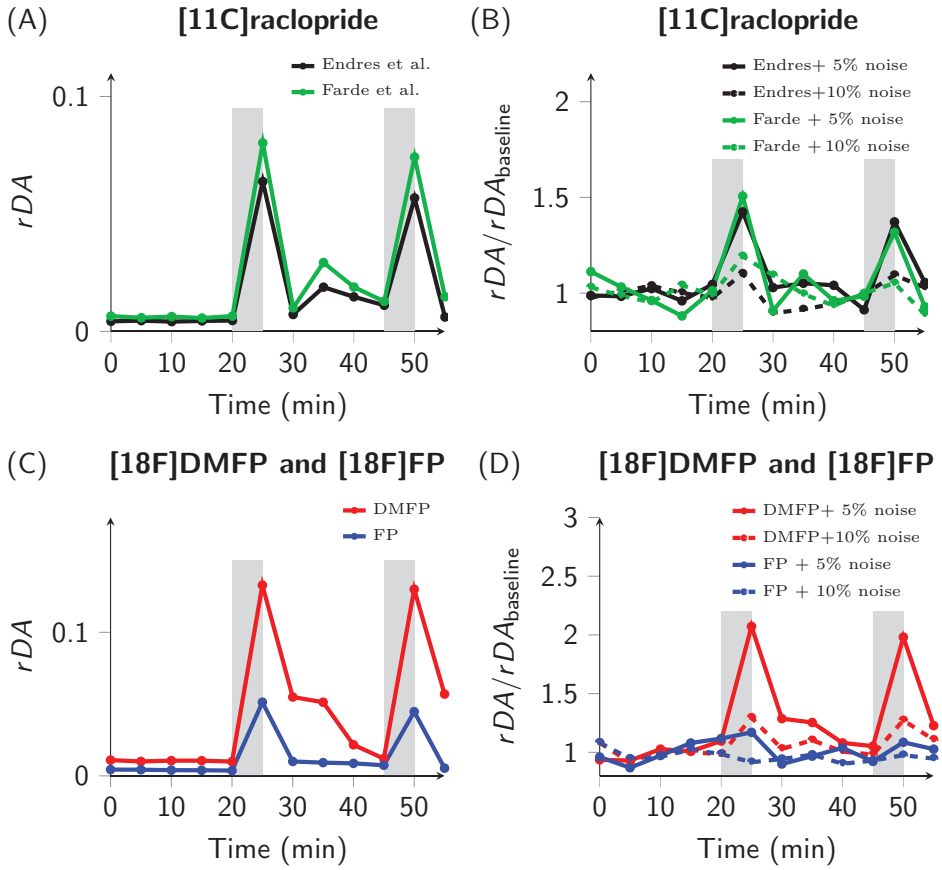

Figure 3.12: Temporal signal variations assessed by [11C]raclopride, [18F]DMFP and [18F]fallypride. (A) Temporal signal variations, rDA, in response to temporal variations in extracellular dopamine concentrations calculated for [11C]raclopride with parameters from Endres et al. and Farde et al.. (B) Normalized temporal signal variations, $rDA/rDA_{\text{baseline}}$, for [11C]raclopride with parameters from Endres et al. and Farde et al. in the cases that 5 or 10 % noise is added to the signal. (C) Temporal signal variations, rDA, in response to temporal variations in extracellular dopamine concentrations calculated for [18F]DMFP and [18F]fallypride ([18F]FP). (D) Normalized temporal signal variations, $rDA/rDA_{\text{baseline}}$, for [18F]DMFP and [18F]fallypride ([18F]FP) in the cases that 5 or 10 % noise is added to the signal.

3.1.4 [11C]Raclopride PET Scans in Mice

To experimentally validate the introduced model, [11C]raclopride PET emission data were acquired in a chemogenetic mouse model, namely $hM3D_{Gq}{}^{DAT}$, in which dopamine release can be induced by a designer drug called clozapine-n-oxide (CNO). A description of the mouse model can be found in the "Material and Methods" section 3.2.4. Note that the results of this study are published in the manuscript by Lippert and Cremer et al. (2019) [86].
Within the [11C]raclopride PET study each animal (n=6) was measured twice, once with Saline injection and once with injection of CNO, to achieve a paired study design. Data were acquired for 60 minutes and Saline/CNO was injected 10 minutes after the start of the scan. To rapidly reach a steady state, [11C]raclopride was injected using a bolus-plus-constant infusion method using programmable syringe pumps (Figure 3.13A+B). The time-activity curves for the striatum and the cerebellum averaged for both scan sessions and all animals are displayed in Figure 3.13C. Steady-state conditions are reached around 10-15 minutes after start of the scan. Further experimental details can be found in the "Material and Methods" section 3.2.5.
Mean [11C]raclopride uptake images for the Saline and CNO measurements of the time interval between 20 and 60 minutes are shown in Figure 3.14A. The striatum shows – as expected – the strongest [11C]raclopride binding due to the high D2 receptor density in the striatum. A voxel-wise t-test between the Saline and CNO data of the mean [11C]raclopride uptake in this time interval was performed. As shown in Figure 3.14A on the right, there are no statistical significant differences within the shown plane. Plotting the number of significantly different voxels between the two groups within the whole brain over time confirms that there are almost no differences in the activity data (Figure 3.15A). Additionally, the activity data of different regions like the striatum and cerebellum did not show any statistical significant differences between the groups (paired Student's t-test of the area under the time-activity curve between the Saline and CNO group, n=6: $p_{Striatum}$=0.18, $p_{cerebellum}$=0.12).

Within the theoretical model calculations given above, it was shown that changes in extracellular neurotransmitter concentrations lead to temporal radiotracer signal variations, while they are not necessarily visible in the activity data. Therefore, temporal variations in the [11C]raclopride signal within a box of 75 voxels (5x5x3) are calculated in analogy to the parameter rN of the theoretical model using equation 3.33 (see "Materials and Methods" section). Here, the parameter is named rDA and is normalized to the time interval before stimulation $rDA_{baseline}$.
The mean parametric images of rDA from the time interval between 20 and 60 minutes for the Saline and CNO group are shown in Figure 3.14B. An increase in temporal signal variations is visible in the parametric image of the CNO group. The voxel-wise t-test between the two groups reveals significant increases in rDA within the shown plane upon CNO injection (Figure 3.14B, right panel). The number of significant different voxels between the two groups in the parametric images across the whole brain is increased around ten minutes after CNO injection and stays

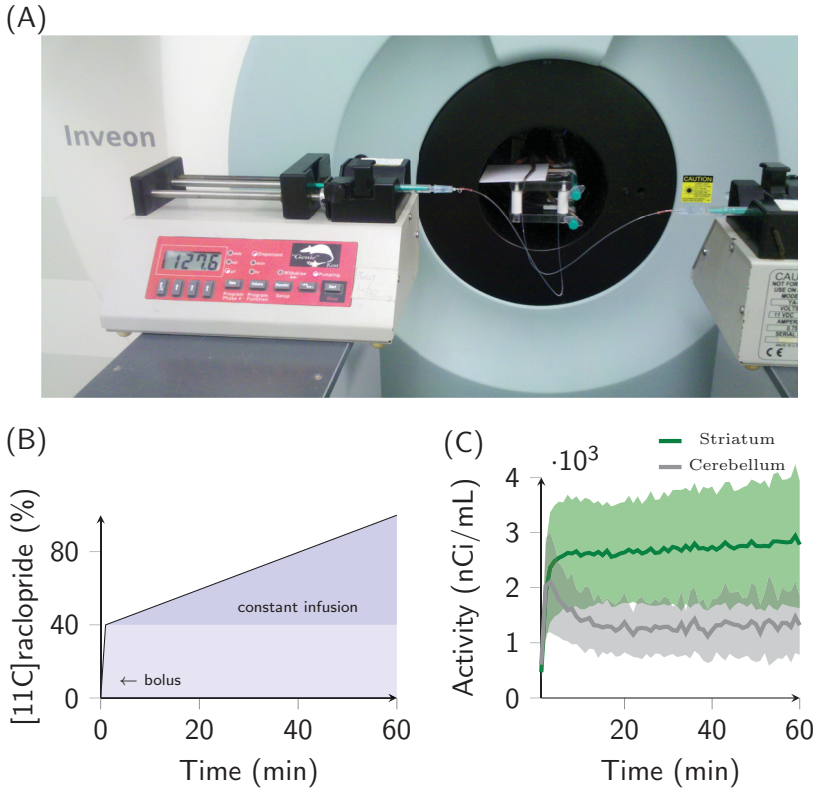

Figure 3.13: Setup for [11C]raclopride PET scans in mice. (A) Picture of the PET scanner including the mouse holder. The injection of [11C]raclopride can be performed according to a defined protocol using syringe pumps. (B) Bolus-plus-constant infusion protocol. 40% of the total amount of injected activity is given as bolus in the first minute (80 μL out of 200 μL). The remaining activity is given in the following 59 minutes of acquisition with a constant rate, i.e. 122 mL/h. (C) Time-activity curves of the striatum and cerebellum.

elevated for the duration of the measurement compared to Saline injection (Figure 3.15B).

The time-curves of the temporal signal variations from the left striatum of the Saline and CNO group are shown in Figure 3.15C. Approximately 10 minutes after CNO injection a significant increase in the temporal signal variations was observed in the striatum compared to Saline-injected mice. The parametric data of $rDA/rDA_{\text{baseline}}$ were averaged for the time from 10 to 60 minutes for each measurements and the results are displayed in Figure 3.15D. The temporal signal variations are higher in every measurement with CNO compared to the Saline measurement of the same mouse, except for one animal (paired Student's t-test: n=6, p=0.035).

According to the results from the [11C]raclopride PET study, it can be concluded that inducing dopamine release in the used mouse model leads to increased temporal variations in the [11C]raclopride PET signal assessed by rDA.

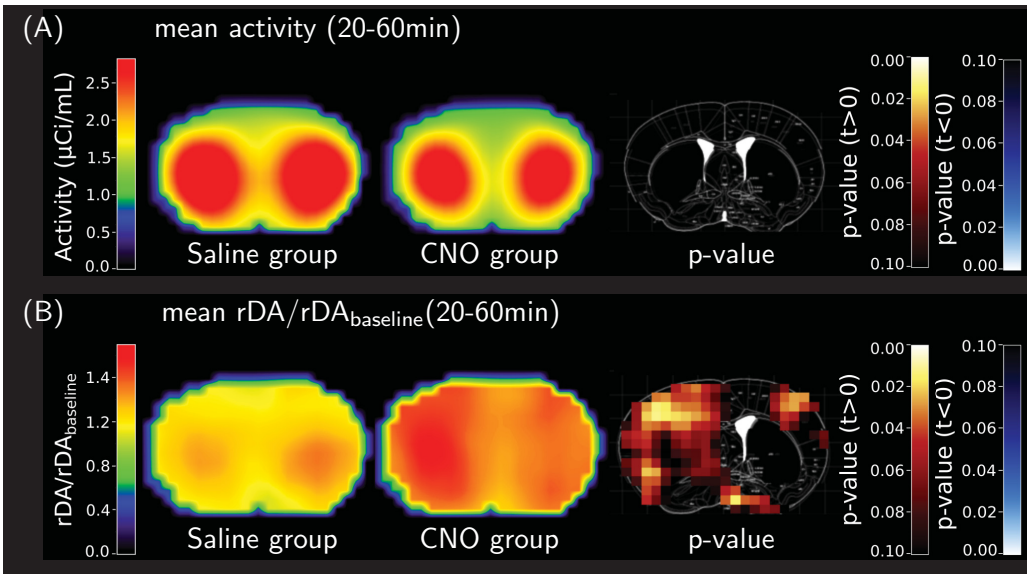

Figure 3.14: Differences between [11C]raclopride uptake and the parameter rDA in hM3D$_{Gq}^{DAT}$ mice. (A) Left: Averaged [11C]raclopride activity of the time interval from 20 to 60 minutes in a transaxial plane of the mouse brain for the Saline and CNO group (n=6). Right: Statistical significant differences between the data projected on the corresponding plane of the mouse atlas. (B) Left: The parameter $rDA/rDA_{\text{baseline}}$ averaged from 20 to 60 minutes for the Saline and CNO group of the same transaxial plane as shown in (A). Right: The p-value map of differences between the groups in rDA projected on the mouse atlas of the corresponding plane displays statistically significant increases upon CNO injection.

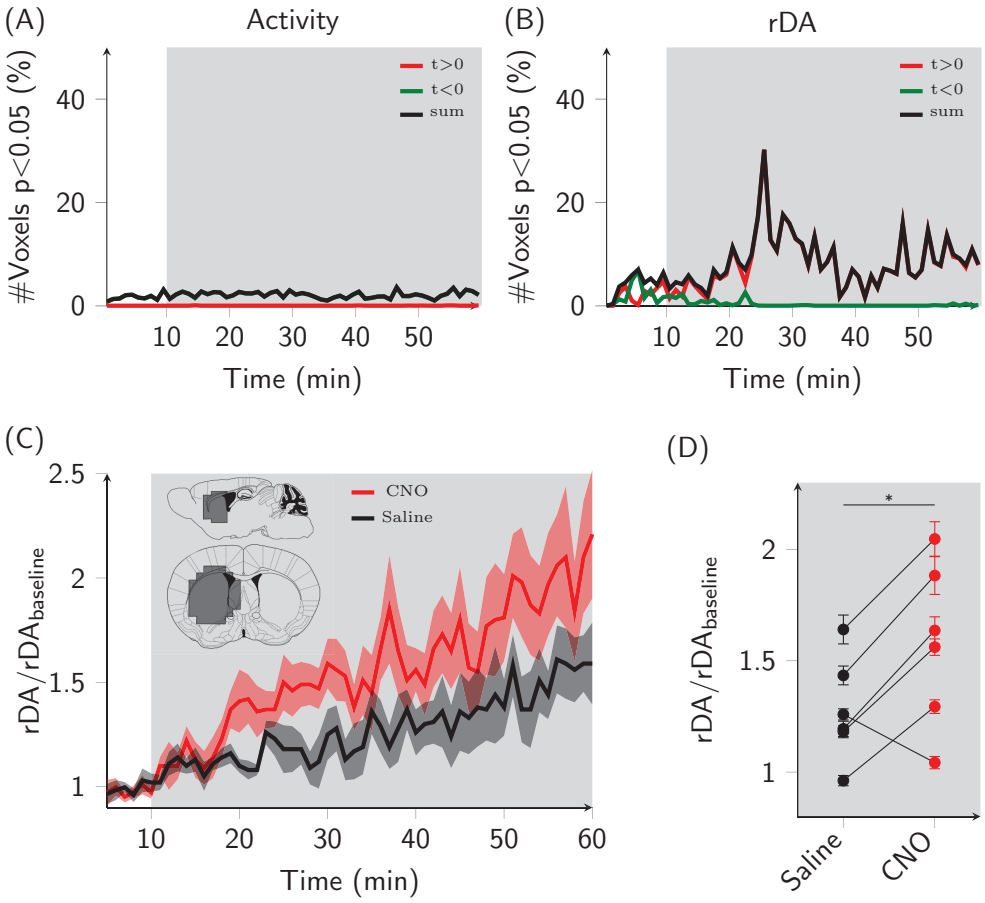

Figure 3.15: Dopamine release assessed by [11C]raclopride PET in $hM3D_{Gq}^{DAT}$ mice. (A) Number of significant different voxels in the brain between the Saline and CNO group of the [11C]raclopride activity data for every time point. (B) Number of significant different voxels in the brain between the Saline and CNO group of the parameter $rDA/rDA_{\text{baseline}}$ for every time point. (C) Temporal variations of the [11C]raclopride signal ($rDA/rDA_{\text{baseline}}$, mean±SEM) of the left striatum for the Saline (black) and CNO (red) groups. The gray background indicates the time after injection. (D) Average $rDA/rDA_{\text{baseline}}$ (mean±SEM) after t=10 min in each mouse after Saline and CNO injection. Paired Student's t-test: p=0.035. Figure panels (C) and (D) (modified) are published in Figure 9 in the manuscript by Lippert and Cremer et al.[86].

3.1.5 [11C]Raclopride PET in Humans

The group of Marc Tittgemeyer in collaboration with Heiko Backes of the Max Planck Institute for Metabolism planned and performed a [11C]raclopride PET study in humans to analyze food intake related changes in the dopamine system. The results are published in the manuscript of Thanarajah and Backes et al. (2018) [87] and partly in the manuscript by Lippert and Cremer et al. (2019) [86]. Data analysis based on the method developed within the framework of this thesis was performed with my contribution by Heiko Backes and Sharmili Edwin-Thanarajah. Within this section, parts of the results are shown to demonstrate the power of the developed method.
[11C]raclopride PET scans in ten healthy volunteers with a bolus-plus-infusion injection protocol were performed. Within two scan sessions the human subjects either received milkshake or a tasteless solution in a randomized order.
Mean uptake images for the time of 20-60 min of the scans for the tasteless and milkshake group are shown in Figure 3.16A. Over the whole time course of measurement there are only few significant different voxels between the groups in the radiotracer concentration given by voxel-wise calculated t-tests (Figure 3.16B).
By application of the proposed method to analyze temporal variations in the PET signal by the parameter, rDA (calculated by equation 3.35 within a box of 125 voxels, see sections 3.1.1 and 3.2.5), an increased number of significant different voxels in the brain between milkshake and tasteless conditions predominantly at two time-points is found (Figure 3.16D). The first time-point indicates an immediate food-induced dopaminergic activation at the time of milkshake supply [86,87]. The second time interval at 35-40 minutes indicates a secondary delayed interval of food-induced dopaminergic activation [86,87]. Both time intervals are further analyzed.
At the time of milkshake/tasteless solution supply significant increases in rDA for the milkshake group are found in reward-related regions of the dopamine system, i.e. in the ventral striatum: $p_{\mathrm{FWE,cluster}}$ =0.003, the habenula: $p_{\mathrm{FWE,cluster}}$=0.0007, the substantia nigra/VTA: $p_{\mathrm{FWE,cluster}}$<0.0001, and the pons/NTS: $p_{\mathrm{FWE,cluster}}$=0.001 [86]. These regions are highlighted in red in Figure 3.17B. While the increases in rDA upon milkshake intake can clearly be seen (Figure 3.17C), the time-activity curves of the same regions do not show any differences (Figure 3.17A). Remarkably, stimulation appears to induce detectable variations in the [11C]raclopride signal even in extrastriatal regions although there is less [11C]raclopride binding [86,87].
The significant differences in dopaminergic activity at the second-time interval 15-20 min post-stimulation are highlighted in green in Figure 3.17B. Dopaminergic activation in response to the milkshake is again visible in the pons although at a different location as at the primary activation interval ($p_{\mathrm{FWE,cluster}}$<0.0001) [86], as well as in neighboring activation sites to the earlier activations, i.e. the ventral posterior medial nucleus of the thalamus (VPM: $p_{\mathrm{FWE,cluster}}$=0.018) and the dorsal striatum ($p_{\mathrm{FWE,cluster}}$=0.0003) [86]. Note that in contrast to the temporal signal variations, the net [11C]raclopride uptake in the corresponding regions does not show any significant differences between milkshake and tasteless condition (Figure 3.17A).

A possible mechanism for the origin of the delayed dopamine activity observed here, could be signaling by the vagus nerve, which was shown – in rodents – to transmit postingestive signals from the gut into the brain that can induce dopamine responses[105,106,86]. Moreover, it was shown that vagal nerve afferent terminals have D2 receptors[105,106,86].
All in all, these results signify the relation between temporal signal variations assessed by rDA and dopaminergic activation and therefore demonstrate the power of the novel method to analyze [11C]raclopride PET data in humans[86]. Further results of the human study can be found in the manuscript of Thanarajah and Backes et al.[87].

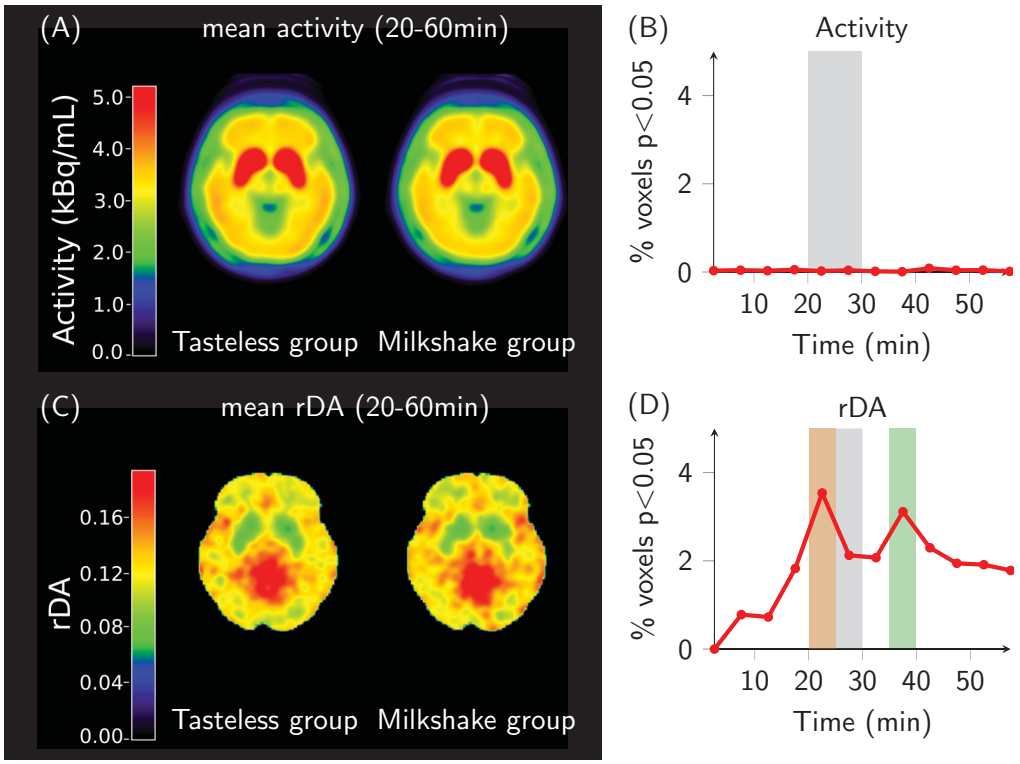

Figure 3.16: Differences between milkshake and tasteless solution intake in [11C]raclopride uptake and the parameter rDA. (A) Mean uptake images of [11C]raclopride for the tasteless and milkshake measurements (n=10). (B) Percent of voxels (of the whole brain) with significantly increased activity between milkshake and tasteless condition. The gray box indicates the time of milkshake/tasteless solution supply. There are only negligible differences in tracer uptake. (C) rDA parametric maps for the milkshake and tasteless group. (D) Percent of voxels with significantly increased rDA in milkshake versus tasteless condition. The data indicate an immediate (20-25 min, orange box) and a delayed (35-40 min, green box) time interval of food-induced dopaminergic activation.

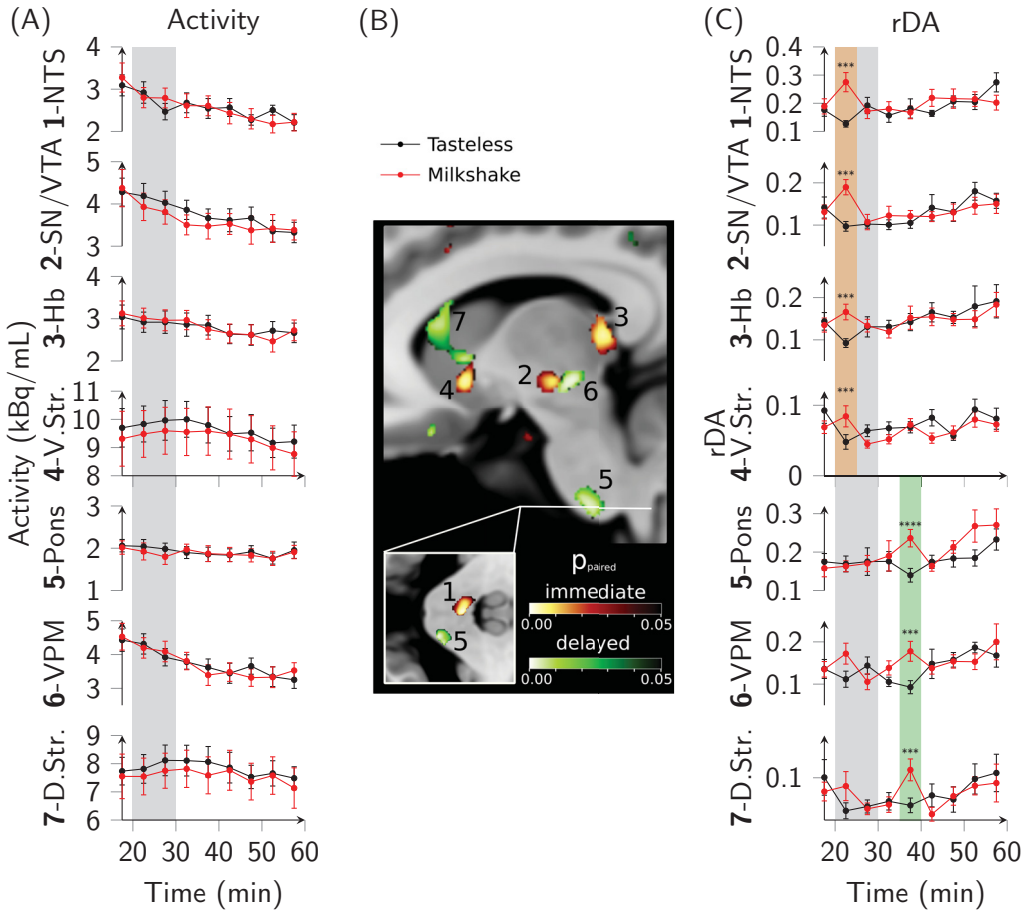

Figure 3.17: Dopamine release assessed by [11C]raclopride PET in humans in response to milkshake intake. (A) Time-activity curves of the regions indicated in (B) showing no detectable differences between tasteless (black) and milkshake (red) condition. The gray box indicates the time of milkshake/tasteless solution administration. (B) Location of regions with significant differences of rDA between milkshake and tasteless condition in the 20-25 min (red color scale) or 35-40 min (green color scale) time interval. (C) Time course of rDA in regions with significant differences between milkshake (red) and tasteless (black) condition in the 20-20 min (orange box) or 35-40 min (green box) time interval. Identified regions are 1: nucleus of the solitary tract (NTS), 2: substantia nigra/VTA, 3: habelula, 4: ventral striatum, 5: pons, 6: ventral posterior medial nucleus of the thalamus (VPM), and 7: dorsal striatum. All data are represented as mean±SEM, paired Student's t-test: df=9, ****=p<0.001 (t>4.78), ***=p<0.005 (t>3.69),*=p<0.05 (t>2.26) (uncorrected). The Figure (modified) is published in the manuscript by Lippert and Cremer et al. [86].

3.1.6 [18F]Desmethoxyfallypride PET Scans in Mice

Since [11C]raclopride has a short half-live of only ∼20 minutes, it needs to be produced on site. The tracer [18F]desmethoxyfallypride ([18F]DMFP) has similar kinetics, but has a half-live of 110 minutes. Therefore [18F]DMFP can be supplied by a remote radiochemistry facility. Within the model calculations [18F]DMFP shows high potential in assessing temporal signal variations upon dopamine release events (section 3.1.3). To experimentally test the application of [18F]DMFP to assess dopaminergic activity by the introduced method a first study with [18F]DMFP was performed. For the study the same chemogenetic mouse model, setup and procedures were used as for the [11C]raclopride experiments.
Analyzing the time-activity data showed that, due to the slightly different kinetics of [18F]DMFP, steady-state conditions were not reached by the bolus-plus-constant infusion protocol optimized for [11C]raclopride (Figure 3.18). For further experiments the bolus injection and the rate of constant infusion should be adjusted.

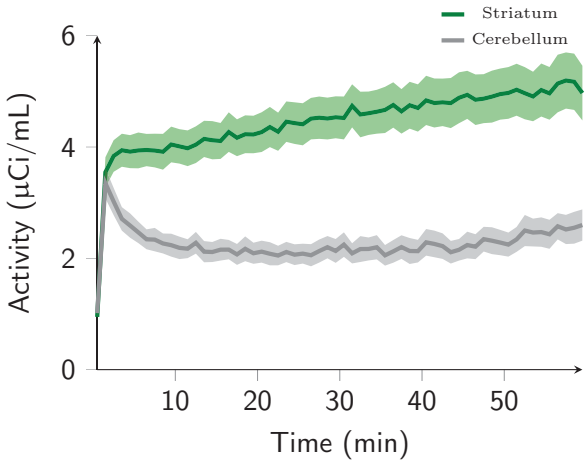

Figure 3.18: Time-activity curves of [18F]DMFP PET scans in mice. Time-activity curves of the striatum and cerebellum. Steady-state is not reached since activity increases with time.

The mean uptake images of [18F]DMFP for the Saline and CNO group (n=7) are shown in Figure 3.19A, where the striatum shows the strongest binding. Between the mean uptake images from 20 to 60 minutes for the Saline and CNO group a voxel-wise t-test was performed. As shown in Figure 3.19A there is no statistical significant difference in the activity within the shown plane. Plotting the number of significant different voxels in the activity data between the groups for the whole brain and each time point confirms that there are almost no differences in the time-activity data upon CNO injection (Figure 3.20A).
Temporal variations, $rDA/rDA_{\text{baseline}}$, in the [18F]DMFP signal were calculated in the same manner as for [11C]raclopride data. The averaged images of this parameter for the time interval between 20 and 60 minutes for both groups are shown in Figure

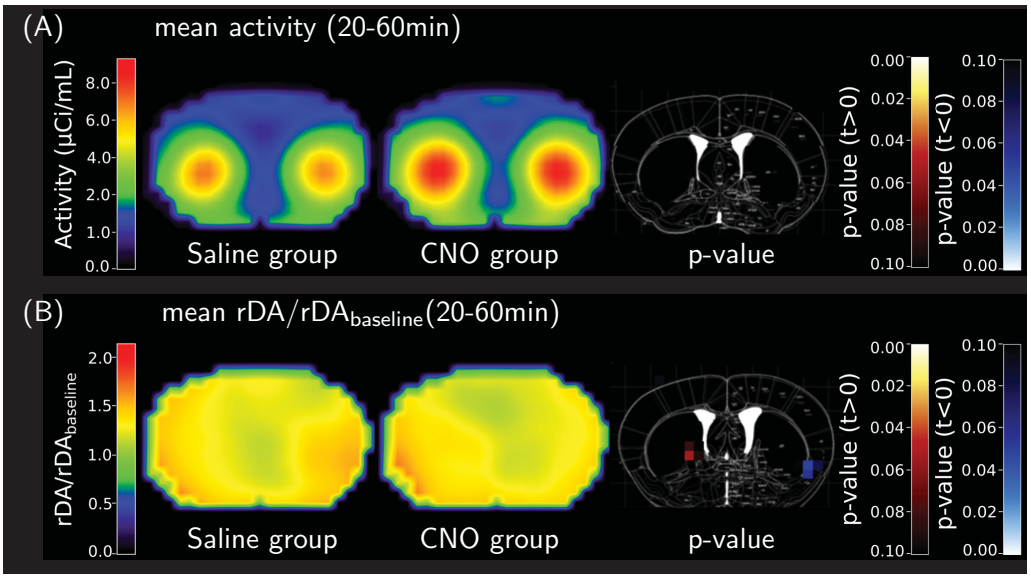

Figure 3.19: Differences between [18F]DMFP uptake and the parameter rDA in hM3D$_{Gq}^{DAT}$ mice. (A) Left: Averaged [18F]DMFP activity of a transaxial plane of the mouse brain for the Saline and CNO group of the time interval from 20 to 60 minutes (n=7). Right: Statistical significant differences between the data projected on the corresponding plane of the mouse atlas. In [18F]DMFP activity no significant differences between the groups are found. (B) Left: Parametric images of $rDA/rDA_{\text{baseline}}$ averaged for the Saline and CNO group for the time interval from 20 to 60 minutes and from the same transaxial plane as shown in (A). Right: The p-value map projected on the mouse atlas of the corresponding plane displays only few statistically significant differences between the groups.

3.19B, revealing no obvious differences in temporal variations between the groups. The voxel-wise t-test between both groups also reveals almost no significant differences in the temporal variation parameter in the shown plane. Furthermore, there are also only a few statistically different voxels for the calculated rDA parameter in the whole brain over time between the groups (Figure 3.20B).
The mean time-curves of $rDA/rDA_{\text{baseline}}$ of the left striatum for the Saline and CNO group are shown in Figure 3.20C. No increase in the temporal signal variations was observed in the striatum upon CNO injection compared to Saline-injected mice. The average rDA data after injection for each measurements is displayed in Figure 3.20D, showing that only in three of seven measurements the temporal variations were increased by CNO injection and is even decreased in the others.
A probable reason why the application of the method to [18F]DMFP did not provide similar results as with [11C]raclopride might be that steady-state conditions were not reached due to the slightly different kinetics of [18F]DMFP. Further studies have to be conducted using an adjusted injection protocol and maybe another type of stimulation protocol or mouse model could be advantageous.

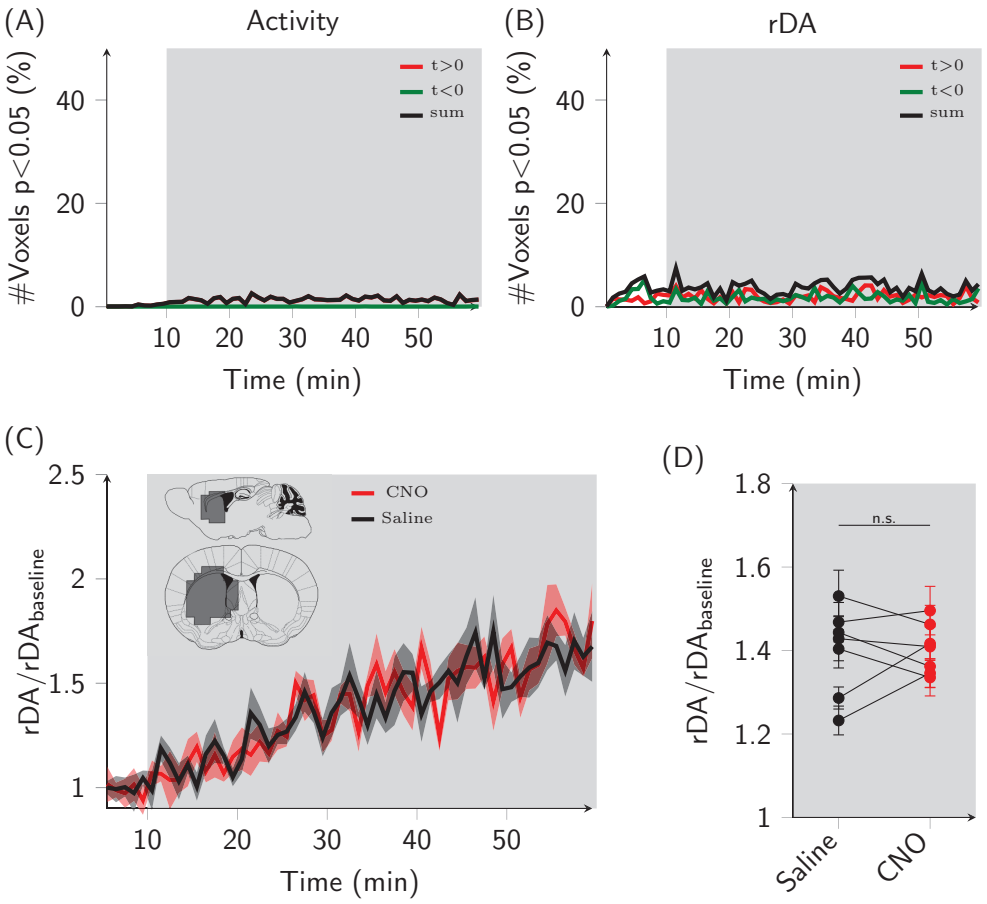

Figure 3.20: Dopamine release assessed by [18F]DMFP PET in $hM3D_{Gq}^{DAT}$ mice. (A) Number of significant different voxels between the Saline and CNO group of the activity data for each time point. (B) Number of significantly different voxels between the Saline and CNO group of rDA for each time point. (C) Temporal variations of the [18F]DMFP signal (rDA, mean±SEM). No difference in rDA within the left striatum is observed upon CNO injection (red) in comparison to Saline injection (black). The gray background indicates the time after injection. (D) Average rDA (mean±SEM) after t=10 min of each mouse after Saline and CNO injection. Paired Student's t-test: p=n.s..

3.1.7 Direct Measurement of Synaptic Release Events in the ECS

The model results for approach (I) show that temporal PET signal variations are more sensitive to slower changes of endogenous neurotransmitter concentrations in the ECS than to rapid fluctuations. In order to demonstrate that rapid phasic release events can be related to slower variations in extracellular neurotransmitter concentrations, direct measurements of dopamine and serotonin concentrations in the ECS were performed.
Extracellular dopamine levels over one hour were measured in mice using fast-scan cyclic voltammetry (FSCV). The experiments were performed at the Oxford University by Clio Korn and Lauren Burgeno of the group of Mark Walton and are published within the manuscript of Lippert and Cremer et al. (2019) [86]. FSCV experiments were performed in two different mouse models: once in the chemogenetic mouse model used for the PET scans and once in wild-type mice with electrical stimulation of dopaminergic neurons. The continuously acquired FSCV data was used to analyze correlations between fast synaptic release events and slower concentration changes in the ECS by frequency analysis.
Within this section the technique FSCV is introduced and the results of the dopamine recordings as well as the frequency analyses of the data are shown. The results are further substantiated by theoretic model calculations, providing a potential mechanism of the occurrence of "long" lasting extracellular neurotransmitter concentrations.
Furthermore continuous FSCV data of serotonin is shown, which were acquired in wild-type mice at the University of South Carolina by Alyssa West of Parastoo Hashemi's group.

Fast-scan cyclic voltammetry

Fast-scan cyclic voltammetry (FSCV) is a technique that permits *in vivo* measurement of electroactive substances such as dopamine (applicable to dopamine, serotonin and norepinephrine). For a FSCV measurement a carbon-fiber microelectrode is implanted at the location of interest. By applying rapid potential sweeps the analytes of interest, e.g. dopamine, are oxidized and reduced. From the resulting "cyclic voltamogramms", in which measured current is displayed as a function of applied potential, the oxidized compound can be identified by its specific current-potential characteristics [107]. In the voltammetry field, elevations in extracellular concentrations of the studied analyte above the ambient level upon release events are called transients (see Figure 3.21). Shape, magnitude, and duration of FSCV transients can be modeled as integrated neurotransmitters from synapses surrounding the microelectrode diffusing into the extracellular space taking into account removal of the neurotransmitter from the ECS [86]. The extracellular neurotransmitter concentration, N_e, measured at the electrode is given by [99,88,86]:

$$N_e(r,t) = \sum_{i,j(t>t_{i,j})} \frac{l_s V_s N_s}{\alpha(4\pi D(t-t_{i,j}))^{3/2}} exp(\frac{-(r-r_i)^2}{4D(t-t_{i,j})}) exp(-k(t-t_{i,j})). \quad (3.13)$$

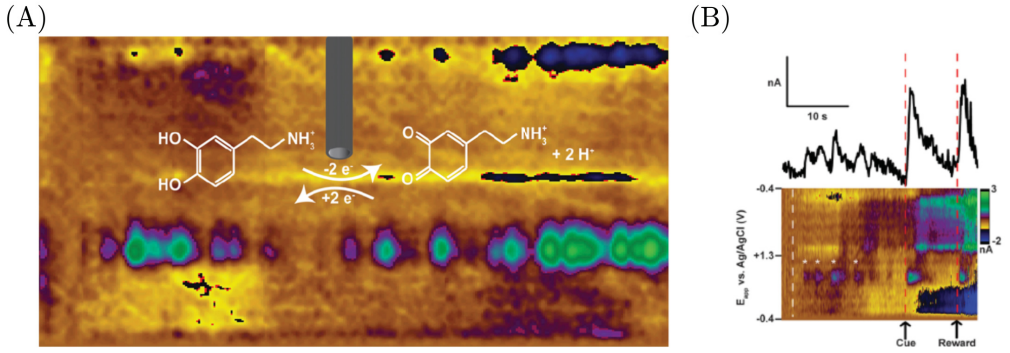

Figure 3.21: Fast-scan cyclic voltammetry to measure neurotransmitter release. (A) A carbon fiber micro-electrode is used to oxidize and reduce monoamine neurotransmitters like dopamine, serotonin or norepinephrine by applying rapid potential sweeps. By analyzing the "fingerprint" of the measurement, i.e. the so-called cyclic voltammograms, in which the measured current is plotted as a function of the applied potential, one can identify the measured compound. (B) Measured dopamine transients at chronically implanted carbon-fiber micro-electrodes of spontaneous transients observed during a behavioral session of Pavlovian conditioning. Figure modified from [107].

V_s is the fractional volume of the synapse, N_s the neurotransmitter concentration within the synapse, D the apparent diffusion coefficient, α the fraction of extracellular volume, and l_s the fraction of synaptic leakage or spillover [86]. Typical values for the striatum for dopamine are V_s=0.02μ m^3, N_s=0.8 mmol/L, D=7.63e^6 cm^2/s, $\alpha = 0.21$, $l_s = 0.01$ [86,88,99]. Dopamine is removed from the extracellular space by dopamine transporters (DATs) with an effective removal rate constant of k, which reflects the local density of DATs. Reported values for the removal rate k range from k=0.01 s^{-1} to 20 s^{-1} (see section 3.1.3) [88,101]. The fraction, l_s, that was able to diffuse out of the synapse, and not the total amount of neurotransmitter released, needs to be inserted into equation 3.13 [86]. Equation 3.13 applies to spherical neurotransmitter diffusion in the extracellular space outside of the synapse [86]. Within the synapse the narrow space confined by pre- and postsynaptic membranes and the high density of transporters and receptors would require a mathematical description different from equation 3.13 [86]. Equation 3.13 includes neurotransmitter diffusion from the synapses at locations, r_i, and removal from extracellular space with an effective removal rate constant of k [86]. The summation is over all synapses, i, and release times, j, with $t_{i,j}$ being the times of neurotransmitter release of a synapse at location r_i [86]. Plotting equation 3.13 with realistic values leads to a typical transient shape as reported in literature and is shown in Figure 3.22. All in all, equation 3.13 successfully describes the dopamine concentrations in the extracellular space observed after phasic release and should also apply for FSCV measurements of serotonin [99,88,86]. The solution given in equation 3.13 assumes homogeneous distribution of transporters. A numerical instead of analytical solution allows to insert different distributions of k in space.

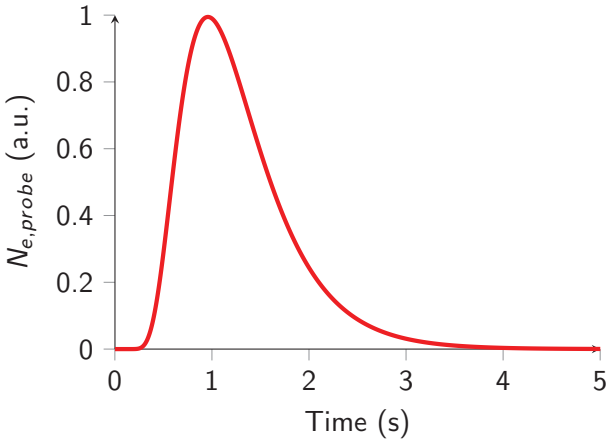

Figure 3.22: Calculated extracellular neurotransmitter concentration at the FSCV electrode after synaptic release. Solution of equation 3.13 for the probe at r=100 μ m with a re-uptake rate of k=2 s^{-1}, a fractional volume of V_s=0.02·10^{-9} mm^3, a diffusion coefficient of D=0.00763 mm^2/s, a fraction of extracellular volume of α=0.21, a synaptic leakage of l_s=0.01, and arbitrary concentration of neurotransmitter within the synapse N_s.

Fast-scan cyclic voltammetry measurements of dopamine

To directly assess dopamine concentrations in the ECS, fast-scan cyclic voltammetry (FSCV) was performed in electrically stimulated wild-type mice and in the chemogenetic mouse model of the PET scans (see also "Material and Methods" section 3.2.7 for the detailed experimental protocol). The measured transients by FSCV are directly linked to synaptic dopamine release, so that the number of transients per time is a measure of dopaminergic activity.
Electrical stimulation of the VTA in the wild-type mice (n=4) was performed at rates of 5 or 10 transients/minute for one-minute intervals followed by a four-minute (measurement 1) or a nine-minute interval (measurements 2, 3, and 4) without stimulation. In the chemogenetic mouse model (hM3D$_{Gq}^{DAT}$) dopamine release was induced by injection of the drug clozapine-n-oxide (CNO) in analogy to the PET experiments (n=7) [86]. In both models data was continuously acquired in the ventral striatum over the time of one hour at a rate of 10 Hz, a second hour was acquired in the chemogenetic mouse model.
First, the data was used to validate the hM3D$_{Gq}^{DAT}$ mouse model by analysis of the rate and size of measured transients. Second, we were interested in the kinetics, i.e. the time scales, of dopamine in the extracellular space and therefore used the data to analyze different frequency contributions in the signal. The continuous recordings over one hour at 10 Hz enable the analysis of frequencies between 5 Hz (Nyquist-Shannon sampling theorem: $\Delta f/2$) and $\sim 2 \cdot 10^{-4}$ Hz.

In this chapter it is shown that (i) electrical stimulation leads to measurable transients of the provided frequency (5 or 10 transients/minute) and that chemogenetic activation of dopamine neurons increases the rate, but not the magnitude, of spontaneous dopamine transients measured in the ventral striatum of $hM3D_{Gq}{}^{DAT}$ mice. Furthermore it is pointed out that (ii) the rate of transients – electrically or chemogenetically induced – is correlated with frequency variations of ∼0.5 Hz in dopamine levels extracted from the continuous FSCV data. This frequency reflects the typical duration of ∼2 s transients and is further referred to as "high frequency". To link this high frequency variations to slower concentration variations in the ECS it is demonstrated that (iii) transient rates and high frequency variations are correlated with "low frequency" variations (∼0.01 Hz) in both models (cf. [86]). Note that the following analysis of the data is published in the manuscript by Lippert and Cremer et al. (2019) [86].

i **Stimulation of dopamine neurons increases the rate of dopamine transients.**
Electrical stimulation of the VTA with a defined frequency of 5 or 10 transients/minute leads to measurable transients in the striatum with the provided rate (Figure 3.23A). For the CNO- and Saline-treated $hM3D_{Gq}{}^{DAT}$ mice the rate of transients is counted in one-minute intervals of the continuous FSCV data (Figure 3.23B). Minor differences in the spontaneous activity in the first 5 minutes of baseline recording are found. After that, a significant increase of the dopamine transient rate following CNO-treatment at 10 minutes are observed, which are not present in the Saline-treated mice (main effect of treatment: $F(1,5)_{1st\ hour}=14.31$, $p=0.0129$, $F(1,5)_{2nd\ hour}=6.99$, $p=0.0458$). No consistent change in the size of the transients between the Saline or CNO group is found over the recording time, when the pre-drug period is compared with the 1st or 2nd hour after CNO administration (period x group interaction: $F(2,8)=0.946$, $p=0.428$, Two-way ANOVA; one saline-treated mouse had no transients in the pre-drug period and was excluded from this analysis). Note that the transient size recorded in the CNO-treated group is on average marginally higher throughout recording (main effect of group: $F(1,4)=12.34$, $p=0.025$) (Figure 3.24). Taking together, CNO administration in $hM3D_{Gq}{}^{DAT}$ mice increases the transient rate, but has only a minor effect on the amplitude of each measured release event. Cf. [86]

ii **The dopamine transient rate correlates with dopamine variations with a frequency of 0.5 Hz**
The continuous FSCV signal is decomposed into contributions from different frequencies by performing a wavelet transform [108]. In contrast to a Fourier transformation the wavelet transform allows for frequency analysis without completely losing the temporal resolution.
Figure 3.25 shows the traces of continuously recorded FSCV data in the ventral striatum of a single $hM3D_{Gq}{}^{DAT}$ mouse with CNO injection and of a wild-type

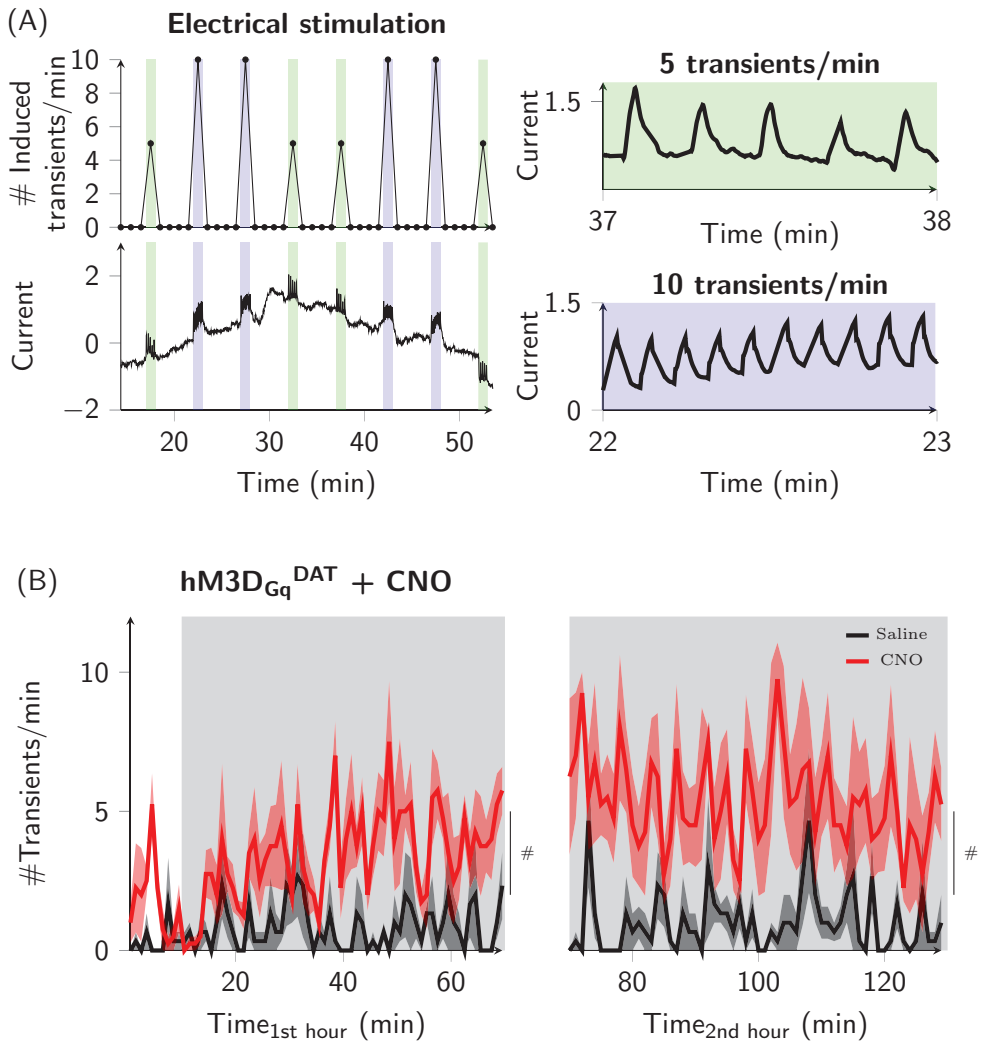

Figure 3.23: Transients per minute after electrical stimulation and chemogenetic activation. (A) Induced transients per minute and the continuous FSCV signal. Intervals with 5 induced transients/minute are highlighted by a green background, intervals with 10 induced transients/minute in blue. Two exemplary stimulation intervals are displayed on the right: 5 and 10 transients are clearly visible in the data. (B) Spontaneous transients per minute±SEM recorded in hM3D$_{Gq}$^{DAT} mice before (white background) and after (gray background) CNO (n=4) or Saline (n=3) injection. Data were analyzed via Two-way ANOVA, #=p<0.05 for an overall main effect of treatment type. Figure panel (A) displays the data published in Figure 6 in the manuscript by Lippert and Cremer et al. [86], panel (B) (modified) is published in Figure 4 (C) [86].

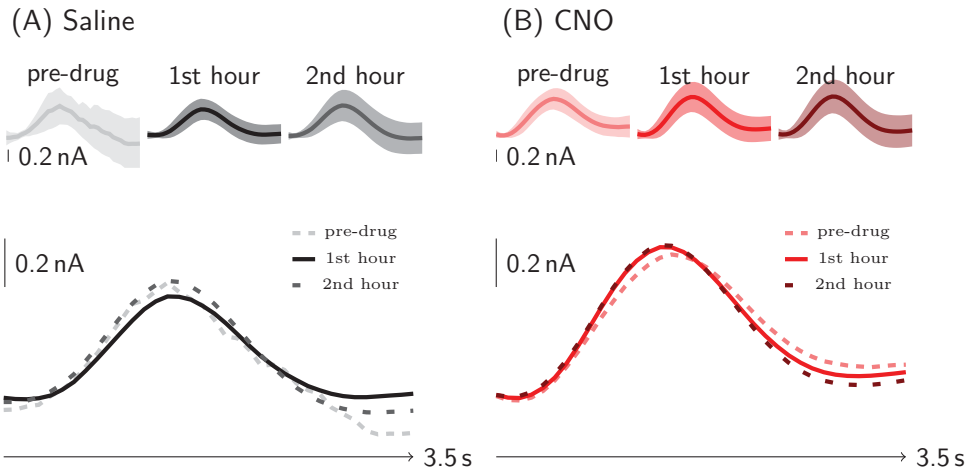

Figure 3.24: Transient size of dopamine transients in the hM3D$_{Gq}$^{DAT} mouse model. (A) Average transients (mean±SD across all recorded transients) during 15 minutes before drug administration, during the first and second hour of measurement for the hM3D$_{Gq}$^{DAT} Saline-treated animals. (B) Average transients (mean±SD across all recorded transients) during 15 minutes before drug administration, during the first and second hour of measurement for the hM3D$_{Gq}$^{DAT} CNO-treated animals. Figure displays the same data published in Figure 4 (B) in the manuscript by Lippert and Cremer et al. [86].

mouse with electrical stimulation, as well as the corresponding wavelet power spectrum. The wavelet transform is calculated using a Gaussian mother function of order 3 (see "Material and Methods" section) and the resulting wavelet power is further analyzed in one-minute time intervals. A significant correlation between the induced rates of electrically stimulated dopamine transients (5 or 10 transients/minute) in the wild-type mice with the logarithm of the wavelet power at a frequency of 0.5 Hz of each one-minute interval is found (Pearson product moment correlation: r=0.89, p<10^{15}) (Figure 3.26C). Additionally, transients measured in the chemogenetic mice in one-minute intervals are significantly correlated with the logarithm of the wavelet power at a frequency of 0.5 Hz (Pearson's product-moment correlation: r_{CNO}=0.64, p_{CNO}<10^{16}, r_{Saline}=0.63, p_{Saline}<10^{16}, r_{combined}=0.73, p_{combined}<10^{16}, Figures 3.27 and 3.28A-D). The transient rate and the wavelet power at a frequency of 0.5 Hz not only correlate on group level, but also in individual measurements (see Appendix, Figure A.1). This indicates that the power at 0.5 Hz calculated from the FSCV data can be used as a measure of the transient rate. An advantage of this kind of analysis is, that the wavelet power is calculated following a well-defined standard procedure, which does not require any thresholds or assumptions on the shape of transients. Taken together, the data demonstrate that activation of dopamine neurons in mice, either electrically or chemogenetically, increases not only the transient rate, but also the wavelet power at 0.5 Hz. Cf. [86]

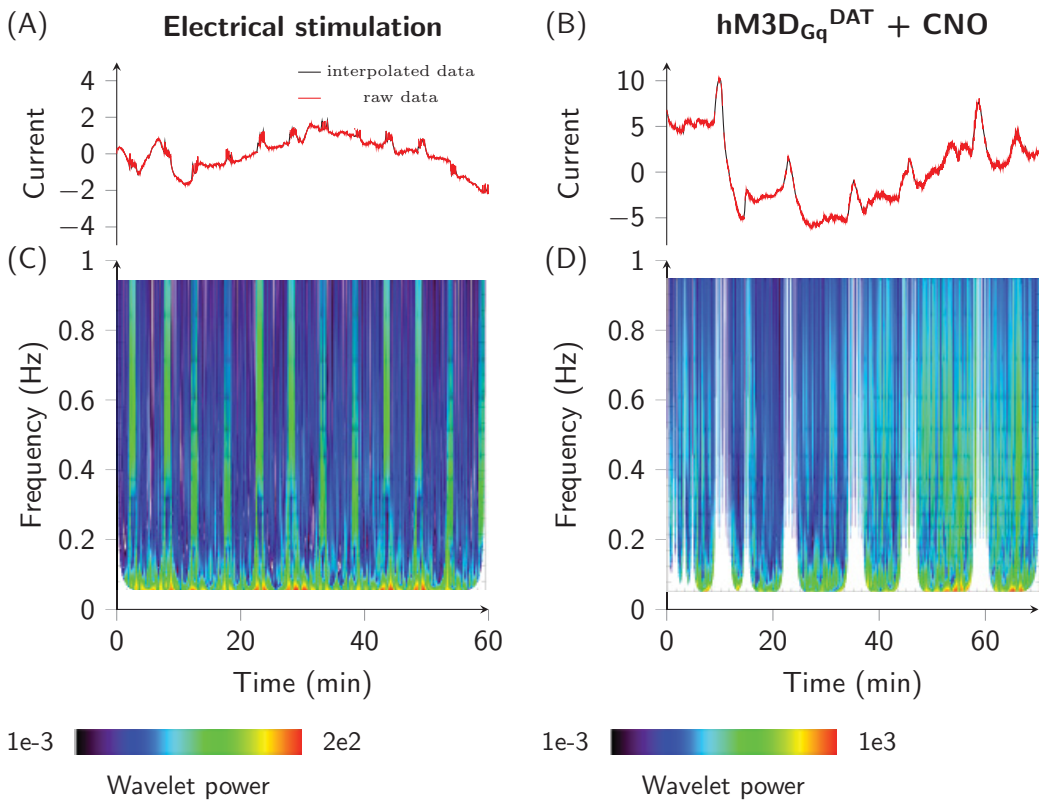

Figure 3.25: Wavelet power of continuous FSCV recordings. (A) Continuous FSCV data recorded in the ventral striatum of a single mouse. CNO was injected interperitoneally at t=10 min. (B) Continuous FSCV data recorded in the ventral striatum of a single mouse with electrical stimulation of the VTA. (C) Contour plot of the wavelet power calculated from the FSCV data shown in (A). (D) Contour plot of the wavelet power calculated from the FSCV data shown in (B).

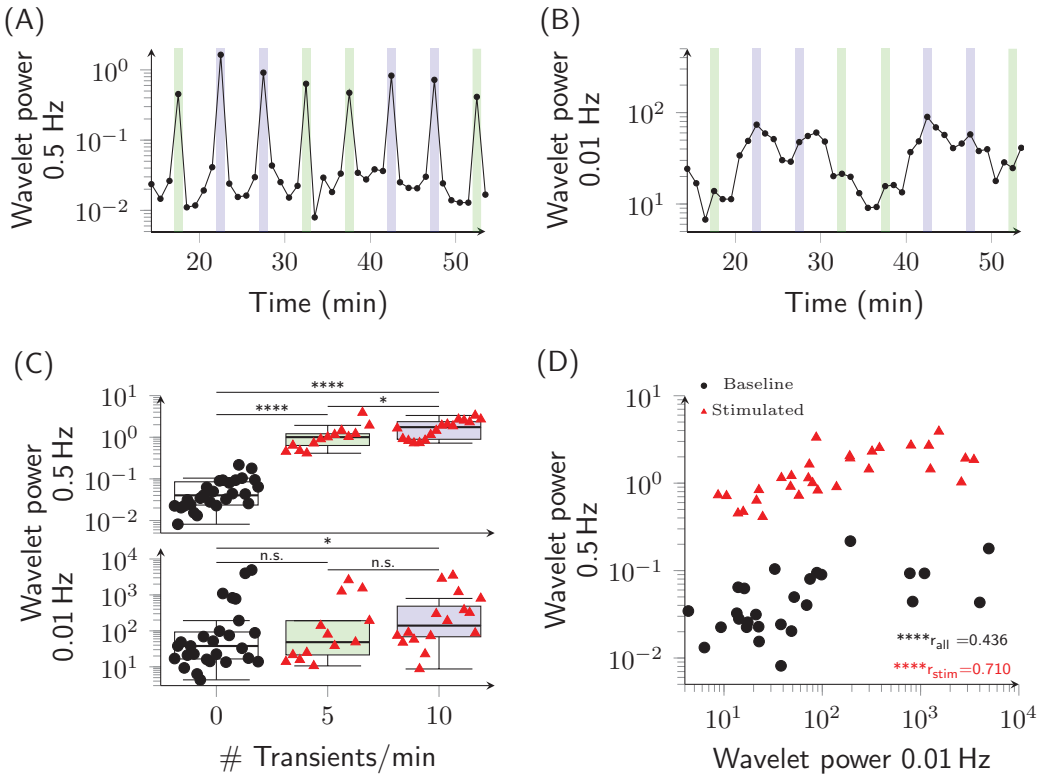

Figure 3.26: Correlations between transient rates and high and low-frequency power after electrical stimulation. (A) Wavelet power in one-minute intervals as a function of induced transients (n=4 mice). A Welch two-sample t-test was used for the statistics. (B) Correlation of wavelet power at 0.5 Hz and 0.01 Hz in stimulated one-minute intervals (red triangles) and non-stimulated one minute intervals taken from the center of non-stimulated time intervals (black circles). *: p-value≤0.05, **: p-value≤0.01, ***: p-value≤0.001 and ****: p-value≤0.0001. Figure displays the data published in Figure 6 in the manuscript by Lippert and Cremer et al.[86].

iii **Transient rates, high and low-frequency variations**
From theory extracellular dopamine concentration variations on a time scale of $\sim$ minutes are needed to induce detectable signal variations in the PET signal as demonstrated above (see section 3.1.2). Therefore, the wavelet transform was used to analyze the contribution of the frequency of 0.01 Hz (referred to as "low") in the FSCV data. Relations between the wavelet power at 0.5 Hz (referred to as "high") and the low frequency power, as well as between the transient rate and the low frequency variations are investigated. In electrically stimulated mice a significant correlation between the logarithm of high and low frequency power (Pearson's product-moment correlation of log(0.5 Hz power) vs. log(0.01 Hz power): r=0.55, p=0.00012; Figure 3.26B) and also between transient rates and the logarithm of low frequency power (Pearson's product-moment correlation of transient rates vs. log(0.01 Hz power): r=0.44, p=0.0031, Figure 3.26A) is found. In the chemogenetic mice, transient rates and the logarithm of high and low frequency wavelet power correlate significantly within the Saline and the CNO group and in the combined data (Pearson's product-moment correlation between logarithmic power at 0.5 Hz and 0.01 Hz: r_{CNO}=0.13, p_{CNO}=0.030, r_{Saline}=0.14, p_{Saline}=0.042, r_{combined}=0.34, $p_{\mathrm{combined}}<10^{14}$, correlation between transient rates and logarithmic power at 0.01 Hz: r_{CNO}=0.15, p_{CNO}=0.008, r_{Saline}=0.16, p_{Saline}=0.016, r_{combined}=0.32, $p_{\mathrm{combined}}<10^{12}$) (Figure 3.28). Taken together, increases in the high frequency wavelet power, which reflect dopamine concentration increases on a time scale of $\sim$2 seconds, are systematically related to low frequency wavelet power increases. This demonstrates that dopamine release, i.e. dopaminergic activation, upon stimulation not only increases temporal variations in the FSCV signal on a time scale of seconds (high frequency), but also on a minute time scale (low frequency). Or in other words, activation of dopamine neurons and the resulting dopamine release can induce temporal fluctuations on a time scale of minutes in extracellular dopamine concentration. Cf. [86]

All together, the FSCV data and its frequency analysis relate dopamine release events with extracellular dopamine concentration variations at different time scales, i.e. at a time scale of seconds and at a time scale of minutes. It was shown that activation of dopaminergic neurons – electrically or chemogenetically – increases the rate of dopamine transients measured by FSCV as well as the high and low frequency power in the signal as assessed by a wavelet transform. This indicates that those three different components are all measures of *in vivo* dopaminergic activity [86]. Therefore, assessing the minute scale temporal variations of dopamine concentrations in the ECS – using the introduced method for data analysis of PET data – provides a measure of dopaminergic activity.

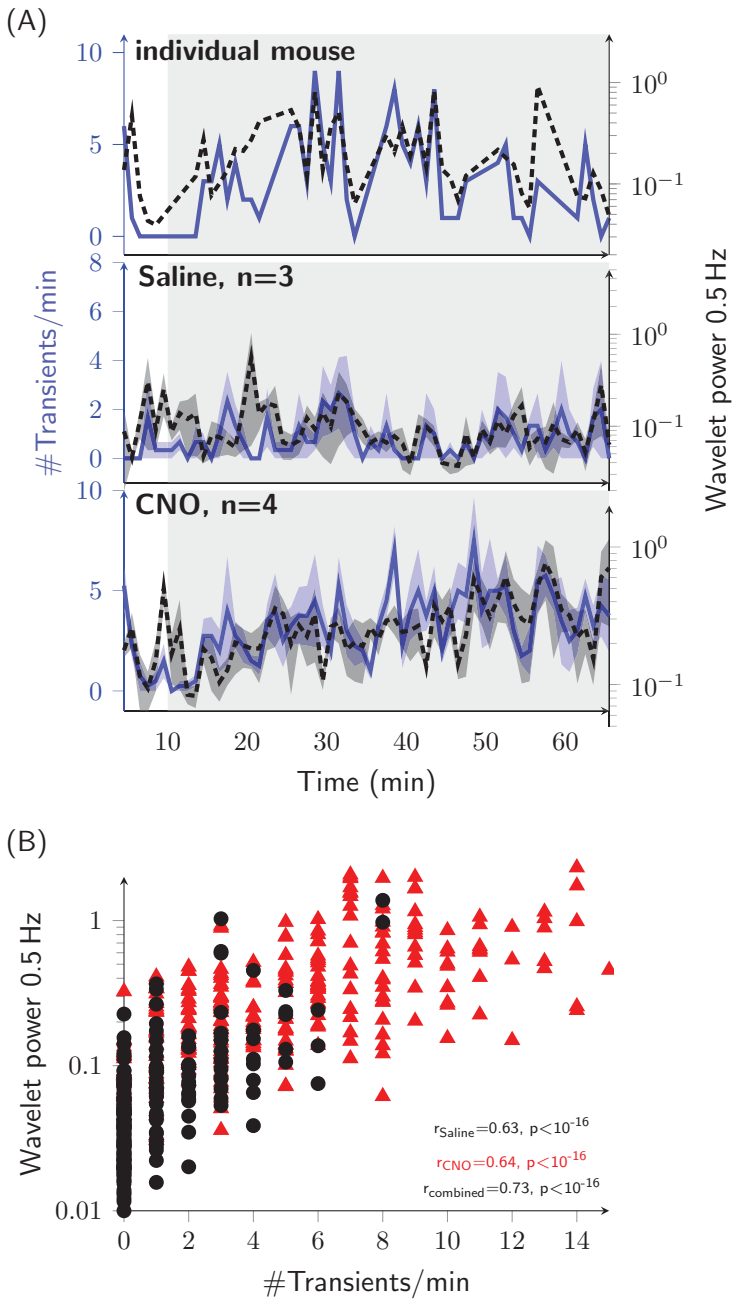

Figure 3.27: Transient rates and high frequency power of the hM3D$_{Gq}^{DAT}$ mouse model measurements. (A) Comparison of the number of transients (blue) and the wavelet power at 0.5 Hz (black) in one individual mouse and in the CNO and Saline group (mean±SEM). The gray box indicates the time after CNO/Saline injection. (B) Correlation of transient rate with the logarithm of the wavelet power at 0.5 Hz from all mice (red triangles=hM3D$_{Gq}^{DAT}$+CNO, n_{CNO}=4; black circles=hM3D$_{Gq}^{DAT}$+Saline, n_{Saline}=3). For the statistics a Pearson product moment correlation was used. Figure (modified) as published Figure 7 in the manuscript by Lippert and Cremer et al. [86].

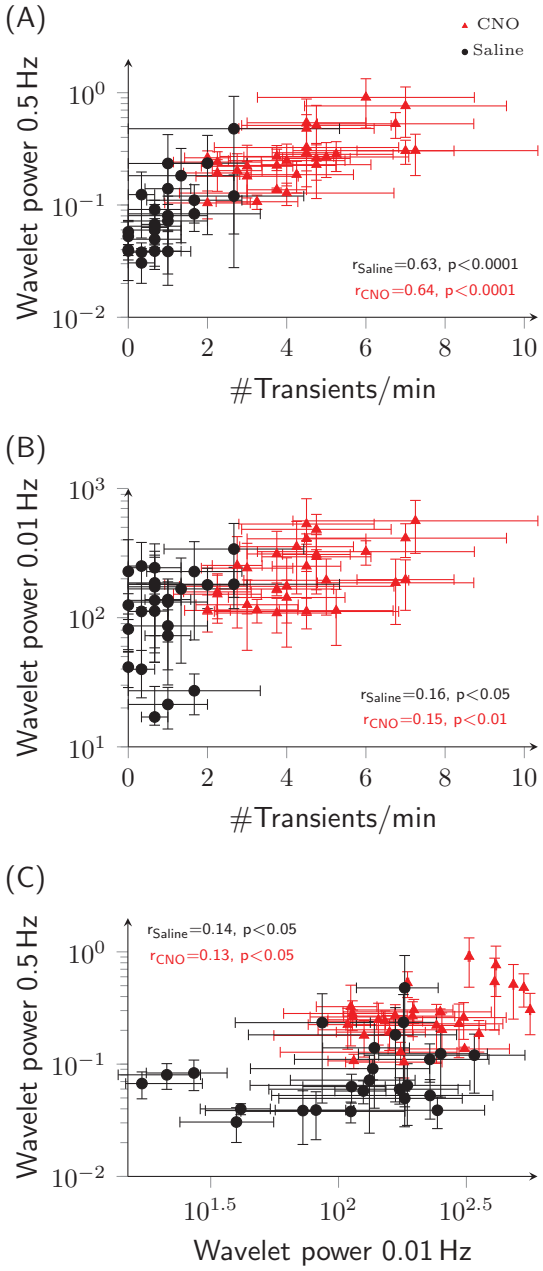

Figure 3.28: Correlations between transient rates and high and low-frequency power of the hM3D$_{Gq}^{DAT}$ mouse model measurements. (A) Correlations of the logarithm of high-frequency power (0.5 Hz) with transient rate. (B) Correlations of the logarithm of low-frequency power (0.01 Hz) with transient rate. (C) Correlations of the logarithm of high-frequency power (0.5 Hz) with the logarithm low-frequency power (0.01 Hz). Data points are shown for each one-minute interval as mean±SEM for each group (red triangles=hM3D$_{Gq}^{DAT}$+CNO, n_{CNO}=4; black circles=hM3D$_{Gq}^{DAT}$+Saline, n_{Saline}=3). Pearson's product-moment correlation coefficients were calculated within each group and were all statistically significant. Figure (modified) displays the data published in Figure 8 in the manuscript by Lippert and Cremer et al. [86].

Heterogeneous transporter expression explains minute-long concentration increases in the ECS

To further substantiate that FSCV signal variations on a time scale of minutes indeed reflect variations of neurotransmitter (dopamine) concentrations and are not only an artifact, a probable mechanism for the occurrence of these long lasting concentration changes is derived on basis of model calculations. The FSCV signal can be modeled by taking into account diffusion and transport of the neurotransmitter in the ECS, as introduced above (section 3.1.7). These two processes are described within the following equation:

$$\frac{\partial}{\partial t} N_e(r,t) = D \triangle N_e(r,t) - kN_e(r,t). \tag{3.14}$$

$N_e(r,t)$ is the neurotransmitter concentration at the probe at position r at time t. D is the diffusion constant of the neurotransmitter in the extracellular space, which is assumed to be constant. k is the removal rate constant in units of time^{-1}. $\triangle$ is the Laplace operator. To analyze the neurotransmitter concentrations in the ECS after release this equation was solved numerically. The numerical solution offers the possibility to not only analyze the influence of the distance r of the probe to the synaptic release site at a homogeneous and constant removal rate k (see [99,88]), but also to insert different spatial distributions for k. For the calculations spherical distribution is assumed and diffusion and re-uptake are calculated as function of radius r. Details on the model calculations can be found in the "Material and Methods" section 3.2.7. Note that the calculations are performed with parameters for the dopamine system.

The influence of the removal rate k on extracellular neurotransmitter concentration is investigated by assuming different k's, including only non-specific uptake (k_1=0.007 s^{-1}), the maximally reported removal rate of k_2=20 s^{-1} (for dopamine) [88,101], and two heterogeneous distributions of removal rate in space: k_3=50e$^{-r/20\mu m}$ s^{-1} and k_4=20e$^{-r/10\mu m}$ s^{-1}. In Figure 3.29A these removal rates are shown as function of the distance r. The removal rate k_3 is chosen under the assumption that the maximally reported removal rate k_2=20 s^{-1} only occurs very close to the release site, where the maximal number of re-uptake sites are placed, and that it decays exponentially with distance from the release site. This would correspond to a constant removal rate of k=10 s^{-1} in a sphere with radius r=10 μm. Note that the removal rate has at least the value of the only-non-specific uptake rate k_1. k_4 is chosen to have an equivalent average removal rate like k_2 in a sphere with a radius of 25 μm around the release site and decays exponentially with distance from release site. The neurotransmitter concentration at the FSCV probe in the ECS as a function of time at the distances r=1, 5, 20 and 100 μm from the release site for the named removal rates k is shown in Figure 3.29B-E, respectively. The model successfully describes neurotransmitter concentrations in the ECS after release as measured with FSCV and the analytical results for k=const. (equation 3.13) are reproduced [88].

If the removal rate is constant within space and relatively high (k_2), the neurotransmitter will be cleared very fast from the ECS, so that with further distance from the

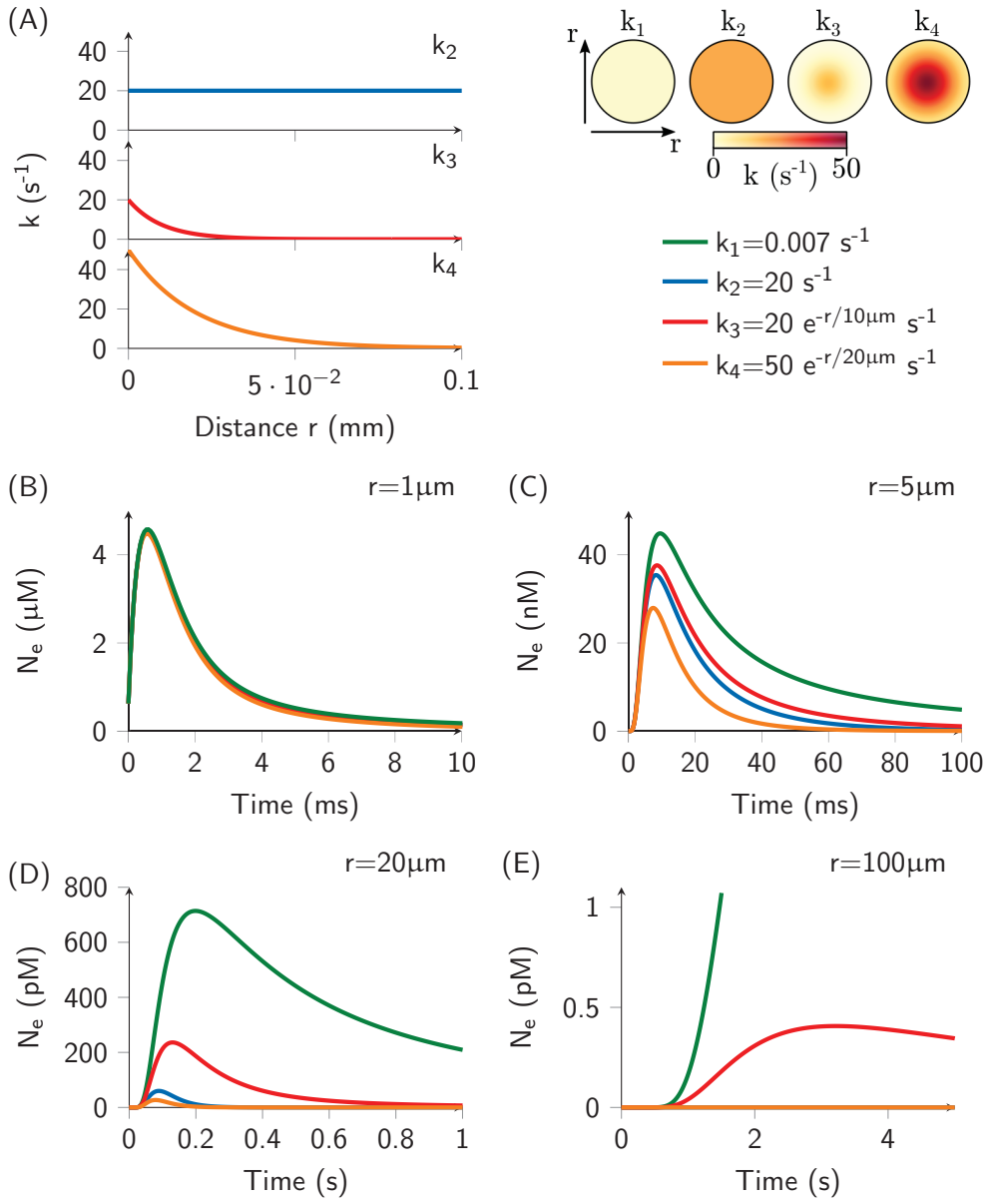

Figure 3.29: Extracellular neurotransmitter concentrations taking into account different removal rates. (A) Removal rates k_2 to k_4 as a function of distance r from the release site and contour plots of the spherical distribution. (B-E) Neurotransmitter concentration as a function of time after release at different positions (1 μm, 5 μm, 20 μm, 100 μm) of the FSCV probe for the named removal rates k. The results for the removal rates k_1=0.007 s^{-1} (green) and k_2=20 s^{-1} (blue) reproduce the results of the analytical solution with a constant removal rate (equation 3.13) [88].

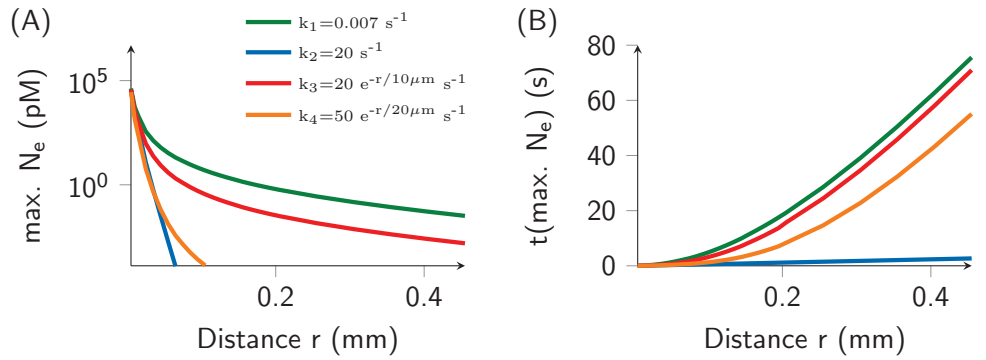

Figure 3.30: Time and concentration of the transient peak as a function of distance. (A) Maximal neurotransmitter concentration at the FSCV probe after release as a function of the distance of the probe from the release site. (B) Time of the maximally measured concentration after release as a function of distance of the probe.

release site its concentration becomes negligible. If the re-uptake sites are located predominantly close to the release site, so that a fraction of neurotransmitter can escape from the close vicinity of the synapse, there will be a fraction of neurotransmitter concentration within the pM-range also further away from the release site (k_3, Figures 3.29 and 3.30). This fraction is in the order of the tail concentration of the transient close to the release site and is cleared within a time scale of minutes due to the heterogeneous distribution of removal rates. Hence, while the transient peak, i.e. maximal concentration at the probe, decreases rapidly with distance from the release site, a fraction is cleared on a slower time scale and remains stable with increasing distance from the release site. Therefore, depending on the distribution of local removal rates net changes of extracellular neurotransmitter concentrations can occur at time scales of seconds to minutes [86]. This indicates that a heterogeneous distribution of transporters (e.g. DATs for dopamine) in the ECS, which determine the local removal rate, can explain the minute-long concentration variations that are found in the continuous FSCV data.
In Figure A.3 in the Appendix it is again clearly displayed that the amplitude of the transient peak (the fast component) rapidly decreases as a function of distance from the release site, while the long-lasting fraction (the transient tail) of neurotransmitter concentration remains rather constant. This means the further away from the release site the more pronounced is the minute-lasting component compared to the peak in the signal [86]. The results from the calculations agree well with observations reported in literature [109,110] (see Figure A.2), in which often a “hang-up”, i.e. tail in the transient data is observed. This tail is often found to be independent of the total peak height, so that a pure adsorption effect can be excluded (see data in [109,110]). Furthermore, in the measured data the contribution of the minute scale component (the tail) relative to the peak critically depends on the distance of the probe from the release site [111,110]. Comparing the amplitude of the minute scale component

close to the release site with the minute scale component further distant, they are approximately similar (Figure A.3D and in data from [110]).
Taken together, the model calculations and data from literature show that transport (removal) and not diffusion determines the minute scale dynamics [86]. From theory, the absolute rate of removal is given by the product of removal rate constant and extracellular neurotransmitter concentration ($-kN_e$). Furthermore, the amplitude of neurotransmitter concentration changes ($\mathrm{d}N_\mathrm{e}(\mathrm{r,t})/\mathrm{d}t$) in the ECS is proportional to the extracellular neurotransmitter concentration $N_\mathrm{e}(\mathrm{r,t})$, which by its origin is directly proportional to synaptic release (equation 3.14) [86]. Therefore, also the amplitude of minute scale concentration variations – low frequencies – is proportional to the amount of released neurotransmitter. This explains why the low frequency component (0.01 Hz wavelet power) in the FSCV signal is related to transient release. Summarizing, a heterogeneous distribution of re-uptake mechanisms, i.e. DATs, in the ECS can explain the observed minute-long increases of dopamine concentration after phasic release within the FSCV signal. This furthermore substantiates that the minute scale component of neurotransmitter (dopamine) concentration in the ECS is a measure of phasic release.

Fast-scan cyclic voltammetry measurements of serotonin/5-HT

To investigate if the considerations of longer lasting concentration increases in the ECS also apply to other neurotransmitter systems than the dopamine system, FSCV measurements of extracellular serotonin/ 5-HT levels are analyzed within this section. The provided data were acquired in electrically stimulated wild-type mice with a similar protocol as for the dopamine measurements (see "Material and Methods" section 3.2.7). Electrical stimulation of the raphe nucleus in the wild-type mice was performed at rates of 3 or 6 transients per minute for one-minute intervals followed by a four-minute interval without stimulation. The scans were performed continuously over the time of one hour at a rate of 10 Hz in the hippocampus for n=4 mice. Within this section, frequency analyses of the 5-HT FSCV signals are performed in analogy to the dopamine FSCV data analysis. It will be shown that (i) electrical stimulation evokes measurable transients in the hippocampus of the provided frequency of 5-HT transients (3 or 6 transients/minute). Furthermore, it is demonstrated that (ii) the rate of electrically induced transients is correlated with frequency variations of ∼0.5 Hz in 5-HT levels extracted from the continuous FSCV data. Just as for the dopamine analysis, this frequency reflects the typical duration of ∼2 s long transients and is further referred to as "high frequency". To link the high frequency variations to slower concentration variations in the ECS, it will be shown that (iii) transient rates as well as high frequency variations are correlated with "low frequency" variations at a frequency of ∼0.02 Hz.

i **Electrical stimulation of serotonin neurons increases the rate of serotonin transients.**
Electrical stimulation of the raphe nucleus with a defined frequency of 3 or 6 transients/minute leads to measurable transients in the FSCV signal of the hippocampus. Within the measured current in the hippocampus the induced rate of transients is clearly visible (Figure 3.31A). The area under the curve in one-minute intervals was calculated from the continuous FSCV signal (Figure 3.31B). The area under the curve for time intervals with 0, 3 and 6 induced transients correlates with the number of transients (Pearson's product-moment correlation: r=0.92, $p<2e^{-16}$). The mean area under the curve for no induced transients is 12.6±5.2, for three 31.0±5.8 and for six 46.4±7.4 (Welch Two Sample t-test: $p_{\#0\text{-}\#3}=1.58e^{-14}$, $p_{\#3\text{-}\#6}=1.02e^{-6}$, $p_{\#0\text{-}\#6}=5.55e^{-12}$; Figure 3.31C).

ii **Serotonin transient rate correlates with serotonin variations with a frequency of 0.5 Hz**
In analogy to the FSCV data of dopamine, the continuous 5-HT FSCV signal was decomposed into contributions from different frequencies by a wavelet transform. Since 5-HT transients have a similar duration (∼2 s) like dopamine transients, the wavelet power at a frequency of 0.05 Hz in one-minute intervals is further analyzed. As shown in Figure 3.32A the wavelet power at 0.05 Hz in the one-minute intervals clearly shows increases at times of stimulation. Furthermore, the wavelet power at a frequency of 0.05 Hz strongly correlates

with the number of induced transients (Figure 3.32C, upper panel). For no induced transients the wavelet power at a frequency of 0.5 Hz averages to 0.0019±0.0017, for three induced transients to 0.0228±0.0010 and for six transients to 0.0695±0.0435 (Pearson's product-moment correlation: r=0.9, p<2e^{-16}; Welch Two Sample t-test: $p_{\#0\text{-}\#3}$=5.24e^{-9}, $p_{\#3\text{-}\#6}$=0.0015, $p_{\#0\text{-}\#6}$=6.00e^{-5}; Figure 3.32C).

iii **Transient rates, high and low-frequency variations**
In a next step, it is investigated if low-frequency variations in the 5-HT signal can be related to the induced transient rates as well as to the high frequency variations. In contrast to dopamine, the wavelet power at a frequency of 0.01 Hz was not significantly correlated with the frequency variations at 0.5 Hz (Pearson's product-moment correlation: r=0.119, p=0.3), although the wavelet power at 0.01 Hz increases with the number of induced transients (#0: 39.47±23.34, #3: 50.84±29.45, #6: 57.07±22.93, Welch Two Sample t-test: $p_{\#0\text{-}\#3}$=0.146, $p_{\#3\text{-}\#6}$=0.423, $p_{\#0\text{-}\#6}$=0.017).
Additionally, the wavelet power at a frequency of 0.02 Hz was analyzed: the frequency variations in the signal at 0.02 Hz are significantly correlated with the number of induced transients. For no induced transients the wavelet power at 0.02 Hz averages to 24.23±13.64, for three induced transients to 33.11±13.90 and for six transients to 41.73±10.67 (Welch Two Sample t-test: $p_{\#0\text{-}\#3}$=0.024, $p_{\#3\text{-}\#6}$=0.046, $p_{\#0\text{-}\#6}$=3.88e^{-5}, 3.32C, lower panel). Furthermore, the wavelet power at a frequency of 0.02 Hz is significantly correlated with the high frequency wavelet power (Pearson's product-moment correlation: r=0.365, p=0.001; Figure 3.32D). Note that the correlation between the high frequency variations and the wavelet power at a frequency of 0.05 Hz provides even better results (Pearson's product-moment correlation: r=0.68, p=4.1e^{-12}).

Taken together, similar behavior of serotonin concentrations in the ECS after release as for dopamine is observed within the continuous FSCV data. This fits to results from literature as in [98,112]: "Biochemically, their [dopamine and 5-HT] regulation is quite similar, with similar proteins regulating synthesis, storage, release, uptake, and metabolism" [112]. This furthermore indicates that serotonin release might be detectable with the method introduced within this thesis using PET.

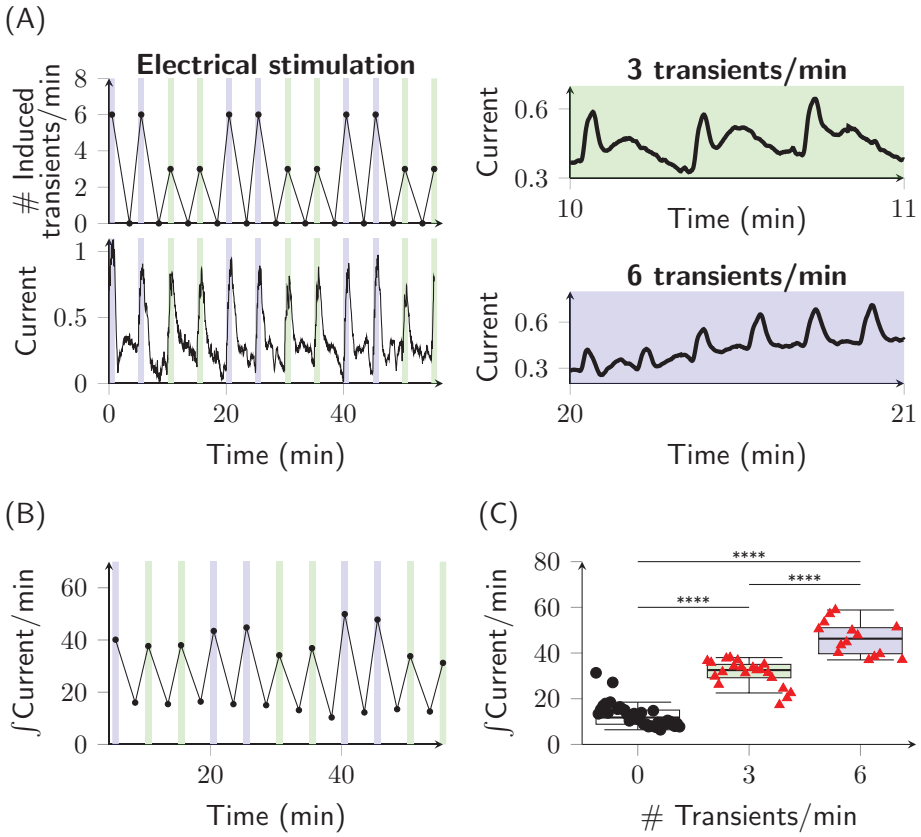

Figure 3.31: Continous FSCV measurements of 5-HT levels. (A) Number of induced transients and measured FSCV current as a function of time. In the right panel two one-minute intervals are shown in more detail – one interval with 3 induced transients/minute and one for 6 transients/minute. (B) Area under the curve of the continuous FSCV signal in one-minute intervals over time. (C) Correlation of the area under the curve of the FSCV signal in one-minute intervals with the number of induced transients. *: p-value≤0.05, **: p-value≤0.01, ***: p-value≤0.001 and ****: p-value≤0.0001.

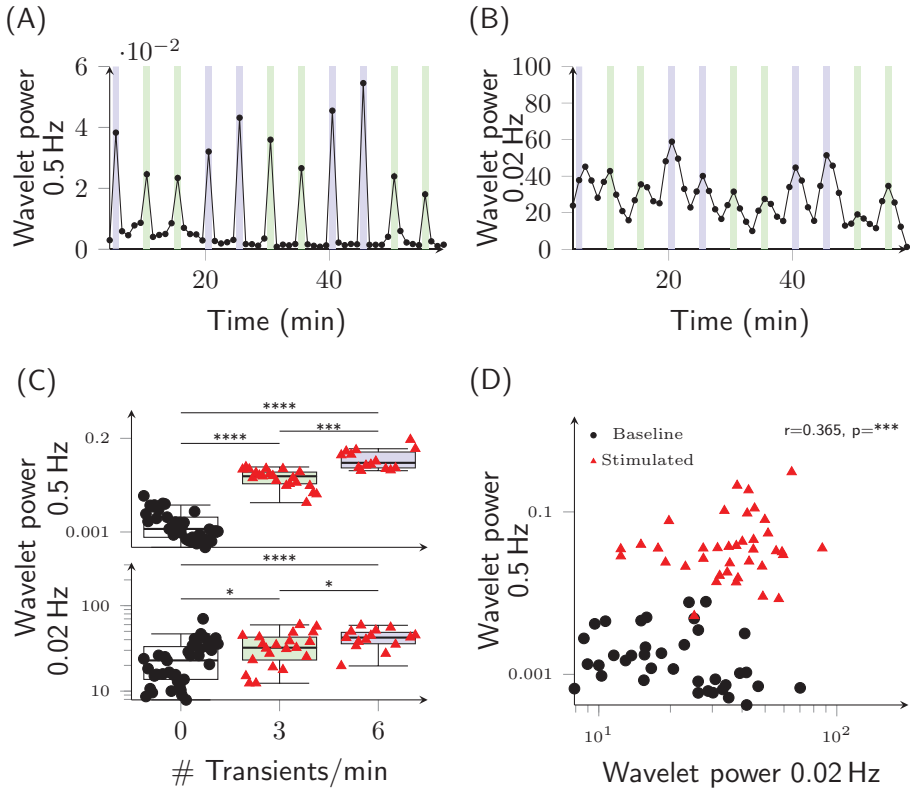

Figure 3.32: Wavelet analysis of continuous FSCV measurements of 5-HT. (A) Wavelet power at 0.5 Hz over time, where clear increases are seen at time intervals of stimulation. (B) Wavelet power at 0.02 Hz over time. (C) Wavelet power of 0.5 Hz and 0.02 Hz averaged for the time intervals of no, three and six transients per minute. (D) Correlation between low and high frequency wavelet power. *: p-value≤0.05, **: p-value≤0.01, ***: p-value≤0.001 and ****: p-value≤0.0001.

3.1.8 The Serotonin, Acetylcholine and Glutamate Systems

The underlying model for the new PET method was formulated for neurotransmitter systems in general and was then applied to the dopamine system. The method was experimentally validated by assessment of dopamine release in mice and humans using [11C]raclopride PET scans, substantiated by fast-scan cyclic voltammetry data. Moreover, it was shown that also for serotonin/5-HT longer lasting ECS concentrations are present after release events, indicating that the proposed PET method might be applicable to the serotonin system by using suitable radiotracers. This further suggests that for every system, which functions according to the processes underlying the model – namely diffusion and transport – neurotransmitter release events might be studied by analyzing temporal PET signal variations.
In this section characteristics of the 5-HT, acetylcholine and glutamate system are investigated with regard to applicability of the novel PET method to assess release events. The three neurotransmitter systems are selected for the following reasons: Serotonin is quite similar to dopamine [98,112], well studied and a potential system to apply the method without major modifications. The continuous 5-HT FSCV measurements presented in section 3.1.7 yielded similar results as for dopamine, making serotonin release events potentially detectable by the introduced method. The acetylcholine system differs from the catecholamine systems (dopamine and serotonin) in its anatomical structure, i.e. in the organization of the choliergic projections [113] and therefore might reveal boundaries of the method. Glutamate was analyzed as representative of the group of amino acids. Major challenges for the application of the method to the glutamate system are that glutamatergic neurons are wide spread across the whole brain, glutamate itself is reported to only occur in low extracellular concentrations and to be rapidly cleared from the ECS [114,99].
Apart from shortly introducing the characteristics of those neurotransmitter systems in the following subsections, a focus is on available radiotracers to study the systems. Furthermore, model calculations are performed using typical parameters for the respective systems and according radiotracers.

Serotonin

5-HT belongs like dopamine to the class of monoamine neurotransmitters [81,83]. The functions of serotonin include the regulation of emotion, mood, appetite and sleep, as well as cognitive processing like memory and learning [83,81,98].
5-HT neurons are predominantly located in the raphe nuclei with axons projecting to almost the entire brain (for details see Figure 3.33) [83]. Moreover, 5-HT projections are often co-located with projections of other monoamines [98]. Specificity for signal transmission is achieved by a large number of different 5-HT receptors. 5-HT receptors can be divided into seven subgroups: 5-HT_1 to 5-HT_7 [81]. Except for 5-HT_3, which is a ligand-gated ion channel, they are all G protein-coupled receptors [81,83]. The subgroups can be further divided into at least 14 subtypes (1A-1F, 2A-C and 5A-B) [83,98]. With that, more than twice as many 5-HT receptors are known for

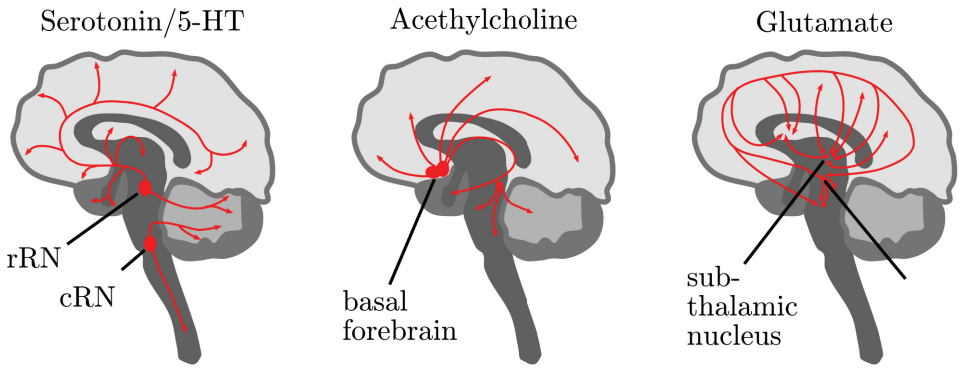

Figure 3.33: Pathways of the 5-HT, acetylcholine and glutamate systems. Left: 5-HT is located in groups of neurons in the raphe region of the pons and upper brainstem. The pathways can be separated into projections from the caudal raphe nuclei (cRN) and the rostal raphe nuclei (rRN). The caudal parts project to the spinal cord and brain stem, while the rostal parts primarily project to the forebrain.[115]. Middle: Acetylcholine neurons are located in the basal forebrain, where two groups of cholinergic neurons can be found: the first group is located in the medial septal nucleus and the second group in the nucleus basalis. The medial septal nucleus group projects to the hippocampus and parahippocampal gyrus. The nucleus basalis group projects to the neocortex, to parts of the limbic cortex and to the amygdala. Another group from the cholinergic pontomesencephalon innervates the hindbrain, thalamus, hypothalamus and the basal forebrain[116,117]. Right: Glutamate neurons innervate almost the entire brain. Most prominent glutamatergic pathways are the cortico-cortical pathways, the pathways between the thalamus and cortex and the extrapyramidal pathway between the cortex and striatum[118].

the serotonin system compared to the dopamine system[98]. Further specificity of serotonin signal transmission is given by the distinct localization of the different receptors within the brain. 5-HT_{1A} receptors for example have a high density in the hippocampus, amygdala, septum and raphe nuclei, while the 5-HT_2 receptors are predominantly found in cortical regions[83,81]. After release excess 5-HT can be taken up back to the presynaptic neuron through the monoamine transporter for 5-HT, the so-called serotonin transporter (SERT)[81,98].
PET imaging of the serotonin system has been focused on parameters analogous to those assessed for the dopamine system, e.g. quantification of receptor and transporter binding/density[11,119]. Today, a number of radiotracers exist to assess 5-HT synthesis, to quantify SERT or 5-HT receptor densities. Within this thesis, the focus is on radiotracers binding to the 5-HT_{1A} receptor type, since it is the most studied receptor subtype of 5-HT_1 receptors. Note, that 5-HT_{1A} receptors – as many other receptors – exists in high and low agonist affinity states[120]. Reviews about further radioligands can be found in literature, e.g by Paterson et al. (2013) or Kumar and Mann (2015)[119,120].
[11C]WAY-100635 is the most extensively studied 5-HT_{1A} receptor antagonist radiotracer in human subjects with a high affinity and selectivity to its target re-

ceptors[120,119]. Nevertheless, [11C]WAY-100635 was also reported to bind to α-1A adrenoreceptor and D4 receptors, questioning its specificity[120,119]. Note that at least D4 receptors have a low abundance within the human brain[120,119]. A study by Hume et al.[121] demonstrated that pharmacologically induced increase in serotonin concentration decreased [11C]WAY-100635 binding in the hippocampus of rats, while further studies by other groups could not confirm this finding[121,122,53].
[18F]MPPF is a fluorophenyl analogue of [11C]WAY-100635 and has been used in rodents, monkeys and human subjects. It has as similar 5-HT_{1A} receptor affinity and selectivity as [11C]WAY-100635[119]. [18F]MPPF binding to 5-HT_{1A} autoreceptors in the raphe nuclei was found to be sensitive to endogenous 5-HT concentrations in some studies[119].
[11C]CUMI-101 is the only 5-HT_{1A} agonist radiotracer so far tested in non-human primates and human subjects[120]. Milak et al.[123] reported in 2011 that [11C]CUMI-101 might be sensitive to endogenous 5-HT concentration changes by pharmacological intervention in a non-human primate study. This effect could so far not be verified and human studies are still lacking[119]. Since only a small effect with a strong pharmacological intervention was observed, it remains questionable if more subtle release events could be detected with [11C]CUMI-101[119].
For [11C]WAY-100635, [18F]MPPF and [11C]CUMI-101 kinetic rate constants reported in literature are summarized in Table 3.2 ("Material and Methods" section 3.2.2). These kinetic rate constants were used to apply the model for analyzing PET signal variations to the serotonin system. Model calculations were performed in analogy to the calculations performed for the dopamine system, i.e. a trace of free serotonin concentration is simulated and the parameter, rN, to assess temporal signal variations was calculated by equation 3.12 introduced in section 3.1.1. The same baseline and stimulation pulse sequence was applied as for dopamine. The receptor density, $B_{\max}$, and binding affinity, n_{D}, were adjusted for the serotonin system (Table 3.1, "Material and Methods" section 3.2.2). The results are summarized in in Figure 3.34. For [11C]WAY-100635 and [11C]CUMI-101 the model reveals signal variations in the order of 3% (for [11C]raclopride and dopamine 6-8% are achieved). In the case that 5% noise is added to the data the clear activation patterns cannot be seen anymore. For [18F]MPPF the resulting signal variations are even lower.

Acetylcholine

Acetylcholine acts in the CNS as a neurotransmitter, but is also highly abundant in the peripheral nervous system, where it activates skeletal muscles and excites or inhibits internal organs[83,81]. Acetylcholine signalling in the brain has widespread functions and is associated – amongst others – with arousal, attention, memory and motivation[83,81]. The main cholinergic regions and pathways are illustrated in Figure 3.33. The CNS contains groups of cholinergic projections (Ch1-Ch8), i.e. projection neurons, interneurons in the striatum, cortex, hippocampus and olfactory bulb as well as cholinergic motorneurons in the spinal cord[92,81]. Acetylcholine receptors can be divided into groups of muscarinic G protein-coupled receptors and nicotinic ligand-gated ion channels[83,81]. The group of muscarinic receptors in

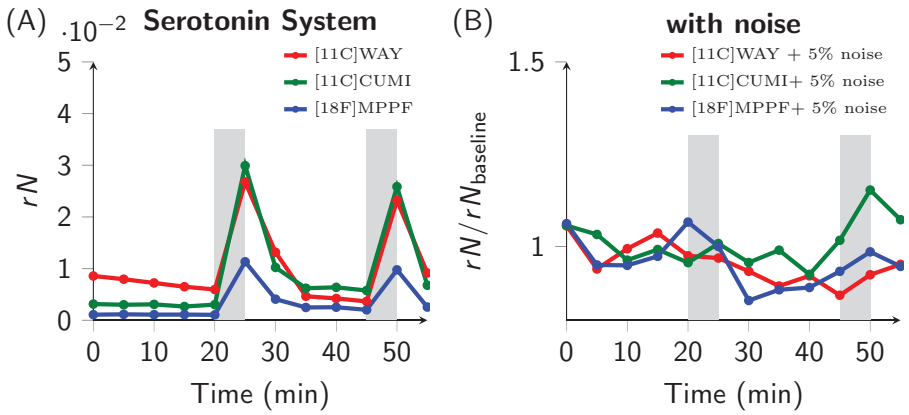

Figure 3.34: Temporal signal variations assessed by [18F]WAY-100635, [18F]CUMI-101 and [18F]MPPF. (A) Parameter of temporal signal variations, rN, as a function of time. A trace of extracellular 5-HT concentration with 10 pulses/min induced between 20-25 and 45-50 minutes in addition to pseudo-randomly distributed baseline pulses of in average 1 pulses/min is simulated. Parameters from literature for the radiotracers [11C]WAY-100635, [11C]CUMI-101 and [18F]MPPF are applied. (B) To baseline normalized temporal signal variations, rN/rN_{baseline}, for the same trace of extracellular serotonin concentration variations as in (A), in the case that 5 % noise is added to the signal.

turn can be divided into five subtypes called M1 to M5 [83,81]. Within the nicotinic receptor group two different types exist: the muscle-type and the neuronal-type [83,81]. Nicotinic acetylcholine receptors are formed from combinations of 17 – so far identified – subunits: α1-α10, β1-β4, γ, δ, and ϵ [124]. The two predominant subtypes of nicotinic acetylcholine receptors (nAChRs) found within the CNS are the $\alpha4\beta2$ and $\alpha7$ nAChRs, which are involved in higher brain functions [124]. Acetylcholine is inactivated within the synaptic cleft by the enzyme acetylcholinesterase, which converts acetylcholine into the inactive metabolites choline and acetate [83]. While choline will be taken back up into the presynaptic cell, acetate diffuses into the surrounding medium [125]. To summarize, the acetylcholine system consists of even more different receptor types as the 5-HT system and neuronal projections are widely spread within the CNS. This challenges imaging and quantification.

To study the cholinergic systems *in vivo* in the brain, [11C]nicotine was one of the first radioligands synthesized [11]. Unfortunately, its uptake appeared to reflect rather perfusion and extraction across the blood-brain barrier than specific binding parameters [11]. Newer PET radioligands for $\alpha4\beta2$* receptors such as [18F]flubatine, [18F]AZAN, and [18F]XTRA have been evaluated in humans, for example by Sabri et al. (2015) [126] and Kuwabara et al. (2017) [127]. $\alpha4\beta2$* refers to the combined $\beta2$*subtypes, i.e. $\alpha4\beta2$, $\alpha3\beta2$, and $\alpha2\beta2$, and because $\alpha4\beta2$ has the highest abundance in the brain these subtypes are collectively named $\alpha4\beta2$* [128].

[18F]nifene, a high affinity $\alpha4\beta2$* radioligand, was introduced in 2006 by Pichika et al. [129]. Its major advantage is its fast kinetics compared to the other acetylcholine re-

ceptor tracers, which results in significantly shorter scan times [128]. Here, [18F]nifene was analyzed with regard to applicability to assess PET signal variations upon acetylcholine release according to the method introduced within the framework of this thesis. Published kinetic rate constants are summarized in Table 3.2 ("Material and Methods" section 3.2.2). Calculations were performed analogous to the ones for the dopamine and serotonin systems with parameters adjusted for the acetylcholine system. The results are displayed in Figure 3.35. Temporal PET signal variations, rN, in the of 8.4% were obtained, i.e. in the same order as for [11C]raclopride and dopamine. Also in the case that 5% noise is added to the signal, the variations induced by acetylcholine variations are visible.

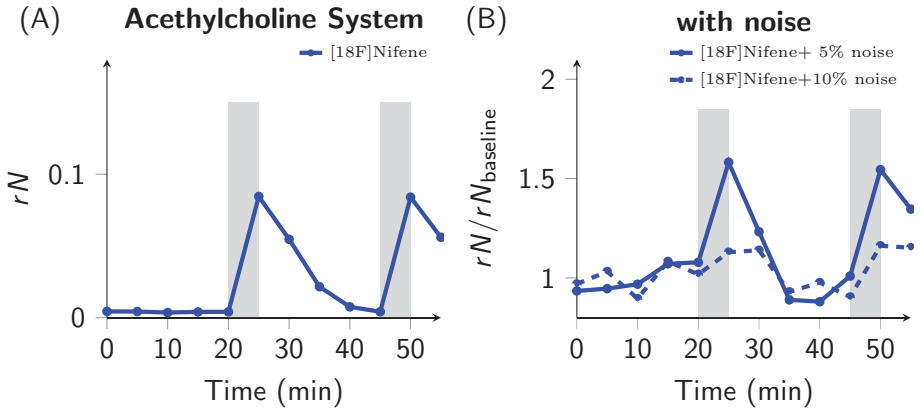

Figure 3.35: Temporal signal variations assessed by [18F]Nifene. (A) Temporal signal variations, rN, as a function of time. A trace of free extracellular acetylcholine concentration variations was simulated including 10 pulses/min induced at 20-25 and 45-50 minutes in addition to pseudo-randomly distributed baseline pulses of in average 1 pulse/min. Parameters from literature for the radiotracer [18F]nifene are applied. (B) To baseline normalized signal variations, rN/rN_{baseline}, in the case that 5 % noise is added to the signal for the same trace of acetylcholine variations as in (A).

Glutamate

Glutamate is the most abundant excitatory neurotransmitter in the CNS and plays a major role in learning and memory [83,81]. It is used by almost all excitatory functions in the brain, accounting in total for over 90% of the synaptic connections in the human brain [125,83,81]. The major pathways formed by glutamatergic projections are displayed in Figure 3.33. Four classes of glutamatergic receptors exist: N-methyl-D-aspartate (NMDA), α-amino-3-hydroxy-5-methyl-4-isoxazolepropionic acid (AMPA), kainate and a group of metabotropic receptors [83,81]. Except of the metabotropic glutamate receptors (mGluRs), glutamate receptors are ionotropic receptors. NMDA receptors can be divided into four subtypes, which are known to be involved in learning and memory [130]. AMPA receptors have four subtypes that play a role for fast excitation. Kainate receptors can be divided into 5 subtypes, whose functions are

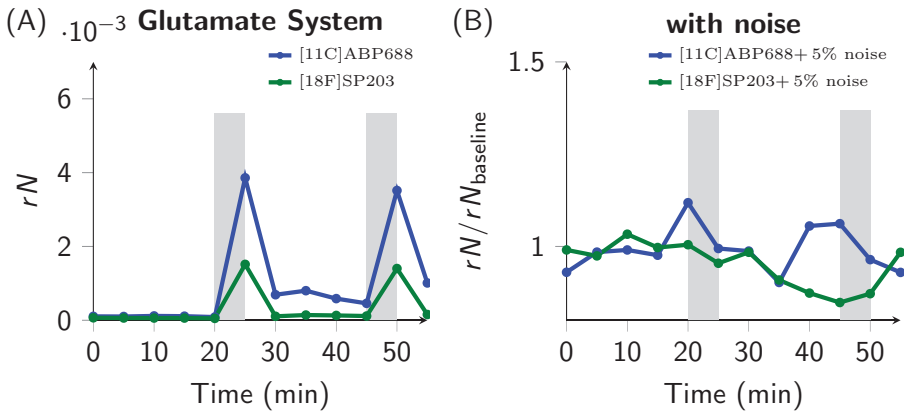

Figure 3.36: Temporal signal variations assessed by [18F]SP203 and [11C]ABP688. (A) Temporal signal variations, rN, as a function of time. A trace of free extracellular glutamate concentration variations was simulated including 10 pulses/min induced at 20-25 and 45-50 minutes in addition to pseudo-randomly distributed baseline pulses of in average 1 pulse/min. Parameters from literature for the radiotracers [11C]ABP688 and [18F]SP203 are applied. (B) To baseline normalized signal variations, rN/rN_{baseline}, in the case that 5 % noise is added to the signal for the same trace of glutamate variations as in (A).

so far not well defined and their abundance is rather low. mGluRs work via the second messenger system (G-protein coupled receptors) and are therefore involved in slower glutamatergic effects[81]. Eight different types of mGluRs ($mGluR_1$-$mGluR_8$) exist and are classified in three groups: group I including $mGluR_1$ and $mGluR_5$ that are mainly postsynaptic, group II with $mGluR_2$ and $mGluR_3$, and group III with $mGluR_4$ as well as $mGluR_6$-$mGluR_8$[81,131]. Groups II and III are predominantly located on presynaptic membranes, but have as well been found postsynaptic[131,81]. Glutamate is cleared from the extracellular space by excitatory amino acid transporters (EAATs), of which four types exist: EAAT1-4[81].

PET radioligands have been developed for NMDA receptors, e.g. [11C]ketamine, while for AMPA and kainate receptors no radioligands have been developed so far[53]. For metabotropic glutamate receptors several radiotracers exist. Here, the focus is on two radiotracers, which bind to the mGluR5 subtype, namely [18F]SP203 and [11C]ABP688. [11C]ABP688 shows accumulation in mGluR5-rich brain regions in rats and humans as it is a highly selective radioligand for mGluR5s[130,132,133]. Moreover, [11C]ABP688 was displaced in a dose-dependent manner by an other highly potent GluR5-selective ligand in one study[134,130]. The PET radiotracer [18F]SP203 is used in humans to study mGluR5 receptors[130,133]. A high uptake in mGluR5-rich brain regions was observed and using the mGluR5-selective ligand MPEP led to a decrease in [18F]SP203 uptake in monkeys[135,130].

In analogy to the analysis of the other neurotransmitter systems and radiotracers, model calculations were performed for glutamate system with the radiotracers

[18F]SP203 and [11C]ABP688. The results are displayed in Figure 3.36. With [11C]ABP688 signal variations as assessed by the parameter rN in the order of $\sim$0.4 % are achieved. For the tracer [18F]SP203 signal variations were only in the order of $\sim$0.1-0.2 %. Adding 5 % to the signal leads to negligible signal variations as assessed using [18F]SP203, while the signal variations obtained for [11C]ABP688 are still visible. If signal variations induced by glutamate release would be experimentally detectable using PET needs to be further tested.

3.2 Material and Methods

The Material and Methods section describes the experiments and methods shown within the thesis. Further experimental and methodological details are published in Lippert and Cremer et al. (2019) and Thanarajah and Backes et al. (2018) [86,87].

3.2.1 Numerical model

The modeling procedures are written in C. The equations derived in section 3.1.1 were discretized for numerically simulations with the finite difference method.
For the numerical calculations time and space domains for t ∈ [0,T] and $\vec{x}$ ∈ [-X/2,X/2], [-Y/2,Y/2], [-Z/2,Z/2] were replaced by a set of mesh points.
Within the space domain equally spaced mesh points [x_i, y_j, z_k] with discrete distances in steps of Δx=Δy=Δz, i.e. $x_i = i\Delta x$, and i, j, k from -N_{tot}/2 to N_{tot}/2 each are implemented. One element [x_i, y_j, z_k] is for simplicity denoted by [i,j,k] or in short $\vec{I}$. A box of 343 elements, i.e. N_{tot}=6, was simulated and a inner box of 125 elements, i.e. N_{box}=4, is analyzed to exclude border effects. Note that each element $\vec{I}$=[i,j,k] represents a tissue volume element $\vec{x}$ and that Δx corresponds to 1 mm. The time is given by discrete time points in steps of Δt from 0 to T, i.e. $t_n = n\Delta t$ (n=0,...,N_t). $R_e([i,j,k],t_n)$, or in short $R_e(\vec{I},t_n)$, denotes the mesh function that approximates the free radiotracer concentration at element $\vec{I}$=[i,j,k] and time t_n. The same applies for R_b, and the free and bound neurotransmitter concentrations N_e and N_b. The plasma radiotracer concentration is given by R_p, which is assumed to be constant (bolus-plus infusion injection).
First, steady-state conditions of neurotransmitter and radiotracer concentrations are calculated, which are assumed to be homogeneous within the region analyzed. The free and bound neurotransmitter concentration at time t=0, i.e. n=0, in absence of the neurotransmitter is set to zero. Free and bound radiotracer concentrations, R_e and R_b, at t=0, i.e. n=0, are given by:

$$R_b([i,j,k],0) = \frac{r_{pe}r_{eb,max}}{r_{ep}r_{be}}R_p(0) \tag{3.15}$$

and

$$R_e([i,j,k],0) = \frac{r_{pe}}{r_{ep}}R_p(0). \tag{3.16}$$

The change in bound neurotransmitter concentration over time as given by 3.2 in section 3.1.1, i.e.

$$\frac{dN_b(\vec{x},t)}{dt} = n_{eb}(\vec{x},t)N_e(\vec{x},t) - n_{be}N_b(\vec{x},t), \tag{3.17}$$

is implemented in the numerical procedure within a time step of Δt for each element i, j, k as:

$$\Delta N_b([i,j,k],t_n) = n_{eb}([i,j,k],t_n)N_e([i,j,k],t_n) - n_{be}([i,j,k],t_n)N_b([i,j,k],t_n) \tag{3.18}$$

The bound neurotransmitter concentration at the next time step n+1 is given by:

$$N_b([i,j,k],t_{n+1}) = N_b([i,j,k],t_n) + \Delta N_b([i,j,k],t_n)\Delta t \tag{3.19}$$

The rate constants $n_{eb}([i,j,k],t_n)$ and $r_{eb}([i,j,k],t_n)$ are, according to equations 3.4 and 3.8 in section 3.1.1, i.e.

$$n_{eb}(\vec{x},t) = n_{eb,max}(\vec{x})(1 - \frac{N_b(\vec{x},t)}{B_{max}(\vec{x})}) \tag{3.20}$$

and

$$r_{eb}(\vec{x},t) = r_{eb,max}(\vec{x})(1 - \frac{N_b(\vec{x},t)}{B_{max}(\vec{x})}), \tag{3.21}$$

implemented in the numerical procedure by:

$$n_{eb}([i,j,k],t_n) = n_{eb,max}(1 - \frac{N_b([i,j,k],t_n)}{B_{max}}) \tag{3.22}$$

and

$$r_{eb}([i,j,k],t_n) = r_{eb,max}(1 - \frac{N_b([i,j,k],t_n)}{B_{max}}). \tag{3.23}$$

The rate of change of the free and bound radiotracer concentrations given by (equations 3.5 and 3.6 in section 3.1.1)

$$\frac{dR_e(\vec{x},t)}{dt} = r_{pe}R_p(\vec{x},t) - (r_{ep} + r_{eb}(\vec{x},t))R_e(\vec{x},t) + r_{be}R_b(\vec{x},t) + D_R \triangle R_e(\vec{x},t) \tag{3.24}$$

and

$$\frac{dR_b(\vec{x},t)}{dt} = r_{eb}(\vec{x},t)R_e(\vec{x},t) - r_{be}R_b(\vec{x},t) \tag{3.25}$$

are calculated by:

$$\begin{aligned}
\triangle R_e([i,j,k],t_n) = {} & r_{pe}R_p(0) - (r_{ep} + r_{eb}([i,j,k],t_n))R_e([i,j,k],t_n) \\
& + r_{be}R_b([i,j,k],t_n) - r_{diff}\Delta_{i,j,k}R_e([i,j,k],t_n),
\end{aligned}$$

$$\begin{aligned}
& \text{with } r_{diff}\Delta_{i,j,k}R_e([i,j,k],t_n) = \\
& r_{diff}((R_e([i,j,k],t_n) - R_e([i-1,j,k],t_n)) \\
& +(R_e([i,j,k],t_n) - R_e([i,j-1,k],t_n)) \\
& +(R_e([i,j,k],t_n) - R_e([i,j,k-1],t_n)) \\
& +(R_e([i,j,k],t_n) - R_e([i+1,j,k],t_n)) \\
& +(R_e([i,j,k],t_n) - R_e([i,j+1,k],t_n)) \\
& +(R_e([i,j,k],t_n) - R_e([i,j,k+1],t_n))
\end{aligned} \tag{3.26}$$

and

$$\Delta R_b([i,j,k],t_n) = r_{eb}([i,j,k],t_n)R_e([i,j,k],t_n) - r_{be}R_b([i,j,k],t_n). \tag{3.27}$$

Since steady-state conditions for the plasma radiotracer concentration are assumed (bolus-constant infusion injection protocol) the plasma concentration R_p is constant in time and independent of i, j, k. Diffusion is implemented by approximating linear transport given a diffusion transport velocity r_{diff} estimated using the Einstein-Smoluchowski-Equation [89,90,91] (see equation 3.9, section 3.1.1). r_{diff} is a rate constant with units min^{-1} and its order of magnitude is estimated by assuming that diffusion of the radiotracer in the ECS has the same order of magnitude as the neurotransmitter. Dopamine has a diffusion constant of $D_{DA} \approx 7 \cdot 10^{-6}$ $cm^2 s^{-1}$ [88], which yields a r_{diff} in the order of $\sim 2\,min^1$ (see section 3.1.1). If not otherwise noted r_{diff}=2 min^1 was applied.
The free and bound radiotracer concentrations for the next time step n+1 are given by:

$$R_e([i,j,k],t_{n+1}) = R_e([i,j,k],t_n) + \Delta R_e([i,j,k],t_n)\Delta t \tag{3.28}$$

and

$$R_b([i,j,k],t_{n+1}) = R_b([i,j,k],t_n) + \Delta R_b([i,j,k],t_n)\Delta t. \tag{3.29}$$

The sum of $R_e([i,j,k],t_n)$ and $R_b([i,j,k],t_n)$ is the total radiotracer concentration $R([i,j,k],t_n)$ at position i, j, k and at time t_n.

Approach I: periodically changing binding rate

In approach (I) the influence of a periodically changing neurotransmitter concentration is mimicked by a periodically changing binding rate for the radiotracer, r_{eb}, according to:

$$r_{eb}([0,0,0],t_n) = r_{eb}(0)(1 + A_I \sin(2\pi f_I t_n)). \tag{3.30}$$

Only the element at i=j=k=0 was varied and analyzed in the calculations, while diffusion can take place between the elements. The binding rate in the other elements stayed constant at $r_{eb}(0)$. The following algorithm was applied: First, $r_{eb}([i,j,k],0)$ is set for all i, j, k to the initial value of $r_{eb}(0)$. Following, $r_{eb}([0,0,0],t_{n+1})$ is computed for the next time step n+1 by equation 3.30. Then, the concentrations $R_e([i,j,k],t_{n+1})$ and $R_b([i,j,k],t_{n+1})$ at time t_{n+1} are calculated for all i, j, k by equations 3.28 and 3.29 by inserting equations 3.26 and 3.27 for $\Delta R_e([i,j,k],t_n)$ and $\Delta R_b([i,j,k],t_n)$. This is repeated for N_t time steps until T is reached.
The parameter for the temporal variations in the signal rN_f is calculated as described in section 3.1.1 in equation 3.11, i.e.:

$$rN_f([i,j,k]) = \frac{\Delta R_f([i,j,k])}{R_{baseline,f}([i,j,k]} = \frac{R_{max,f}([i,j,k]) - R_{min,f}([i,j,k])}{R_{baseline,f}([i,j,k])}. \tag{3.31}$$

With $R_{baseline,f}$([i,j,k]) being the mean concentration calculated by $\frac{1}{2}(R_{max,f}([i,j,k]) + R_{min,f}([i,j,k]))$, $R_{max,f}([i,j,k])$ the maximal signal over time and $R_{min,f}([i,j,k])$ the minimal signal over time. For the results shown within the thesis, only the element i=0, j=0, k=0 was analyzed. Note, that rN_f was calculated after steady-state conditions were reached.

Approach II: variations of free neurotransmitter concentration

In approach II the free neurotransmitter concentration $N_e([i,j,k],t_n)$ is simulated for each time step. The temporal curve for $N_e([i,j,k],t_n)$ consists of pseudo-randomly distributed baseline pulses. The time points of the baseline pulses are calculated by a function, which creates Gaussian distributed pseudo-random values around a mean time of 1 min^{-1} with a standard deviation of 0.2 min^{-1} (Box-Mueller algorithm). At the given time points $N_e([i,j,k],t_n)$ is set to the selected amplitude of the baseline pulses (A=100 nM). To mimic exponential decay the concentration is removed with a exponential decay rate of 2 s (typical transient duration). Moreover, the time points for additional stimulation pulses are calculated and are implemented via a increased pulse rate (e.g. 10 min^{-1}) for the duration of the stimulation intervals of 5 min at t=20 min and 45 min. Note, that t=0 is the time point at which steady-state conditions are reached for the radiotracer concentration with the baseline neurotransmitter concentration.

Using the temporal variations of free neurotransmitter concentration as input the change of $N_b([i,j,k],t_n)$ within a time step of Δt for each element i, j, k is calculated by equation 3.18. The following algorithm is applied: first, $N_e([i,j,k],t_n)$ is computed for all i, j, k from 0 to $N_{i,j,k}$. Then, for the next time step the rate constants $n_{eb}([i,j,k],t_n)$ and $r_{eb}([i,j,k],t_n)$ are updated (equations 3.22 and 3.23). The concentrations $N_b([i,j,k],t_{n+1})$, $R_e([i,j,k],t_{n+1})$ and $R_b([i,j,k],t_{n+1})$ are calculated for all i, j, k using equations 3.19, 3.28 and 3.29 with insertion of equations 3.18, 3.26 and 3.27, respectively. This is repeated for the N_t time steps until T is reached.

The sum of the concentrations $R_e(t_f)$ and $R_b(t_f)$ over the elements in a box of $i-d_i, i+d_i, j-d_j, j+d_j, k-d_k, k+d_k$ with $d_i = d_j = d_k = N_{box}/2 = 2$ is written out to obtain a "time-activity curve" as measured with PET. f is the number of the respective time frame of the modeled PET signal, this means the time at frame f is $t_f = f\Delta t_f$ for f=0,..,N_f with N_f being the total number of frames. The temporal difference between Δt_f=t_f-t_{f-1} reflects the duration of a time frame of the reconstructed PET data. For the model calculations a Δt_f of 5 min was used.

The parameter rN was calculated, as in equation 3.12, for the time frames t_f over the elements in the analyzed box:

$$rN([i,j,k],t_f) = \frac{\Delta R([i,j,k],t_f)}{R_{baseline}}$$

$$= \frac{1}{R_{baseline}} \sqrt{\frac{1}{I_{sum}} \sum_{u=i-d_i}^{i+d_i} \sum_{v=j-d_j}^{j+d_j} \sum_{w=k-d_k}^{k+d_k} (R([u,v,w],t_f) - R([u,v,w],t_{f-1})^2} \quad (3.32)$$

$$\text{with, } R_{baseline} = \frac{1}{N_f - fs} \frac{1}{I_{sum}} \sum_{f=fs}^{N_f} \sum_{u=i-d_i}^{i+d_i} \sum_{v=j-d_j}^{j+d_j} \sum_{w=k-d_k}^{k+d_k} R([u,v,w],t_f).$$

The square root term is a measure for $\Delta R(t_f)$, the average change from time t_{f-1} to time t_f of the signal in analyzed box centered at the element $\vec{I}$=[i,j,k]. I_{sum} is the number of elements in the box (here 125 with d_i=d_j=d_k=2). $R_{baseline}$ is calculated

as the average signal in the box after the steady-state has been reached at t_{fs}. Since the time point t=0 is defined in the model as a point in time were steady-state conditions are given fs=0.
Noise was implemented by a pseudo-random Gaussian distribution using the Box-Mueller algorithm for noise levels of 5 % and 10 %, which was added to the total radiotracer concentration of each element.

3.2.2 Rate Constants and Parameters

Kinetic rate constants of the radiotracers and parameters for the neurotransmitter systems are taken from literature. In Tables 3.1 and 3.2 the used parameters for the studied endogenous neurotransmitter systems and for different radiotracers for the respective systems are summarized. The references are given within the table captions.
For the general model a $B_{\max}$=20 nM and a n_{d}=10 nM were taken for the neurotransmitter system and an exemplary radiotracer with r_d=10 nM, r_{pe}=0.20 min^{-1}, r_{ep}=0.20 min^{-1}, $r_{eb,max}$=0.30 min^{-1} and r_{be}=0.15 min^{-1} was assumed. For calculations of the influence of the radiotracer rate constants one of the parameters was varied, while the others were kept constant.

Neurotransmitter				
	Dopamine	Serotonin	Acethylcholine	Glutamate
n_{d} (nM)	10	5	52 (-35,000)	700 (-10,000)
n_{on}[1] (min^{-1}nM^{-1})	0.06	0.06	0.06	0.06
n_{off}=n_{be} (min^{-1})	0.6	0.3	3 (-2,100)	42 (-600)
$B_{\max}$ (nM)	20	(2-) 10	5	6 (up to >1,000)

Table 3.1: Parameters for different neurotransmitter systems. Values are estimates (orders of magnitude) based on literature for prominent regions of that neurotransmitter system, i.e. the putamen/caudate for dopamine, the raphe nucleus for serotonin, thalamic region for acetylcholine and caudate putamen for glutamate. $B_{\max}$ was chosen for the receptors of interest, i.e. D2R, 5-HT$_{1A}$, nAChR $\alpha4\beta2$* and MGluR5. Values for dopamine from [103,65,136], for serotonin from [137], for acetylcholine from [138,139,140], for glutamate from [114,141,142].

[1] From basic biochemistry the maximal value for $n_{\mathrm{on,max}}$ for two molecules moving in aqueous solution (free diffusion) is 10^9 M^{-1}s^{-1} (diffusion-controlled reaction) [143]. As a rule of thumb, n_{on} values for proteins and ligands are in the range from 10^5 to 10^7 M^{-1}s^{-1}, i.e. 0.006-0.6 nM^{-1}min^{-1} [144,145]. Here, a n_{on} of 0.06 nM^{-1}min^{-1} was used for all calculations.

Dopamine				
		[11C]raclopride	[18F]DMFP	[18F]FP
r_{d}	(nM)	8.46/ 5.76	8.73	1.08
r_{pe}	(1/min)	0.13/ 0.16	0.33	0.17
r_{ep}	(1/min)	0.43/ 0.23	0.09	0.21
$r_{\mathrm{eb,max}}$	(1/min)	0.26/ 0.25	0.55	1.08 ($0.04 \cdot B_{\mathrm{max}}$)
r_{be}	(1/min)	0.11/ 0.072	0.24	0.043
Serotonin				
		[11C]WAY-100635	[18F]MPPF	[11C]CUMI-101
r_{d}	(nM)	1.25 (0.2-2.2)	2.4 (0.3-3.3)	$0.51 \cdot B_{\mathrm{max}}$ (0.1-0.15)
r_{pe}	(1/min)	0.14	0.10	0.34
r_{ep}	(1/min)	0.41	0.15	0.11
$r_{\mathrm{eb,max}}$	(1/min)	0.16	$0.016 \cdot B_{\mathrm{max}}$	0.07
r_{be}	(1/min)	0.02	0.039	0.04
Acethylcholine				
		[18F]Nifene		
r_{d}	(nM)	2.3 (0.5)		
r_{pe}	(1/min)	0.88		
r_{ep}	(1/min)	0.21		
$r_{\mathrm{eb,max}}$	(1/min)	$0.14 \cdot B_{\mathrm{max}}$		
r_{be}	(1/min)	0.32		
Glutamate				
		[18F]SP203	[11C]ABP688	
r_{d}	(nM)	$0.26 \cdot B_{\mathrm{max}}$	$0.26 \cdot B_{\mathrm{max}}$	
r_{pe}	(1/min)	0.32	1.10	
r_{ep}	(1/min)	0.08	0.60	
$r_{\mathrm{eb,max}}$	(1/min)	0.085	0.23	
r_{be}	(1/min)	0.021	0.06	

Table 3.2: Parameters for different radiotracers systems. Parameters from literature for a selection of common radiotracers for the dopamine, serotonin, acetylcholine and glutamate system for the caudate putamen (dopamine), raphe nucles (serotonin), thalamic regions (acetylcholine) and caudate putamen (glutamate). Values for [11C]raclopride are from Farde et al. and Endres et al.[103,65] respectively, for [18F]DMFP from[146] and personal communication, for [18F]FP from[136], for [11C]WAY-100635 from[147,119], for [18F]MPPF from[148,137,119], for [11C]CUMI-101 from[149], for [18F]Nifene from[138,150,129,128], for [18F]SP203 from[151] and for [11C]ABP688 from[142].

3.2.3 Ethical Approval for Experimental Studies

All animal procedures were conducted in compliance with protocols approved by local governmental authorities (Bezirksregierung Köln) and were also in accordance with NIH guidelines for animal research. All subjects included in the human PET study gave written informed consent prior to study, which was approved by the local ethics committee of the Medical Faculty of the University of Cologne (Cologne, Germany).[86]

3.2.4 Chemogenetic Mouse Model

The transgenic mouse model is based on the so-called "Designer Receptors Exclusively Activated by Designer Drugs" (Designer Receptors Exclusively Activated by Designer Drugs (DREADD)) technology. The DREADD approach was introduced in 2005 by Roth, Armbruster and colleagues[152,153]. The idea of the DREADD technique is to bring an artificial receptor into cells of interest by genetic means, which then can be activated by a designer drug.
The most common approaches use the mutated human muscarinic receptors $hm3D_q$ and $hm4D_i$ (Gq-coupled: excitatory or Gi-coupled: inhibitory). Those receptors are not activated by acetylcholine or other endogenous neurotransmitters. Therefore they can be exclusively activated by the "designer drug" clozapine N-oxide (CNO). CNO is an inert and inactive metabolite of clozapine.[153,154] By this technique the endogenous stimulation of a receptor through a neurotransmitter is mimicked and its regulation can be studied. Moreover, neuronal circuitries and signals can be analyzed using "DREADDs".[153,154,57]
For the studies within this thesis, a mouse model in which all dopamine transporter expressing cells carry the hm3D*Gq* receptor is used[86]. To generate the experimental model, homozygous $hM3D_{Gq}$ females were crossed to DAT-Cre males, to generate mice with heterozygous expression of the $hM3D_{Gq}$ specifically in dopamine neurons[86]. Cre positive animals were used in the experiments and are referred to as $hM3D_{Gq}{}^{DAT}$. The Rosa26CAGSloxSTOPloxhM3DGq ($hM3D_{Gq}$) and DAT-Cre expressing mice were described before in[155,156]. All animal lines were maintained on C57BL/6N backgrounds[86]. Mice were housed at 22°C-24°C with a 12 h light/12 h dark cycle. Animals had ad libitum access to food and water in the home cage at all times. In Lippert and Cremer et al. (2019)[86] behavioral test results for the $hM3D_{Gq}{}^{DAT}$ mice are shown. The mice show behavioral changes after CNO injection, which are indicative of dopaminergic activation, thus validating the mouse model. The PET experiments were performed in adult male mice (age: 13±37 weeks, body weight: 24.6±47.9 g) to exclude hormonal effects of female mice or age related effects[86].
CNO was purchased from Sigma (Cat. No. C0832-5MG). A 5 mg/mL stock solution was made using DMSO (Sigma). 32 µL aliquots were stored at ∼20°C, and on individual test days, a working solution of 0.03 mg/mL was generated using sterile saline (0.9%; Aquapharm)[86]. All injections were made intraperitoneally (i.p.). Sterile Saline (with 0.6% DMSO) was used for vehicle injection in all experiments[86].

3.2.5 [11C]Raclopride PET Scans and Data Analysis

Synthesis of [11C]raclopride

[11C]raclopride was synthesized on side at the University Hospital Center of Cologne by the radiochemistry group as described in Lippert and Cremer et al. (2019) [86].

[11C]raclopride PET data acquisition in mice

The measurements were performed at the Max Planck Institute for Metabolism Research in Cologne. Dynamic PET data were acquired using a combined preclinical PET/CT scanner (Inveon, Siemens). For each scan session of 60 minutes two animals were placed on a water-heated mouse carrier with stereo-tactic holders (Medres). During the procedure mice were anesthetized with ∼2% isoflurane vaporized in 1.0 L/min of oxygen-nitrogen gas (30% O_2/70% N_2). At the start of the PET data acquisition the animals received a bolus-plus-constant infusion injection of 10.5±2.6 MBq of [11C]raclopride via the tail vein: a bolus of 80 μL was injected in one minute, followed by additional 120 μl injected via constant infusion until the end of data acquisition using programmable syringe pumps ("Genie" Kent, Kent Scientific Corp., Torrington, CT). The specific activity at the time of injection was 22.8 ± 9.0 GBq/μmol. 10 min after the start of the PET scan the mice either received CNO (0.3 mg/kg body weight) or sterile saline (10 μL/kg body weight) intraperitoneally. Each animal was measured twice in a randomized order, once receiving CNO and once saline. Following the PET scan the animals were automatically moved into the CT gantry and a CT scan was performed (180 projections/360°, 200 ms, 80 kV, 500 μA). CT data were used for attenuation correction of the PET data and the CT image of the skull was used for image co-registration. Cf. [86]

[11C]raclopride PET data processing (mouse data)

PET data were histogrammed in 60 time frames of 1 minute each, Fourier rebinned and corrected for attenuation and decay. Images were reconstructed using the MAP-SP algorithm provided by the manufacturer. The images were co-registered to a reference mouse brain CT by rigid body transformation using the imaging software VINCI[157]. Parametric images were calculated using Equation 3.33 and 3.34 (see below) by procedures written in IDL and C. Using a 3D mouse atlas constructed from a 2D mouse brain atlas[158], an anatomical volume of interest (VOI) of the left striatum was drawn. This region was analyzed, since FSCV data were acquired from this region. Cf. [86]

Calculation of parametric rDA images (mouse data)

[11C]raclopride PET parametric maps were calculated, to assess the variations of the [11C]raclopride signal, which are described to be related to variations of D2 receptor-bound dopamine in the ECS as introduced in section 3.1.1.
Temporal variation of the [11C]raclopride PET signal at time t_f and location (image

voxel) i, j, k are calculated as:

$$rDA_{ijk}(t_f) = \frac{\Delta R_{ijk}}{R_{0,ijk}}(t_f)$$
$$= \frac{1}{R_{0,ijk}} \sqrt{\frac{1}{I_{sum}} \sum_{u=i-d_i}^{i+d_i} \sum_{v=j-d_j}^{j+d_j} \sum_{w=k-d_k}^{k+d_k} (R_{uvw}(t_f) - R_{uvw}(t_{f-1}))^2} \tag{3.33}$$

$$R_{0,ijk} = \frac{1}{N_f - fs} \frac{1}{I_{sum}} \sum_{f=fs}^{N_f} \sum_{u=i-d_i}^{i+d_i} \sum_{v=j-d_j}^{j+d_j} \sum_{w=k-d_k}^{k+d_k} R_{uvw}(t_f) \tag{3.34}$$

For the mouse data we used $d_i = d_j = 2$ and $d_k = 1$ (asymmetric voxel size). The square root term is a measure of $\Delta R(t_f)$, the average change of the [11C]raclopride signal from time $t_{\text{f-1}}$ to time t_f in the box centered at i, j, k (I_sum, the number of voxels in the box is $(2d_i + 1)(2d_j + 1)(2d_k + 1)$). R_0 is calculated according to Equation 3.34 as the average signal in the box after the quasi steady-state has been reached at t_fs=20 min after bolus injection. For the mouse data we used a frame length of Δt=1 min. Cf. [86]

[11C]raclopride PET data acquisition in humans

The measurements were performed at the Max Planck Institute for Metabolism Research in Cologne. Human subjects (n=10) were monitored in two different conditions: in one session they received a palatable milkshake and in the other session a tasteless solution. The two PET imaging sessions were performed in a randomized order [86,87]. Subjects were ten healthy, male, normal-weight (BMI: 25.73±2.67 kg/m^2, age: 57.1±10.55 years) and non-smoking volunteers recruited from a preexisting database of Max Planck Institute for Metabolism Research [86,87]. No history of neurological, psychiatric or eating disorders were present [86,87]. Further exclusion criteria were special diets, lactose intolerance, diabetes, the participation in a previous PET study and a score higher than 12 in the Beck Depression Inventory (BDI II) [86,87].

PET data were acquired for 60 minutes on a brain dedicated HRRT Siemens PET scanner with a spatial resolution of ∼2.5 mm FWHM [86,87]. The head of the subjects was fixed by an inflatable helmet to prevent motion during data acquisition and the participants were instructed not to sleep as well as to lie still [86,87]. The participants were fitted with a custom designed Teflon mouth-piece that was attached to the PET gantry for fluid (i.e. the milkshake or tasteless solution) delivery to the tongue tip [86,87]. The "gustometer" setup as well as milkshake selection and rating is described in detail in Lippert and Cremer et al. (2019) [86].

Data for attenuation correction were acquired by performing a ten minute transmission scan using a rotating germanium-68/gallium-68 source [86]. Afterwards, 220-370 MBq [11C]raclopride were injected using a programmable syringe pump (Perfusor compact, Braun, Melsungen): 70% was applied in a bolus within the first minute, 30% was constantly infused during the remaining 59 min [86]. To ensure steady-state and

acquire dynamic PET data, the gustometer task started 20 min after the onset of data collection and lasted 10 min [86]. The PET scan was continued for 30 min after task completion [86]. In addition to the PET scans, anatomic MR images were acquired for each patient, as well as a fMRI study including Milkshake delivery was performed. Details to this can be found in Thanarajah and Backes et al. (2018) [87], as well as in Lippert and Cremer et al. (2019) [86]. Cf. [86]

[11C]raclopride PET data processing (human data)

After correcting for attenuation and scatter, PET images were reconstructed in 12 time intervals of 5 min duration using the three-dimensional ordinary Poisson ordered subset expectation maximization (OP-3D-OSEM) algorithm including the modeling of the system's point spread function (PSF) [86]. Individual PET images were smoothed by application of a 10 mm Gaussian filter and co-registered with respective T1-weighted MR image using the imaging software VINCI [157,86]. The individual MR images were then non-linearly transformed into the stereotaxic Montreal Neurological Institute (MNI) space and the transformation matrix was applied to the corresponding multiframe PET images (VINCI) [86].

Calculation of parametric rDA images (human data)

Parametric maps of the parameter rDA to assess temporal signal variations upon dopamine release events were calculated by procedures written in IDL and C from the [11C]raclopride PET data. Temporal variation of the [11C]raclopride signal at time t_f and location (image voxel) i, j, k was calculated according to:

$$rDA_{ijk}(t_f) = \frac{1}{R_{0,ijk}} \sqrt{\frac{1}{125} \sum_{u=i-2}^{i+2} \sum_{v=j-2}^{j+2} \sum_{w=k-2}^{k+2} (R_{uvw}(t_f) - R_{uvw}(t_{f-1}))^2}$$
$$with\ R_{0,ijk} = \frac{1}{8} \frac{1}{125} \sum_{f=5}^{12} \sum_{u=i-2}^{i+2} \sum_{v=j-2}^{j+2} \sum_{w=k-2}^{k+2} R_{uvw}(t_f). \tag{3.35}$$

$R_{ijk}(t_n)$ is the [11C]raclopride PET signal in voxel i, j, k at time t_f. For the human data analysis a frame length of Δt=5 min was used. Although shorter time frames provide higher temporal resolution, Figure 3.5 indicates that shorter time frames (i.e. higher frequencies) are less sensitive to variations of dopamine and apart from that include more noise inherent in the measurement procedure. The choice of the region $i - d_i, i + d_i, j - d_j, j + d_j, k - d_k, k + d_k$ depends on the system used for data acquisition and on the quality of the data. For the human data $d_i = d_j = d_k = 2$ was used resulting in an analyzed region that contains 125 voxels. R_0 is calculated as the average signal in that region after the quasi steady-state has been reached at t_fs=20 min after bolus injection (i.e. from frame 4 to 12). As introduced in section 3.1.1 rDA is a measure for local temporal variations of the [11C]raclopride signal (ΔR) relative to total local [11C]raclopride signal (R_0). Thereby, rDA is a measure for local dopamine activity (see sections 3.1.5 and 3.1.7). The parameter rDA is comparable between subjects within one region [86]. However, it cannot be compared

between regions (see also "Discussion" section 3.3.5), since the D2 receptor density in extrastriatal regions is lower than in the striatum leading to less total [11C]raclopride binding, which influences the absolute amplitude of rDA. This means higher rDA values in an extrastriatal region compared to values in the striatum, do not necessarily mean that more dopamine was released within that region. Nevertheless, the time course of rDA within a region indicates temporal variations of dopamine activity [86]. Voxel-wise paired t-tests were performed between the tasteless solution or milkshake parametric images of rDA. Clusters of contiguous voxels with a p-values $p_{\text{uncorrected}}<0.05$ were found between the two groups indicating differences in food intake dependent rDA. The clusters were further analyzed by their time activity curves as well as by the time courses of rDA [86]. Further details on the analysis of the human [11C]raclopride PET data, as well as further results, can be found in Lippert and Cremer et al. (2019) and Thanarajah and Backes et al. (2018). Cf. [86]

3.2.6 [18F]DMFP PET Scans in Mice and Data Analysis

Synthesis of [18F]DMFP

[18F]DMFP was synthesized at the Department of Nuclear Medicine of the University of Mainz as described in Gründer et al. (2003) [104].

[18F]DMFP PET data acquisition

Dynamic [18F]DMFP PET data were acquired using the same combined preclinical PET/CT scanner (Inveon, Siemens) and with the same protocol as for the [11C]raclopride PET scans in mice (see section 3.2.5). The injected radioactivity was 6.0±1.3 MBq in 200 μL. The specific activity at the time of injection was 83±44 GBq/μmol.

[18F]DMFP PET data processing

The [18F]DMFP PET data was processed similar to the [11C]raclopride PET data, see section 3.2.5.

Calculation of parametric rDA images

The same IDL and C procedures as described in 3.2.5 were used for the calculation of parametric images for the [18F]DMFP data.

3.2.7 Fast-Scan Cyclic Voltammetry Measurements and Model Calculations

Dopamine FSCV data acquisition

The dopamine fast-scan cyclic voltammetry data was acquired in Oxford (Department of Psychiatry and Department of Experimental Psychology, University of Oxford) by Clio Korn and Lauren Burgeno of the group of Mark Walton. The detailed method part is published in Lippert and Cremer et al. (2019) [86]. The FSCV experiments were conducted under the auspices of the UK Home Office laws for the treatment of animals under scientific procedures and of the University of Oxford ethical review board.
FSCV recordings of *in vivo* nucleus accumbens core (NAc) dopamine levels were made under isoflurane anesthesia in the $hM3D_{Gq}{}^{DAT}$ mouse model (n=7) (see section 3.2.4) as well as in a wild-type mouse model with electrical stimulation. After electrode placement and signal validation the main experiment was started to determine the effect of chemogenetic activation of dopamine neurons by CNO in the dorsal NAc [86]. The positions of the recording and stimulating electrodes were optimized by moving them to find the maximal changes in dopamine that could be detected after stimulation (50 x 2 ms monophasic pulses, 200 μA current, at 50 Hz) [86]. 10 minutes after the start of the continuous recordings an intraperitoneal injection of either CNO (0.3 mg/kg body weight) or Saline (0.6% DMSO in sterile saline) was given and FSCV was recorded for 60 minutes post-injection. Another 60 minutes were recorded after a middle set of stimulation. The potential applied to the carbon fiber was ramped from -0.4 V (vs Ag/AgCl) to +1.3 V and back at a rate of 400 V/s during a voltammetric scan and held at -0.4 V between scans. After electrode conditioning a scan rate of 10 Hz was used [86]. Additional continuous FSCV recordings were performed in the ventral striatum of four wild-type mice. In one-minute time intervals dopamine release was induced by electrical stimulation of the VTA at a rate of either 5 or 10 transients/minute followed by a resting time interval of either 4 minutes (mouse 1) or 9 minutes (mouse 2, 3, and 4) [86]. Electrical stimulation was applied by an isolated current simulator (DS3, Digimeter). Stimuli were generated and recordings collected using Tarheel CV (National Instruments). The parameters of the electrical stimulation were adjusted to 50 Hz, 4-7 pulses, and 100-200 μA in order to obtain transients with an average amplitude of $\sim$1-2 nA. Recordings of mouse 3 and 4 displayed periods where the chemometric model failed. Affected time intervals were excluded from the analysis. Note, that all reported significances remain significant if these intervals are included in the analysis [86]. Cf. [86]

Dopamine FSCV transient analysis

A primary by the Oxford group, voltammetric analysis was carried out using custom-written scripts in Matlab. Therefore, all FSCV curves were low-pass filtered at 2 kHz. The average current recorded between 1.5-0.5 s before the target cyclic voltammogram was subtracted to account for large changes in capacitance current [86]. Periods within the cyclic voltammograms recorded over the course of the experiment which correlated

with a correlation coefficient of R $\geq$ 0.86 with a dopamine "template", derived by electrically stimulating the ventral tegmental area (VTA) before the experiment began, were searched [159,160,86]. The numbers of transients per minute before and after either CNO or Saline injections were then compared. To extract an estimate of changes in dopamine levels over time across the session, a principal component analysis was performed using a standard training set of stimulated dopamine release detected by chronically implanted electrodes, with dopamine treated as the first principal component among other unrelated electrochemical fluctuations such as changes in pH [86]. For this analysis, the data was divided into non-overlapping 30 s bins and the average current recorded over the initial 1 s in each bin was subtracted. Given that it is only possible to derive a relative and not an absolute measurement of dopamine levels using FSCV, the extracted dopamine in each bin were combined by assuming that the first recorded value in bin N+1 continued relative to the last time point in bin N [86]. Cf. [86]

Serotonin FSCV data acquisition

The 5-HT fast-scan cyclic voltammetry data were acquired at the University of South Carolina (Department of Chemistry and Biochemistry) by Alyssa West of the group of Parastoo Hashemi. Recording of *in vivo* hippocampal serotonin levels were made under anesthesia using FSCV in wild-type mice (n=4). During 60 minutes of measurement either 3 or 6 transients per minute were induced by electrical stimulation of the raphe nucleus with 4 minutes of no stimulation in between. The parameters of electrical stimulation were adjusted to 60 Hz, a pulse width of 2 ms and 350 μA. The continuous FSCV data were given as current (nA) over time. First, the data were high-pass filtered at 0.1 1/min. To get an estimate of the number of transients per minute the area under the curve in one minute intervals of the trace was calculated and correlated to the number of induced transients. Furthermore data were normalized to the minimal and maximal measured value, so that the experiments are comparable.

Wavelet transform analysis

A wavelet transform decomposes the signal into harmonic functions of different frequencies, but in contrast to the Fourier transform the harmonic functions have a finite duration [108,86]. Thereby, a wavelet transform does not lose the temporal information of the signal [108,86]. The wavelet power calculated as the square of the wavelet coefficients gives the power in variations of extracellular dopamine/serotonin levels as a function of frequency and time. In order to analyze "high" and "low"-frequency variations in the FSCV data a wavelet transform with a Gaussian mother function (3. order) was applied. Since continuous data is needed for the wavelet transform missing points in the data were interpolated. Using a cone of influence the wavelet data of these segments were removed from the resulting spectra ($t \pm 2 \cdot 1/f$). Additionally, to avoid edge effects the borders of the wavelet transform were also removed ($t_{min} + 4/f$ and $t_{max} - 4/f$) [86]. The power in the wavelet spectrum of the dopamine data at 0.01 and 0.5 Hz was averaged in windows of 1 minute to

yield time courses of wavelet power at 0.01 Hz and at 0.5 Hz for each animal. Note that correlation analyses were restricted to time intervals that contained continuous data in all three parameters (#transients/minute, wavelet power at 0.01 Hz and at 0.5 Hz).[86] For the serotonin FSCV data the time-courses of 0.01, 0.02 and 0.05 Hz and 0.05 Hz were calculated in 1 minute time intervals.

FSCV model calculations

A typical transient measured by FSCV can be described by diffusion of the neurotransmitter out of the synapse into the ECS after release and by exponential removal of the extrasynaptic extracellular neurotransmitter by re-uptake mechanisms:

$$\frac{\partial}{\partial t}C(\vec{x},t) = D \triangle C(\vec{x},t) - kC(\vec{x},t) \tag{3.36}$$

with $C(\vec{x},t)$ being the neurotransmitter concentration at position $\vec{x}$ and time t. Note that $C(\vec{x},t)$ equals the concentration $N_e(\vec{x},t)$ in section 3.1.7. D is the diffusion constant of the neurotransmitter in the extracellular space, which is assumed to be constant. k is the removal rate constant in units of time^{-1}. Spherical symmetry for diffusion and re-uptake is assumed.
The diffusion term in 3D is[161]:

$$\frac{\partial}{\partial t}C(r,t) = D\frac{1}{r^2}\frac{\partial}{\partial r}(r^2\frac{\partial}{\partial r}C(r,t)), \tag{3.37}$$

which yields the following equation for the neurotransmitter concentration including re-uptake:

$$\frac{\partial}{\partial t}C(r,t) = D\frac{1}{r^2}\frac{\partial}{\partial r}(r^2\frac{\partial}{\partial r}C(r,t)) - kC(r,t). \tag{3.38}$$

For the calculations an initial 3D Gaussian distribution of concentration after release is used for time t=0:

$$C(r,t=0) = \frac{C_0}{(\sigma\sqrt{2\pi})^3}e^{-\frac{1}{2}(\frac{r}{\sigma})^2}. \tag{3.39}$$

At position r=0 the rule of L'Hosptial's rule needs to be applied to the derivative $\frac{\partial}{\partial t}C(0,t)$, which then gives[161]:

$$\frac{\partial}{\partial t}C(0,t) = 3D\frac{\partial^2}{\partial r^2}C(r,t). \tag{3.40}$$

For step-wise calculations of equation 3.38 in C the finite difference method was used. To do so, time and space domains for r $\in$ [0,R] and t $\in$ [0,T] were replaced by a set of mesh points. Equally spaced mesh points were assumed with discrete time points in steps of Δt from 0 to T, i.e. $t_n = n\Delta t$ (n=0,...,N_t), and with discrete distances in steps of Δr from 0 to R, i.e. $r_i = i\Delta r$ (i=0,...,N_r). C_i^n denotes the mesh function that approximates the neurotransmitter concentration $C(r_i,t_n)$ for i=0,..,N_r and n=0,...,N_t.

The derivatives in equation 3.40 were replaced by finite approximations using a forward difference in time and a central difference in space (forward Euler scheme) [161]:

$$\Delta C_0^n = 3D(C_1^n - C_0^n)\frac{\Delta t}{\Delta r^2}, \tag{3.41}$$

which yields

$$C_0^{n+1} = C_0^n + 3D(C_1^n - C_0^n)\frac{\Delta t}{\Delta r^2} \tag{3.42}$$

for the neurotransmitter concentration at position r_i=0.
For any other mesh point it is:

$$C_i^{n+1} = C_i^n + \frac{D}{r_i^2}[r_{i+\frac{1}{2}}^2(C_{i+1}^n - C_i^n) - r_{i-\frac{1}{2}}^2(C_i^n - C_{i-1}^n)]\frac{\Delta t}{\Delta r^2} \tag{3.43}$$

The re-uptake term $kC(r,t)$ was implemented as

$$-k_i C_i^n \Delta t \tag{3.44}$$

and is added to equations 3.42 and 3.43 in every step.
This gives the two operational equations:

$$C_0^{n+1} = C_0^n + 3D(C_1^n - C_0^n)\frac{\Delta t}{\Delta r^2} - k_i C_i^n \Delta t \tag{3.45}$$

and

$$C_i^{n+1} = C_i^n + \frac{D}{r_i^2}[r_{i+\frac{1}{2}}^2(C_{i+1}^n - C_i^n) - r_{i-\frac{1}{2}}^2(C_i^n - C_{i-1}^n)]\frac{\Delta t}{\Delta r^2} - k_i C_i^n \Delta t. \tag{3.46}$$

The removal rate constant k_i can have a spatial distribution and is given for the mesh points of r.
Taken together, this leads to the following algorithm: first, $C_i^{n=0}$ is computed for all i from 0 to N_r by:

$$C_i^0 = \frac{C_0}{(\sigma\sqrt{2\pi})^3} e^{-\frac{1}{2}(\frac{r_i}{\sigma})^2}. \tag{3.47}$$

Then, for the next time step the concentration at distance r=0 is calculated by equation 3.45. Followed by application of equation 3.46 for all distance r_i. This procedure is repeated for N_t time steps, so that time T is reached.
Note, that the Forward Euler scheme is unstable for [161]

$$D\frac{\Delta t}{\Delta r^2} > \frac{1}{2} \tag{3.48}$$

and that Δt and Δr have to be selected accordingly.
To obtain the FSCV signal at a certain position r_{out}, the resulting $C_{r_{out}}^n$ is written out over time. For the calculation of dependency of the maximal concentration from the distance, the maximal calculated value for C_i^n over time was taken for each distance. The time of the peak value can be written out accordingly.

3.3 Discussion

3.3.1 Premises, Parameters and Controversies

The introduced model within this thesis describes the dynamics of neurotransmitters, radiotracer and their interaction. It is used to link temporal PET signal variations to synaptic neurotransmitter release events. In contrast to former approaches the novel method is capable to assess temporal variations in the signal instead of analyzing net reductions in regional radiotracer binding. This enables spatiotemporal assessment of neurotransmitter release events with a reasonable time and spatial resolution.

Model premises

The proposed method is based on three premises: (i) the PET signal originates predominantly from the extrasynaptic extracellular space, (ii) there is detectable diffusion of the neurotransmitter from synapses to the extrasynaptic extracellular space, and (iii) part of extrasynaptic extracellular neurotransmitter is removed at a minute time scale.[86]

Originally, it was assumed that radiotracer displacement measured by PET occurs at intrasynaptic receptors[58]. However, this view is changing over the last years leading to the assumption that the PET signal stems predominantly from extrasynaptic receptor binding. In the PET field, especially regarding [11C]raclopride and dopamine, it is widely discussed where the interaction between neurotransmitter and radiotracer occurs: in some reviews it is stated that "[...] changes in radioligand binding were found to mainly reflect modulation of dopamine in the synaptic cleft, instead of inherently reflecting changes in the extracellular fluid dopamine concentration"[53], in contrast to: "[...] significant spillover of DA [(dopamine)] to the extrasynaptic space and the predominant activation of extrasynaptic over intrasynaptic D2 receptors" might exist, so "[...] that extrasynaptic receptors play a significant if not predominant role in the binding and displacement D2/3 radiotracers in the striatum"[73].

In early days of PET, it was assumed that D2/3 recepetors and DATs were predominantly located within synapses and that the PET signal reflected intrasynaptic binding[162,58,53]. All observations were interpreted accordingly. Immunohistochemistry in combination with light and electron microscopy, however, revealed that a large fraction of these receptors and transporters were located outside of the synapses[163,164,73]. Today, it is well accepted that receptors are also located outside of the synaptic cleft.

Based on published data, the volume of the synaptic space in a tissue volume of $1\,\mu m^3$ can be estimated to be in the order of $\sim 0.0003\,\mu m^3$, i.e. 0.03 %. This volume is approximated given that striatal dopamine synapses have a diameter of ~0.3-0.6 μm[99] and a typical synaptic cleft distance of $0.02\,\mu m$[165], which results in a synaptic volume of $\sim 0.0057 \mu m^3$. Furthermore, the synaptic density in the striatum is reported to be ~0.05 synapses per μm^3[99]. Therefore, assuming the synaptic volume contribution to a tissue compartment to be less than 1 % ($V_s \ll V_e$, even in a region with a high density of dopamine neurons) and a prominent fraction of receptors at extrasynaptic locations, it is convincing that the radiotracer signal stems

predominantly from the extrasynaptic ECS space.
Furthermore, it is well accepted that dopamine diffuses into the ECS after phasic release events and acts via volume transmission, which supports the view that extrasynaptic receptors exist once more [166,99,88]. Model calculations of striatal dopamine transmission predict dopamine effects up to 2 μm distant from the release site (release of a single dopamine vesicle, low affinity receptor effect) [99,88]. Moreover, within the framework of this thesis, it was shown that a heterogeneous distribution of re-uptake mechanisms, i.e. transporters, can increase the distance of noticeable concentration changes in the ECS (up to hundreds of μm, see section 3.1.7 and discussion section 3.3.6).
Altogether, spillover of neurotransmitters into the ECS after a release event is well reported, especially for the dopamine and serotonin system. For glutamate rapid clearance mechanisms and low ECS concentrations are described [99]: "GluTs are better positioned than DATs, anatomically, numerically and kinetically, to limit spillover and active lifetime of transmitter" [99]. Nevertheless, it was reported that glutamate can – under certain physiological conditions – diffuse outside the synapse and "reach a concentration in the ECF [extracellular fluid] sufficiently high to activate glutamate receptors outside the source synapse" [166]. For acetylcholine evidences for volume transmission, despite direct synaptic transmission, are given as well [113]. Further discussion on the glutamate and acetylcholine systems can be found in section 3.3.7.
The third premise for the model, i.e. that part of extrasynaptic extracellular neurotransmitter concentration is removed at a minute time scale, will be discussed in detail in section 3.3.6. Shortly summarizing: data from literature of FSCV and microdialysis measurements indicate the presence of a minute scale dopamine concentration component in the ECS [109,110,167,168,169]. Furthermore, model calculations and frequency analysis of continuous FSCV data performed within the framework of this thesis relate phasic release events with minute-by-minute dopamine variations in the ECS.
Taken together, all three premises are well supported by literature for the dopamine system. For serotonin, acethylcholine and glutamate there are strong evidences that extrasynaptic binding sites exist and that spillover occurs, which could lead to longer lasting extrasynaptic ECS concentration increases of those neurotransmitters. The characteristics of these neurotransmitter systems will be discussed in more detail below (section 3.3.7).

Modeled neurotransmitter concentrations and diffusion of the radiotracer

Model calculations, based on the premises discussed above, were performed to analyze the impact of neurotransmitter activity on the PET signal of displacable radiotracers. As a first approach a periodically changing binding rate of the radiotracer was assumed. This indirectly mimics a periodically changing neurotransmitter concentration in the ECS. The results of the calculations show that the temporal variations of the PET signal are sensitive to variations of the binding rate – and therefore to variations in neurotransmitter concentration – on a time scale of minutes. As expected due to the kinetics of typical radiotracers, rapid changes cannot be picked

up. The amplitude of the changes of the binding rate is directly proportional to the amplitude of radiotracer signal variations. Therefore, the "strength" of neurotransmitter activity is related to the size of the variations in the PET signal (rN, see also further discussion on the size of rN below).
The strength of the temporal signal variations is moreover influenced by the diffusion of the radiotracer within the ECS. To our knowledge none of the common models include diffusion of the radiotracer. However, it is likely that the radiotracer diffuses within the ECS and was found to play a major role in the strength of measured signal fluctuations from the model calculations. A realistic diffusion rate was derived to be in the order of $\sim 2.4\,\mathrm{min}^{-1}$ on basis of the diffusion constant of dopamine in the ECS. The diffusion of the radiotracer is a key factor in our model. The total radiotracer signal is the sum of the radiotracer in the bound and the free compartment. This means that locally a change from the bound to free compartment does not alter the total radiotracer signal. In the case that diffusion of the radiotracer takes place, an increase in the free concentration will lead to diffusion to neighboring elements/voxels. This process induces a phase shift between bound and free concentration, which results in detectable changes within the total radiotracer signal (Figure 3.6 in section 3.1.2).
In a second approach variations of free neurotransmitter concentration were modeled to mimic a more realistic situation. A pulse sequence consisting of a series of baseline pulses, which create a steady-state neurotransmitter concentration in the ECS is simulated. At certain time intervals the pulse frequency was increased, which reflects phasic neurotransmitter release events. The impact of this stimulation events on temporal PET signal variations were analyzed using different parameters. As expected stronger stimulation parameters like an increase in the pulse frequency or a larger area of stimulation lead to higher temporal variations in the PET signal. The model results of approach (II) furthermore indicate that the exact size of the diffusion constant might not be relevant, but that the presence of diffusion (within a realistic range) is essential.
The amplitude and removal rate of the baseline pulses in the modeled free neurotransmitter concentration curves are based on reported values in literature and on the traces of dopamine transients from the FSCV data shown within this thesis. The stimulation intervals, i.e. the increase in pulse frequency, are based as well on the results from the FSCV data, in which release events were found to induce a higher transient rate per minute without a change in size of the transients. Therefore, the assumptions made within the model calculations reflect realistic conditions.
Under the circumstances assumed, temporal signal variations in the order of $\sim 25\,\%$ can be achieved, while no change in the net radiotracer binding, i.e. the time activity curve, is visible. This clearly reveals that the analysis of temporal signal variations is superior to the measurement of net reductions in radiotracer binding.

Radiotracer rate constants

Analysis of the influence of parameters of the neurotransmitter system ($B_{\max}$ and n_{D}), as well as parameters of the radiotracer (r_{pe}, r_{ep}, r_{eb} and r_{be}) revealed optimal sizes of rate constants for radiotracers to assess neurotransmitter activity with the proposed method.

It was found that with a realistic set of parameters an optimal affinity of the radiotracer exists to achieve maximal signal variations. A tracer with a dissociation constant of $r_{d,opt}$=2.6 nM was found to be optimal for a system with a total receptor density of B_{max}=20 nM and an endogenous neurotransmitter with a dissociation constant of n_d=10 nM. This means the optimal binding affinity of the radiotracer would need to be higher than the affinity of the neurotransmitter.

The classical competition model is based on the assumption that the radiotracer binds to the receptors of interest with a lower affinity than the endogenous neurotransmitter. While this statement is quite intuitive and well accepted, it may not be entirely true in any situation, see also review by Laruelle (2000) [58]. For non-equilibrium situations, i.e. when dopamine concentration are varying, Endres and Carson [170,58] worked out that the change in binding potential (of [11C]raclopride) induced by a dopamine pulse will be larger when k_{off}, i.e. the dissociation rate (within this thesis referred to as r_{be}) is larger. Note that a larger value for k_{off} results in a lower binding affinity (k_{on}/k_{off}) in the case that the binding constant k_{on} remains unaltered. A lower binding affinity might improve the capability of the radiotracer to be displaced by the endogenous neurotransmitter, but also means lower net binding, i.e. a worse signal-to-noise ratio. Moreover, according to Endres and Carson, a faster clearance of tracer to plasma k_2 (r_{ep}) leads to a larger change in binding potential. Within our model and the according calculations we found, that there is an optimal value of k_{off} (r_{be}) and that larger values do not contribute to an increase in signal variations as assessed by the parameter rN. This indicates that a low affinity radiotracer is less sensitive to capture endogenous release events by temporal signal variations. Moreover, we could not find a dependence of the clearance rate k_2 (r_{ep}) on rN. Since, we assume steady-state conditions, which are predominantly influenced by K_1 (r_{pe}) and k_2 (r_{ep}), and we normalize the temporal variations to the steady-state signal to obtain rN, the effect of those rate constants cancels out (see also discussion in section 3.3.2: “Steady-state conditions”). Additionally, in contrast to Endres and Carson [170], we include diffusion of the radiotracer in our model, which locally acts like an increased clearance rate (k_2). Accordingly, a larger diffusion constant leads to larger signal variations also within our model.

Receptor density $B_{\max}$ and receptor affinity states

An assumption that is widely used in the PET field and that was as well presumed for the model introduced here, is a constant receptor density within the region of interest. This premise is the reason, that the receptor density of different regions can be compared using PET. Note, that the receptor density is reported to be influenced by age, body weight, genetics, diseases and further factors [171,172,173,174]. These factors however are not relevant within the time of a PET scan in the order

of ∼hours and also not for a two-scan study design within a time interval of weeks. Usually a good test-retest reliability is given using PET and binding potentials can be measured reliably: e.g. for the [11C]raclopride binding potential the test-retest variability is in the order of <5 % in the striatum and thalamus and a bit higher in cortical regions[175]. This shows that no significant changes in radiotracer binding occur between two measurements of the same subject under similar conditions.
For some neurotransmitter systems it was reported that receptors can be internalized on a time scale of ∼seconds. Internalization means that the receptor will be relocated from the plasma membrane to the inside of the cell in response to agonist activation of G-protein coupled receptors[92,176]. This would question the assumption of a stable $B_{\max}$ within the scan duration and a region of interest upon endogenous release events. Receptor internalization could impact the available receptor density B_{avail} and therefore influence the effective binding rates $n_{\text{eb}}(\text{t})$ and $r_{\text{eb}}(\text{t})$.
However, a *in vitro* study by Guo et al. (2010) showed that even though agonist mediated (i.e. pharmacological intervention) internalization of D2 receptors occurs, [3H]raclopride was able to access surface and internalized receptors[177]. The affinity of raclopride to internalized receptors was reported to be by a factor of 2.1 lower[177]. While in this study around 40 % of the receptors were internalized, the situations were not comparable to physiological *in vivo* conditions as non-neuron cells and a strong pharmacological intervention were used. Moreover, the changes in affinity were measured after keeping the cells for "3-4h after triggering internalization and at 4°C to prevent receptors from recycling back to the plasma membrane."[177] Therefore it is not clear, if an affinity shift occurs *in vivo* under physiological conditions and in the case that back recycling is not prevented. Moreover, the time scale of internalization is not fully explored. Guo et al. mention a study by Vickery and von Zastrow and state that in "HEK-293 cells, at 37°C, D2 receptors degrade slowly ($t_{1/2}$ >7 h) but recycle rapidly back to the membrane ($t_{1/2}$ >30 min) (Vickery and von Zastrow, 1999)"[177]. This time scale of receptor internalization would not affect temporal fluctuations on a minute time scale in the PET signal. For serotonin 5-HT_{1A} receptors more rapid internalization was reported and is discussed to play a role in radiotracer binding[178]. However, PET receptor binding studies to investigate serotonin receptor internalization used drugs like the selective serotonin reuptake inhibitor (SSRI) fluoxetine, which increases extracellular serotonin concentrations, so that not necessarily receptor internalization but radiotracer displacement could lead to reductions in the binding potential. Moreover it is questionable if those two processes can be disentangled using PET.
Taken together, it is still controversially discussed if and to what extend receptor internalization exists *in vivo* and under physiological conditions. Nevertheless, even if receptor internalization plays a role, PET studies would measure a mixture of binding to surface and internalized receptors. Within our model receptor internalization would impact on B_{avail} in relation to increases in free neurotransmitter concentration, and therefore on the radiotracer binding rate. However the complete interaction is complex and would need to be studied in detail. Note, that within this work baseline

scans are compared with scans including a physiological stimulus (food intake), but without any pharmacological intervention, so that no or only negligible effects by receptor internalization are expected.
For some receptors it was reported that they can be present in high or low affinity states for agonists – *in vitro*. However, antagonist ligands bind both states (high and low affinity) with similar affinity [53,179]. This means antagonist radiotracer binding should not influenced by the presence of (agonist) high or low affinity states, whereas for agonist tracers this effect could become relevant. However, the fraction of receptors accessible by an antagonist tracer and for the interaction between the radiotracer and the endogenous agonist is affected: For dopamine D2 receptors it was reported that *in vitro* 50% of the receptors contribute to each state. This would leave only about 50% of the bound radiotracer susceptible to endogenous competition, since endogenous dopamine will predominantly bind to the high affinity state [58]. Anyway, there are reports questioning the *in vivo* existence of two different affinity states [179]. A review by Skinbjerg et al. (2012) on this topic concludes, that "more studies are needed to establish whether D2Rs (and other GPCRs) are stably configured in high and low-affinity states in vivo" [179].
So far, the impact of receptor internalization and different affinity states on the PET signal, especially on radiotracer displacement studies, is controversial and needs to be further investigated. The good reproducibility of PET scans, however indicates that those processes are not of great relevance for measurements under similar conditions. Within the framework of this thesis and the model introduced, the kinetics of the neurotransmitter itself are taken into account. This means realistic baseline concentrations are simulated, so that part of the receptors are already occupied and the interaction of neurotransmitter and radiotracer is analyzed. Affinities for the endogenous neurotransmitter and the radiotracer based on reported values are implemented in the model, while different affinity states or receptor internalization are not included, since it is questionable if and how strong these processes occur *in vivo* under physiological conditions. Furthermore, temporal variations in the PET signal are analyzed in the case that the time activity curve is unchanged. Receptor internalization would most likely also affect the time activity curve.

Temporal radiotracer concentration variations assessed by the parameter rN

Within the framework of this thesis the parameter rN is derived as a measure for temporal PET signal variations. rN is composed of the average change of the total radiotracer concentration between two time points in a box centered at the element of interest normalized to the total radiotracer concentration in this box. This means that rN is a measure for temporal variations of the radiotracer concentration relative to total radiotracer concentration and therefore its order of magnitude is dependent on the total radiotracer concentration. The calculation of the parameter rN as introduced in the model is directly applicable to experimental PET data. The size of the box analyzed reduces the spatial resolution, but also reduces spatial noise in the parameter for measured data. The choice of the size of the box depends on the system used for data acquisition and on the quality of the data [86]. Within the

model calculations, the box was selected to reflect the size of the regions that were analyzed within the experimental PET data. A discussion on the meaning of rN is given in section 3.3.5, as well as in the manuscript by Lippert and Cremer et al. [86].

Simulated noise

Measured PET data inherently contains noise. Since noise contributes to temporal signal variations assessed by the parameter rN, noise was simulated within the model calculation to analyze its impact on rN. Noise was added to the total radiotracer concentration, which was calculated including the temporal neurotransmitter concentration variations. The parameter rN was then calculated from the noisy data. To make values of rN comparable for different simulated noise levels, time courses of rN were normalized to their baseline levels, i.e. the time interval before stimulation. Within the model calculations, induced temporal signal variations are found in the order between 5 %-15 % with the set of applied parameters and for the analyzed radiotracers. As a results rN was found to be insensitive in cases that noise levels are higher than that. The effect of noise on the experimental data will be further discussed in the respective sections (sections 3.3.3 and 3.3.5).

3.3.2 Classical Methods vs. Novel Method

Comparison between common methods and the proposed method

Over the last decades several groups have provided evidence that PET and SPECT can be applied to measure acute f1uctuations in (synaptic) neurotransmitter concentrations *in vivo* in humans. Hereby, competition between the endogenous neurotransmitter and a radioligand, that binds to receptors of the respective neurotransmitter system, is the underlying principle (see section 2.5 and Figure 3.37). This concept has been applied predominantly to the measurements of changes in dopamine levels using [11C]raclopride. But also other neurotransmitter systems have been studied by using PET with the aim to measure neurotransmitter concentration changes, including the serotonin, noradrenaline, GABA, glutamate and acetylcholine system [53].
For most applications neurotransmitter release events were induced by pharmacological intervention prior to the measurement, in order to significantly reduce the net regional radiotracer binding. In [11C]raclopride PET studies measurable radiotracer displacement was observed in cases, in which robust and long-lasting (>minute time scale) changes in neurotransmitter/dopamine concentrations were induced. However, using more subtle interventions, e.g. smoking, not always significant changes in [11C]raclopride binding potential were found when compared to control conditions [180,181]. Moreover, the methods are in general restricted to the analysis of a single or few regions of interest. For the dopamine system this is the striatum, which displays the highest density of D2 receptors. Due to lower binding and therefore noisier data in extrastriatal regions, [11C]raclopride is said to not be suitable to assess binding potential changes in extrastriatal regions [175,182,183].
Furthermore, common methods lack the ability to measure subsequent release events, as usually the used stimulus induces one long lasting concentration increase and the

reduction in binding potential is observed for the duration of the measurement.
With the novel method developed within the framework of this thesis, temporal signal fluctuations are analyzed instead of net reductions in regional tracer binding. The difference between common approaches and the novel method can clearly be seen by comparing time activity curves (TACs) with time courses of rDA ($=rN$ for dopamine). In the human PET data, the time activity curves remain unaltered between tasteless and milkshake condition, while in the time course of rDA two subsequent time intervals with milkshake-induced activation become visible. Note, that the TACs, reflecting the net regional tracer binding, and the time courses of rDA, reflecting temporal signal variations, are calculated from the same dataset (Figures 3.16 and 3.17 in section 3.1.5)[86,87]. Also in the [11C]raclopride PET data from mice no changes in the TACs could be identified, while significant differences in rDA are yielded between dopaminergic activated mice and control measurements (section 3.1.4).
The different results obtained by the analysis of the net radiotracer binding and the temporal signal variations can be explained as follows: The exchange rates between free radiotracer and plasma are rather small, so that the net amount of the tracer within a region remains constant after endogenous neurotransmitter release and according displacement of the radiotracer from the receptors. In other words, the sum of bound and free radiotracer concentrations remains constant, even though the fraction of free or bound concentrations is altered. This means no changes in the time activity curve can be observed. However, the radiotracer concentration, which is displaced from the receptor after endogenous release diffuses within the extracellular space. This leads to concentration increases and decreases in subparts of the region, which can be assessed by signal variations as introduced within this thesis by the parameter rN. Taken together, endogenous release events lead to displacement of the radiotracer from receptors without altering the total amount of radiotracer within the region, but induces temporal signal variations due to radiotracer diffusion within the extracellular space. Since former approaches are based on analyzing the net differences in the radiotracer signal, they would not be capable of detecting the release events assessed within this thesis.
The power of the novel method is furthermore revealed by the data of the human study, in which subsequent and physiological dopamine release events were assessed for the first time and extrastriatal regions were analyzed (Thanarajah and Backes et al.[87]). Discussion on the extrastriatal analysis is given in the manuscripts by Lippert and Cremer et al. (2019)[86] and Thanarajah and Backes et al.[87].
All in all, the novel method is capable to assess physiological dopamine – and potentially other neurotransmitter – release events, that would not be detectable by commonly used PET methods[86].

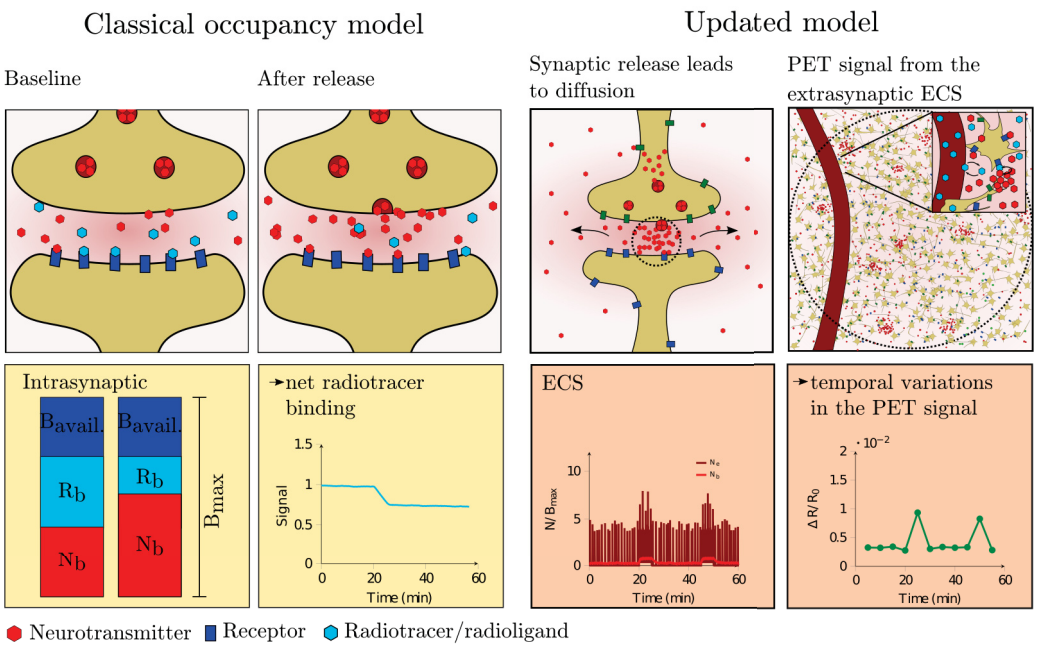

Figure 3.37: Classical occupancy model vs. new proposed model. The occupancy model predicts that stimuli, which increase synaptic neurotransmitter concentrations, will result in an increased occupancy of receptors by the neurotransmitter, and reduced availability of receptors for binding of the radiotracer and vice versa. A reduction in the radiotracer signal and binding potential therefore reflects an increase in neurotransmitter concentrations. Classically the interaction between radiotracer and endogenous neurotransmitter is thought to occur in the synaptic cleft. The radiotracer is usually injected as a bolus at the begin of the measurement and the binding potential is derived from the data by different methods for baseline and stimulated conditions, which are usually given by pharmacological intervention (see section 2.5). In the updated model, developed within the framework of this thesis, it is assumed that the neurotransmitter diffuses to and within in the extrasynaptic extracellular space and that the radiotracer signal predominantly reflects binding to receptors in the extracellular space. Note that diffusion of the neurotransmitter and radiotracer play a major role in the proposed model. Temporal signal variations instead of net radiotracer binding are analyzed by a parameter taking into account a number of voxels. Important for the novel method is moreover a bolus-plus-constant infusion radiotracer injection to achieve steady-state conditions.

Steady-state conditions

The proposed method requires a bolus-plus-constant infusion injection of the radiotracer, since steady-state conditions are important for the analysis of temporal fluctuations in the signal. Therefore, it is of importance to to adjust the injection protocol for every radiotracer to rapidly achieve steady-state conditions. The stimulus to induce neurotransmitter release should not occur before equilibrium is obtained. The bolus-plus-constant infusion method makes the radiotracer signal independent of changes in blood flow, so that artifacts in temporal signal variations induced by blood flow changes upon activation can be excluded. At steady-state conditions the (extracellular) radiotracer concentration is equal to $R_e = r_{pe}/r_{ep} \cdot R_p$ (in literature usually: $K_1/k_2 \cdot C_p$), with the kinetic rate constants r_{pe} and r_{ep} describing the transport between blood and tissue. These transport constants, r_{pe} and r_{ep}, have the same functional dependence on blood flow, because they are proportional to CBF·(1-exp(-PS/CBF)) with CBF being the cerebral blood flow and PS the permeability surface product [184]. This means that changes in blood flow cannot alter the steady-state conditions, since the ratio of r_{pe}/r_{ep} is independent of blood flow (see also review [58]).

3.3.3 Assessment of Dopamine Release with [11C]Raclopride in Mice

The method to analyze temporal PET signal variations as introduced within this thesis was applied to [11C]raclopride PET measurements in mice to assess dopamine release event. Within this section, considerations for the post-processing and data analysis of PET data in mice as well as effects of anesthesia and the chemogenetic mouse model are discussed.

Data acquisition, post-processing and analysis

For the individual scan session it is important to ensure similar conditions with regard to injected tracer activity, temperature, etc., in order to increase comparability between the scans [86]. For the analysis of temporal signal variations it is necessary to bin the PET data into time frames of equal duration. It is furthermore important that the duration of the time frames is selected to be sufficiently long enough to provide a good signal-to-noise ratio even at the end of the scan time [86]. For the PET data acquired in mice a time resolution of 1 min was selected. Parametric maps of rDA were directly calculated from the PET data by application of equation 3.33. This calculation can be easily performed with any type of script language or even manually, since no step of data fitting to a model is necessary [86]. Note that even though the experimental protocols were unchanged we observed different noise levels between the scan session, so that rDA was normalized to baseline fluctuations ($rDA_{baseline}$).

Effect of anesthesia

To perform PET scans in mice the animals have to be anesthetized. For the study we used isoflurane in a gas mixture of N_2/O_2. This gas recombination was used since

N_2O, which is usually used, is known to have influences on the dopamine system. It is not known how the isoflurane anesthesia affects the dopamine system and the action of CNO. Skinbjerg et al. (2012)[179] address the influence of anesthesia in PET displacement studies in their review on high affinity receptor states. They find anesthesia effects on high affinity radioligand binding (displacement) and that the binding potential of [11C]raclopride is reduced at baseline conditions under anesthesia[179]. Since with the method used here, temporal variations normalized to the local signal are analyzed, instead of the net reductions in the signal, a reduction in the baseline binding potential would not influence rDA. Moreover, both scans (baseline and stimulated) were acquired under identical conditions, i.e. both with the same anesthesia protocol. Despite the use of anesthesia, we found increases in the rate of dopamine transients in the continuous FSCV data as well as increases in the temporal signal variations in the [11C]raclopride PET as analyzed by the proposed method. This convincingly shows that the dopamine system can be activated by CNO in the used $hM3D_{Gq}{}^{DAT}$ mice under isoflurane anesthesia.

Chemogenetic mouse model

Recently, a controversial discussion about the mechanism of activation using CNO in DREADD mouse models arouse. A detailed discussion on this topic can be found in the "Supplemental Discussion" of the manuscript by Lippert and Cremer et al.[86]. Summarizing the arguments, we are confident that the results found within our studies in the used $hM3D_{Gq}{}^{DAT}$ mouse model are based on dopaminergic activation induced by CNO injection, while the precise mechanism of activation is not entirely resolved. The aim of using a chemogenetic mouse model was to be able to reliably induce dopamine release, in order to validate the PET method developed within the framework of this thesis. And, we were able to verify on different levels, that upon CNO injection in the $hM3D_{Gq}{}^{DAT}$ mice, dopaminergic activity is increased. First of all, the $hM3D_{Gq}{}^{DAT}$ mouse model was shown to produce dopamine release related behavior upon CNO injection (see Figure 3 in the manuscript by Lippert and Cremer et al.[86] that can be found in the Appendix). Furthermore, by direct recordings of extracellular dopamine levels in the nucleus accumbens core using FSCV an increased rate of transients was observed upon CNO injection compared to vehicle injection. These findings, demonstrate that activation of the dopaminergic system is induced by CNO. Therefore, the $hM3D_{Gq}{}^{DAT}$ model is a good model to validate the introduced PET method. Within the PET study, we found significant increases in the temporal PET signal variations in the CNO group compared to the control group. The strength of the signal changes are in the order of magnitude found by direct assessment of dopamine release using FSCV in the same mouse model. This confirms that the parameter rDA is able to capture dopaminergic activity *in vivo*. The FSCV data acquired in electrically stimulated wild-type mouse show clearer activation patterns than the chemogenetic mouse model. Therefore it would be favorable to repeat [11C]raclopride PET studies with either electrical stimulation in the scanner, or in an other mouse model in which clearer activation patterns are known to be present after a certain stimulus.

3.3.4 Assessment of Dopamine Release with [18F]DMFP in Mice

The method to analyze temporal PET signal variations to assess dopamine release was applied to [18F]DMFP PET measurements in $hM3D_{Gq}{}^{DAT}$ mice in a similar manner as for the [11C]raclopride PET measurements. The data were acquired using the same acquisition and injection protocol. Post-processing and data analysis were identical. Furthermore, the same mouse model as for the [11C]raclopride PET study was used with Saline/CNO injections during the scan.
The main advantage of the use of [18F]DMFP is that with one batch of tracer more scan sessions can be performed due to its longer half-life. Moreover, [18F]DMFP can be provided from a remote radiochemistry facility. Unfortunately we found, that using the same injection protocol as for [11C]raclopride no steady-state conditions were achieved with [18F]DMFP. Therefore, temporal variations in the PET signal cannot reliably be analyzed. This is also visible within the results: no difference between the CNO and Saline group was observed. [18F]DMFP PET scan should be repeated using a pre-determined injection protocol for [18F]DMFP.

3.3.5 Dopamine Release in Humans Assessed with [11C]Raclopride PET

In order to investigate food-intake-related dopamine release events a [11C]raclopride PET study was performed at the Max Planck Institute for Metabolism Research. The data were analyzed based on the method developed within the framework of this thesis and reveal the power of the method. The full set of data from the human study and disscusion can be found in the manuscript by Thanarajah and Backes et al. (2018)[87].

Data acquisition, post-processing and analysis

For the human data twelve time frames of five minutes duration each were reconstructed from the PET data. A frame duration of five minutes was found to provide a good signal-to-noise ratio even at the end of the scan time. To the reconstructed PET images a 10 mm Gaussian filter was applied. From those images parametric maps of rDA were calculated by equation 3.35 using a region of 125 voxels. This means that the parameteric maps of rDA contain a spatial uncertainty. As mentioned before, the analysis of a box of voxels decreases the contribution of noise and leads for the human data to a resolution of $\sim 225\,\mu$L.

Meaning of rDA across regions

Within this section, some important considerations on the parameter rDA are discussed based on the discussion given in Lippert and Cremer et al.[86].
The absolute value of rDA, i.e. the ratio of temporal variations to the absolute [11C]raclopride signal, depends on the following factors: (i) noise resulting from the imperfection of the method, (ii) the absolute [11C]raclopride signal, (iii) the amount of released dopamine and (iv) the fraction of released dopamine which is removed at a minute time scale[86].
Noise will increase the amplitude of rDA, since it is a measure of temporal signal

changes that are larger with a stronger contribution of noise. In measured PET data noise is present due to the stochastic nature of radioactive decay, <100% efficiency of detecting decay events, etc.[86]. The decay over the duration of the measurement leads to a reduction in the signal-to-noise ratio with time (60 minutes measurement with [11C]raclopride with a half-life of ∼20 minutes)[86]. This means that the parameter rDA increases steadily in time, as is visible in the rDA data. However, ensuring stable experimental conditions, including the use of the same PET scanner, using the same amount of injected tracer, etc., the contribution of noise is similar for each measurement[86]. Note that as a result of noise no abrupt changes in temporal variations are expected in the PET data. However, the increases in rDA found within the human study are abrupt, time locked and region-specific. Moreover, rDA was highly reproducible within subjects (see Thanarajah and Backes et al.[87]). This supports that rDA does not only reflect noise in the signal, but is a measure for dopaminergic activity.[86]

The absolute [11C]raclopride concentration determines the order of magnitude of rDA, as the parameter rDA is normalized to the absolute [11C]raclopride signal. This means that temporal signal variations at the same amplitude in a region with lower net binding result in a higher rDA than in regions with higher net [11C]raclopride binding. The striatum is the region with the highest D2 receptor density in the human brain, i.e. with the highest [11C]raclopride binding. This means that temporal variations at the same amplitude as in the striatum would result in a higher rDA within extrastiatal regions.[86]

Furthermore, not only the receptor density, but also the density of synapses is region-dependent. Again the striatum is the region with the highest density of dopaminergic synapses. Since the amount of released dopamine is dependent on the density of dopaminergic synapses, a lower amount of dopamine is usually released in extrastiatal regions, i.e. regions with a low density of dopaminergic synapses, compared to the striatum. However, it was worked out that the signal variations assessed by rDA are predominantly induced by slow (minute scale) dopamine concentration fluctuations. Furthermore, it was shown that the component of minute scale concentration variations in both regions is of the same order of magnitude due to different transporter densities, even though the absolute released dopamine concentration is different[86]. This argument will be outlined in more detail in the next section 3.3.7.

Taken together, it can be explained why dopamine release in extrastriatal regions causes changes in rDA with similar amplitudes as in the striatum in the human [11C]raclopride PET data: although less dopamine is released (less synapses) and reaches the extracellular space, the predominant part is removed by dopamine transporters at a much slower rate (lower transporter density) than in the striatum. Moreover, the lower radiotracer binding (lower receptor density) in extrasriatal regions increases rDA.[86]

Summarizing, these arguments show that rDA represents dopamine release within a region, but cannot be compared between regions. The results from the human study are in accordance with these considerations (see Thanarajah and Backes et al. (2018)[87]).

Extrastriatal data analysis

There are controversies about the meaning of extrastriatal binding of [11C]raclopride, because of low extrastriatal dopamine D2 receptor densities. However, within several studies pharmacologically-induced or even task-related changes in the [11C]raclopride binding are observed in extrastiatal regions, which confirms specific binding of [11C]raclopride in extrasriatal regions[185,186,187]. Using the method described within the framework of the thesis, temporal variations in the signal relative to the total signal were analyzed instead of the absolute [11C]raclopride uptake. As discussed above, this makes the method more sensitive for the detection of signal variations in regions with low binding in comparison to methods that analyze stimulation-related changes in the absolute binding. With the results found within the human study, we are confident that the extrasriatal changes in rDA are related to dopaminergic activity, as the regions identified within the study are well-known to be involved in reward processing[86]. A detailed discussion on the extrastiatal [11C]raclopride data analysis can be found in Lippert and Cremer et al.[86] and Thanarajah and Backes et al.[87].

3.3.6 Direct Measurement of Extracellular Neurotransmitter Concentrations

A premise for the method developed within the framework of this thesis is that minute-long variations of neurotransmitter concentrations are present in the extracellular space and that they are related to phasic release events. To test this hypothesis continuous FSCV data were acquired, which enable frequency analysis to determine contributions of different temporal scales to the signal.

Continuous dopamine FSCV data in mice and wavelet transform analysis

FSCV data were acquired in the $\mathrm{hM3D_{Gq}}^{\mathrm{DAT}}$ mouse model used for the [11C]raclopride PET measurements (see discussion above) and in a wild-type mouse model with electrical stimulation for the time course of at least one hour. To analyze the contribution of different frequencies in the continuous signal a wavelet transform was applied. The wavelet power at a frequency of 0.5 Hz was investigated, since the typical duration of a dopamine transient is in the order of ∼2 seconds. The data show a strong correlation between the wavelet power at 0.5 Hz in one-minute time intervals and the transient rate assessed using a template approach. This correlation was not only significant on group level, but also on individual level, i.e. within data of one mouse (Figure A.1 in the Appendix). Therefore, the results indicate that the application of a wavelet transform can be used to derive transient rates from the continuous FSCV data.
The advantage of a wavelet transform is, that is does not require any assumptions or thresholds[86]. In contrast, the template application is based on a pre-defined threshold, which leads to both, false positive and false negative results[86]. Or in other words, if the shape of the transient is somehow altered, e.g. a double peak occurs or other properties are changed, it will most likely not be detected by the

template approach [86]. The wavelet transform on the other hand, can be applied in a more generalized and objective manner, as it is a well defined formalism without any adjustable parameters [86]. This means that the power of the 0.5 Hz frequency band of the wavelet transform might be a more reliable measure of phasic dopaminergic activity than the transient rate obtained using the template approach [86]. However, to our knowledge, this is the first time a wavelet transform is used for the analysis of continuous FSCV data and therefore needs further investigation [86].
Within this thesis, the continuous FSCV data and the wavelet transform were used to identify systematic relations between second-by-second and minute-by-minute variations in the data. Therefore, not only the wavelet power at the frequency band of 0.5 Hz, but also at a frequency of 0.01 Hz was analyzed. The results reveal a significant correlation between the minute scale (0.01 Hz) wavelet power and the rate of transients assessed by the template application. Furthermore, the low frequency variations correlate with the wavelet power of the 0.5 Hz frequency band (second time scale). This shows that transients, i.e. phasic release events, systematically induce minute-scale variations in the ECS. Cf. Lippert and Cremer et al. [86].

Minute long extracellular dopamine concentration variations

Minute long extracellular dopamine concentrations in the extracellular space are known to exist and are commonly measured for example by microdialysis. However, these slow concentration variations are often thought to be consequence of so-called tonic firing events and therefore to be distinct from fast, phasic release events. A discussion on the controversial topic of tonic and phasic dopamine firing and its physiological functions can be found elsewhere. Within the framework of this theses, it was demonstrated that fast phasic release events systematically induce minute scale variations in continuous FSCV signal. Furthermore a mechanism on how these longer lasting concentration increases emerge is proposed on basis of model calculations. Note that we don't claim any physiological relevance of these minute-by-minute concentration variations in the extracellular space, as this is out of scope of this work. However, we show that they can be related to release events and are therefore a measure of dopaminergic activity.
The findings can be well supported by indications from literature. In published FSCV transients data one can very often observe that the measured levels do not rapidly return to baseline, i.e. the the tail of the transient remains elevated above baseline levels [101,188]. This tail is often also referred to as "hang-up" and was interpreted to be an artifact by adsorption of molecules on the surface of the measurement electrode in *in vitro* experiments [189,190]. Thereby, the order of magnitude of adsorption is directly related to the amplitude of the transient, i.e. a high dopamine concentration (peak) leads to high adsorption and vice versa. However, in *in vivo* data often a minute lasting component (tail) without the presence of a large peak is found. In these cases the tail can not be explained by adsorption. The following two examples from literature nicely show this effect: In a study by Garris et al. (1993) [109] simultaneous voltammetry recordings in the striatum and the medial prefrontal cortex were performed upon stimulation of the ventral tegemental area. The tails of

the transients measured in the respective regions are in the same order of magnitude, even though the peak in the extrastriatal region is much lower (Figure A.2 in the Appendix). In a further study by Robinson et al. (2003)[110] a FSCV probe was moved through the nucleus accumbens. In these data a strong dependence of the transient peak from the probe location is visible. However, the minute lasing component remains stable. Together, these data indicate that at least part of the released dopamine is cleared on a minute time scale independent from the absolute dopamine concentration and that this fraction has a similar order of magnitude across different regions.

Within this thesis, typical transients were simulated by numerical model calculations and analytical results by Cragg and Rice (2004)[99] could be reproduced. The analytical results are based on a constant removal rate within the extracellular space, i.e. a homogeneous transporter density. Since more recent literature indicates that the transporter density might not be homogeneous within a region but to vary on subcellular levels[191], the effect of a heterogeneous transporter distribution on the transient shape was investigated. Assuming a heterogeneous transporter expression with a high density close to the release site which decreases with distance from the release site, prolonged clearance rates are found (Figure 3.29 and A.3 in the Appendix). This shows that under these conditions part of the released dopamine diffuses into subcellular regions with a low expression of transporters, i.e. further away from the release site, where it is then cleared by a slower removal rate (lower transporter density). These results are supported by a report by Kaya et al. (2018)[192] in which this effect is described as well.

Our calculations further demonstrate that the contribution of the minute time scale component compared to the peak depends on the distance of the probe from the release site. Or in other words, close to the release site the transient has a high peak (large concentration) and the tail (minute scale component) is negligible compared to the peak. However, with distance from the release site the peak rapidly decreases and the slow component, the tail, becomes more pronounced within the signal (see also Figure A.3 in the Appendix).

Therefore, a heterogeneous transporter density is a potential mechanism to explain the minute scale extracellular concentration variations in the FSCV data and is also in accordance with the data found in literature. Taken together, observations from literature, the continuous FSCV data analysis, as well as model calculations support the presence of a minute time scale dopamine component in the extracellular space in relation to release events. Note that the relation between phasic release events and the slow concentration variations is derived based on fundamental processes, i.e. diffusion and transport. There processes also apply to other neurotransmitter systems and are not exclusive for dopamine[86]. Cf. Lippert and Cremer et al.[86]

Extracellular serotonin concentrations

Data of continuous 5-HT FSCV recordings in a wild-type mouse model with electrical stimulation of a defined rate of transients were provided. The data were analyzed in the same way as the dopamine FSCV data using a wavelet transform to search for correlations of high and low frequency correlations. A significant correlation between the wavelet power of 0.5 Hz of the one-minute stimulation intervals and the wavelet power of 0.02 Hz was found. The correlation for 0.01 Hz was less strong. This indicates that the serotonin system itself might have a bit faster kinetics as the dopamine system. Anyway, also for serotonin minute scale lasting concentration changes in the ECS can be found in relation to phasic release events. This means, that also for serotonin minute-by-minute concentration variations in the ECS can be related to phasic release events and are therefore a measure of neuronal activity.

3.3.7 Application of the Method to further Neurotransmitter Systems

Neurotransmission is based on release of molecules into the synaptic cleft, where they mediate secondary processes by binding to certain receptors. Two principle classes of neurotransmission exist: traditional direct synaptic transmission (also referred to as "wired" or "point-to-point" transmission) or volume transmission. Wired transmission occurs within the synaptic cleft, while volume transmission includes diffusion into the extracellular space for distances larger than the synaptic cleft [166].
The model introduced within the framework of this thesis, is based on interaction between the neurotransmitter and the radiotracer in the extrasynaptic extracellular space. This means, that the method can theoretically be applied to any neurotransmitter that acts via volume transmission. If the transmission is restricted to the volume of the synaptic cleft and no diffusion of the neurotransmitter into the extrasynaptic ECS occurs (i.e. wired transmission), the method can not be applied. Within the framework of this thesis model calculations have been performed for the serotonin, acetylcholine and glutamate systems. The receptor density and the affinity of these neurotransmitters systems were approximated by values from literature and adjusted within the calculations accordingly. Furthermore, radiotracers to assess the respective systems were selected and kinetic rate constants were identified from published data. However, for all neurotransmitter systems the same traces of baseline and stimulation pulses were assumed to make the results comparable. For the serotonin system, which is quite similar to the dopamine system, this is an appropriate estimation. This is also supported by the FSCV data shown within this thesis, which reveals a similar kinetic for dopamine and serotonin. Acetylcholine is, on the one hand, a "fast-acting, point-to-point neurotransmitter at the neuromuscular junction and in the autonomic ganglia" [117] (periphery) and, on the other hand, acts as neuromodulator in the CNS [117,99,193]. There is evidence that the action of acetylcholine in the brain occurs via volume transmission as well as by point-to-point transmission [117]. To our knowledge, time courses of acetylcholine concentrations in the extracellular space are not reported. Glutamate transmission is reported to be very fast and synaptically confined, i.e. glutamate action occurs

via wired transmission (point-to-point) and the proportion of glutamate that escapes the synapse by diffusion after release is negligible. However, there is also evidence that glutamate can act via volume transmission and different physiological functions are reported to involve glutamatergic volume transmission [194]. On basis of these findings, it is only a first approximation to use the same temporal variations of extracellular neurotransmitter concentrations as for dopamine.
For the serotonin systems, several radioligands to serotonin receptors exist and are approved for application in humans. Within the model calculations three different radiotracers were analyzed with regard to their capability to detect temporal signal variations upon fluctuations of serotonin in the extracellular space by the parameter rN. While with [11C]WAY-100635 and [11C]CUMI-101 signal variations in the order of 3 % were achieved, the results for [18F]MPPF were only in the order of 1 %. When noise was simulated, the temporal signal variations assessed by all three radiotracers became negligible. However, due to the similarity to the dopamine system and the existing radiotracers, the serotonin system would be most suitable to be studied with the proposed method in a next step.
For the acetylcholine system the radiotracer [18F]nifene was investigated. [18F]nifene was found to be a suitable radiotracer to pick up signal changes in the PET signal upon acetylcholine release with temporal signal variations in the order of ∼8 %. The temporal signal variations remail visible even with noise. Applying the method developed within the framework of this thesis to the acetylcholine system might yield new insight in acetylcholine signaling, e.g. in which brain areas volume transmission of acetylcholine is the prominent processes.
Suitable radiotracer binding to glutamate receptors exist as well, for example [11C]ABP688 or [18F]SP203. However, the model results reveal rather low temporal signal variations assessed by those radiotracers (<1 %). To apply the method proposed within the framework of this thesis to the glutamate system other radiotracers should be developed.
Theoretically, all neurotransmitters acting via volume transmission could be studied with the PET approach introduced within this thesis. Hereby, a suitable radiotracer is the prerequisite. However, the method has to be adjusted, tested and validated for each application, which is beyond the scope of this work.

3.4 Conclusion and Outlook

A new method to analyze PET data using receptor radioligands to assess neurotransmitter release is introduced. In contrast to former methods to image neurotransmitter release, the new method allows spatiotemporal assessment of release events, i.e. the analysis is not restricted to single brain regions and a time curve of subsequent release events is obtained. This is possible by calculating temporal signal variations, given by the parameter rN that was derived within the framework of this thesis, instead of analyzing reductions in the net radiotracer signal.
Within this thesis, the method is substantiated by model calculations and is experimentally validated for the dopamine system with the radiotracer [11C]raclopride. The proposed model is based on the premise that longer lasting extracellular dopamine concentrations are present after release events and that they are related to each other. Evidence for the existence of minute long extracellular dopamine concentrations is given in literature, is validated within this thesis using continuous dopamine FSCV data and is substantiated by additional model calculations. With the use of this additional model a potential mechanism for the occurrence of minute long concentration variations is given: a heterogeneous expression of dopamine transporters leads to a prolonged dopamine lifetime in the extracellular space.
[11C]raclopride PET data was acquired in a chemogenetic mouse model, as well as in human volunteers. Both studies provided correlations between increases in temporal signal variations, as calculated by the parameter rDA ($=rN$ for dopamine), and dopamine release events. The results from the human study, which provide insight into dopaminergic signaling in response to food intake in striatal as well as extrastriatal regions reveal the power of the novel method. Furthermore, within both, the [11C]raclopride PET measurements in humans and mice, it was clearly shown that former methods would not be able to detect the dopamine release events assessed here.
Further studies – in mice and humans – would be favorable to confirm the results found within the framework of this thesis. For example a different mouse model with clearer activation patterns would be of advantage. Moreover, the use of [18F]DMFP, which has a longer half-life than [11C]raclopride is favorable, because from one batch of produced tracer multiple subjects could be investigated. From model calculations good results for [18F]DMFP were obtained, while a pilot study in mice revealed negative results. This might be attributed to the fact that with the used bolus-plus-infusion protocol no steady-state conditions were achieved, which are necessary for the application of the novel method. A study in humans with [18F]DMFP is planned.

Since the introduced model is based on fundamental processes, i.e. diffusion and transport, which are not unique for dopamine and also apply to other neurotransmitter systems that act via volume transmission, the method theoretically applies to those as well. Therefore, the model is formulated in a general manner and by using the respective parameters model calculations for the serotonin, acetylcholine and glutamate system with selected radioligands are performed within the framework of

this thesis. Additionally, phasic release events of serotonin are related to minute-by-minute concentrations in the extracellular space by continuous FSCV data analysis, in analogy to the dopamine FSCV data. This supports the fact that serotonin release might be assessable with PET using the proposed method. However, future experiments and application will reveal the real power of the novel method.

4 Advancements in the Application of [18F]FDG PET and CT for Whole-Body Analyses

In basic research the use of rodent models is common. With the progression in the generation of genetic mouse models for example by the "Cre/loxP" system or CRISPR/Cas9 single genes can be "knocked out/in" or single groups of neurons can be activated by chemical or optical means. In the obtained animals disease mechanism can be examined *in vivo*.
A lot of state-of-the-art and cutting edge research techniques to investigate the genetically manipulated animals are invasive and/or the animals need to be sacrificed. The analysis of brain activity *in vivo* is for example restricted to analyze only small brain regions (e.g. by voltammetry, microdialysis or fiber photometry) or to post-mortem measures in brain slices (staining methods). Non-invasive imaging techniques provide a tool to examine the animals *in vivo* and bridge the gap between basic research and clinical application, since the techniques are readily available for human application.
PET imaging allows to perform longitudinal studies within one animal, thereby reduces the number of animals and a paired study design increases the statistical power. Moreover, the data is obtained in *in vivo* conditions and physiological processes are mapped in their natural environment. Co-registration of mouse brain PET data to a standard mouse brain, i.e. a mouse atlas, enables voxel-wise statistical testing between groups of animals. Therefore, differences in genetic mouse models or differences in response to different stimuli between groups in tracer uptake can be imaged and quantified. Application of brain PET imaging can be found for example in Jais and Solas et al. (2016)[195], Steculorum and Ruud et al. (2016)[155] or Jais and Paeger et al. (2020)[196]. For most small-animal scanners not only the brain of the animals is inside of the field-of-view (FOV). In those cases whole-body data of the animal can be acquired. Furthermore, PET systems are usually coupled to a CT or MRI scanner and co-registered anatomical data is therefore accessible from a single scan session.
In the field of metabolism research, different tissues and organs, which contribute to energy expenditure, are of interest. Which tissues or organs contributes to an impaired glucose metabolism in transgenic animals or due to different stimuli/treatments is a common question to be answered. Additionally, with the introduction of the first whole-body PET scanners for humans, the need of methods for whole-body analysis emerges. Therefore, in this chapter the use of whole-body [18F]FDG PET and CT data is introduced proposing methods for analysis and exemplary applications.

First, a short overview on whole-body and tissue analyses by [18F]FDG PET from literature is given, including an introduction on important metabolic tissues. This is followed by a description of methods developed within the framework of this thesis to analyze whole-body [18F]FDG PET and CT mouse data, including fat segmentation and 1D and 2D histogramming of PET/CT data. Exemplary results of the methods from different studies are given in the results section, followed by a discussion of the methods and results as well as by a conclusion and outlook.

4.1 Background

In neurons the primary energy source is glucose. Therefore, [18F]FDG has been used extensively to measure regional cerebral glucose metabolic rates [9]. To calculated the glucose consumption in the brain (CMR_{glc}) kinetic modeling of [18F]FDG PET data is applied (see section 2.3). The kinetic model is based on various premises, which apply well to the brain. If the model is also applicable to whole-body data needs to be discussed and is dependent on the tissue to be studied.
So far peripheral [18F]FDG PET data is mainly used in oncology to stage, characterize and monitor tumors and metastasis [197]. In clinical routine this data is predominantly analyzed using semi-quantitative standardized uptake values (SUVs, see section 2.4). Since the majority of tumors display an increased glucose utilization, i.e. more [18F]FDG is taken up in the metabolically active cancer cells than in the surrounding healthy tissue, the SUV is often thought to be sufficient for tumor detection. However, clinical tasks, including the investigation of treatment response or to distinguish between malignant and bening uptake are limited by the qualitative or semi-quantitative analyses [198]. Moreover, in typical applications the kinetics of the radiotracer, which is substantially different between tumors and normal organs as well as among patients, is often neglected [198]. Measurements including tracer kinetics by dynamic acquisition are therefore of advantage. And it was shown that quantification of tracer uptake based on compartmental modeling approaches can improve both tumor characterization and treatment response monitoring [198]. However, these approaches did not make it to clinical routine. One reason might be that dynamic PET scanning is limited to a single bed position with a typical axial field of view of less than 25 cm [198,199]. Whole-body scans can only be achieved by "multi-bed" procedures. This means that the subject is measured at a certain position for a fixed time interval after which the bed is moved and a further image is acquired. As a consequence, the data of a single bed position is a static image (or has temporal gaps), which makes kinetic modeling not possible or complex. In the case that at least two images at different times are acquired within a field-of-view Patlak plot analysis can be performed [198].
However, dynamic scans of organs, tissues or further structures within the field-of-view can be performed and the data can be used for kinetic modeling to create parametric images of parameters of interest. Moreover, whole-body human PET/CT systems have been developed recently [7,8]. Therefore, methods for future application to whole-body data need to be discussed and developed. Whole-body kinetic modeling and resulting parametric images may hold great potential to enhance diagnosis, prognostic and treatment response monitoring capabilities of PET [198]. Moreover, dynamic whole-body imaging opens up new opportunities to study relations between organs and the brain, e.g. the gut-brain axis or the heart-brain axis. As already whole-body [18F]FDG PET data is available from small-animals imaging, the process in developing methods can be supported using these data.

4.1.1 Metabolic Tissues and PET Applications

Glucose distributed through the blood is the main metabolic energy source for many tissues and a continuous supply of glucose is necessary to ensure proper function of all organs [9,200]. Therefore, plasma glucose levels are usually maintained around a narrow range, the so-called physiological set point, which is in the order of 4-6 mM $\triangleq$ 72-108 mg/dL [200]. The balance between glucose consumption and production is predominantly maintained by the opposing hormones insulin and glucagon [200]. Insulin is released from β-cells of the islets of Langerhans in the pancreas in response to high blood glucose levels, e.g. after a meal [200]. In the case of low plasma glucose levels, e.g. due fasting or exercise, the α-cells in the pancreas release glucagon [200]. Insulin stimulates the storage of glucose in form of glycogen in the liver [201]. Glucagon on the other hand leads to release of glucose from the stored glycogen and stimulates gluconeogenesis, i.e. glucose synthesis.
Fat and muscle tissue are insulin sensitive tissues and play an important role in maintaining glucose homeostasis. Muscle tissue responds to high insulin levels by increasing glucose transport into the cell along with the rates of glycolysis (i.e. conversion of glucose to pyruvate) and glycogen synthesis [9]. In total, skeletal muscle accounts for 60-70% of whole-body glucose uptake stimulated by insulin [201]. Note, that when glucose is available from blood the muscle tissue is prevented from using glycogen stores mediated by insulin signaling [9]. In adipose tissue high insulin levels lead to increased glucose uptake into the adipocytes and to glycolysis. In adipocytes glucose can be transformed into lipids by lipogenesis to store energy [202,201].

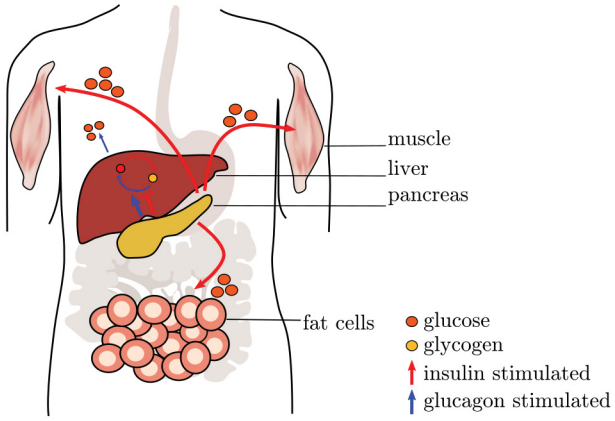

Figure 4.1: Insulin and glucagon stimulated glucose utilization. The pancreas releases insulin when blood glucose levels are high, e.g. after food intake. Insulin stimulates glucose uptake in muscles and adipose tissue, and suppresses gluconeogenesis in the liver along with increasing glycogenesis (synthesis of glycogen). In the case that blood glucose levels are low, the pancreas secretes glucagon, which stimulates gluconeogenesis and glycogenolysis (break down of glycogen) in the liver.

Skeletal muscle

During resting state the major energy source for skeletal muscles is fatty acid oxidation [203,204]. In this case [18F]FDG uptake into muscle tissue is diffuse ("mild and homogeneous") [203]. However, insulin release can induce a rapid increase in glucose uptake (for example postprandially) [203,204]. The increase in glucose uptake is induced by translocation of the glucose transporter 4 (GluT4) from the intracellular vesicles to the plasma membrane [203]. In that case, skeletal muscle tissue is a major consumer of glucose and it displays increased [18F]FDG uptake in a PET scan.
Since muscles constitute a large part to the body mass, they can account for up to 60-70% of whole-body glucose uptake [201,204]. [18F]FDG uptake in skeletal muscle depends on the nutritional status of the scanned subject (fasted or postprandial) and on muscle activity. Therefore, the patient preparation is of importance for clinical [18F]FDG PET applications, e.g. fasting and avoidance of exercise before the examination, to be able to decide between physiological and pathological [18F]FDG uptake in the muscle. So far, [18F]FDG muscle uptake is investigated within tumor diagnosis and staging [203] by the use of SUVs. The kinetic of [18F]FDG muscle uptake in the basal state was rarely investigated in detail, but Gheysens et al. (2015) [205] for example applied kinetic modeling to investigate skeletal muscle glucose utilization. More effort was made in type 2 diabetic subjects. As it is a major challenge to differentiate abnormal, potentially pathologic uptake from physiological uptake [203,204], dynamic uptake data are of advantage.

Adipose tissues

In general two types of adipose tissue can be distinguished in mammals: the white adipose tissue (WAT) and the brown adipose tissue (BAT). Furthermore, a third type of "intermediate" adipose tissue exists: the beige fat, which has the same origin as white adipocytes, but has properties of BAT [206,207,208].
WAT is the major site for lipid storage serving as energy deposit. BAT is a metabolic active tissue, which can "burn" fatty acids to produce heat. This process is mediated by the uncoupling protein 1 (UCP-1), which can uncouple electron transport in the mitochondria, so that heat instead of ATP is generated. Therefore, BAT plays a role in energy expenditure and non-shivering thermogenesis.
In contrast to WAT, BAT can be found at discrete locations in the body (Figure 4.2). In humans, as well as in mice, BAT is typically present in the neck area. [9,209,210]
BAT thermogenesis is regulated by the sympathetic nervous system [209]. Higher amounts of BAT are associated with better glucose homeostasis, better blood lipid profiles and BAT activity in humans is negatively correlated with BMI [9,209].
[18F]FDG PET can be used to estimate BAT activity. When [18F]FDG PET became a tool for whole-body staging in oncology in the 1990's, occasionally high uptake areas were found in the cervical area [211]. First interpreted as increased muscular uptake interfering with tumor diagnosis, it was later identified as BAT [18F]FDG uptake [211]. Exemplary [18F]FDG PET images displaying increased BAT activity are shown in Figure 4.3. Routinely acquired [18F]FDG PET/CT data were reassessed at that time, but since no standardized acquisitions conditions were used conclusions

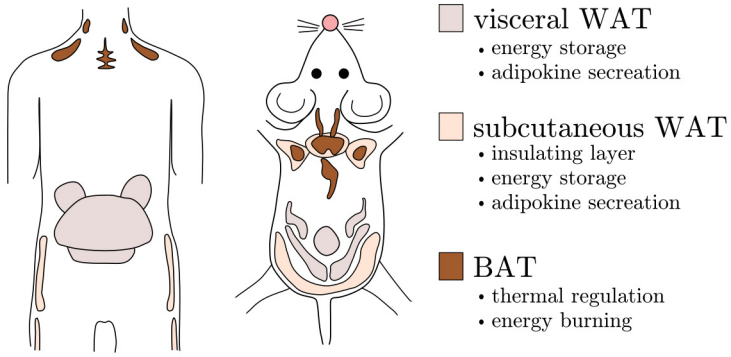

Figure 4.2: Distribution of white and brown adipose tissue in humans and mice. BAT in humans is localized around the shoulders. Visceral WAT surrounds intra-abdominal organs, and subcutaneous WAT is spread throughout the body beneath the skin. BAT contributes to thermogenesis, as it contains a high density of mitochondria and UCP-1, WAT tissue stores energy and can secrete various adipokines. Visceral WAT is associated with metabolic disorders, while subcutaneous fat is not correlated with metabolic impairments. In mice BAT is also located in the region of the shoulders. Visceral and subcutaneous WAT depots exist like in humans, while for example the visceral fat around the gonadal (around the ovaries/ testes) does not exist in humans.

on BAT prevalence could not be drawn [211].

To measure BAT uptake reliably, cold-exposure protocols have been developed. This means the subject is exposed to (mild) cold for a certain time before the scan session to stimulated thermogenesis in BAT. Cold exposure increases the number of mitochondria and UCP-1 synthesis in BAT cells through sympathetic adrenergic stimulation. It was demonstrated that [18F]FDG uptake in human BAT is directly proportional to the expression of UCP-1 and cold-induced increase in energy expenditure [211]. Therefore, it was concluded that [18F]FDG uptake from PET scans can be used as a marker to measure BAT activity.

Quantification of [18F]FDG BAT uptake from the data by SUVs requires delineation of BAT. The product of total BAT volume and the mean SUV in the BAT region is most commonly used to quantify BAT activation. Drawing the region of interest around the BAT region is either done manually or by more automatized techniques based on the use of threshold values for the PET and CT data. Note that the hounsfield units (HU) of the CT depend on the BAT composition and can vary between active and non-active BAT [212]. It was shown that activated BAT contains less lipids compared to non-activated BAT, likely because of increased lipid consumption [212]. This change in density leads to higher HU [212]. However, the combined PET/CT data analysis is limited by the fact that, if BAT delineation is based on the CT data spillover due the lower spatial resolution of the PET data is neglected causing systematic underestimation of BAT activity.

In the following methods for the analysis of combined PET/CT data of the whole-body and the neck area (BAT) of mice will be introduced.

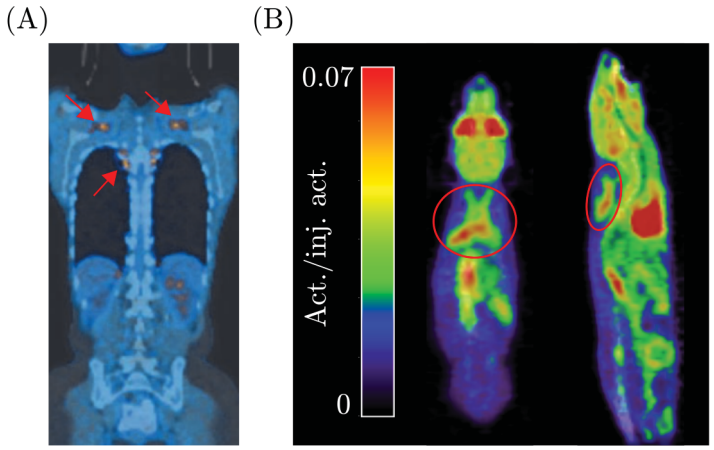

Figure 4.3: Brown adipose tissue [18F]FDG uptake in humans and mice. (A) Increased [18F]FDG uptake in BAT in humans localized around the shoulders. Image is taken from Hany et al. (2002) [213]. (B) [18F]FDG uptake in BAT in mice is clearly visible in the neck area.

4.2 Material and Methods

4.2.1 Data Acquisition and Post-Processing

All [18F]FDG PET and CT scans were performed using the Inveon preclinical PET/CT system by Siemens. For the scan session mice are anesthetized with 2% isoflurane mixed with 65%/35% nitrous oxide/oxygen gas. The animals are positioned on a water-heated (37.0±0.5°C) mouse carrier carrying two mice (MEDRES, Germany). For the injection of [18F]FDG, a catheter is inserted into the tail vein of each mouse and fixated by a drop of glue. The catheter consists of a 30G cannula connected to a polythene tubing (ID=0.28 mm). With start of the PET scan, 7-8 MBq of [18F]FDG in 40-150 μL saline is injected per mouse. Emission data are then acquired for 45 minutes. Afterwards, the animals are automatically moved into the CT gantry, where a CT scan is performed. Parameters for the CT scan are: 180 projections/360°, 200 ms, 80 kV, 500 μA. The resolution of the CT image is 0.1 mm x 0.1 mm x 0.1 mm. CT data is used for attenuation correction of the PET data and for image co-registration of brain data, i.e. CT data of the scull is used to co-register the PET brain data. After the scan, plasma glucose levels are measured from a tail vein blood sample after removing the catheter using a standard glucometer (Bayer). PET data are histogrammed in time frames of 12x30 s, 3x60 s, 3x120 s, 7x240 s, Fourier rebinned, and images were reconstructed using the MAP-SP algorithm provided by the manufacturer. The resolution of the PET image is 0.4 mm x 0.4 mm x 0.8 mm. Brain images are co-registered to a 3D mouse brain atlas constructed from the 2D mouse brain atlas published by Paxinos[158] using the software Vinci[157]. Cf.[195,155] Whole-body PET and CT data are co-registered to each other, but cannot be co-registered to a reference mouse because of the individual distribution of organs within the body.

4.2.2 Kinetic Modeling

The kinetic model explained in section 2.3 is applied to [18F]FDG PET data (see also Figure 2.5). For this IDL and C scripts are used.
First, an image-derived input function is extracted from the PET data of the aorta, which can be identified in the image of the first time frame of each animal. The input function data are corrected for partial volume effects by assuming a standardized volume fraction of 0.6[214,35]. Parametric maps of the [18F]FDG kinetic constants K_1^*, k_2^*, k_3^*, and k_4^* were determined by a voxel-by-voxel (voxel size= 0.4 mm x 0.4 mm x 0.8 mm) fitting of data to the two-tissue compartment kinetic model explained in section 2.3. A blood volume of V_B=0.03 was assumed.
Furhter, parametric maps of the cerebral metabolic rate of glucose (CMR_{glc}) and the extracellular glucose level are then calculated. CMR_{glc} is calculated as described in section 2.3 by taking into account the different efficiencies of [18F]FDG and glucose[35]:

$$CMR_{glc} = \frac{K_i^*}{0.38 + 1.1\frac{K_i^*}{K_1^*}} C_P. \tag{4.1}$$

The parameters L_1=1.48 and L_3/L_2=0.26 are already inserted here[35,39,40]. Note that this method is insensitive to changes of the lumped constant[35]. Cf.[35,195,155] The model is applied to the whole-body data of the mouse to calculate the metabolic rate (MR_{glc}) of peripheral tissues. An exemplary [18F]FDG uptake image and a parametric image of the whole-body metabolic rate is shown in Figure 4.4.

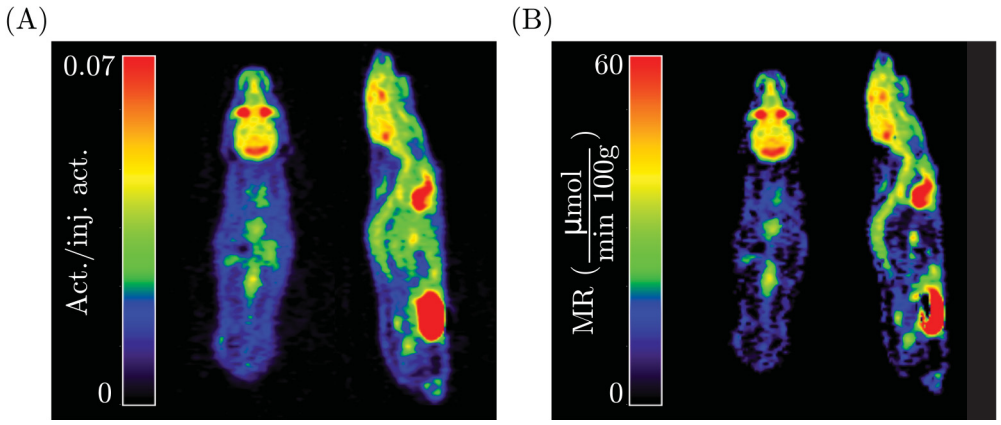

Figure 4.4: Exemplary [18F]FDG uptake data and parametric metabolic rate image. (A) Average [18F]FDG uptake between 25 and 45 min of the measurement of a exemplary mouse. The data is normalized to the whole-body activity averaged over the same time interval ("injected activity"). (B) Parametric image of the metabolic rate for the same mouse.

4.2.3 Segmentation of PET/CT Data

The segmentation of CT data into different tissues is a method to analyze body mass composition. Fatty tissues, lean tissue and bone tissue have linear attenuation coefficients and therefore different Hounsfield units (HU) (see Figure 4.5). To segment the data according to their HU, the CT scanner has to be calibrated accordingly.
For the data acquired within this thesis, the CT data was not well calibrated to Hounsfield units, since the CT was originally only used for attenuation correction and for this purpose no correct calibration was necessary. In Figure 4.6C the histograms of a CT scan of two phantoms, each containing air, oil, water and salt are shown. The phantoms were positioned on the mouse carrier used for all the PET/CT scans with which two mice are measured simultaneously in an upper and lower position. The histograms of the phantoms are shifted depending on the position in the FOV, e.g. the different peaks (oil, water, salt) are not at the same position.
To make the CT data comparable between measurements and independent of the position in the FOV, the CT data was histogrammed into bins of the different CT data units from the minimal to the maximal value (Figure 4.6C), then the minimal value was set to -1000 and the maximal peak was shifted to 0. This means that the attenuation is assumed to be similar for a certain material regardless of the position inside of the FOV. In this example oil is present in highest proportion, so that the

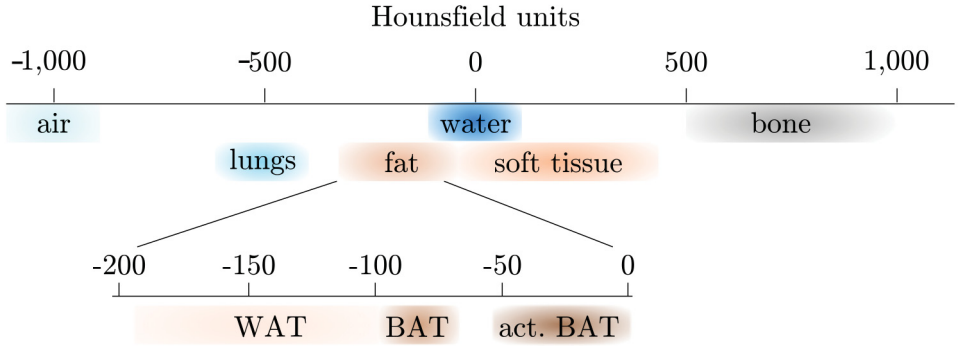

Figure 4.5: Hounsfield units. Hounsfield unit express X-ray attenuation as a measure of attenuation relative to air and water. Air is defined by a HU value of -1000 and water by 0. Different tissues have different X-ray attenuation and therefore different HU's.

oil peak will be shifted to zero (Figure 4.6D).
Usually the scanned object is a mouse and it can be assumed that the overall tissue composition of the body of the mouse is similar. The peak of the histogram is therefore expected to be at the same position of CT units. To obtain only the data of the mouse without the surrounding holder and air the [18F]FDG PET data was taken into account. A threshold was defined, so that only voxels with a uptake above this value are extracted, and which ideally are part of the mouse body. The threshold was found to provide good results for a value of 0.68·mean [18F]FDG activity in the image after 25-45 min (Figure 4.7). A mask of the mouse data was created by applying this threshold, which can then be used for the CT data as well. The peak of the CT histogram of the mouse data was then shifted according to the procedure applied to the phantom. By this method we obtain CT images, which are comparable among different measurements and are independent of the position of the animals inside of the FOV (Figure 4.8). Note, that to be able to analyze CT and PET data in combination the CT resolution was adjusted to the PET resolution and a gaussian filter of 1 mm was applied to the low resolution CT.
The corrected CT images can be used for segmentation of the data into contributions of different tissues in order to analyze the body composition of the mice. Within the obtained CT data distribution adipose tissue was determined to be in the range from -300 to -50 "corrected CT units", lean tissue from -50 to 300 "corrected CT units" and bone tissue above that, as visualized in Figure 4.9A. An exemplary image of the distribution of fat and lean mass in mice is shown in Figure 4.9B). The mass of the different tissues can be calculated as the product of the volume of tissue and the density of the respective tissue properties. For adipose tissue a density of 0.92 g/cm^3 [215], for lean tissue 1.06 g/cm^3 [216] and for bone 1.92 g/cm^3 [216] were used.
Combined PET and CT data were used to segment the data into 2D histograms showing the distribution of [18F]FDG uptake in relation to CT units and [18F]FDG

uptake values as displayed in Figure 4.10.

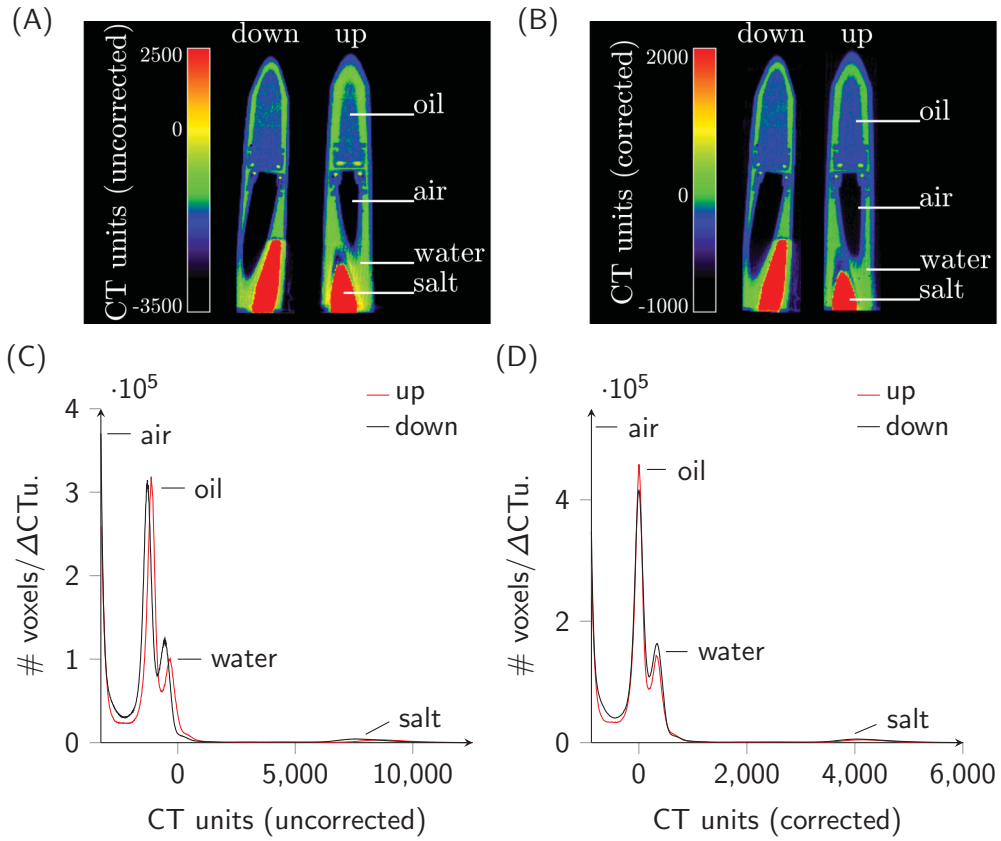

Figure 4.6: Correction for shifts in CT units in phantoms. (A) and (B) images of the phantoms before and after correction of the data with the corresponding color bar. (C) Distribution of CT units without correction for a phantom containing air, oil, water and salt. When the phantom is placed at different positions inside of the FOV the peaks of the different materials are shifted. (D) To correct for this the CT data were corrected so that the different materials have the same CT units.

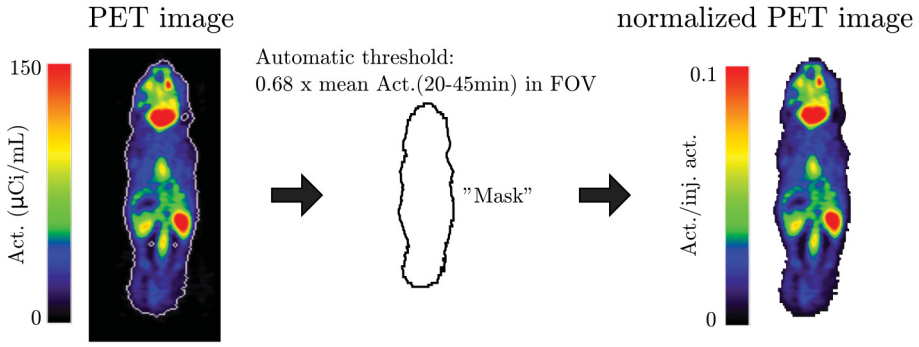

Figure 4.7: PET threshold for mouse data detection. The average [18F]FDG uptake image between 25 and 45 minutes was used to define a threshold to create a "mouse mask". A threshold of 0.68·mean activity in the FOV was found to provide good results. The "mouse mask" is applied to calculate the whole-body [18F]FDG activity for normalization of the data.

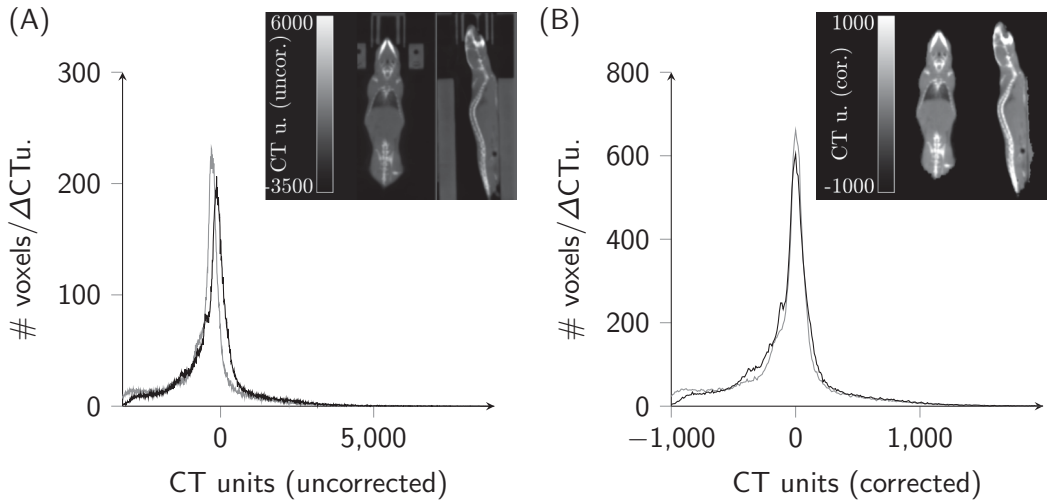

Figure 4.8: Correction for shifts in CT units in mouse data. (A) Distribution of CT units without correction for an exemplary mouse with the CT image shown in the inlay. In gray the data of a second mouse is shown, where the shift becomes visible. (B) Corrected CT unit distribution and CT image for the exemplary mouse as well as corrected CT unit distribution for the second mouse. Note, that here a PET threshold was used to extract only mouse tissue and therefore the holder is not included in the data.

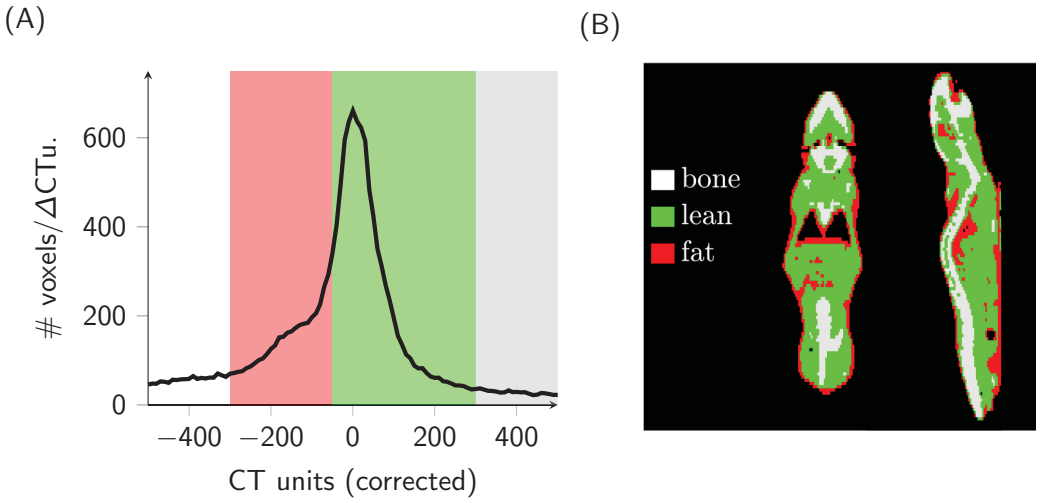

Figure 4.9: Tissue segmentation from CT mouse data. (A) Distribution of CT units for a exemplary mouse. The background indicates in red the range of CT units, which were assigned to be adipose tissue, in green the range of CT units of lean tissue and in gray the CT unit range of bones. (B) Exemplary image of mouse CT data segmented into lean, adipose and bone tissue.

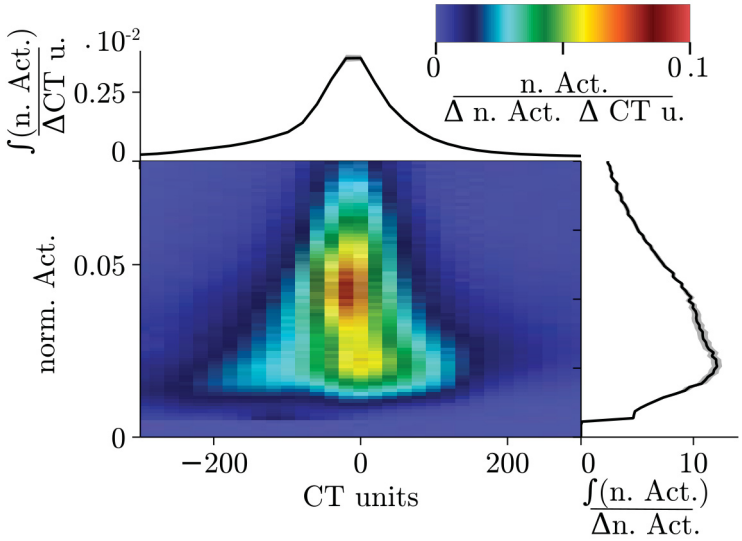

Figure 4.10: 2D histogramming of PET/CT data. 2D histogram of a exemplary cohort of mice (n=37, fasted): Normalized activity for the respective histogram bins (Δ norm. activity and Δ CT units) displayed in dependence of CT units and normalized activity. The data can be integrated along the respective axes to yield the distribution of [18F]FDG activity in dependence of CT units (top) or of the normalized activity (right).

4.3 Results

4.3.1 Tissue Segmentation

The data of different cohorts of mice was used to calculate body mass, lean tissue and fat mass from the CT data (n=40, male). Validating the method a strong linear correlation between measured body weight (BW) after the scan and the calculated body mass (BM) was found (Figure 4.11A, linear regression model in R, multiple R^2=0.999, p-value<$2.2e^{-16}$). Moreover the calculated lean body mass (LM) correlates – as expected – strongly with the body weight (Figure 4.11B, R^2=0.998, p-value<$2.2e^{-16}$). Furthermore a strong correlation between body weight and fat tissue mass (FM) was found (Figure 4.11C, R^2=0.989, p-value<$2.2e^{-16}$). Additionally, the calculated lean and fat mass correlate significantly (Figure 4.11D, R^2=0.981, p-value<$2.2e^{-16}$). Note, that the lean and fat tissue masses not necessarily correlate with body weight. If mice were, for example, fed with high fat diet (HFD) for a longer period, the body composition changes and can not be compared with lean animals. Furthermore, the results will presumably vary for female mice, as they usually have a lower total body weight despite having a similar percentage of fat content [217].
A further cohort of mice (n=14) was measured under control conditions and after 20 days of feeding with HFD. The histograms of the number of voxels over bins of CT units in Figure 4.12A clearly reveal an increase in the range of CT units defined as "adipose tissue" after HFD feeding compared to control conditions. Analyzing the tissue composition reveals a significant increase in fat mass (Figure 4.12B, $FM_{control}$=5.6±0.8 g vs. FM_{HFD}=10.4±2.6 g, p-value paired Student's t-test: $2.5e^{-6}$), while the lean mass is more or less preserved (Figure 4.12C, $LM_{control}$=13.1±3.1 g vs. LM_{HFD}=12.9±2.8 g, p-value paired Student's t-test: 0.69). An exemplary image of the tissue segmentation for a lean and a HFD fed mouse is shown in Figure 4.12D.
The cohort consisted out of n=7 female and n=7 male mice. Dividing the data into the two groups, female and male, reveals that male mice are – as expected – heavier in control conditions compared to the female mice ($BW_{ctrl,m}$=26.0±2.0 g vs. $BW_{ctrl,f}$=18.8±1.0 g, p-value Student's t-test: $5.2e^{-6}$) and while the male mice gain around 18 % body weight through the HFD feeding, the female mice gain ∼28 % ($BW_{hfd,m}$=30.6±2.8 g, $BW_{hfd,f}$=26.0±2.0 g vs, p-value Student's t-test: $1.4e^{-4}$). The fat mass in both groups increased around 87-88 % with HFD feeding and is not significantly different after HFD in male and female mice ($FM_{ctrl,m}$=6.1±0.6 g vs. $FM_{hfd,m}$=11.4±3.2 g, Student's t-test p-value: $3.9e^{-3}$, and $FM_{ctrl,f}$=5.0±0.4 g vs. $FM_{hfd,f}$= 9.4±1.3 g, Student's t-test p-value: $6.5e^{-5}$). The lean mass however remained unchanged in both groups ($LM_{ctrl,m}$=15.8±2.1 g vs. $LM_{hfd,m}$=15.1±2.2 g, p-value: n.s.; $LM_{ctrl,f}$=10.4±0.7 g vs. $LM_{hfd,f}$=10.8±1.1 g, p-value: n.s.) (Figure 4.13A+B).

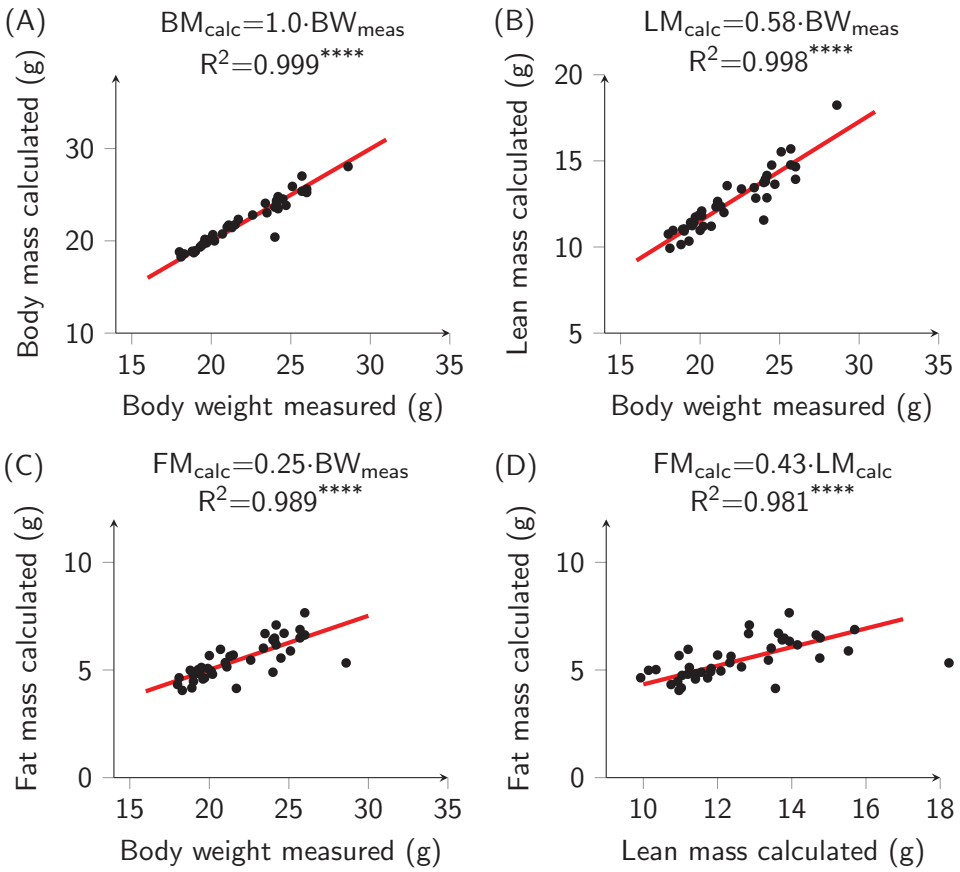

Figure 4.11: CT segmentation into lean and adipose tissue. (A) Correlation between body weight measured after the scan and the calculated body mass from the CT data for n=44 mice. (B) Correlation between body weight and lean tissue mass calculated from the CT data. (C) Correlation between body weight and calculated fat mass. (D) Correlation between calculated lean and fat mass. *: p-value≤0.05, **: p-value≤0.01, ***: p-value≤0.001 and ****: p-value≤0.0001.

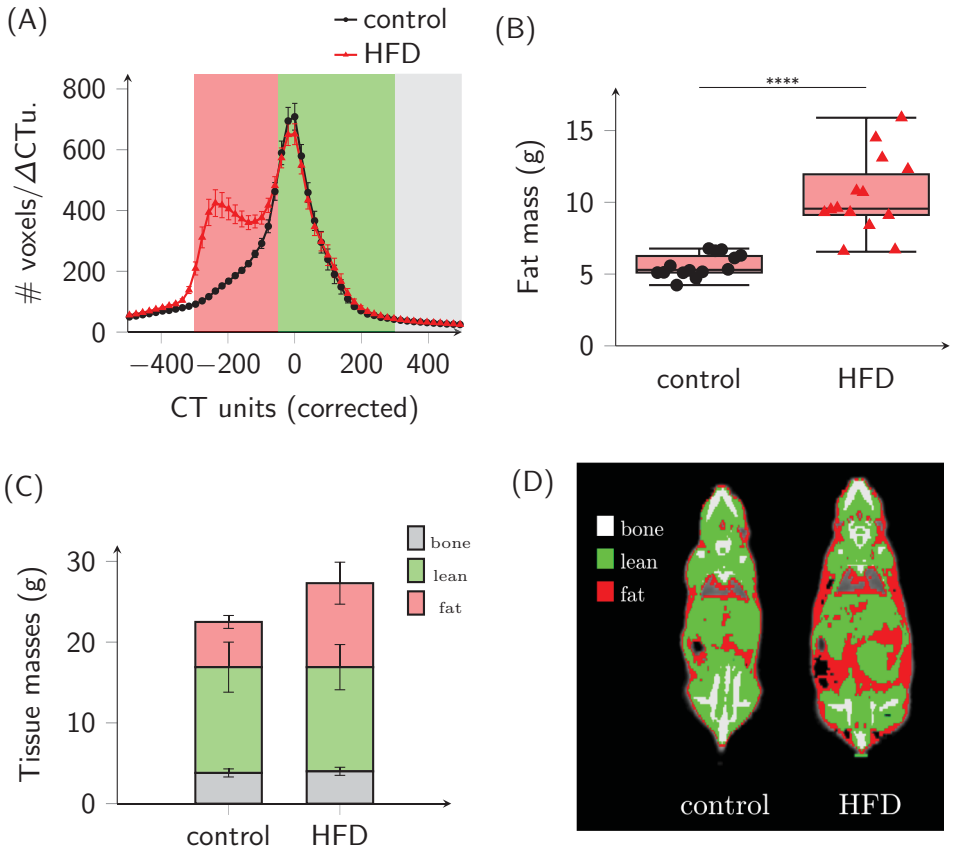

Figure 4.12: CT segmentation of high fat died fed mice. (A) Histogram of the CT data of control (black) and HFD fed (red) mice. The background in red indicates the CT unit range which was assigned to be adipose tissue, in green the CT unit range of lean tissue and in gray the CT unit range of bones. (B) Adipose tissue mass of the individual animals. (C) Average mean bone, lean and fat mass of the control and HFD fed mice. (D) Exemplary image of tissue distribution of one individual mouse before and after 20 days of feeding HFD.

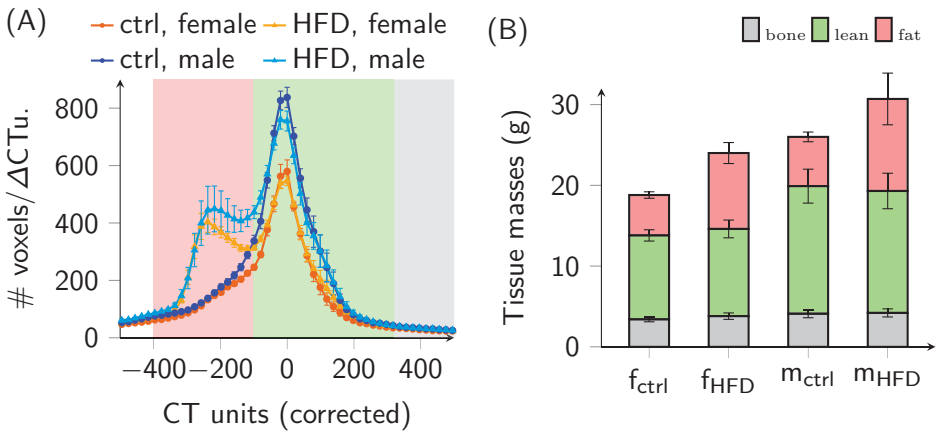

Figure 4.13: Female and male mice before and after high fat diet feeding. (A) Histogram of the CT data of female and male mice under control conditions and after 20 days of HFD. Dark orange: female mice under control conditions, orange: female mice after 20 days of HFD; blue: male mice under control conditions and cyan: male mice after 20 days of HFD. (B) Average mean bone, lean and fat mass of the female and male mice under control and HFD conditions. The values for the mean tissue masses are given within the text.

4.3.2 Glucose Consumption in Brown Adipose Tissue

The combined PET/CT data can be used to analyze [18F]FDG uptake and glucose consumption in brown adipose tissue. For the analysis of BAT, volume of interest (VOI) within around the shoulders were drawn containing the whole neck area of the mice. The common approach would be to analyze [18F]FDG uptake or the metabolic rate of glucose (MR_{glc}), in the case that kinetic modeling was applied, within that area as total [18F]FDG uptake in units of [nCi] or total metabolic rate in units of [μmol/min]. Here, the CT data was additionally used to segment the adipose tissue from other tissues in the neck area. In order to test this approach a cohort of n=12 mice was scanned three times: first without any intervention, a second time with presentation of the smell of normal chow diet (NCD) and a third time with presentation of the smell of HFD. The mice were fasted over night prior to each scan session. In Figure 4.14A the histograms of the metabolic rate (in μmol/min per ΔCT unit) over CT units of the neck area are displayed for all three groups. An increase in the metabolic rate is visible for the groups with presentation of food smell in the area from -300 to ~200 CT units. Analyzing the total metabolic rate in the neck area from the drawn VOI's reveals significant increases from the basal to the NCD and HFD group, as well as between the NCD and HFD groups: MR_{basal}=5.9±3.7 nmol/min, MR_{NCD}=9.7±5.3 nmol/min, MR_{HFD}=11.4±4.5 nmol/min (paired Student's t-test; MR_{basal} vs. MR_{NCD}: p-value=0.02, MR_{basal} vs. MR_{HFD}: p-value=0.002, MR_{NCD} vs. MR_{HFD}: p-value=0.01, Figure 4.14C).
Analyzing the area, which was classified as adipose tissue (CT units -300 to -50, displayed for one animal for each condition in Figure 4.14B) yields a significant increase from basal to the food smell stimulated groups, but the NCD and HFD stimulated groups are not significantly different anymore: MR_{basal}=2.9±2.3 nmol/min, MR_{NCD}=5.2±3.7 nmol/min, HFD 5.9±3.2 nmol/min (paired Student's t-test; MR_{basal} vs. MR_{NCD}: p-value=0.01, MR_{basal} vs. MR_{HFD}: p-value=0.005, MR_{NCD} vs. MR_{HFD}: p-value=0.15, Figure 4.14D).
On the image of the HFD group mouse in Figure 4.14B spillover of the PET data can be seen (red arrow), which indicates that analyzing PET data with thresholds from CT data might not adequate here in order to calculate the total metabolic rate in the BAT. Therefore, the analysis of the whole neck area is a better measure for the total metabolic rate of BAT. Care has to be taken if [18F]FDG uptake in skeletal muscle in the neck area is high, which is sometimes observed in other cohorts. In that case the total metabolic rate of the whole neck area does not reflect BAT activity, but also includes muscular glucose consumption and does therefore not only reflect the BAT activity in response to the stimulus.

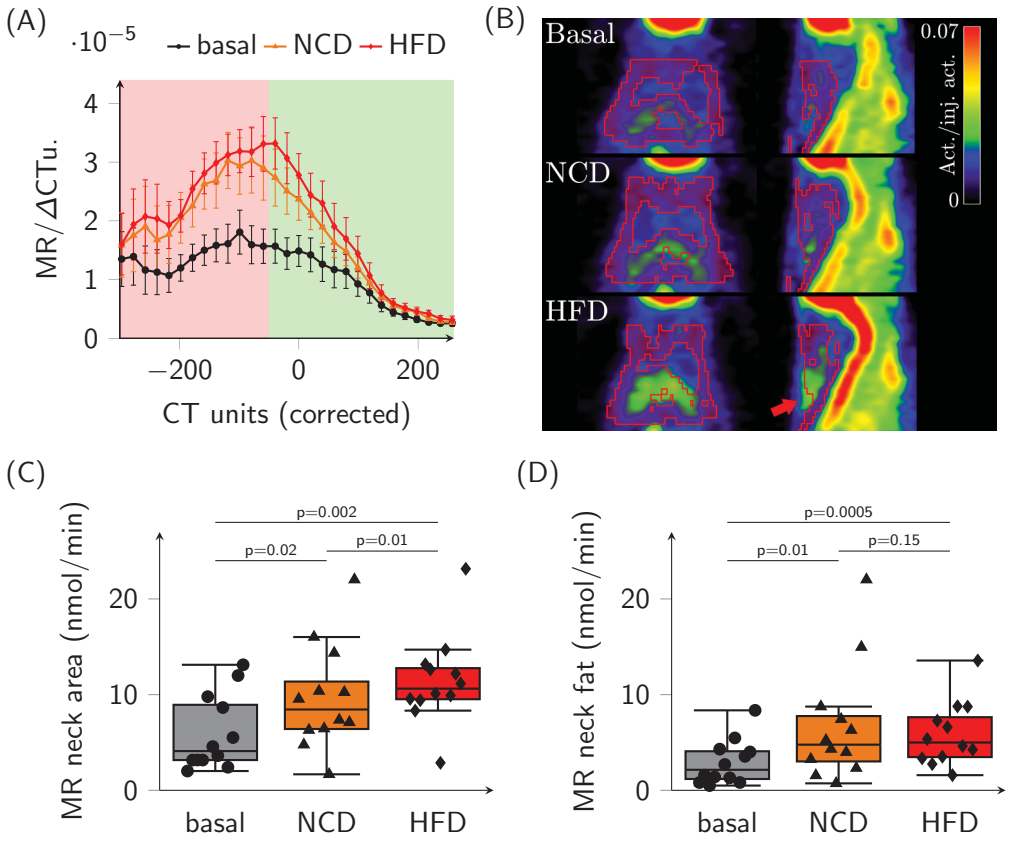

Figure 4.14: Metabolic rate of brown adipose tissue. (A) The histogram of the metabolic rate (μmol/min per ΔCT unit) as a function of CT units for a group measured under control conditions (basal, black) and two groups with presentation of food smell during the measurement (NCD, orange or HFD, red). (B) Images of one mouse of [18F]FDG uptake in the neck area for all three conditions, respectively. The adipose tissue (CT units between -300 and -50) is indicated in red. (C) Total metabolic rate in nmol/min of the whole neck area for each mouse and the three groups. (D) Total metabolic rate in nmol/min of the adipose tissue in the neck area for each mouse and the three groups.

4.3.3 Influence of the Nutritional State on [18F]FDG Distribution

As introduced before the glucose uptake and consumption in different tissues is highly dependent on blood glucose and insulin levels and therefore on the nutritional status of the subject.
Different cohorts of mice were analyzed under different conditions: A first group of mice was fasted overnight (∼16 hours) prior to the scan session (n=8). A second group of mice was as well fasted overnight, but together with the [18F]FDG glucose was intravenously injected (1 mg glucose/g (body weight), n=7). The third group of mice was randomly fed and received a sham injection of saline (i.p.) ∼10 minutes prior to the scan (n=7) . This cohort was measured a second time with injection of insulin (i.p., 0.75 I.U./kg body weight ≙ 31.5 mg/g (body weight)), again ∼10 minutes before the scan.
The blood glucose levels immediately after the scan for the different groups are displayed in Figure 4.15. As expected the fasted group shows the lowest blood glucose levels together with the insulin injected group. Injection of glucose in the fasted mice significantly increases the blood glucose levels (Glc_{fasted}=134±26 mg/dL vs. $Glc_{fasted+glucose}$= 320±125 mg/dL, p=0.0021). The randomly fed mice show a wide range of blood glucose levels (Glc_{fed}=411±118 mg/dL), and are significantly higher than in the fasted state (p=4.2e^{-5}), but not different from the fasted+glucose group (p=0.22). The distribution of blood glucose levels for the fed+insulin injected mice is also quite wide ($Glc_{fed+insulin}$=203±105 mg/dL), but the levels are significantly lower than without insulin injection (p_p=0.005). Note, that the fed and fed+insulin groups consists of the same mice and a paired testing is possible.
The PET/CT data was processed as described in the “Material and Methods” section. Note that calculating the glucose metabolic rate by kinetic modeling is based on the assumption of steady state conditions, i.e. constant blood glucose, constant tissue metabolism, etc. This condition is violated by the injection of glucose or insulin at the beginning of the scan. Therefore, only uptake or time courses of uptake can be analyzed in these conditions. The PET data was normalized to the average whole body activity in the image from minute 25 to 45 of the scan.
2D histograms of [18F]FDG distribution in dependence of normalized activity and CT units were calculated. The histograms for the four groups are displayed in Figure 4.16, indicating differences in [18F]FDG uptake for different states of the animals.
To analyze the differences the fasted vs. fasted+glucose cohort and the fed vs. fed+insulin cohort are compared in more detail.

Fasted vs. fasted+glucose group

To investigate in which tissues differences in [18F]FDG uptake between the groups take place, three “areas” (ranges of CT units and norm. activity values) were identified within the 2D histograms and further analyzed. These areas are visualized in Figure 4.17. By integrating the 2D histogram data along the respective axes, 1D histograms of [18F]FDG uptake over CT units or normalized [18F]FDG uptake units are provided. In these 1D histograms a different distribution of [18F]FDG can

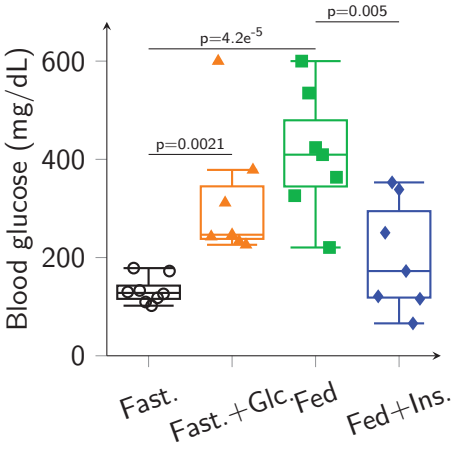

Figure 4.15: Blood glucose levels after the PET scan at different metabolic states. Blood glucose levels for a cohort of fasted mice (n=8), fasted mice which received a glucose injection with the start of the scan (n=7), randomly fed mice (n=7) and randomly fed mice with insulin injection before the scan (n=7). The average glucose levels are: Glc_{fasted}=134±26, $Glc_{fasted+glucose}$=320±125, Glc_{fed}=411±118 and $Glc_{fed+insulin}$=203±105. Note, that the cohort of fed and fed+insulin consists of the same mice.

be more clearly identified. For example, it can be detected that the peak of the normalized [18F]FDG activity is increased for the fasted+glucose group compared to the fasted group in the range from CT units between -70 and 20 (Figure 4.17 (top)). Moreover, also in the histogram over the normalized activity (right) variations in the distribution of [18F]FDG uptake between the two groups can be seen.
In the first analyzed area for normalized activities between 0.005 and 0.017 as well as CT units in the range from -300 and 100, an increase in [18F]FDG uptake in the fasted state is found compared to the fasted+glucose state (displayed in "pink" in Figure 4.17). From visualizing these ranges within the mouse images by creating masks between the thresholds, this area can be identified to most likely reflect skeletal muscle and lean tissue (Figure 4.17, right panel). A second analyzed area, normalized activity between 0.017 and 0.033 and CT units between -200 and 150 (displayed in "purple" in Figure 4.17), is identified by increased [18F]FDG uptake in response to glucose injection. The location of this area in the images indicates, that this could reflect uptake in adipose tissue, especially in visceral and subcutaneous fatty tissue. Even higher [18F]FDG uptake is found in the gastrointestinal tract and the organs for the fasted+glucose group (displayed in "turquoise" in Figure 4.17, normalized activity between 0.033 and 0.08 and CT units between -100 and 70). Summarizing, the glucose stimulus seams to lead to an increase in [18F]FDG uptake into the organs, the gastrointestinal tract and fatty tissues after fasting.
Different metabolic tissues were analyzed in more detail for the two groups: the heart, liver and neck area (BAT). The results are summarized in Figure 4.18.
To analyze [18F]FDG uptake in the heart a VOI was drawn around the whole

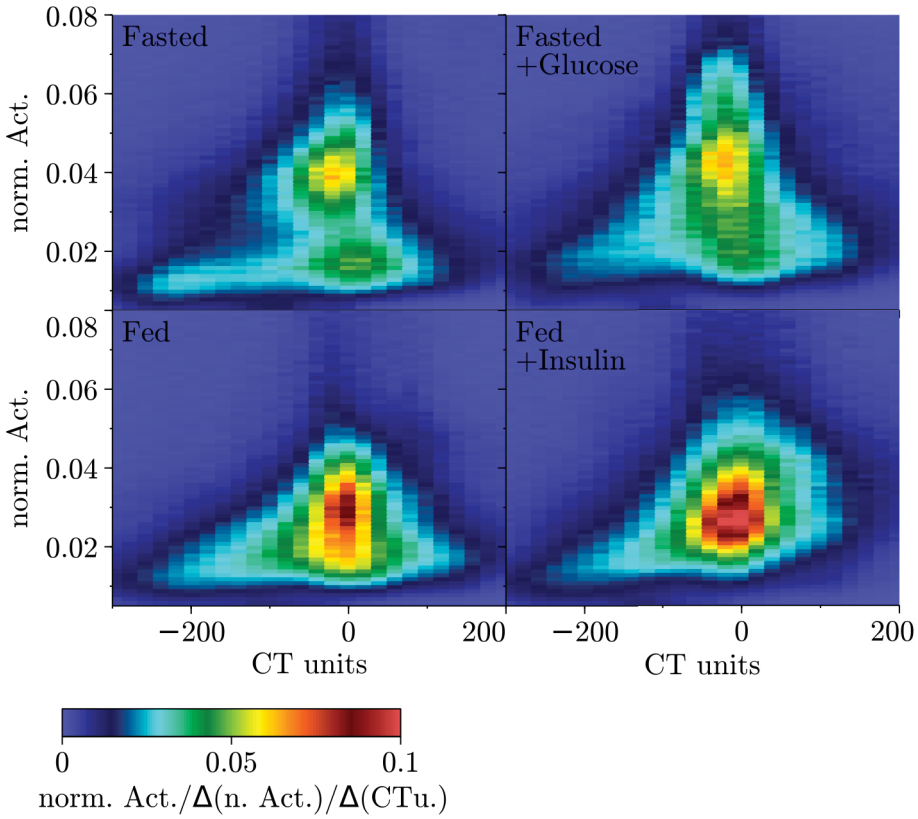

Figure 4.16: [18F]FDG uptake histograms at different metabolic states. 2D histograms of [18F]FDG uptake for the fasted, fasted+glucose, fed and fed+insulin groups. Clearly different distributions of [18F]FDG uptake is visible between all groups.

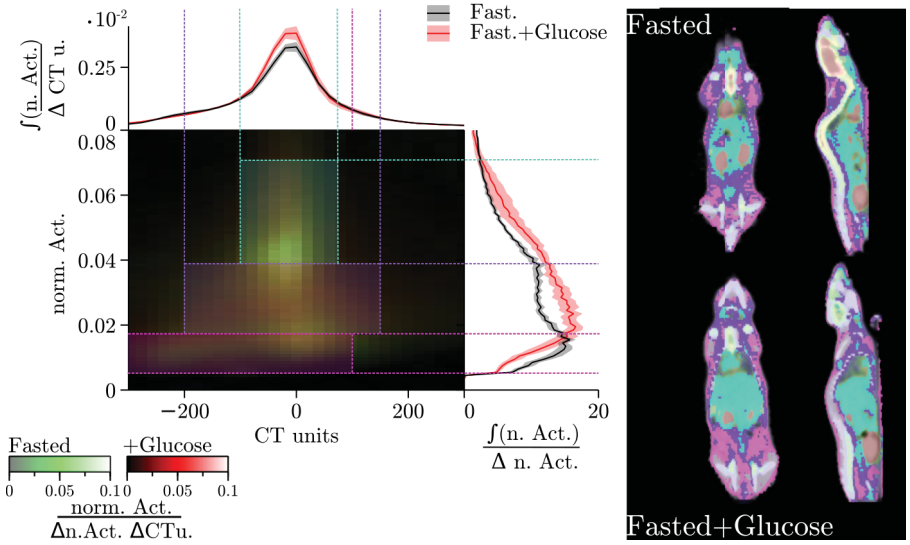

Figure 4.17: Difference in [18F]FDG uptake between the fasted and fasted+glucose group. Left panel: The 2D histograms for the fasted and fasted+glucose group are superimposed. By integrating the data from the 2D histogram along the axes provides 1D histograms of [18F]FDG uptake in dependence of the CT units (on top) and of the normalized [18F]FDG data (on the right). Three different areas were analyzed in more detail, in which differences in the 1D histograms are found: pink - CT units -300 to 100 and norm. Act. from 0.005 to 0.017; purple - CT units -200 to 150 and norm. Act. from 0.017 to 0.033; turquoise - CT units -100 to 70 and norm. Act. from 0.033 to 0.08. Right panel: The distribution of the different areas in two exemplary mice. The "pink" area seems to reflect muscular and lean tissue uptake, which is higher in the fasted state. The "purple" area most likely reflects visceral and further adipose tissues, while the "turquoise" area reflects uptake in the gastrointestinal tract.

organ and the total normalized activity within that area is analyzed. The kinetic of [18F]FDG uptake in the heart and the average activity between 25 to 45 minutes of the scan in the heart are different for the fasted and fasted+glucose state (Figure 4.18A+B). Note, that [18F]FDG uptake of two fasted mice seemed to be very high compared to the values of all other mice, so that they were excluded from the analysis (Student's t-test p-value:0.0038, mean total normalized activity in the heart for the fasted group: 0.036±0.01 and for the fasted+glucose group: 0.065±0.02). To analyze [18F]FDG uptake in the liver a small VOI was drawn at a representative part of the tissue and the mean [18F]FDG uptake was calculated. Significantly increased [18F]FDG uptake in the liver was found after glucose injection (mean average normalized activity in the liver for the fasted group: 0.038±0.003 and for the fasted+glucose group: 0.051±0.008, p-value=0.002; Figure 4.18C+D). For the neck area the histogram of [18F]FDG uptake over CT units was calculated. An increase in uptake in the fasted+glucose state is visible across a CT range from -200 to 150. The average total uptake in the neck area between 25 and 45 minutes of the PET scan is significantly increased (mean total normalized activity in the neck area for the fasted group: 0.018±0.005 and for the fasted+glucose group: 0.025±0.006, p-value=0.041).

Fed vs. fed+insulin group

For the fed and fed+insulin groups the same three areas within the 2D histograms are examined. In the fed state an increase in [18F]FDG uptake is found for normalized activity in the "pink" area compared to the fed+insulin state (normalized activity between 0.005 and 0.017 as well as CT units between 300 and 100; Figure 4.19). In the images this area is identified to most likely reflect skeletal muscle and lean tissue, but also parts of adipose tissue.

The second area ("purple", normalized activity between 0.017 and 0.033 and CT units between -200 and 150) shows increased [18F]FDG uptake in response to insulin injection. The location of this area in the images indicates, that this reflects increased uptake in the visceral adipose tissue and lean tissue as well as parts of the gastrointestinal tract. Even higher [18F]FDG uptake is located close to the organs like the heart, bladder and the kidneys, which are all tissues with high [18F]FDG uptake (displayed in "turquoise" in Figure 4.17, normalized activity between 0.033 and 0.08 and CT units between -100 and 70). Note, [18F]FDG activity in the kidney and bladder does not reflect glucose consumption, but extraction of [18F]FDG, since in the kidney glucose transporters (secondary glucose transporters) exist, which have a high affinity for [18F]FDG. All together, insulin injection leads to an increase in [18F]FDG uptake into the organs (gastrointestinal tract) and fatty tissues. A comparison of the results of the fed and fed+insulin group with the fasted and fasted+glucose groups indicates differences in [18F]FDG uptake in the organs and the gastrointestinal tract.

For the fed and fed+insulin group again the metabolic tissues heart, liver and neck area (BAT) are analyzed in more detail. The results are summarized in Figure 4.20. The kinetic of [18F]FDG uptake in the heart is different in the fed+insulin

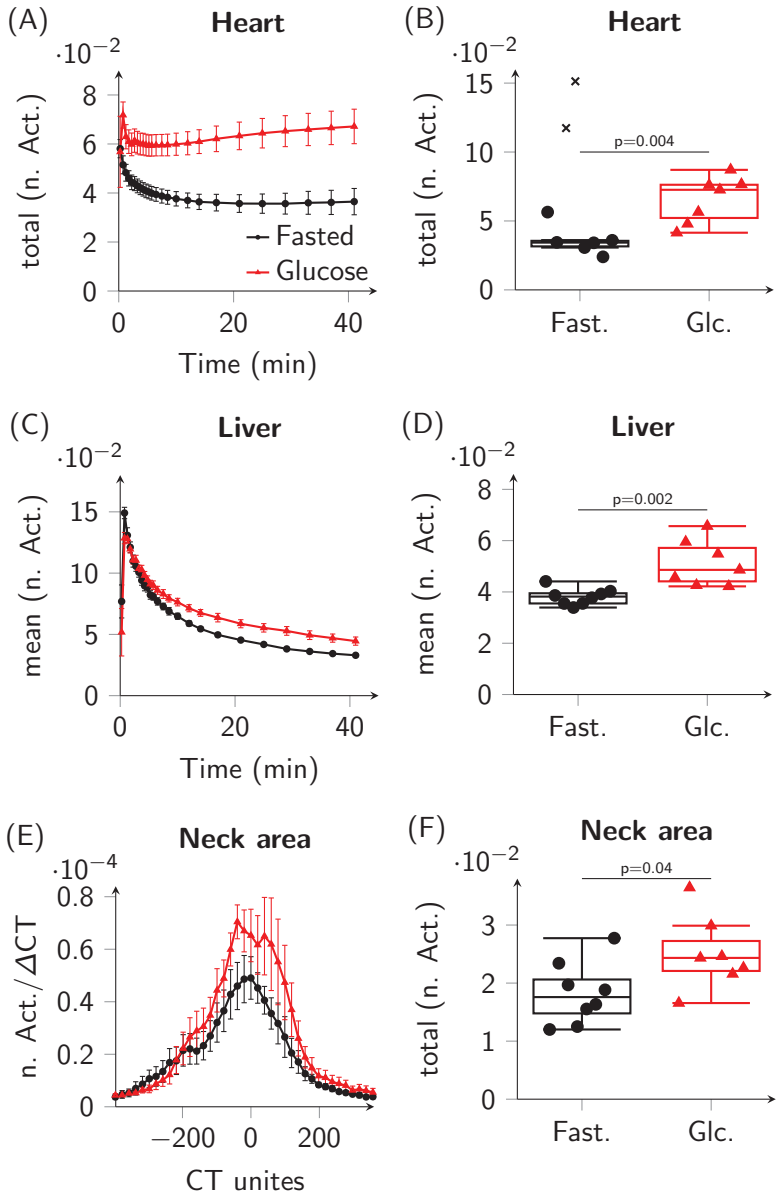

Figure 4.18: [18F]FDG uptake into metabolic tissues after glucose injection. (A) Total activity in the heart normalized to the injected activity over time for a fasted control cohort with two data sets excluded (n=6) and a fasted cohort with i.v. glucose injection (n=7). (B) Average total normalized activity in the heart from 25 to 45 min for control mice (n=8) and after glucose injection. (C) Mean normalized activity in the liver over time for control mice and glucose injected mice. (D) Average normalized activity in the liver from 25 to 45 min for control and glucose injected mice. (E) Histogram of normalized [18F]FDG over CT units in the neck area of the mice. (F) Average total normalized activity between 25 and 45 min in the neck area for both groups.

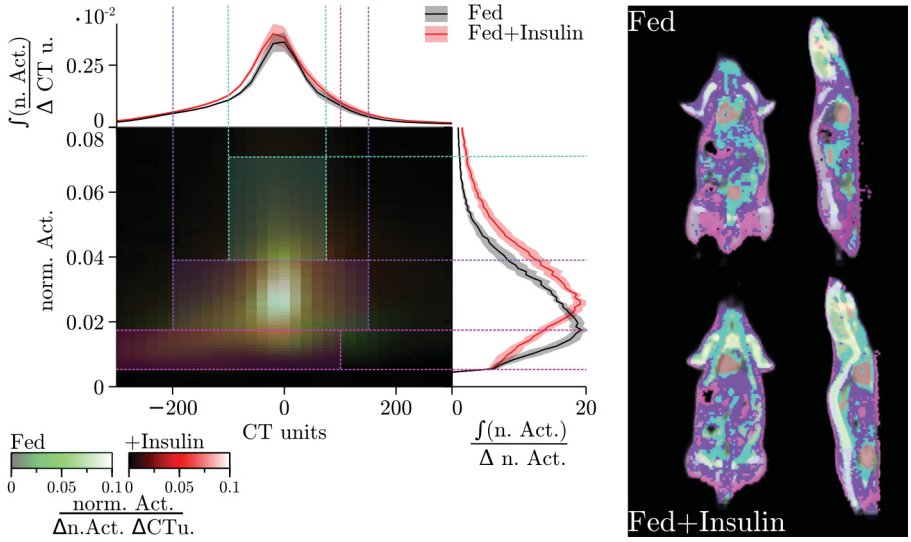

Figure 4.19: Difference in [18F]FDG uptake between the fed and fed+insulin group. Left panel: The 2D histograms for the fed and fed+insulin state are superimposed. Three different areas were analyzed in more detail: pink - CT units -300 to 100 and norm. Act. from 0.005 to 0.017; purple - CT units -200 to 150 and norm. Act. from 0.017 to 0.033; turquoise - CT units -100 to 70 and norm. Act. from 0.033 to 0.08. Right panel: The distribution of the different areas in two exemplary mice are displayed. The "pink" are seems to reflect muscular and lean tissue uptake. The "purple" area most likely reflects uptake in the gastrointestinal tract as well as adipose tissue. The "turquoise" area is rather diffusely located next to organs which are strongly supplied by blood, i.e. might not reflect a type of tissue.

state leading to an increased average activity between 25 and 45 minutes of the scan (Figure 4.18A+B: mean total normalized activity in the heart for the fed group: 0.054±0.033 and for the fed+insulin group: 0.083±0.018, p-value=0.01). Significantly decreased [18F]FDG uptake in the liver was found after insulin injection (mean average normalized activity in the liver for the fed group: 0.032±0.005 and for the fed+insulin group: 0.022±0.006, p-value=0.014; Figure 4.18D+E). For the neck area the histogram of [18F]FDG uptake over CT units was calculated, revealing an increase in the fed+insulin state across a range from -150 to 250. However, the average total uptake in the neck area between 25 and 45 minutes of the PET scan is not significantly increased (mean total normalized activity in the neck area for the fed group: 0.019±0.004 and for the fed+insulin group: 0.029±0.01, p-value=0.1).

Comparison between the four different states

To further compare the four different states, the dependences of [18F]FDG uptake in the different tissues (heart, liver and neck area) in correlation with blood glucose levels are shown in Figure 4.21A-C. The fasted group was excluded from the correlation calculations, since thee data form a singular group, i.e. the state of the mice cannot be compared to the "stimulated" (food, glucose, insulin) mice. The analysis shows a negative significant correlation between blood glucose levels and [18F]FDG uptake in the heart (R^2=0.65, p=9.3e^{-6}). This means that in the case that glucose is available from the blood and glucose uptake is stimulated (especially with insulin injection, but also by glucose injection or food) [18F]FDG and therefore also glucose is taken up into the heart (and most likely into further tissues) lowering the blood glucose levels leading to the negative correlation. In the fasted state this behavior cannot be observed and a relative steady [18F]FDG uptake into the heart and low blood glucose levels is found.
For [18F]FDG uptake in liver tissue the behavior is different: a positive correlation between blood glucose levels and the mean [18F]FDG activity is found. Since the liver is highly supplied with blood it is likely that a high fraction of [18F]FDG in the blood stream contributes to the signal and the data has to be taken with caution. The positive correlation could then indicate that in case of stimulation more [18F]FDG and glucose are taken up into different tissues leading to lower [18F]FDG and glucose levels in the blood. In the fasted state there is no relation between blood glucose level and liver [18F]FDG uptake.
The correlation between blood glucose levels and the [18F]FDG uptake in the neck area, i.e. BAT, is not significant, indicating that [18F]FDG uptake into BAT is not driven by blood glucose levels and is rather stimulated by different stimuli. This is also expected from literature. BAT is known to be activated by sympathetic activation and therefore for example cold, stress or anxiety lead to increased BAT activity. None of those conditions (temperature or experimental procedure, which might increase stress or anxiety) was varied, so that the more or less stable [18F]FDG uptake is reasonable. Only two animals of the insulin group displayed a rather high glucose uptake in the neck area, which could on the one hand be induced by

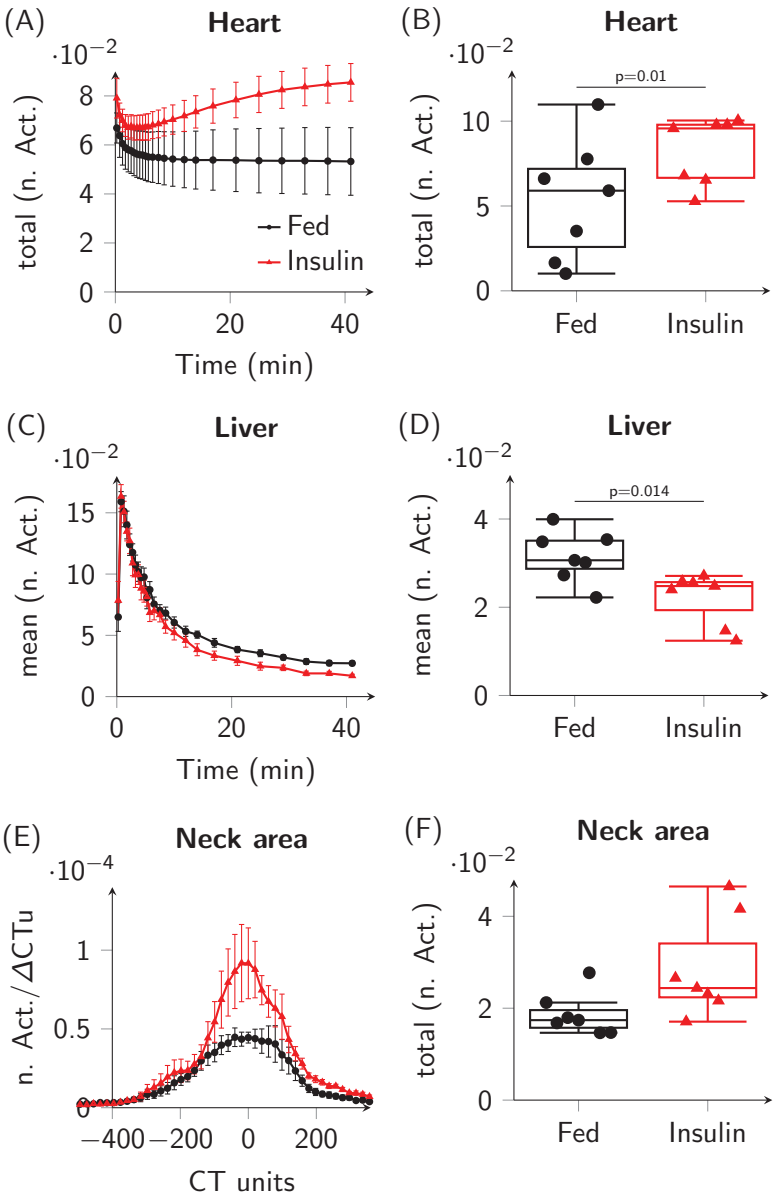

Figure 4.20: [18F]FDG uptake into metabolic tissues after insulin injection. (A) Total activity in the heart normalized to injected activity in the heart over time for a cohort of mice, n=7, after saline and insulin injection. (B) Average total normalized activity in the heart from 25 to 45 min after injection of saline or insulin. (C) Mean normalized activity in the liver over time after saline and insulin injection. (D) Average normalized activity in the liver from 25 to 45 min after injection of saline or insulin. (E) Histogram of [18F]FDG uptake over CT units in the neck area for the saline and insulin injected mice. (F) Average total normalized activity in the neck area from 25 to 45 min after injection of saline or insulin.

insulin, but could also indicate stress. Moreover, the increase between the fasted and fasted+glucose group is rather explainable by the different states the body is in and that in the fasted state no excess glucose is available to be "burned" in BAT.
Under the assumption that the brain is stably provided with glucose, i.e. glucose consumption in the brain is in any – physiological – condition reserved to be around 20 % of glucose derived energy, the correlation between [18F]FDG uptake in the brain in correlation to blood glucose levels is plotted in Figure 4.21D. It is foremost visible, that [18F]FDG brain uptake in the fasted group is higher compared to the other groups (average total normalized activity in the brain for the fasted group 0.032±0.003, p-value(fasted vs. stimulated groups)= $9.9e^{-14}$). This indicates that in the fasted state a large fraction of the available – relative to the whole body [18F]FDG activity – is taken up in the brain and therefore less excess glucose is available to be consumed in other tissues. The brain uptake in the other groups is as expected quite stable and not dependent on blood glucose levels (R^2=0.003 and p-value=0.82).
However, while [18F]FDG brain uptake normalized to whole body [18F]FDG activity is not different between the fed and fed+insulin state (average total norm. activity in the brain for the fed group 0.013±0.002 and for the fed+insulin group 0.012±0.001, p-value=0.49), it is increased in the fasted+glucose state (0.017±0.002, p-value(fed and fed+insulin vs fasted+glucose)=8.2^{-5}). Interestingly, a high correlation between mean liver [18F]FDG uptake and brain [18F]FDG uptake is found for the stimulated groups (R^2=0.95, p-value=$3.9e^{-14}$, Figure 4.21F).

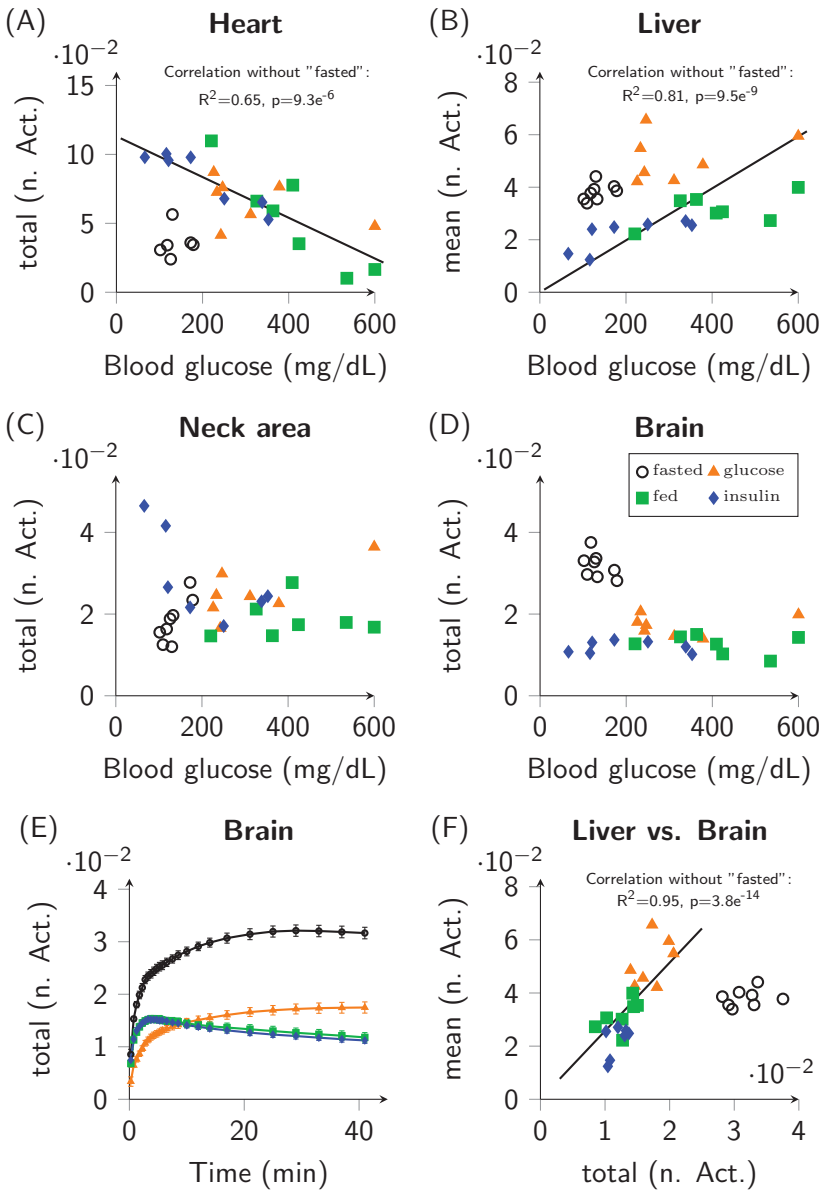

Figure 4.21: Dependence of [18F]FDG uptake from blood glucose levels and relation to [18F]FDG brain uptake. (A) Total normalized activity of the heart for the different groups of mice (fasted: black circles, fasted+glucose: orange triangles, fed: green squares, and fed+insulin:blue diamonds) in dependence of measured blood glucose levels. Note, that for the fasted group two values are exclude, see above. (B) Mean normalized activity in the liver for the different groups in dependence of blood glucose levels. (C) Total normalized activity of the neck area for the different groups in dependence of blood glucose levels. (D) Total normalized activity of the heart for the different groups in dependence of the total normalized activity of the brain. Note, that for the fasted group two values are exclude, see above. (E) Mean normalized activity of the liver for the different groups in dependence of the total normalized activity of the brain. (F) Total normalized activity of the neck area for the different groups in dependence of the total normalized activity of the brain.

4.4 Discussion

4.4.1 Tissue Segmentation

Tissue segmentation by the use of CT data is one technique that is used to analyze the body composition. Using CT relatively consistent tissue attenuation values within and among images are generated, which provide reliable and reproducible data [218]. Adipose tissue has a different X-ray attenuation compared to soft tissues (lean tissue) or bones and therefore those tissues can be discriminated from CT data. Adipose tissue can be quantified by the volume with CT values (usually Hounsfield units) in a certain range from the images and by taking the average fat density into account tissue weights can be determined.
Commonly used methods are either manual, semi-automatic or fully automatic segmentation approaches [218]. For manual segmentation adipose tissue is delineated by hand by the investigator, which is very time consuming and subjective [218]. Fully automatic methods are reported to be of low accuracy and therefore mostly semi-automatic methods are applied [218]. Threshold-based, semi-automatic, approaches are based on differences between HU for adipose and other tissues. Algorithms identify all voxels within the defined range of HU, which are assigned to be representative for the tissue to be analyzed [218]. Within most approaches the investigator has to manually control the results. Note that the chosen thresholds for tissue segmentation vary for different studies, but usually for adipose tissue HU values in the range from -30 to -300 HU are used. The choice of method depends on the image quality, the subjects and the needed accuracy [218]. For an estimate of whole body fat content an automatic threshold-based algorithm might provide reliable and robust results, without manual correction [218].
Within this thesis CT data – from the attenuation scan to correct the PET data – was used for segmentation of the data into contributions from adipose and lean tissue as well as bone mass using a threshold-based method. The thresholds were determined from analyzing histograms of different cohorts of mice and the resulting distribution of tissues on the images. Since the attenuation scan, even when transformed into HU, showed a quite high spatial dependency, we here normalized the CT data for each mouse by adjusting the peak in the CT histogram to zero and the minimum (air) to -1000. The CT units therefore do not reflect HU and thresholds from literature could not be applied. However, in published data the peak of a typical CT histogram of the body of a mouse is located at $\sim$60 HU [219], so that the corrected CT units used here can be related to HU values.
Robust results were found for the following thresholds: CT units in the range from -300 to -50 reflect adipose tissue, CT units in the range from -50 to 300 reflect lean (also called non-adipose or soft tissue) and higher units reflect bones. The method was validated by analyzing data of n=40 mice. The tissue mass was calculated by using average densities for the respective tissue types. The total calculated body weight was then compared to the body weight by weighing the animals on a commercial scale immediately after the CT scan. The correlation between the measured body

weight and the calculated body weight from the CT data was found to be very strong (R^2=0.999, p-value<2.2^{-16}), so that the body weight can be determined from the CT scan with a high confidence. Moreover the calculated lean mass significantly correlates with the body weight of the mice (R^2=0.998, p-value<2.2^{-16}). Note that within this analysis all mice were male animals and fed with normal chow diet. In average those mice consist of ∼58 % lean mass and ∼25 % fat mass, which is well in accordance with the values published in literature [217]. Moreover, a strong correlation of body weight and fat mass, as well of fat mass with lean mass was found for the analyzed cohort of mice.
The method introduced in this thesis provides reliable results. Therefore, within one scan session anatomical data, tissue segmentation and functional information can be obtained and correlated.

4.4.2 Glucose Consumption in Brown Adipose Tissue

[18F]FDG PET is from a historical point of view the standard technique to investigate brown adipose tissue. While BAT was long known to exist in infants and mammals and to play a role in heat production as well as energy expenditure, its metabolic role was (re-)discovered in humans by functional imaging ([18F]FDG PET) [220,221]. BAT became of high interest in the context of obesity research and its therapeutic potential by increasing energy expenditure. Due to very high [18F]FDG uptake in some humans it was thought to act as a "glucose sink", which could be used to get rid of excess energy [222].
[18F]FDG PET has been – and still is – useful to detect and analyze BAT. It was found that [18F]FDG BAT uptake is very sensitive to experimental and environmental factors like temperature, nutritional state, stress, anxiety or muscular activity. This might contribute to the large heterogeneity of [18F]FDG uptake reported in retrospective studies of human data, in which it was not controlled for experimental conditions like temperature, nutritional state and further factors [220,223,224,225].
To make future studies more comparable the NIH in 2016 introduced guidelines on reporting [18F]FDG PET studies, the "Brown Adipose Tissue Reporting Criteria in Imaging Studies". The expert panel recommends to use HU's between -190 and -10 and SUV's of 1.2/(lean body mass)/(body mass) to label BAT. Furthermore, reporting the body weight, height, BMI as wells as liver and aorta SUV for background activity is advised. Additionally, instructions for the preparation of the subject before the scan sessions are given, including fasting the subject for 6 h, no consumption of fatty meals for 24 h or caffeine for 48 h prior to the scan. More details and the full spectrum of the criteria can be found in the publication by Chen et al. 2016 [223].
Nevertheless, [18F]FDG PET allows to analyze different experimental and environmental factors, which influence BAT activity. BAT is metabolically active, very variable and activation is reported to be of advantage for body weight, glucose tolerance and insulin tolerance [226,225,220]. Therefore, BAT is subject of current research and the method introduced within this thesis can make a contribution to examine BAT *in vivo*.

A challenge using PET/CT imaging to analyze BAT is that BAT is typically distributed in narrow fascial layers among muscle groups, organs and bones, which makes it hard to delineate[227]. Additionally, PET and CT data need to be exactly co-registered for a combined analysis[227]. Moreover, the usually different resolutions of PET and CT data have to be taken into account. And last but not least, labeling BAT by normalized SUV's may not be appropriate[227].
For combined PET/CT scanners for rodents PET and CT images are co-registered automatically and there is no need for complex registration methods. Note that the resolution of CT images acquired within this thesis is higher than the maximal PET image resolution. To combine the data we scaled the CT image down to the resolution of the PET image and applied a 1 mm gaussian filter. This allows for a voxelwise combined analysis of the functional [18F]FDG and the anatomical CT data.
Within this thesis, data of the neck area of mice is analyzed. By calculating histograms of the metabolic rate in the neck area as a function of CT units, increases in MR_{glc} upon stimulation are clearly revealed. Moreover, the histograms provide the possibility to investigate, if in the volume of interest differences in glucose consumption are visible at certain CT units, i.e. in different tissues. In the neck area the only metabolically active tissue beside BAT is muscle tissue. Note that in general muscle activation should not play a role under anesthesia. However, contribution of muscular activity to the MR_{glc} in the neck area would be visible within the histogram – even though spillover and partial volume effects cause inaccuracies in the histogram. In Figure 4.22 an exemplary histogram of seven mice is shown, in which the metabolic rate peaks at CT units of approx. 40 and also the distribution of [18F]FDG uptake in the images is located around the shoulder bones of the mice, so that here the metabolic rate reflects rather glucose consumption in muscular tissue than in BAT. In the data analyzed within this thesis an increase of MR_{glc} across a broad range of CT units is observed after "stimulation", but the predominant part that is altered upon stimulation is within CT units assigned to be adipose tissue. Therefore, the analysis by the histogram does not only easily indicate, if changes in MR_{glc} occur within the neck area, but also verifies, if the changes occur within adipose tissue. Note that the histogram is obtained without delineation of BAT by hand, i.e. the volume of interest is just drawn across the whole neck area. Ranges in the histogram can be easily visualized in the image and vice versa.
All in all, analysis of glucose consumption using [18F]FDG PET and CT in mice can provide valuable information on BAT activity and can play a role in deciphering the regulation of BAT. The data can give indications if in a certain cohort, or due to a stimulus or treatment differences in glucose uptake occur, so that further investigations can be performed. That the method is very sensitive for the assessment of BAT activity is demonstrated by the data shown within this thesis, where significant differences in MR_{glc} in the neck area are found upon presentation of a food smell.
Most likely 1D and also 2D histograms provide even better results for human data. CT resolution and delineation of fatty tissue is better in human data and differences in HU for active and non-active brown fat as well as white adipose tissue were

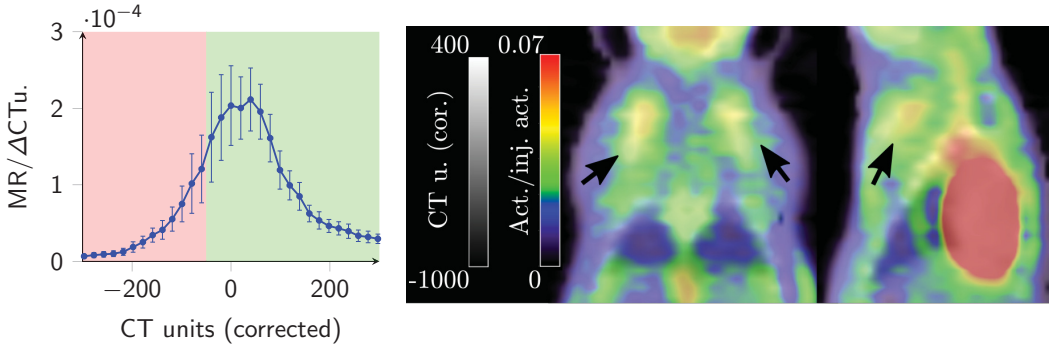

Figure 4.22: Histogram of the neck area MR_{glc}. Histogram of n=7 animals of the neck area for the MR_{glc} over CT units. The distribution and peak of MR_{glc} indicates that in this group rather muscular uptake instead of adipose tissue uptake is increased. The analysis of the images agrees with this finding.

reported[212]. So far for human data analysis most commonly SUVs are used, and often BAT is labeled according to its SUV. 1D and 2D histograms might extend the possibilities of a systematic examination of brown adipose tissue. Furthermore, with the introduction of whole-body human scanners it might soon be possible to acquire dynamic data to calculate the metabolic rate of different tissues for humans.

Simultaneous quantitative assessment of glucose metabolism in a whole group of mice allows for correlation analysis between regions. Correlations between regions can indicate connections between regions and can help to identify signaling pathways. In the group of mice analyzed within this thesis, apart from BAT, also certain well-defined brain regions were activated by the stimulus of food smell. One of the most obvious and expected regions is the olfactory bulb. Apart from BAT also certain well-defined brain regions were activated by the stimulus of food smell. One of the most obvious and expected regions is the olfactory bulb. The MR_{glc} in BAT can be correlated to the brain's CMR_{glc} in a voxel-wise manner. For the cohort with food smell stimulation a significant linear correlation between the CMR_{glc} in the olfactory bulb and the total MR_{glc} in the BAT is found (Figure 4.23, R^2=0.42, p-value=2.2e^{-5}). This combination of peripheral and CNS data reveal the power of whole-body PET scans, especially for animal research.

Recent scientific investigations show that BAT thermogenesis is not only or at least not necessarily directly linked to glucose uptake[222,220,221]. It is claimed that glucose is not the primary energy substrate for heat production in brown fat. Instead studies suggest that fatty acids derived from intracellular triglycerides are the substrate for thermogenesis[228].
Despite various different research studies, it is still not fully clarified what role exactly the increased glucose uptake in brown adipose tissue observed in a large number of studies plays. Nevertheless, glucose uptake is an important indicator for BAT

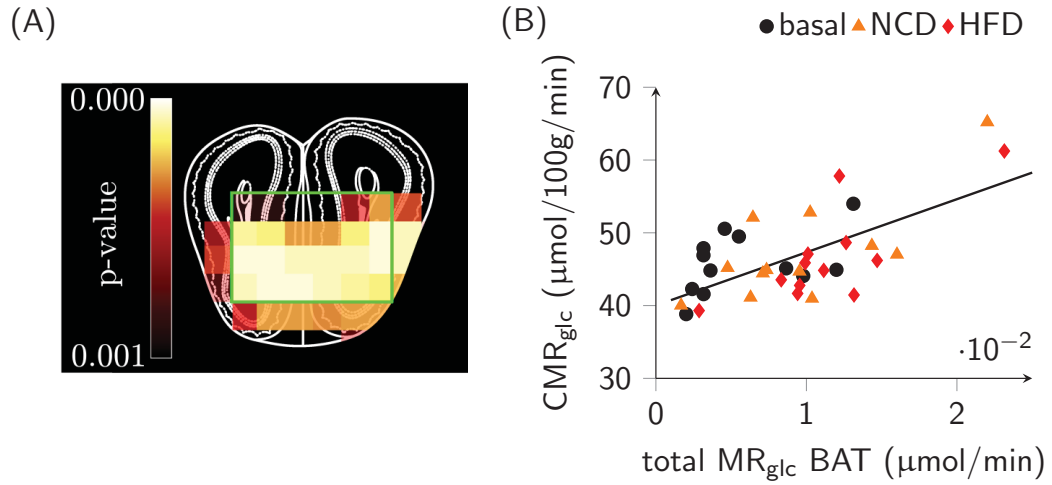

Figure 4.23: Correlation of the MR_{glc} of the neck area with the CMR_{glc} in the olfactory bulb. (A) Atlas image of the olfactory bulb with a voxel-wise map of significant p-values from the Pearson's product-moment correlation between the metabolic rate of the neck area and the CMR_{glc} in the brain. (B) Correlation of the CMR_{glc} of the VOI indicated in green on the image in (A) (olfactory bulb) with the total metabolic rate of the neck area of the mice.

thermogenesis[222]. That fact is underlined by statements in critical reviews, like "[...] quantitatively speaking glucose may only modestly contribute to fueling BAT thermogenesis compared to fatty acids, [but] it is nevertheless essential"[222] or that "a role in regulating glucose metabolism of BAT in adult humans is established"[229]. Therefore, [18F]FDG PET imaging can give insight into glucose metabolism in brown adipose tissue and its changes due to different interventions. Moreover, [18F]FDG data already revealed lots of important knowledge about brown fat metabolism like the inverse correlation of temperature with BAT activity. In conclusion, [18F]FDG PET is a good quantitative measure for BAT activity but – since BAT is presumably predominantly burning fat – it is not appropriate to estimate total heat production of the BAT.

Next to [18F]FDG PET further *in vivo* techniques are being used for functional BAT analysis. These techniques include PET/CT imaging with different radiotracers, e.g. [18F]-fluro-heptadonic acid ([18F]FTHA) or [11C]acetate, SPECT methods with appropriate tracers, MRI/MRS applications and infrared imaging. A graphical summary of those methods is displayed in Figure 4.24 taken from Richard et al., 2020[230].

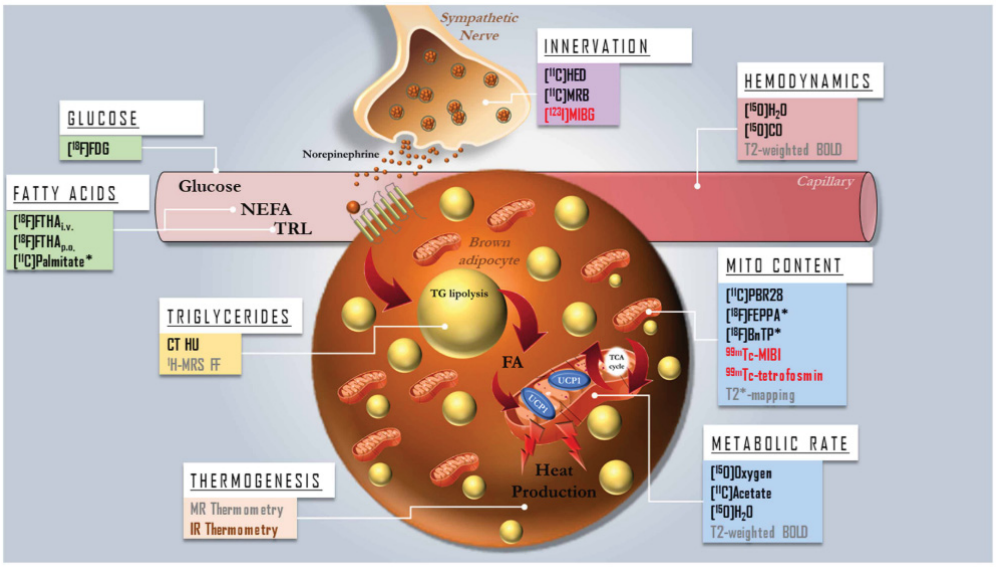

Figure 4.24: Non-invasive methods for *in vivo* assessment of human brown adipose tissue. Image taken from Richard et al. 2020 [230]. Words in black represent PET/CT methods, in red SPECT methods, in gray MRI/MRS methods and in brown infrared imaging. * indicates that the tracers not used in humans yet.

4.4.3 Influence of the Nutritional State on [18F]FDG Distribution

Data of mice under four different conditions were analyzed to analyze how the "nutritional state" or glucose and insulin challenges influence the [18F]FDG uptake in PET data in different tissues. The groups were either fasted or randomly fed animals, animals that received an injection of glucose or an injection of insulin. Due to the glucose and insulin stimuli the blood glucose cannot be assumed to be constant during the time of the measurement and kinetic modeling was not applied. Instead, temporal and spatial distribution of [18F]FDG within the whole mouse body was examined. 2D histograms of [18F]FDG activity over CT units reflecting the [18F]FDG uptake reveal different distributions of whole-body [18F]FDG uptake within the different groups of animals. To our knowledge this kind of 2D histograms for [18F]FDG and CT data were not shown before.
Within the 2D histograms three different ranges of CT units and normalized [18F]FDG activity values were identified, which were found to reflect different types of tissues like muscular and soft tissue, the inner organs and fatty tissue. All three ranges indicate differences in [18F]FDG uptake depending on the state of the animals, i.e. fasting, fed or glucose or insulin injected. To analyze the data in more detail [18F]FDG uptake in different organs was analyzed: the heart, liver, neck area (brown adipose tissue uptake), and the brain. Significantly different [18F]FDG uptake was found for the heart and liver for all four groups, while the uptake in brown adipose tissue (neck area) was only different between the fasted and fasted+glucose group (with a

trend to an increase between the fed and fed+insulin group). Excluding the fasted group a significant negative correlation between blood glucose levels and [18F]FDG uptake in the heart is found. This shows that stimulation of glucose metabolism by food intake, glucose or insulin injection leads to an increase of [18F]FDG uptake in the heart. The "stronger" the stimuli, i.e. the decrease in blood glucose, the higher the [18F]FDG uptake in the heart. Since the mice are anesthetized for the scan session skeletal muscle uptake cannot be analyzed. However, the heart can presumably serve as a muscle surrogate, i.e. [18F]FDG uptake in the heart might be used as indicator for skeleton muscle uptake. For liver [18F]FDG uptake a significant positive correlation with blood glucose was found (excluding the fasted group). Since the liver is supplied by blood from the hepatic artery and the portal vein, it contains larger blood compartments. This might explain the correlation between [18F]FDG uptake in the liver and blood glucose, i.e. that [18F]FDG in the liver to a large part reflects [18F]FDG in the blood stream. The [18F]FDG in the neck area, which was used as a surrogate for BAT glucose uptake, was not correlated to blood glucose levels. That underlines the sympathetic nature of BAT tissue. BAT uptake of glucose or other fuels (see discussion on glucose consumption in BAT) is not stimulated by the nutritional state, but by cold, stress or anxiety. Brain [18F]FDG uptake levels are relatively stable for the three "stimulated" groups, but is increased for the fasted animals. This can be explained by the whole-body normalization of [18F]FDG activity.

Taking together, these results show that [18F]FDG PET is a valuable tool for the *in vivo* assessment of nutritional state-dependent whole-body glucose distribution. Examination of gene-dependent modifications of these distributions in transgenic animals can help to decipher pivotal mechanisms in metabolic regulation.

4.5 Conclusion and Outlook

Combined analysis of [18F]FDG PET and CT data in mice provides a tool to obtain a large set of anatomical and physiological data *in vivo* within an individual animal in one scan session. CT data can be used to reliably calculate the body weight, fat and lean tissue mass. Moreover, the metabolic activity of brown adipose tissue can be analyzed. Histograms of the metabolic rate of glucose over CT units were found to be useful to discriminate between BAT and skeletal muscle uptake. Additionally, by the set of acquired data the glucose metabolism in different organs can be assessed. The co-registered brain data can be used for voxel-wise statistical comparison of the cerebral metabolic rate of glucose (CMR_{glc}) between groups of different mice or different treatments/interventions. Moreover, correlations of the CMR_{glc} with calculated tissue masses from the CT data or tissue/organ glucose metabolism in the periphery can be determined (see example in Figure 4.23). Taken together, combined [18F]FDG PET and CT data in rodents give a broad set of data of interest for metabolic research.

Procedures to analyze combined [18F]FDG PET and CT data from mice to automatically calculate the different data sets were introduced, applied and validated within this thesis. The procedures include calibration of the CT data and normalization of [18F]FDG PET data or application of kinetic modeling. Furthermore, CT data is segmented into contributions from adipose and lean tissue, the combination of PET and CT data is used to analyze glucose uptake in brown adipose tissue located in the neck of the mice and 2D histograms of whole-body data are investigated. By this the full potential of [18F]FDG PET and CT data is exploited.

With the introduction of the first whole-body PET scanners for humans, there is a need for methods and applications. The use of preclinical data, which is already available, can help in developing novel data analysis approaches as shown within this thesis.

Bibliography

[1] WHO — Controlling the global obesity epidemic, 2013. URL `https://www.who.int/topics/obesity/en/`.

[2] S. Jay Olshansky, Douglas J. Passaro, Ronald C. Hershow, Jennifer Layden, Bruce A. Carnes, Jacob Brody, Leonard Hayflick, Robert N. Butler, David B. Allison, and David S. Ludwig. A potential decline in life expectancy in the United States in the 21st century. *New England Journal of Medicine*, 352(11): 1138–1145, mar 2005. ISSN 00284793. doi: 10.1056/NEJMsr043743.

[3] Parul Singla. Metabolic effects of obesity: A review. *World Journal of Diabetes*, 1(3):76, 2010. ISSN 1948-9358. doi: 10.4239/wjd.v1.i3.76.

[4] Katharina Timper and Jens C. Brüning. Hypothalamic circuits regulating appetite and energy homeostasis: pathways to obesity. *Disease Models & Mechanisms*, 10(6):679–689, jun 2017. ISSN 1754-8403. doi: 10.1242/dmm.026609.

[5] Richard D. Palmiter. Is dopamine a physiologically relevant mediator of feeding behavior? *Trends in Neurosciences*, 30(8):375–381, 2007. ISSN 01662236. doi: 10.1016/j.tins.2007.06.004.

[6] Zane B. Andrews and Tamas L. Horvath. Tasteless Food Reward. *Neuron*, 57 (6):806–808, mar 2008. ISSN 08966273. doi: 10.1016/j.neuron.2008.03.004.

[7] Ramsey D. Badawi, Hongcheng Shi, Pengcheng Hu, Shuguang Chen, Tianyi Xu, Patricia M. Price, Yu Ding, Benjamin A. Spencer, Lorenzo Nardo, Weiping Liu, Jun Bao, Terry Jones, Hongdi Li, and Simon R. Cherry. First human imaging studies with the explorer total-body PET scanner. *Journal of Nuclear Medicine*, 60(3):299–303, 2019. ISSN 2159662X. doi: 10.2967/jnumed.119.226498.

[8] UC Davis. Total-body PET Scanner. URL `www.explorer.ucdavis.edu`.

[9] Jason S. Lewis and Kayvan R. Keshari. *Imaging and metabolism*. 2017. ISBN 9783319614014. doi: 10.1007/978-3-319-61401-4.

[10] Gopal B Saha. *Basics of PET Imaging*, volume 202. Springer New York, New York, NY, 2010. ISBN 978-1-4419-0804-9. doi: 10.1007/978-1-4419-0805-6.

[11] Michael E. Phelps. *PET*. Springer New York, New York, NY, 2004. ISBN 978-1-4419-2332-5. doi: 10.1007/978-0-387-22529-6.

[12] Luc Zimmer and André Luxen. PET radiotracers for molecular imaging in the brain: Past, present and future. *NeuroImage*, 61(2):363–370, jun 2012. ISSN 10538119. doi: 10.1016/j.neuroimage.2011.12.037.

[13] Kerstin Heurling, Antoine Leuzy, My Jonasson, Andreas Frick, Eduardo R. Zimmer, Agneta Nordberg, and Mark Lubberink. Quantitative positron emission tomography in brain research. *Brain Research*, 1670:220–234, sep 2017. ISSN 00068993. doi: 10.1016/j.brainres.2017.06.022.

[14] Klaus Wienhard, Rainer Wagner, and Wolf-Dieter Heiss. *PET - Grundlagen und Anwendungen der Positronen-Emissions-Tomographie*. Springer-Verlag Berlin Heidelberg, 1989. ISBN 3-540-19451-7.

[15] Michael E. Phelps. Positron emission tomography provides molecular imaging of biological processes. *Proceedings of the National Academy of Sciences of the United States of America*, 97(16):9226–9233, 2000. ISSN 00278424. doi: 10.1073/pnas.97.16.9226.

[16] Arion F. Chatziioannou. Molecular imaging of small animals with dedicated PET tomographs. *European Journal of Nuclear Medicine*, 29(1):98–114, 2002. ISSN 03406997. doi: 10.1007/s00259-001-0683-3.

[17] Fabian Kiessling and Bernd J. Pichler. *Small animal imaging: Basics and practical guide*, volume 66. Springer Berlin Heidelberg, Berlin, Heidelberg, 2011. ISBN 9783642129445. doi: 10.1007/978-3-642-12945-2.

[18] Craig S. Levin and Edward J. Hoffman. Calculation of positron range and its effect on the fundamental limit of positron emission tomography system spatial resolution. *Physics in Medicine and Biology*, 44(3):781–799, 1999. ISSN 00319155. doi: 10.1088/0031-9155/44/3/019.

[19] Jasna Mihailovic, Stanley J. Goldsmith, and Ronan P. Killeen. *FDG PET/CT in Clinical Oncology*, volume 1. Springer Berlin Heidelberg, Berlin, Heidelberg, nov 2012. ISBN 978-3-642-29865-3. doi: 10.1007/978-3-642-29866-0.

[20] Sophie Lancelot and Luc Zimmer. Small-animal positron emission tomography as a tool for neuropharmacology. *Trends in Pharmacological Sciences*, 31(9): 411–417, sep 2010. ISSN 01656147. doi: 10.1016/j.tips.2010.06.002.

[21] Lars Farde, Hakan Hall, Erling Ehrin, and Göran Sedvall. Quantitative analysis of D2 dopamine receptor binding in the living human brain by PET. *Science*, 231(4735):258–261, jan 1986. ISSN 0036-8075. doi: 10.1126/science.2867601.

[22] Anna Lena Nordström, Lars Farde, Frits Axel Wiesel, Kaj Forslund, Stefan Pauli, Christer Halldin, and Gunilla Uppfeldt. Central D2-dopamine receptor occupancy in relation to antipsychotic drug effects: A double-blind PET study of schizophrenic patients. *Biological Psychiatry*, 33(4):227–235, 1993. ISSN 00063223. doi: 10.1016/0006-3223(93)90288-O.

[23] A. Breier, T. P. Su, R. Saunders, R. E. Carson, B. S. Kolachana, A. De Bartolomeis, D. R. Weinberger, N. Weisenfeld, A. K. Malhotra, W. C. Eckelman, and D. Pickar. Schizophrenia is associated with elevated amphetamine-induced synaptic dopamine concentrations: Evidence from a novel positron emission tomography method. *Proceedings of the National Academy of Sciences of the United States of America*, 94(6):2569–2574, 1997. ISSN 00278424. doi: 10.1073/pnas.94.6.2569.

[24] Shitij Kapur, Robert Zipursky, Corey Jones, Gary Remington, and Sylvain Houle. Relationship between dopamine D2 occupancy, clinical response, and side effects: A double-blind PET study of first-episode schizophrenia. *American Journal of Psychiatry*, 157(4):514–520, 2000. ISSN 0002953X. doi: 10.1176/appi.ajp.157.4.514.

[25] Martin S. Judenhofer, Hans F. Wehrl, Danny F. Newport, Ciprian Catana, Stefan B. Siegel, Markus Becker, Axel Thielscher, Manfred Kneilling, Matthias P. Lichy, Martin Eichner, Karin Klingel, Gerald Reischl, Stefan Widmaier, Martin Röcken, Robert E. Nutt, Hans Jürgen Machulla, Kamil Uludag, Simon R. Cherry, Claus D. Claussen, and Bernd J. Pichler. Simultaneous PET-MRI: A new approach for functional and morphological imaging. *Nature Medicine*, 14 (4):459–465, 2008. ISSN 10788956. doi: 10.1038/nm1700.

[26] P. Werner, H. Barthel, A. Drzezga, and O. Sabri. Current status and future role of brain PET/MRI in clinical and research settings, 2015. ISSN 16197089.

[27] Simon R. Cherry and Sanjiv S. Gambhir. Use of positron emission tomography in animal research. *ILAR Journal*, 42(3):219–232, 2001. ISSN 10842020. doi: 10.1093/ilar.42.3.219.

[28] Richard E Carson. Tracer Kinetic Modeling in PET. In Dale L Bailey, David W Townsend, Peter E Valk, and Michael N Maisey, editors, *Positron Emission Tomography: Basic Sciences*, pages 127–159. Springer London, London, 2005. ISBN 978-1-84628-007-8. doi: 10.1007/1-84628-007-9_6.

[29] Mark A. Mintun, Marcus E. Raichle, Michael R. Kilbourn, G. Frederick Wooten, and Michael J. Welch. A quantitative model for the in vivo assessment of drug binding sites with positron emission tomography. *Annals of Neurology*, 15(3): 217–227, 1984. ISSN 15318249. doi: 10.1002/ana.410150302.

[30] L. Sokoloff, M. Reivich, C. Kennedy, M. H. Des Rosiers, C. S. Patlak, K. D. Pettigrew, O. Sakurada, and M. Shinohara. THE [14 C]DEOXYGLUCOSE METHOD FOR THE MEASUREMENT OF LOCAL CEREBRAL GLUCOSE UTILIZATION: THEORY, PROCEDURE, AND NORMAL VALUES IN THE CONSCIOUS AND ANESTHETIZED ALBINO RAT. *Journal of Neurochemistry*, 28(5):897–916, may 1977. ISSN 0022-3042. doi: 10.1111/j.1471-4159.1977.tb10649.x.

[31] M. E. Phelps, S. C. Huang, E. J. Hoffman, C. Selin, L. Sokoloff, and D. E. Kuhl. Tomographic measurement of local cerebral glucose metabolic rate in humans with (F-18)2-fluoro-2-deoxy-D-glucose: Validation of method. *Annals of Neurology*, 6(5):371–388, 1979. ISSN 15318249. doi: 10.1002/ana.410060502.

[32] S. S. Kety. The theory and applications of the exchange of inert gas at the lungs. *Pharmacological reviews*, 3(1):1–41, 1951. ISSN 00316997.

[33] Evan D. Morris, Christopher J Endres, Kathleen C. Schmidt, Bradley T. Christian, Raymond F. Muzic Jr., and Ronald E. Fisher. Kinetic Modeling in Positron Emission Tomography. In *Emission Tomography*, volume 46, pages 499–540. Elsevier, 2004. ISBN 9780080521879. doi: 10.1016/B978-012744482-6.50026-0.

[34] M Reivich, D E Kuhl, A Wolf, J Greenberg, M Phelps, T Ido, V Casella, E Hoffman, A Alavi, and L Sokoloff. The 18F fluorodeoxyglucose method for the measurement of local cerebral glucose metabolism in man. *Circ*, 44: 127–137, 1979.

[35] H. Backes, M. Walberer, H. Endepols, B. Neumaier, R. Graf, K. Wienhard, and G. Mies. Whiskers Area as Extracerebral Reference Tissue for Quantification of Rat Brain Metabolism Using 18F-FDG PET: Application to Focal Cerebral Ischemia. *Journal of Nuclear Medicine*, 52(8):1252–1260, 2011. ISSN 0161-5505. doi: 10.2967/jnumed.110.085266.

[36] Klaus Wienhard. Measurement of glucose consumption using [18F]fluorodeoxyglucose. *Methods*, 27(3):218–225, jul 2002. ISSN 10462023. doi: 10.1016/S1046-2023(02)00077-4.

[37] Philipp Mergenthaler, Ute Lindauer, Gerald A. Dienel, and Andreas Meisel. Sugar for the brain: the role of glucose in physiological and pathological brain function. *Trends in Neurosciences*, 36(10):587–597, oct 2013. ISSN 01662236. doi: 10.1016/j.tins.2013.07.001.

[38] Michael M. Graham, Mark Muzi, Alexander M. Spence, Finbarr O'Sullivan, Thomas K. Lewellen, Jeanne M. Link, and Kenneth A. Krohn. The FDG lumped constant in normal human brain. *Journal of Nuclear Medicine*, 43(9): 1157–1166, 2002. ISSN 01615505.

[39] Steen G. Hasselbalch, Gitte M. Knudsen, Søren Holm, L. Pinborg Hageman, Brunella Capaldo, and Olaf B. Paulson. Transport of D-glucose and 2-fluorodeoxyglucose across the blood-brain barrier in humans. *Journal of Cerebral Blood Flow and Metabolism*, 16(4):659–666, 1996. ISSN 0271678X. doi: 10.1097/00004647-199607000-00017.

[40] Steen G. Hasselbalch, Peter L. Madsen, Gitte M. Knudsen, Søren Holm, and Olaf B. Paulson. Calculation of the FDG lumped constant by simultaneous

measurements of global glucose and FDG metabolism in humans. *Journal of Cerebral Blood Flow and Metabolism*, 18(2):154–160, 1998. ISSN 0271678X. doi: 10.1097/00004647-199802000-00005.

[41] Vincent J. Cunningham and Jill E. Cremer. A method for the simultaneous estimation of regional rates of glucose influx and phosphorylation in rat brain using radiolabeled 2-deoxyglucose. *Brain Research*, 221(2):319–330, 1981. ISSN 00068993. doi: 10.1016/0006-8993(81)90781-2.

[42] Marie Claude Asselin, Vincent J. Cunningham, Shigeko Amano, Roger N. Gunn, and Claude Nahmias. Parametrically defined cerebral blood vessels as non-invasive blood input functions for brain PET studies. *Physics in Medicine and Biology*, 49(6):1033–1054, 2004. ISSN 00319155. doi: 10.1088/0031-9155/49/6/013.

[43] Paolo Zanotti-Fregonara, Kewei Chen, Jeih San Liow, Masahiro Fujita, and Robert B. Innis. Image-derived input function for brain PET studies: Many challenges and few opportunities. *Journal of Cerebral Blood Flow and Metabolism*, 31(10):1986–1998, 2011. ISSN 0271678X. doi: 10.1038/jcbfm.2011.107.

[44] Anders N. Christensen, Michala H. Reichkendler, Rasmus Larsen, Pernille Auerbach, Liselotte Højgaard, Henning B. Nielsen, Thorkil Ploug, Bente Stallknecht, and Søren Holm. Calibrated image-derived input functions for the determination of the metabolic uptake rate of glucose with [18F]-FDG PET. *Nuclear Medicine Communications*, 35(4):353–361, apr 2014. ISSN 0143-3636. doi: 10.1097/MNM.0000000000000063.

[45] Jean Logan. Graphical analysis of PET data applied to reversible and irreversible tracers. *Nuclear Medicine and Biology*, 27(7):661–670, oct 2000. ISSN 09698051. doi: 10.1016/S0969-8051(00)00137-2.

[46] C. S. Patlak, R. G. Blasberg, and J. D. Fenstermacher. Graphical evaluation of blood-to-brain transfer constants from multiple-time uptake data. *Journal of Cerebral Blood Flow and Metabolism*, 3(1):1–7, 1983. ISSN 0271678X. doi: 10.1038/jcbfm.1983.1.

[47] Jean Logan, Joanna S. Fowler, Nora D. Volkow, Alfred P. Wolf, Stephen L. Dewey, David J. Schlyer, Robert R. MacGregor, Robert Hitzemann, Bernard Bendriem, S. John Gatley, and David R. Christman. Graphical Analysis of Reversible Radioligand Binding from Time—Activity Measurements Applied to [N - 11 C-Methyl]-(-)-Cocaine PET Studies in Human Subjects. *Journal of Cerebral Blood Flow & Metabolism*, 10(5):740–747, sep 1990. ISSN 0271-678X. doi: 10.1038/jcbfm.1990.127.

[48] Vesa Oikonen. Turku PET Centre. URL `http://www.turkupetcentre.net/petanalysis/`.

[49] Lammertsma AA and Hume SP. Simplified reference tissue model for PET receptor studies. *Neuroimage*, 4(4):153–158, 1996.

[50] V. J. Cunningham, S. P. Hume, G. R. Price, R. G. Ahier, J. E. Cremer, and A. K.P. Jones. Compartmental analysis of diprenorphine binding to opiate receptors in the rat in vivo and its comparison with equilibrium data in vitro. *Journal of Cerebral Blood Flow and Metabolism*, 11(1):1–9, 1991. ISSN 0271678X. doi: 10.1038/jcbfm.1991.1.

[51] Joseph A. Thie. Understanding the standardized uptake value, its methods, and implications for usage. *Journal of Nuclear Medicine*, 45(9):1431–1434, 2004. ISSN 01615505.

[52] Wolf Dieter Heiss and Karl Herholz. Brain receptor imaging, 2006. ISSN 01615505.

[53] Sjoerd J Finnema, Mika Scheinin, Mohammed Shahid, Jussi Lehto, Edilio Borroni, Benny Bang-Andersen, Jukka Sallinen, Erik Wong, Lars Farde, Christer Halldin, and Sarah Grimwood. Application of cross-species PET imaging to assess neurotransmitter release in brain. *Psychopharmacology*, 232(21-22): 4129–4157, nov 2015. ISSN 0033-3158. doi: 10.1007/s00213-015-3938-6.

[54] Roger N. Gunn, Adriaan A. Lammertsma, Susan P. Hume, and Vincent J. Cunningham. Parametric Imaging of Ligand-Receptor Binding in PET Using a Simplified Reference Region Model. *NeuroImage*, 6(4):279–287, nov 1997. ISSN 10538119. doi: 10.1006/nimg.1997.0303.

[55] Robert B. Innis, Vincent J. Cunningham, Jacques Delforge, Masahiro Fujita, Albert Gjedde, Roger N. Gunn, James Holden, Sylvain Houle, Sung Cheng Huang, Masanori Ichise, Hidehiro Iida, Hiroshi Ito, Yuichi Kimura, Robert A. Koeppe, Gitte M. Knudsen, Juhani Knuuti, Adriaan A. Lammertsma, Marc Laruelle, Jean Logan, Ralph Paul Maguire, Mark A. Mintun, Evan D. Morris, Ramin Parsey, Julie C. Price, Mark Slifstein, Vesna Sossi, Tetsuya Suhara, John R. Votaw, Dean F. Wong, and Richard E. Carson. Consensus nomenclature for in vivo imaging of reversibly binding radioligands. *Journal of Cerebral Blood Flow and Metabolism*, 27(9):1533–1539, 2007. ISSN 0271678X. doi: 10.1038/sj.jcbfm.9600493.

[56] Mark Slifstein and Marc Laruelle. Models and methods for derivation of in vivo neuroreceptor parameters with PET and SPECT reversible radiotracers. *Nuclear Medicine and Biology*, 28(5):595–608, 2001. ISSN 09698051. doi: 10.1016/S0969-8051(01)00214-1.

[57] Kristina Herfert, Julia G. Mannheim, Laura Kuebler, Sabina Marciano, Mario Amend, Christoph Parl, Hanna Napieczynska, Florian M. Maier, Salvador Castaneda Vega, and Bernd J. Pichler. Quantitative Rodent Brain Recep-

tor Imaging. *Molecular Imaging and Biology*, 2019. ISSN 18602002. doi: 10.1007/s11307-019-01368-9.

[58] Marc Laruelle. Imaging synaptic neurotransmission with in vivo binding competition techniques: A critical review. *Journal of Cerebral Blood Flow and Metabolism*, 20(3):423–451, mar 2000. ISSN 0271678X. doi: 10.1097/00004647-200003000-00001.

[59] Philip Seeman, H. -C Guan, and Hyman B. Niznik. Endogenous dopamine lowers the dopamine D2 receptor density as measured by [3H]raclopride: Implications for positron emission tomography of the human brain. *Synapse*, 3 (1):96–97, 1989. ISSN 10982396. doi: 10.1002/syn.890030113.

[60] Lars Farde, Håkan Hall, Stefan Pauli, and Christer Halldin. Variability in D2-dopamine receptor density and affinity: A PET study with [11C]raclopride in man. *Synapse*, 20(3):200–208, 1995. ISSN 10982396. doi: 10.1002/syn.890200303.

[61] Lars Farde, Anna Lena Nordström, Frits Axel Wiesel, Stefan Pauli, Christer Halldin, and Göran Sedvall. Positron Emission Tomographic Analysis of Central D1 and D2 Dopamine Receptor Occupancy in Patients Treated With Classical Neuroleptics and Clozapine. *Archives of General Psychiatry*, 49(7):538, jul 1992. ISSN 0003-990X. doi: 10.1001/archpsyc.1992.01820070032005.

[62] Stephen L. Dewey, Gwenn S. Smith, Jean Logan, Jonathan D. Brodie, Joanna S. Fowler, and Alfred P. Wolf. Striatal binding of the PET ligand 11C-raclopride is altered by drugs that modify synaptic dopamine levels. *Synapse*, 13(4): 350–356, apr 1993. ISSN 10982396. doi: 10.1002/syn.890130407.

[63] Nora D. Volkow, Gene-Jack Wang, Joanna S. Fowler, Jean Logan, David Schlyer, Robert Hitzemann, Jeffrey Lieberman, Burton Angrist, Naomi Pappas, Robert MacGregor, Gail Burr, Thomas Cooper, and Alfred P. Wolf. Imaging endogenous dopamine competition with [11C]raclopride in the human brain. *Synapse*, 16(4):255–262, apr 1994. ISSN 0887-4476. doi: 10.1002/syn.890160402.

[64] Richard E Carson, Alan Breier, Andrea De Bartolomeis, Richard C. Saunders, Tom P Su, Bernard Schmall, Margaret G Der, David Pickar, and William C Eckelman. Quantification of amphetamine-induced changes in [11 C]raclopride binding with continuous infusion. *Journal of Cerebral Blood Flow and Metabolism*, 17(4):437–447, apr 1997. ISSN 0271678X. doi: 10.1097/00004647-199704000-00009.

[65] Christopher J Endres, Bhaskar S. Kolachana, Richard C. Saunders, Tom Su, Daniel Weinberger, Alan Breier, William C Eckelman, and Richard E Carson. Kinetic modeling of [11C]raclopride: combined PET-microdialysis studies. *Journal of cerebral blood flow and metabolism : official journal of the*

International Society of Cerebral Blood Flow and Metabolism, 17(9):932–942, sep 1997. ISSN 0271-678X. doi: 10.1097/00004647-199709000-00002.

[66] S. Pappata, S. Dehaene, J. B. Poline, M. C. Gregoire, A. Jobert, J. Delforge, V. Frouin, M. Bottlaender, F. Dolle, L. Di Giamberardino, and A. Syrota. In Vivo detection of striatal dopamine release during reward: A PET study with [11C]raclopride and a single dynamic scan approach. *NeuroImage*, 16(4): 1015–1027, 2002. ISSN 10538119. doi: 10.1006/nimg.2002.1121.

[67] Rajendra D. Badgaiyan, Alan J. Fischman, and Nathaniel M. Alpert. Striatal dopamine release during unrewarded motor task in human volunteers. *NeuroReport*, 14(11):1421–1424, 2003. ISSN 09594965. doi: 10.1097/00001756-200308060-00003.

[68] Nathaniel M. Alpert, Rajendra D. Badgaiyan, Elijahu Livni, and Alan J. Fischman. A novel method for noninvasive detection of neuromodulatory changes in specific neurotransmitter systems. *NeuroImage*, 19(3):1049–1060, jul 2003. ISSN 10538119. doi: 10.1016/S1053-8119(03)00186-1.

[69] Yun Zhou, Ming Kai Chen, Christopher J. Endres, Weiguo Ye, James R. Brašić, Mohab Alexander, Andrew H. Crabb, Tomás R. Guilarte, and Dean F. Wong. An extended simplified reference tissue model for the quantification of dynamic PET with amphetamine challenge. *NeuroImage*, 33(2):550–563, 2006. ISSN 10538119. doi: 10.1016/j.neuroimage.2006.06.038.

[70] Yoko Ikoma, Hiroshi Watabe, Takuya Hayashi, Yoshinori Miyake, Noboru Teramoto, Kotaro Minato, and Hidehiro Iida. Quantitative evaluation of changes in binding potential with a simplified reference tissue model and multiple injections of [11C]raclopride. *NeuroImage*, 47(4):1639–1648, 2009. ISSN 10538119. doi: 10.1016/j.neuroimage.2009.05.099.

[71] Marc D. Normandin, Wynne K. Schiffer, and Evan D. Morris. A linear model for estimation of neurotransmitter response profiles from dynamic PET data. *NeuroImage*, 59(3):2689–2699, 2012. ISSN 10538119. doi: 10.1016/j.neuroimage.2011.07.002.

[72] Evan D. Morris, Su J.in Kim, Jenna M. Sullivan, Shuo Wang, Marc D. Normandin, Cristian C. Constantinescu, and Kelly P. Cosgrove. Creating dynamic images of short-lived dopamine fluctuations with lp-ntPET: dopamine movies of cigarette smoking. *Journal of Visualized Experiments*, (78), aug 2013. ISSN 1940087X. doi: 10.3791/50358.

[73] Alice Egerton, Mitul A. Mehta, Andrew J. Montgomery, Julia M. Lappin, Oliver D. Howes, Suzanne J. Reeves, Vincent J. Cunningham, and Paul M. Grasby. The dopaminergic basis of human behaviors: A review of molecular imaging studies. *Neuroscience and Biobehavioral Reviews*, 33(7):1109–1132, jul 2009. ISSN 01497634. doi: 10.1016/j.neubiorev.2009.05.005.

[74] Richard E. Carson. PET physiological measurements using constant infusion. *Nuclear Medicine and Biology*, 27(7):657–660, 2000. ISSN 09698051. doi: 10.1016/S0969-8051(00)00138-4.

[75] N. D. Volkow, G.-J. Wang, J. S. Fowler, J. Logan, S. J. Gatley, R. Hitzemann, A. D. Chen, S. L. Dewey, and N. Pappas. Decreased striatal dopaminergic responsiveness in detoxified cocaine-dependent subjects. *Nature*, 386(6627): 830–833, apr 1997. ISSN 0028-0836. doi: 10.1038/386830a0.

[76] M. J. Koepp, R. N. Gunn, A. D. Lawrence, V. J. Cunningham, A. Dagher, T. Jones, O. J. Brooks, C. J. Bench, and P. M. Grasby. Evidence for striatal dopamine release during a video game. *Nature*, 393(6682):266–268, 1998. ISSN 00280836. doi: 10.1038/30498.

[77] Hiroshi Ito, Jarmo Hietala, Gunnar Blomqvist, Christer Halldin, and Lars Farde. Comparison of the transient equilibrium and continuous infusion method for quantitative PET analysis of [11C]raclopride binding. *Journal of Cerebral Blood Flow and Metabolism*, 18(9):941–950, 1998. ISSN 0271678X. doi: 10.1097/00004647-199809000-00003.

[78] Evan D. Morris, Karmen K. Yoder, Chunzhi Wang, Marc D. Normandin, Qi-Huang Zheng, Bruce Mock, F. Muzic Raymond, and Janice C. Froehlich. ntPET: A New Application of PET Imaging for Characterizing the Kinetics of Endogenous Neurotransmitter Release. *Molecular Imaging*, 4(4):7290.2005.05130, 2005. ISSN 1536-0121. doi: 10.2310/7290.2005.05130.

[79] Cristian C. Constantinescu, Charles Bouman, and Evan D. Morris. Nonparametric extraction of transient changes in neurotransmitter concentration from dynamic PET data. *IEEE Transactions on Medical Imaging*, 26(3):359–373, 2007. ISSN 02780062. doi: 10.1109/TMI.2006.891501.

[80] E.D. Morris, C.C. Constantinescu, J.M. Sullivan, M.D. Normandin, and L.A. Christopher. Noninvasive visualization of human dopamine dynamics from PET images. *NeuroImage*, 51(1):135–144, may 2010. ISSN 10538119. doi: 10.1016/j.neuroimage.2009.12.082.

[81] Oliver Von Bohlen und Halbach, Rolf Dermietzel, Oliver von Bohlen und Halbach, and Rolf Dermietzel. *Neurotransmitters and Neuromodulators*, volume 10. Wiley-VCH Verlag GmbH & Co. KGaA, 2006. ISBN 3-527-31307-9. doi: 10.1258/096914103321824151.

[82] R. Werman. A review - critical for idenctification of a central nervous system transmitter. *Comparative Biochemistry And Physiology*, 18(4):745–766, 1966. ISSN 0010406X. doi: 10.1016/0010-406X(66)90209-X.

[83] Roy Webster. *Neurotransmitters, Drugs and Brain Function*. Wiley, sep 2001. ISBN 9780471978190. doi: 10.1002/0470846577.

[84] Marianne O. Klein, Daniella S. Battagello, Ariel R. Cardoso, David N. Hauser, Jackson C. Bittencourt, and Ricardo G. Correa. Dopamine: Functions, Signaling, and Association with Neurological Diseases. *Cellular and Molecular Neurobiology*, 39(1):31–59, 2019. ISSN 15736830. doi: 10.1007/s10571-018-0632-3.

[85] Rui Wang. *Signal Transduction and the Gasotransmitters*. Humana Press, 2004. ISBN 978-1-61737-512-5. doi: 10.1007/978-1-59259-806-9.

[86] Rachel N. Lippert, Anna Lena Cremer, Sharmili Edwin Thanarajah, Clio Korn, Thomas Jahans-Price, Lauren M. Burgeno, Marc Tittgemeyer, Jens C. Brüning, Mark E. Walton, and Heiko Backes. Time-dependent assessment of stimulus-evoked regional dopamine release. *Nature Communications*, 10(1):336, 2019. ISSN 2041-1723. doi: 10.1038/s41467-018-08143-4.

[87] Sharmili Edwin Thanarajah, Heiko Backes, Alexandra G. DiFeliceantonio, Kerstin Albus, Anna Lena Cremer, Ruth Hanssen, Rachel N. Lippert, Oliver A. Cornely, Dana M. Small, Jens C. Brüning, and Marc Tittgemeyer. Food Intake Recruits Orosensory and Post-ingestive Dopaminergic Circuits to Affect Eating Desire in Humans. *Cell Metabolism*, 29(3):1–12, 2018. ISSN 1550-4131. doi: 10.1016/J.CMET.2018.12.006.

[88] Margaret E. Rice and Stephanie J. Cragg. Dopamine spillover after quantal release: Rethinking dopamine transmission in the nigrostriatal pathway. *Brain Research Reviews*, 58(2):303–313, aug 2008. ISSN 01650173. doi: 10.1016/j.brainresrev.2008.02.004.

[89] Albert Einstein. Über die von der molekularkinetischen Theorie der Wärme geforderte Bewegung von in ruhenden Flüssigkeiten suspendierten Teilchen. *Annalen der Physik*, 322(8):549–560, 1905. ISSN 00033804. doi: 10.1002/andp.19053220806.

[90] M. von Smoluchowski. Zur kinetischen Theorie der Brownschen Molekularbewegung und der Suspensionen. *Annalen der Physik*, 326(14):756–780, 1906. ISSN 00033804. doi: 10.1002/andp.19063261405.

[91] Oxford University Press. *A Dictionary of Chemistry*. Oxford University Press, 6 edition, jan 2008. ISBN 9780199204632. doi: 10.1093/acref/9780199204632.001.0001.

[92] S. Nakamura. *Neurotransmitters*, volume 37. 1985. ISBN 3527313079. doi: 10.5005/jp/books/12674_91.

[93] Oscar Arias-Carrián, Maria Stamelou, Eric Murillo-Rodríguez, Manuel Menéndez-Gonzlez, and Ernst Pöppel. Dopaminergic reward system: A short integrative review. *International Archives of Medicine*, 3(1):1–6, 2010. ISSN 17557682. doi: 10.1186/1755-7682-3-24.

[94] Anders Björklund and Stephen B. Dunnett. Dopamine neuron systems in the brain: an update. *Trends in Neurosciences*, 30(5):194–202, 2007. ISSN 01662236. doi: 10.1016/j.tins.2007.03.006.

[95] Dimitri Grigoriadis and Philip Seeman. The Dopamine/Neuroleptic Receptor. *Canadian Journal of Neurological Sciences / Journal Canadien des Sciences Neurologiques*, 11(S1):108–113, feb 1984. ISSN 20570155. doi: 10.1017/S0317167100046242.

[96] A A Grace and B S Bunney. The control of firing pattern in nigral dopamine neurons: burst firing. *The Journal of neuroscience : the official journal of the Society for Neuroscience*, 4(11):2877–90, nov 1984. ISSN 0270-6474. doi: 6150071.

[97] Anthony A Grace. Developmental dysregulation of the dopamine system and the pathophysiology of schizophrenia. *Neurodevelopment and Schizophrenia.*, 17(8):273–294, 2004. ISSN 1471-003X. doi: 10.1038/nrn.2016.57.

[98] Katie A. Jennings. A comparison of the subsecond dynamics of neurotransmission of dopamine and serotonin. *ACS Chemical Neuroscience*, 4(5):704–714, may 2013. ISSN 19487193. doi: 10.1021/cn4000605.

[99] Stephanie J. Cragg and Margaret E. Rice. DAncing past the DAT at a DA synapse. *Trends in Neurosciences*, 27(5):270–277, may 2004. ISSN 01662236. doi: 10.1016/j.tins.2004.03.011.

[100] P A Garris, E L Ciolkowski, P Pastore, and R M Wightman. Efflux of dopamine from the synaptic cleft in the nucleus accumbens of the rat brain. *The Journal of neuroscience : the official journal of the Society for Neuroscience*, 14(10): 6084–6093, 1994. ISSN 0270-6474. doi: 10.1007/s00213-006-0502-4.

[101] I. Mitch Taylor, Kathryn M. Nesbitt, Seth H. Walters, Erika L. Varner, Zhan Shu, Kathleen M. Bartlow, Andrea S. Jaquins-Gerstl, and Adrian C. Michael. Kinetic diversity of dopamine transmission in the dorsal striatum. *Journal of Neurochemistry*, 133(4):522–531, may 2015. ISSN 00223042. doi: 10.1111/jnc.13059.

[102] Karmen K. Yoder, David A. Kareken, and Evan D. Morris. What were they thinking?. Cognitive states may influence [11C]raclopride binding potential in the striatum. *Neuroscience Letters*, 430(1):38–42, 2008. ISSN 03043940. doi: 10.1016/j.neulet.2007.10.017.

[103] L. Farde, L. Eriksson, G. Blomquist, and C. Halldin. Kinetic Analysis of Central [11 C]Raclopride Binding to D 2 -Dopamine Receptors Studied by PET—A Comparison to the Equilibrium Analysis. *Journal of Cerebral Blood Flow & Metabolism*, 9(5):696–708, oct 1989. ISSN 0271-678X. doi: 10.1038/jcbfm.1989.98.

[104] Gerhard Gründer, Thomas Siessmeier, Markus Piel, Ingo Vernaleken, Hansgeorg Georg Buchholz, Yun Zhou, Christoph Hiemke, Dean F. Wong, Frank Rösch, and Peter Bartenstein. Quantification of D2-like dopamine receptors in the human brain with 18F-desmethoxyfallypride. *Journal of Nuclear Medicine*, 44(1):109–116, jan 2003. ISSN 01615505.

[105] Luis A. Tellez, Sara Medina, Wenfei Han, Jozelia G. Ferreira, P Licona-Limon, Xueying Ren, Tu Kiet T. Lam, Gary J. Schwartz, Ivan E. De Araujo, Paula Licona-Limón, Xueying Ren, Tu Kiet T. Lam, Gary J. Schwartz, and Ivan E. De Araujo. A gut lipid messenger links excess dietary fat to dopamine deficiency. *Science*, 341(6147):800–802, 2013. ISSN 10959203. doi: 10.1126/science.1239275.

[106] Andrew J. Lawrence, Elena Krstew, and Bevyn Jarrott. Functional dopamine D2 receptors on rat vagal afferent neurones. *British Journal of Pharmacology*, 114(7):1329–1334, 1995. ISSN 14765381. doi: 10.1111/j.1476-5381.1995.tb13352.x.

[107] Nathan T. Rodeberg, Stefan G. Sandberg, Justin A. Johnson, Paul E. M. Phillips, and R. Mark Wightman. Hitchhiker's Guide to Voltammetry: Acute and Chronic Electrodes for in Vivo Fast-Scan Cyclic Voltammetry. *ACS Chemical Neuroscience*, 8(2):221–234, feb 2017. ISSN 1948-7193. doi: 10.1021/acschemneuro.6b00393.

[108] P. Goupillaud, A. Grossmann, and J. Morlet. Cycle-octave and related transforms in seismic signal analysis. *Geoexploration*, 23(1):85–102, 1984. ISSN 00167142. doi: 10.1016/0016-7142(84)90025-5.

[109] Paul A. Garris, Leonard B. Collins, Sara R. Jones, and R. Mark Wightman. Evoked Extracellular Dopamine In Vivo in the Medial Prefrontal Cortex. *Journal of Neurochemistry*, 61(2):637–647, 1993. ISSN 14714159. doi: 10.1111/j.1471-4159.1993.tb02168.x.

[110] Donita L. Robinson, B. Jill Venton, Michael L A V Heien, and R. Mark Wightman. Detecting subsecond dopamine release with fast-scan cyclic voltammetry in vivo. *Clinical Chemistry*, 49(10):1763–1773, 2003. ISSN 00099147. doi: 10.1373/49.10.1763.

[111] Qun Wu, Maarten E.A. Reith, R. Mark Wightman, Kirk T. Kawagoe, and Paul A. Garris. Determination of release and uptake parameters from electrically evoked dopamine dynamics measured by real-time voltammetry. *Journal of Neuroscience Methods*, 112(2):119–133, 2001. ISSN 01650270. doi: 10.1016/S0165-0270(01)00459-9.

[112] Parastoo Hashemi, Elyse C. Dankoski, Rinchen Lama, Kevin M. Wood, Pavel Takmakov, and R. Mark Wightman. Brain dopamine and serotonin differ in regulation and its consequences. *Proceedings of the National Academy of*

Sciences of the United States of America, 109(29):11510–11515, 2012. ISSN 00278424. doi: 10.1073/pnas.1201547109.

[113] Martin Sarter, Vinay Parikh, and W Matthew Howe. Phasic acetylcholine release and the volume transmission hypothesis: time to move on. *Nature reviews. Neuroscience*, 10(5):383–90, 2009. ISSN 1471-0048. doi: 10.1038/nrn2635.

[114] Brian S. Meldrum. Glutamate as a Neurotransmitter in the Brain: Review of Physiology and Pathology. *The Journal of Nutrition*, 130(4):1007S–1015S, apr 2000. ISSN 0022-3166. doi: 10.1093/jn/130.4.1007s.

[115] Jean Pierre Hornung. The human raphe nuclei and the serotonergic system. *Journal of Chemical Neuroanatomy*, 26(4):331–343, 2003. ISSN 08910618. doi: 10.1016/j.jchemneu.2003.10.002.

[116] Anissa Abi-Dargham and Olivier Guillin. *Integrating the neurobiology of schizophrenia*, volume 78. 2007. ISBN 9780123737373. doi: 10.1016/S0074-7742(06)78003-5.

[117] Marina R Picciotto. Acetylcholine as a neuromodulator. *Neuron*, 76(1):116–129, 2013. doi: 10.1016/j.neuron.2012.08.036.Acetylcholine.

[118] Tsuneya Ikezu and Howard E. Gendelman. *Neuroimmune pharmacology*. 2016. ISBN 9783319440224. doi: 10.1007/978-3-319-44022-4.

[119] Louise M. Paterson, Birgitte R. Kornum, David J. Nutt, Victor W. Pike, and Gitte M. Knudsen. 5-HT radioligands for human brain imaging with PET and SPECT. *Medicinal Research Reviews*, 33(1):54–111, jan 2013. ISSN 01986325. doi: 10.1002/med.20245.

[120] J.S. Kumar and J. Mann. PET Tracers for Serotonin Receptors and Their Applications. *Central Nervous System Agents in Medicinal Chemistry*, 14(2):96–112, jan 2014. ISSN 18715249. doi: 10.2174/1871524914666141030124316.

[121] Susan Hume, Ella Hirani, Jolanta Opacka-Juffry, Ralph Myers, Claire Townsend, Victor Pike, and Paul Grasby. Effect of 5-HT on binding of [11C] WAY 100635 to 5-HT1A receptors in rat brain, assessed using in vivo microdialysis and PET after fenfluramine. *Synapse*, 41(2):150–159, aug 2001. ISSN 0887-4476. doi: 10.1002/syn.1069.

[122] Jun Maeda, Tetsuya Suhara, Masanao Ogawa, Takashi Okauchi, Kouichi Kawabe, Ming-Rong Zhang, Jun'Ichi Semba, and Kazutoshi Suzuki. In vivo binding properties of [carbonyl-11C]WAY-100635: Effect of endogenous serotonin. *Synapse*, 40(2):122–129, may 2001. ISSN 0887-4476. doi: 10.1002/syn.1033.

[123] Matthew S. Milak, Alin J. Severance, Jaya Prabhakaran, J. S.Dileep Kumar, Vattoly J. Majo, R. Todd Ogden, J. John Mann, and Ramin V. Parsey. In vivo serotonin-sensitive binding of [11C]CUMI-101: A serotonin 1A receptor agonist positron emission tomography radiotracer. *Journal of Cerebral Blood Flow and Metabolism*, 31(1):243–249, 2011. ISSN 0271678X. doi: 10.1038/jcbfm.2010.83.

[124] Akaike Akaike, Shun Shimohama, and Yoshimi Misu. Nicotinic Acetylcholine Receptor Signaling in Neuroprotection. *Nicotinic Acetylcholine Receptor Signaling in Neuroprotection*, pages 1–191, 2018. doi: 10.1007/978-981-10-8488-1.

[125] Dale Purves, George J Augustine, David Fitzpatrick, William C Hall, Anthony-Samuel LaMantia, James O McNamara, and S Mark Williams, editors. *Neuroscience, 3rd ed.* Sinauer Associates, Sunderland, MA, US, 2004. ISBN 0-87893-725-0 (Hardcover).

[126] Osama Sabri, Georg Alexander Becker, Philipp M. Meyer, Swen Hesse, Stephan Wilke, Susanne Graef, Marianne Patt, Julia Luthardt, Gudrun Wagenknecht, Alexander Hoepping, René Smits, Annegret Franke, Bernhard Sattler, Bernd Habermann, Petra Neuhaus, Steffen Fischer, Solveig Tiepolt, Winnie Deuther-Conrad, Henryk Barthel, Peter Schönknecht, and Peter Brust. First-in-human PET quantification study of cerebral $\alpha4\beta2$* nicotinic acetylcholine receptors using the novel specific radioligand (-)-[18F]Flubatine. *NeuroImage*, 118:199–208, 2015. ISSN 10959572. doi: 10.1016/j.neuroimage.2015.05.065.

[127] Hiroto Kuwabara, Yongjun Gao, Michael Stabin, Jennifer Coughlin, Sridhar Nimmagadda, Robert F. Dannals, Martin G. Pomper, and Andrew G. Horti. Imaging $\alpha4\beta2$ Nicotinic Acetylcholine Receptors (nAChRs) in Baboons with [18F]XTRA, a Radioligand with Improved Specific Binding in Extra-Thalamic Regions. *Molecular Imaging and Biology*, 19(2):280–288, 2017. ISSN 18602002. doi: 10.1007/s11307-016-0999-9.

[128] Patrick J. Lao, Tobey J. Betthauser, Dana L. Tudorascu, Todd E. Barnhart, Ansel T. Hillmer, Charles K. Stone, Jogeshwar Mukherjee, and Bradley T. Christian. [18 F]Nifene test-retest reproducibility in first-in-human imaging of $\alpha4\beta2$* nicotinic acetylcholine receptors. *Synapse*, 71(8):e21981, aug 2017. ISSN 08874476. doi: 10.1002/syn.21981.

[129] Rama Pichika, Balasubramaniam Easwaramoorthy, Daphne Collins, Bradley T. Christian, Bingzhi Shi, Tanjore K. Narayanan, Steven G. Potkin, and Jogeshwar Mukherjee. Nicotinic $\alpha4\beta2$ receptor imaging agents. *Nuclear Medicine and Biology*, 33(3):295–304, apr 2006. ISSN 09698051. doi: 10.1016/j.nucmedbio.2005.12.017.

[130] Takeshi Fuchigami, Morio Nakayama, and Sakura Yoshida. Development of PET and SPECT probes for glutamate receptors. *Scientific World Journal*, 2015, 2015. ISSN 1537744X. doi: 10.1155/2015/716514.

[131] Arne Schousboe. *The Glutamate/GABA-Glutamine Cycle*, volume 13 of *Advances in Neurobiology*. Springer International Publishing, Cham, 2016. ISBN 978-3-319-45094-0. doi: 10.1007/978-3-319-45096-4.

[132] Valerie Treyer, Johannes Streffer, Simon M. Ametamey, Andrea Bettio, Peter Bläuenstein, Mark Schmidt, Fabrizio Gasparini, Uta Fischer, Christoph Hock, and Alfred Buck. Radiation dosimetry and biodistribution of 11C-ABP688 measured in healthy volunteers. *European Journal of Nuclear Medicine and Molecular Imaging*, 35(4):766–770, apr 2008. ISSN 1619-7070. doi: 10.1007/s00259-007-0638-4.

[133] Linjing Mu, P. August Schubiger, and Simon M. Ametamey. Radioligands for the PET Imaging of Metabotropic Glutamate Receptor Subtype 5 (mGluR5). *Current Topics in Medicinal Chemistry*, 10(15):1558–1568, 2012. ISSN 15680266. doi: 10.2174/156802610793176783.

[134] Simon M. Ametamey, Valerie Treyer, Johannes Streffer, Matthias T. Wyss, Mark Schmidt, Milen Blagoev, Samuel Hintermann, Yves Auberson, Fabrizio Gasparini, Uta C. Fischer, and Alfred Buck. Human PET studies of metabotropic glutamate receptor subtype 5 with 11C-ABP688. *Journal of Nuclear Medicine*, 48(2):247–252, 2007. ISSN 01615505.

[135] Fabrice G. Siméon, Amira K. Brown, Sami S. Zoghbi, Velvet M. Patterson, Robert B. Innis, and Victor W. Pike. Synthesis and simple 18F-labeling of 3-fluoro-5-(2-(2- (fluoromethyl)thiazol-4-yl)ethynyl)benzonitrile as a high affinity radioligand for imaging monkey brain metabotropic glutamate subtype-5 receptors with positron emission tomography. *Journal of Medicinal Chemistry*, 50(14):3256–3266, 2007. ISSN 00222623. doi: 10.1021/jm0701268.

[136] Bradley T Christian, Tanjore Narayanan, Bing Shi, Evan D. Morris, Joseph Mantil, and Jogeshwar Mukherjee. Measuring the In Vivo Binding Parameters of [18F]-Fallypride in Monkeys Using a PET Multiple-Injection Protocol. *Journal of Cerebral Blood Flow and Metabolism*, 24(3):309–322, mar 2004. ISSN 0271678X. doi: 10.1097/01.WCB.0000105020.93708.DD.

[137] Luc Zimmer, Gweltas Mauger, Didier Le Bars, Gregory Bonmarchand, Andre Luxen, and Jean-Francois Pujol. Effect of endogenous serotonin on the binding of the 5-HT1A PET ligand 18F-MPPF in the rat hippocampus: kinetic beta measurements combined with microdialysis. *Journal of Neurochemistry*, 80(2):278–286, jan 2002. ISSN 0022-3042. doi: 10.1046/j.0022-3042.2001.00696.x.

[138] Ansel T. Hillmer, Dustin W. Wooten, Maxim S. Slesarev, Elizabeth O. Ahlers, Todd E. Barnhart, Mary L. Schneider, Jogeshwar Mukherjee, and Bradley T. Christian. Measuring $\alpha 4\beta 2$* nicotinic acetylcholine receptor density in vivo with [18 F]nifene PET in the nonhuman primate. *Journal of Cerebral Blood Flow and Metabolism*, 33(11):1806–1814, 2013. ISSN 0271678X. doi: 10.1038/jcbfm.2013.136.

[139] Balasubramaniam Easwaramoorthy, Rama Pichika, Daphne Collins, Steven G. Potkin, Frances M. Leslie, and Jogeshwar Mukherjee. Effect of acetylcholinesterase inhibitors on the binding of nicotinic $\alpha 4\beta 2$ receptor PET radiotracer,18F-nifene: A measure of acetylcholine competition. *Synapse*, 61(1):29–36, jan 2007. ISSN 08874476. doi: 10.1002/syn.20338.

[140] Jogeshwar Mukherjee, Patrick J. Lao, Tobey J. Betthauser, Gurleen K. Samra, Min-Liang Pan, Ishani H. Patel, Christopher Liang, Raju Metherate, and Bradley T. Christian. Human brain imaging of nicotinic acetylcholine $\alpha 4\beta 2$* receptors using [18 F]Nifene: Selectivity, functional activity, toxicity, aging effects, gender effects, and extrathalamic pathways. *Journal of Comparative Neurology*, 526(1):80–95, jan 2018. ISSN 00219967. doi: 10.1002/cne.24320.

[141] K. Sengmany and K. J. Gregory. Metabotropic glutamate receptor subtype 5: molecular pharmacology, allosteric modulation and stimulus bias. *British Journal of Pharmacology*, 173(20):3001–3017, 2016. ISSN 14765381. doi: 10.1111/bph.13281.

[142] David Elmenhorst, Luciano Minuzzi, Antonio Aliaga, Jared Rowley, Gassan Massarweh, Mirko Diksic, Andreas Bauer, and Pedro Rosa-Neto. In vivo and in vitro validation of reference tissue models for the mGluR 5 ligand [11C]ABP688. *Journal of Cerebral Blood Flow and Metabolism*, 30(8):1538–1549, 2010. ISSN 0271678X. doi: 10.1038/jcbfm.2010.65.

[143] Javier Corzo and Monica Santamaria. Time, the forgotten dimension of ligand binding teaching. *Biochemistry and Molecular Biology Education*, 34(6):413–416, 2006. ISSN 14708175. doi: 10.1002/bmb.2006.494034062678.

[144] Edward C. Hulme and Mike A. Trevethick. Ligand binding assays at equilibrium: Validation and interpretation. *British Journal of Pharmacology*, 161(6):1219–1237, 2010. ISSN 00071188. doi: 10.1111/j.1476-5381.2009.00604.x.

[145] K. Dane Wittrup, Bruce Tidor, Benjamin J. Hackel, and Casim A. Sarkar. *Quantitative Fundamentals of Molecular and Cellular Bioengineering*. The MIT Press, Cambridge, Massachusetts; London, England, 2019. ISBN 978-0262042659.

[146] Thomas Siessmeier, Yun Zhou, Hans-georg Georg Buchholz, Christian Landvogt, Ingo Vernaleken, Markus Piel, Ralf Schirrmacher, Frank Ro, Mathias Schreckenberger, Dean F. Wong, Paul Cumming, Gerhard Gru, Peter Bartenstein, Frank Rösch, Mathias Schreckenberger, Dean F. Wong, Paul Cumming, Gerhard Gründer, and Peter Bartenstein. Parametric mapping of binding in human brain of D2 receptor ligands of different affinities. *The Journal of Nuclear Medicine*, 46(6):964–972, 2005. ISSN 01615505.

[147] Lars Farde, Hiroshi Ito, Carl-gunnar Swahn, Victor W Pike, Christer Halldin, Psychiatiy Section, Engineering Group, and Council Cyclotron. Quantitative Analyses of Carbonyl-Carbon-11 - WA Y-10063 5 Binding to Central 5-Hydroxytryptamine-lA Receptors in Man. *The Journal of Nuclear Medicine*, 39:1965–1971, 1998.

[148] Nicolas Costes, Isabelle Merlet, Luc Zimmer, Franck Lavenne, Luc Cinotti, Jacques Delforge, André Luxen, Jean-François François Pujol, Didier Le Bars, Didier Le Bars, and Didier Le Bars. Modeling [18F]MPPF positron emission tomography kinetics for the determination of 5-hydroxytryptamine(1A) receptor concentration with multiinjection. *Journal of Cerebral Blood Flow and Metabolism*, 22(6):753–765, jun 2002. ISSN 0271678X. doi: 10.1097/00004647-200206000-00014.

[149] Matthew S. Milak, Christine DeLorenzo, Francesca Zanderigo, Jaya Prabhakaran, J. S.Dileep Kumar, Vattoly J. Majo, J. John Mann, and Ramin V. Parsey. In vivo quantification of human serotonin 1A receptor using 11C-CUMI-101, an agonist PET radiotracer. *Journal of Nuclear Medicine*, 51(12):1892–1900, dec 2010. ISSN 01615505. doi: 10.2967/jnumed.110.076257.

[150] Cristian C. Constantinescu, Adriana Garcia, M. Reza Mirbolooki, Min-Liang Pan, and Jogeshwar Mukherjee. Evaluation of [18F]Nifene biodistribution and dosimetry based on whole-body PET imaging of mice. *Nuclear Medicine and Biology*, 40(2):289–294, feb 2013. ISSN 09698051. doi: 10.1016/j.nucmedbio.2012.11.004.

[151] Amira K. Brown, Yasuyuki Kimura, Sami S. Zoghbi, Fabrice G. Siméon, Jeih San Liow, William C. Kreisl, Andrew Taku, Masahiro Fujita, Victor W. Pike, and Robert B. Innis. Metabotropic glutamate subtype 5 receptors are quantified in the human brain with a novel radioligand for PET. *Journal of Nuclear Medicine*, 49(12):2042–2048, 2008. ISSN 01615505. doi: 10.2967/jnumed.108.056291.

[152] Blaine N. Armbruster, Xiang Li, Mark H. Pausch, Stefan Herlitze, and Bryan L. Roth. Evolving the lock to fit the key to create a family of G protein-coupled receptors potently activated by an inert ligand. *Proceedings of the National Academy of Sciences of the United States of America*, 104(12):5163–5168, 2007. ISSN 00278424. doi: 10.1073/pnas.0700293104.

[153] Bryan L Roth. DREADDs for Neuroscientists. *Neuron*, 89(4):683–694, feb 2016. ISSN 08966273. doi: 10.1016/j.neuron.2016.01.040.

[154] Michael Michaelides and Yasmin L Hurd. Chemogenetics: DREADDs. In Donald W Pfaff and Nora D Volkow, editors, *Neuroscience in the 21st Century*, pages 1–10. Springer New York, New York, NY, 2016. ISBN 978-1-4614-6434-1. doi: 10.1007/978-1-4614-6434-1_147-1.

[155] Sophie M. Steculorum, Johan Ruud, Ismene Karakasilioti, Heiko Backes, Linda Engström Ruud, Katharina Timper, Martin E. Hess, Eva Tsaousidou, Jan Mauer, Merly C. Vogt, Lars Paeger, Stephan Bremser, Andreas C. Klein, Donald A. Morgan, Peter Frommolt, Paul T. Brinkkötter, Philipp Hammerschmidt, Thomas Benzing, Kamal Rahmouni, F. Thomas Wunderlich, Peter Kloppenburg, and Jens C. Brüning. AgRP Neurons Control Systemic Insulin Sensitivity via Myostatin Expression in Brown Adipose Tissue. *Cell*, 165(1): 125–138, mar 2016. ISSN 00928674. doi: 10.1016/j.cell.2016.02.044.

[156] Mats I. Ekstrand, Mügen Terzioglu, Dagmar Galter, Shunwei Zhu, Christoph Hofstetter, Eva Lindqvist, Sebastian Thams, Anita Bergstrand, Fredrik Sterky Hansson, Aleksandra Trifunovic, Barry Hoffer, Staffan Cullheim, Abdul H. Mohammed, Lars Olson, and Nils Göran Larsson. Progressive parkinsonism in mice with respiratory-chain-deficient dopamine neurons. *Proceedings of the National Academy of Sciences of the United States of America*, 104(4): 1325–1330, 2007. ISSN 00278424. doi: 10.1073/pnas.0605208103.

[157] Jiří Čížek, Karl Herholz, Stefan Vollmar, Rainer Schrader, Johannes Klein, and Wolf Dieter Heiss. Fast and robust registration of PET and MR images of human brain. *NeuroImage*, 22(1):434–442, 2004. ISSN 10538119. doi: 10.1016/j.neuroimage.2004.01.016.

[158] George Paxinos and Keith Franklin. *The Mouse Brain in Stereotaxic Coordinates, Compact — 978-0-12-374244-5 — Elsevier*. 2008. ISBN 012547640X.

[159] D. P. Daberkow, H. D. Brown, K. D. Bunner, S. A. Kraniotis, M. A. Doellman, M. E. Ragozzino, Paul A. Garris, and Mitchell F. Roitman. Amphetamine Paradoxically Augments Exocytotic Dopamine Release and Phasic Dopamine Signals. *Journal of Neuroscience*, 33(2):452–463, jan 2013. ISSN 0270-6474. doi: 10.1523/JNEUROSCI.2136-12.2013.

[160] Joseph F. Cheer, Kate M. Wassum, Michael L A V Heien, Paul E M Phillips, and R. Mark Wightman. Cannabinoids Enhance Subsecond Dopamine Release in the Nucleus Accumbens of Awake Rats. *Journal of Neuroscience*, 24(18): 4393–4400, 2004. ISSN 02706474. doi: 10.1523/JNEUROSCI.0529-04.2004.

[161] Hans Petter Langtangen and Svein Linge. *Finite Difference Computing with PDEs*, volume 16 of *Texts in Computational Science and Engineering*. Springer International Publishing, Cham, 2017. ISBN 978-3-319-55455-6. doi: 10.1007/978-3-319-55456-3.

[162] Hideo Tsukada, Shingo Nishiyama, Takeharu Kakiuchi, Hiroyuki Ohba, Kengo Sato, and Norihiro Harada. Is synaptic dopamine concentration the exclusive factor which alters the in vivo binding of [11C]raclopride?: PET studies combined with microdialysis in conscious monkeys. *Brain Research*, 841(1-2): 160–169, sep 1999. ISSN 00068993. doi: 10.1016/S0006-8993(99)01834-X.

[163] S. M. Hersch, B. J. Ciliax, C. A. Gutekunst, H. D. Rees, C. J. Heilman, K. K.L. Yung, J. P. Bolam, E. Ince, H. Yi, and A. I. Levey. Electron microscopic analysis of D1 and D2 dopamine receptor proteins in the dorsal striatum and their synaptic relationships with motor corticostriatal afferents. *Journal of Neuroscience*, 15(7 II):5222–5237, 1995. ISSN 02706474. doi: 10.1523/jneurosci.15-07-05222.1995.

[164] K. K.L. Yung, J. P. Bolam, A. D. Smith, S. M. Hersch, B. J. Ciliax, and A. I. Levey. Immunocytochemical localization of D1 and D2 dopamine receptors in the basal ganglia of the rat: Light and electron microscopy. *Neuroscience*, 65 (3):709–730, 1995. ISSN 03064522. doi: 10.1016/0306-4522(94)00536-E.

[165] Leonid P. Savtchenko and Dmitri A. Rusakov. The optimal height of the synaptic cleft. *Proceedings of the National Academy of Sciences of the United States of America*, 104(6):1823–1828, 2007. ISSN 00278424. doi: 10.1073/pnas.0606636104.

[166] Michele Zoli, Carla Torri, Rosaria Ferrari, Anders Jansson, Isabella Zini, Kjell Fuxe, and Luigi F. Agnati. The emergence of the volume transmission concept. *Brain Research Reviews*, 26(2-3):136–147, may 1998. ISSN 01650173. doi: 10.1016/S0165-0173(97)00048-9.

[167] Arif A. Hamid, Jeffrey R. Pettibone, Omar S. Mabrouk, Vaughn L. Hetrick, Robert Schmidt, Caitlin M. Vander Weele, Robert T. Kennedy, Brandon J. Aragona, and Joshua D. Berke. Mesolimbic dopamine signals the value of work. *Nature Neuroscience*, 19(1):117–126, jan 2015. ISSN 15461726. doi: 10.1038/nn.4173.

[168] Joshua D. Berke. What does dopamine mean? *Nature Neuroscience*, 21(6): 787–793, jun 2018. ISSN 1097-6256. doi: 10.1038/s41593-018-0152-y.

[169] Christopher J. Watson, B. Jill Venton, and Robert T. Kennedy. In vivo measurements of neurotransmitters by microdialysis sampling. *Analytical Chemistry*, 78(5):1391–1399, 2006. ISSN 00032700. doi: 10.1021/ac0693722.

[170] Christopher J. Endres and Richard E. Carson. Assessment of dynamic neurotransmitter changes with bolus or infusion delivery of neuroreceptor ligands. *Journal of Cerebral Blood Flow and Metabolism*, 18(11):1196–1210, 1998. ISSN 0271678X. doi: 10.1097/00004647-199811000-00006.

[171] Philip Seeman, Natalie H. Bzowej, H. C. Guan, Catherine Bergeron, Gavin P. Reynolds, E. D. Bird, Peter Riederer, Kurt Jellinger, and Wallace W. Tourtellotte. Human brain D1 and D2 dopamine receptors in schizophrenia, Alzheimer's, Parkinson's, and Huntington's diseases. *Neuropsychopharmacology*, 1(1):5–15, dec 1987. ISSN 0893133X. doi: 10.1016/0893-133X(87)90004-2.

[172] E. G. Jönsson, M. M. Nöthen, F. Grünhage, L. Farde, Y. Nakashima, P. Propping, and G. C. Sedvall. Polymorphisms in the dopamine D2 receptor gene and their relationships to striatal dopamine receptor density of healthy volunteers. *Molecular Psychiatry*, 4(3):290–296, 1999. ISSN 13594184. doi: 10.1038/sj.mp.4000532.

[173] Juha O. Rinne, Jarmo Hietala, Ulla Ruotsalainen, Erkki Säkö, Arto Laihinen, Kjell Någren, Pertti Lehikoinen, Vesa Oikonen, and Erkka Syvälahti. Decrease in human striatal dopamine D2 receptor density with age: A PET study with [11C]raclopride. *Journal of Cerebral Blood Flow and Metabolism*, 13(2):310–314, 1993. ISSN 0271678X. doi: 10.1038/jcbfm.1993.39.

[174] D. Benton and H. A. Young. A meta-analysis of the relationship between brain dopamine receptors and obesity: A matter of changes in behavior rather than food addiction. *International Journal of Obesity*, 40(S1):S12–S21, 2016. ISSN 14765497. doi: 10.1038/ijo.2016.9. URL `http://dx.doi.org/10.1038/ijo.2016.9`.

[175] Kati Alakurtti, Jarkko J Johansson, Juho Joutsa, Matti Laine, Lars Bäckman, Lars Nyberg, and Juha O Rinne. Long-term test-retest reliability of striatal and extrastriatal dopamine D2/3 receptor binding: Study with [11C]raclopride and high-resolution PET. *Journal of Cerebral Blood Flow and Metabolism*, 35 (7):1199–1205, jul 2015. ISSN 15597016. doi: 10.1038/jcbfm.2015.53.

[176] Davide Calebiro and Amod Godbole. Internalization of G-protein-coupled receptors: Implication in receptor function, physiology and diseases. *Best Practice and Research: Clinical Endocrinology and Metabolism*, 32(2):83–91, 2018. ISSN 15321908. doi: 10.1016/j.beem.2018.01.004.

[177] Ningning Guo, Wen Guo, Michaela Kralikova, Man Jiang, Ira Schieren, Raj Narendran, Mark Slifstein, Anissa Abi-Dargham, Marc Laruelle, Jonathan a Javitch, and Stephen Rayport. Impact of D2 receptor internalization on binding affinity of neuroimaging radiotracers. *Neuropsychopharmacology*, 35(3):806–817, 2010. ISSN 0893-133X. doi: 10.1038/npp.2009.189.

[178] Nicolas Aznavour and Luc Zimmer. [18F]MPPF as a tool for the in vivo imaging of 5-HT1A receptors in animal and human brain, mar 2007. ISSN 00283908.

[179] Mette Skinbjerg, David R. Sibley, Jonathan A. Javitch, and Anissa Abi-Dargham. Imaging the high-affinity state of the dopamine D2 receptor in vivo: Fact or fiction?, 2012. ISSN 18732968.

[180] Sean P. Barrett, Isabelle Boileau, Johanna Okker, Robert O. Pihl, and Alain Dagher. The hedonic response to cigarette smoking is proportional to dopamine release in the human striatum as measured by positron emission tomography

and [11C]raclopride. *Synapse*, 54(2):65–71, 2004. ISSN 08874476. doi: 10.1002/syn.20066.

[181] Andrew J. Montgomery, Anne R. Lingford-Hughes, Alice Egerton, David J. Nutt, and Paul M. Grasby. The effect of nicotine on striatal dopamine release in man: A [11C]raclopride PET study. *Synapse*, 61(8):637–645, aug 2007. doi: 10.1002/syn.20419.

[182] Nina Karalija, Lars Jonassson, Jarkko Johansson, Goran Papenberg, Alireza Salami, Micael Andersson, Katrine Riklund, Lars Nyberg, and Carl Johan Boraxbekk. High long-term test–retest reliability for extrastriatal 11C-raclopride binding in healthy older adults. *Journal of Cerebral Blood Flow and Metabolism*, 2019. ISSN 15597016. doi: 10.1177/0271678X19874770.

[183] Goran Papenberg, Lars Jonasson, Nina Karalija, Jarkko Johansson, Ylva Köhncke, Alireza Salami, Micael Andersson, Jan Axelsson, Anders Wåhlin, Katrine Riklund, Ulman Lindenberger, Martin Lövdén, Lars Nyberg, and Lars Bäckman. Mapping the landscape of human dopamine D2/3 receptors with [11C]raclopride. *Brain Structure and Function*, 224(8):2871–2882, 2019. ISSN 18632661. doi: 10.1007/s00429-019-01938-1. URL `https://doi.org/10.1007/s00429-019-01938-1`.

[184] Albert Gjedde. Calculation of cerebral glucose phosphorylation from brain uptake of glucose analogs in vivo: A re-examination. *Brain Research Reviews*, 4(2):237–274, jun 1982. ISSN 01650173. doi: 10.1016/0165-0173(82)90018-2.

[185] Paola Piccini, Nicola Pavese, and David J. Brooks. Endogenous dopamine release after pharmacological challenges in Parkinson's disease. *Annals of Neurology*, 53(5):647–653, 2003. ISSN 03645134. doi: 10.1002/ana.10526.

[186] Nobukatsu Sawamoto, Paola Piccini, Gary Hotton, Nicola Pavese, Kris Thielemans, and David J. Brooks. Cognitive deficits and striato-frontal dopamine release in Parkinson's disease. *Brain*, 131(5):1294–1302, 2008. ISSN 14602156. doi: 10.1093/brain/awn054.

[187] Paul R.A. Stokes, Alice Egerton, Ben Watson, Alistair Reid, Gerome Breen, Anne Lingford-Hughes, David J. Nutt, and Mitul A. Mehta. Significant decreases in frontal and temporal [11C]-raclopride binding after THC challenge. *NeuroImage*, 52(4):1521–1527, 2010. ISSN 10538119. doi: 10.1016/j.neuroimage.2010.04.274.

[188] Seth H. Walters, I. Mitch Taylor, Zhan Shu, and Adrian C. Michael. A novel restricted diffusion model of evoked dopamine. *ACS Chemical Neuroscience*, 5 (9):776–783, 2014. ISSN 19487193. doi: 10.1021/cn5000666.

[189] Bradley D. Bath, Darren J. Michael, B. Jill Trafton, Joshua D. Joseph, Petrise L. Runnels, and R. Mark Wightman. Subsecond Adsorption and Desorption of

Dopamine at Carbon-Fiber Microelectrodes. *Analytical Chemistry*, 72(24): 5994–6002, dec 2000. ISSN 00032700. doi: 10.1021/ac000849y.

[190] Seth H. Walters, Elaine M. Robbins, and Adrian C. Michael. Modeling the Kinetic Diversity of Dopamine in the Dorsal Striatum. *ACS Chemical Neuroscience*, 6(8):1468–1475, 2015. ISSN 19487193. doi: 10.1021/acschemneuro.5b00128.

[191] Ethan R. Block, Jacob Nuttle, Judith Joyce Balcita-Pedicino, John Caltagarone, Simon C. Watkins, Susan R. Sesack, and Alexander Sorkin. Brain region-specific trafficking of the dopamine transporter. *Journal of Neuroscience*, 35(37):12845–12858, 2015. ISSN 15292401. doi: 10.1523/JNEUROSCI.1391-15.2015.

[192] Cihan Kaya, Mary H. Cheng, Ethan R. Block, Tom M. Bartol, Terrence J. Sejnowski, Alexander Sorkin, James R. Faeder, and Ivet Bahar. Heterogeneities in axonal structure and transporter distribution lower dopamine reuptake efficiency. *eNeuro*, 5(1), 2018. ISSN 23732822. doi: 10.1523/ENEURO.0298-17.2017.

[193] Hui Zhang and David Sulzer. Frequency-dependent modulation of dopamine release by nicotine. *Nature Neuroscience*, 7(6):581–582, 2004. ISSN 10976256. doi: 10.1038/nn1243.

[194] Yohei Okubo and Masamitsu Iino. Visualization of glutamate as a volume transmitter. *Journal of Physiology*, 589(3):481–488, 2011. ISSN 00223751. doi: 10.1113/jphysiol.2010.199539.

[195] Alexander Jais, Maite Solas, Heiko Backes, Napoleone Ferrara, Gerard Karsenty, and Jens C Bru. Myeloid-Cell-Derived VEGF Maintains Brain Glucose Uptake and Limits Cognitive Impairment in Obesity Article Myeloid-Cell-Derived VEGF Maintains Brain Glucose Uptake and Limits Cognitive Impairment in Obesity. *Cell*, 165(4):882–895, 2016. ISSN 0092-8674. doi: 10.1016/j.cell.2016.03.033.

[196] Alexander Jais, Lars Paeger, Tamara Sotelo-Hitschfeld, Stephan Bremser, Melanie Prinzensteiner, Paul Klemm, Vasyl Mykytiuk, Pia J M Widdershooven, Anna Juliane Vesting, Katarzyna Grzelka, Marielle Minère, Anna Lena Cremer, Jie Xu, Tatiana Korotkova, Bradford B. Lowell, Hanns Ulrich Zeilhofer, Heiko Backes, Henning Fenselau, F Thomas Wunderlich, Peter Kloppenburg, and Jens C. Brüning. PNOCARC Neurons Promote Hyperphagia and Obesity upon High-Fat-Diet Feeding. *Neuron*, pages 1–17, apr 2020. ISSN 1097-4199. doi: 10.1016/j.neuron.2020.03.022.

[197] Lale Umutlu, Thomas Beyer, Johannes Stefan Grueneisen, Christoph Rischpler, Harald H Quick, Patrick Veit-haibach, Matthias Eiber, Sandra Purz, Gerald Antoch, Sergios Gatidis, Konstantin Nikolaou, Jürgen F Schaefer, and Ivo Rausch. Whole-Body [18F] -FDG-PET / MRI for Oncology : A Consensus

Konsensempfehlungen zur Anwendung der Ganzkörper [18F] -FDG-PET / MRT in der onkologischen Bildgebung Authors. pages 289–297, 2019. doi: 10.1055/a-0828-8654.

[198] Arman Rahmim, Martin A. Lodge, Nicolas A. Karakatsanis, Vladimir Y. Panin, Yun Zhou, Alan McMillan, Steve Cho, Habib Zaidi, Michael E. Casey, and Richard L. Wahl. Dynamic whole-body PET imaging: principles, potentials and applications. *European Journal of Nuclear Medicine and Molecular Imaging*, 46(2):501–518, 2019. ISSN 16197089. doi: 10.1007/s00259-018-4153-6.

[199] Simon R. Cherry, Ramsey D. Badawi, Joel S. Karp, William W. Moses, Pat Price, and Terry Jones. Total-body imaging: Transforming the role of positron emission tomography. *Science Translational Medicine*, 9(381), mar 2017. ISSN 1946-6234. doi: 10.1126/scitranslmed.aaf6169.

[200] Stephan Herzig. *Metabolic Control*, volume 233 of *Handbook of Experimental Pharmacology*. Springer International Publishing, 2016. ISBN 978-3-319-29804-7. doi: 10.1007/978-3-319-29806-1.

[201] Jingjing Zhang and Feng Liu. Tissue-specific insulin signaling in the regulation of metabolism and aging. *IUBMB Life*, 66(7):485–495, 2014. ISSN 15216551. doi: 10.1002/iub.1293.

[202] S. Kersten. Mechanisms of nutritional and hormonal regulation of lipogenesis. *EMBO Reports*, 2(4):282–286, 2001. ISSN 1469221X. doi: 10.1093/embo-reports/kve071.

[203] Sellam Karunanithi, Ramya Soundararajan, Punit Sharma, Niraj Naswa, Chandrasekhar Bal, and Rakesh Kumar. Spectrum of physiologic and pathologic skeletal muscle 18F-FDG uptake on PET/CT. *American Journal of Roentgenology*, 205(2):W141–W149, 2015. ISSN 15463141. doi: 10.2214/AJR.14.13457.

[204] Girish Kumar Parida, Shambo Guha Roy, and Rakesh Kumar. FDG-PET/CT in Skeletal Muscle: Pitfalls and Pathologies. *Seminars in Nuclear Medicine*, 47 (4):362–372, 2017. ISSN 15584623. doi: 10.1053/j.semnuclmed.2017.02.003.

[205] Olivier Gheysens, Andrey Postnov, Christophe M. Deroose, Corinne Vandermeulen, Jan De Hoon, Ruben Declercq, Justin Dennie, Lori Mixson, Inge De Lepeleire, Koen Van Laere, Michael Klimas, and Manu V. Chakravarthy. Quantification, variability, and reproducibility of basal skeletal muscle glucose uptake in healthy humans using 18F-FDG PET/CT. *Journal of Nuclear Medicine*, 56 (10):1520–1526, 2015. ISSN 01615505. doi: 10.2967/jnumed.115.159715.

[206] Alexander Bartelt and Joerg Heeren. Adipose tissue browning and metabolic health. *Nature Reviews Endocrinology*, 10(1):24–36, 2014. ISSN 17595037. doi: 10.1038/nrendo.2013.204.

[207] Natasa Petrovic, Tomas B. Walden, Irina G. Shabalina, James A. Timmons, Barbara Cannon, and Jan Nedergaard. Chronic peroxisome proliferator-activated receptor γ (PPARγ) activation of epididymally derived white adipocyte cultures reveals a population of thermogenically competent, UCP1-containing adipocytes molecularly distinct from classic brown adipocytes. *Journal of Biological Chemistry*, 285(10):7153–7164, 2010. ISSN 00219258. doi: 10.1074/jbc.M109.053942.

[208] P. Young, J. R.S. Arch, and Margaret Ashwell. Brown adipose tissue in the parametrial fat pad of the mouse. *FEBS Letters*, 167(1):10–14, 1984. ISSN 00145793. doi: 10.1016/0014-5793(84)80822-4.

[209] Xukui Wang, Laurie J. Minze, and Zheng Zheng Shi. Functional imaging of brown fat in mice with 18F-FDG micro-PET/CT. *Journal of Visualized Experiments*, (69):1–4, 2012. ISSN 1940087X. doi: 10.3791/4060.

[210] Pasquina Marzola, Federico Boschi, Francesco Moneta, Andrea Sbarbati, and Carlo Zancanaro. Preclinical in vivo imaging for fat tissue identification, quantification, and functional characterization. *Frontiers in Pharmacology*, 7 (SEP):1–14, 2016. ISSN 16639812. doi: 10.3389/fphar.2016.00336.

[211] Matthias Bauwens, Roel Wierts, Bart Van Royen, Jan Bucerius, Walter Backes, Felix Mottaghy, and Boudewijn Brans. Molecular imaging of brown adipose tissue in health and disease. *European Journal of Nuclear Medicine and Molecular Imaging*, 41(4):776–791, 2014. ISSN 16197089. doi: 10.1007/s00259-013-2611-8.

[212] Shingo Baba, Heather A. Jacene, James M. Engles, Hiroshi Honda, and Richard L. Wahl. CT Hounsfield units of brown adipose tissue increase with activation: preclinical and clinical studies. *Journal of Nuclear Medicine*, 51(2): 246–250, 2010. ISSN 01615505. doi: 10.2967/jnumed.109.068775.

[213] Thomas F. Hany, Esmaiel Gharehpapagh, Ehab M. Kamel, Alfred Buck, Jean Himms-Hagen, and Gustav K. Von Schulthess. Brown adipose tissue: A factor to consider in symmetrical tracer uptake in the neck and upper chest region. *European Journal of Nuclear Medicine*, 29(10):1393–1398, 2002. ISSN 03406997. doi: 10.1007/s00259-002-0902-6.

[214] Leeta A. Green, Sanjiv S. Gambhir, Ashok Srinivasan, Pranab K. Banerjee, Carl K. Hoh, Simon R. Cherry, Susan Sharfstein, Jorge R. Barrio, Harvey R. Herschman, and Michael E. Phelps. Noninvasive methods for quantitating blood time-activity curves from mouse PET images obtained with fluorine-18-fluorodeoxyglucose. *Journal of Nuclear Medicine*, 39(4):729–734, 1998. ISSN 01615505.

[215] M. S. Farvid, T. W. K. Ng, D. C. Chan, P. H. R. Barrett, and G. F. Watts. Association of adiponectin and resistin with adipose tissue compartments, insulin resistance and dyslipidaemia. *Diabetes, Obesity and Metabolism*, 7(4): 406–413, jul 2005. ISSN 1462-8902. doi: 10.1111/j.1463-1326.2004.00410.x.

[216] ICRP. Annexes A-D. *Annals of the ICRP*, 39(2):47–70, 2009. ISSN 01466453. doi: 10.1016/j.icrp.2009.07.005.

[217] Danielle R. Reed, Alexander A. Bachmanov, and Michael G. Tordoff. Forty mouse strain survey of body composition. *Physiology and Behavior*, 91(5): 593–600, 2007. ISSN 00319384. doi: 10.1016/j.physbeh.2007.03.026.

[218] TM M John Walker, Gary Foster, Elisabeth Johansen, Yiguo Hong, Peter Nagy, Darwin J Prockop, Douglas G Phinney, Bruce A Brunnell, Greg Davis, Kevin J Kayser, Andreas Marx, and Oliver Seitz. *Adipose Tissue Protocols Methods in Molecular Biology*, volume 457. 2008. ISBN 9781588299161.

[219] Jeffrey T. Yap, Nathan C. Hall, David W. Townsend, Jonathan S. Wall, Alan Solomon, George W. Kabalka, Steve J. Kennel, Danny F. Newport, Stefan B. Siegel, David Bailey, Anne M. Smith, and Robert E. Nutt. Combined clinical PET/CT and microPET® small animal imaging. *IEEE Nuclear Science Symposium Conference Record*, 5(January 2014):2995–2998, 2004. ISSN 10957863. doi: 10.1109/nssmic.2004.1466314.

[220] Srihari C. Sampath, Srinath C. Sampath, Miriam A. Bredella, Aaron M. Cypess, and Martin Torriani. Imaging of Brown Adipose Tissue: State of the Art. *Radiology*, 280(1):4–19, jul 2016. ISSN 0033-8419. doi: 10.1148/radiol.2016150390.

[221] Joseph Frankl, Amber Sherwood, Deborah J. Clegg, Philipp E. Scherer, and Orhan K. Öz. Imaging metabolically active fat: A literature review and mechanistic insights. *International Journal of Molecular Sciences*, 20(21), 2019. ISSN 14220067. doi: 10.3390/ijms20215509.

[222] Mohammed K Hankir and Martin Klingenspor. Brown adipocyte glucose metabolism: a heated subject. *EMBO reports*, 19(9):1–13, 2018. ISSN 1469-221X. doi: 10.15252/embr.201846404.

[223] Kong Y. Chen, Aaron M. Cypess, Maren R. Laughlin, Carol R. Haft, Houchun Harry Hu, Miriam A. Bredella, Sven Enerbäck, Paul E. Kinahan, Wouter van Marken Lichtenbelt, Frank I. Lin, John J. Sunderland, Kirsi A. Virtanen, and Richard L. Wahl. Brown Adipose Reporting Criteria in Imaging STudies (BARCIST 1.0): Recommendations for Standardized FDG-PET/CT Experiments in Humans. *Cell Metabolism*, 24(2):210–222, 2016. ISSN 19327420. doi: 10.1016/j.cmet.2016.07.014.

[224] Kirsi A. Virtanen. The rediscovery of BAT in adult humans using imaging. *Best Practice and Research: Clinical Endocrinology and Metabolism*, 30(4): 471–477, 2016. ISSN 15321908. doi: 10.1016/j.beem.2016.09.001.

[225] Frank J. Ong, Basma A. Ahmed, Stephan M. Oreskovich, Denis P. Blondin, Tahniyah Haq, Norman B. Konyer, Michael D. Noseworthy, Francois Haman,

Andre C. Carpentier, Katherine M. Morrison, and Gregory R. Steinberg. Recent advances in the detection of brown adipose tissue in adult humans: A review. *Clinical Science*, 132(10):1039–1054, 2018. ISSN 14708736. doi: 10.1042/CS20170276.

[226] Alexander Bartelt, Oliver T. Bruns, Rudolph Reimer, Heinz Hohenberg, Harald Ittrich, Kersten Peldschus, Michael G. Kaul, Ulrich I. Tromsdorf, Horst Weller, Christian Waurisch, Alexander Eychmüller, Philip L.S.M. Gordts, Franz Rinninger, Karoline Bruegelmann, Barbara Freund, Peter Nielsen, Martin Merkel, and Joerg Heeren. Brown adipose tissue activity controls triglyceride clearance. *Nature Medicine*, 17(2):200–206, 2011. ISSN 10788956. doi: 10.1038/nm.2297.

[227] Brooks P. Leitner, Shan Huang, Robert J. Brychta, Courtney J. Duckworth, Alison S. Baskin, Suzanne McGehee, Ilan Tal, William Dieckmann, Garima Gupta, Gerald M. Kolodny, Karel Pacak, Peter Herscovitch, Aaron M. Cypess, and Kong Y. Chen. Mapping of human brown adipose tissue in lean and obese young men. *Proceedings of the National Academy of Sciences of the United States of America*, 114(32):8649–8654, 2017. ISSN 10916490. doi: 10.1073/pnas.1705287114.

[228] André C. Carpentier, Denis P. Blondin, Kirsi A. Virtanen, Denis Richard, François Haman, and Éric E. Turcotte. Brown Adipose Tissue Energy Metabolism in Humans. *Frontiers in Endocrinology*, 9(AUG):1–21, aug 2018. ISSN 1664-2392. doi: 10.3389/fendo.2018.00447.

[229] Camilla Scheele and Søren Nielsen. Metabolic regulation and the anti-obesity perspectives of human brown fat. *Redox Biology*, 12(April):770–775, 2017. ISSN 22132317. doi: 10.1016/j.redox.2017.04.011.

[230] Marie Anne Richard, Hannah Pallubinsky, and Denis P. Blondin. Functional characterization of human brown adipose tissue metabolism. *Biochemical Journal*, 477(7):1261–1286, apr 2020. ISSN 0264-6021. doi: 10.1042/BCJ20190464.

Acknowledgment

Scientific research is a group effort: today, most scientific questions are interdisciplinary and contributions from individual experts are combined to progress and succeed. So is this work not a result of my sole contribution, but was supported by a lot of important persons. Therefore, I want to take the chance to thank all who accompanied me towards my PhD graduation in so many different ways.
First, I would like to thank Prof. Dr. Jens Brüning for the opportunity to work at the Max Planck Institute for Metabolism Research. I highly appreciate the scientific insights I could gather and the chance to participate in various different research projects. The scientific environment within the institute is very inspiring, motivating and extremely interesting. For sure, this kind of environment is only sustainable by the contribution of the members. Therefore, I want thank all my great colleagues at the Max Planck Institute for Metabolism Research, especially for the friendly atmosphere at and beyond work. Thank you for the good cooperation, fruitful discussions and personal relationships within the last years. I really enjoyed the time with all of you.
I am glad I had the chance to get to know Prof. Dr. Rudolf Graf, who used to be a very inspiring person and who supported my work for several years. Thank you for giving me the opportunity to be part of the Multimodal Imaging Group and for giving me insights about all your scientific experiences.
I want to acknowledge Prof. Dr. Jens Mittag for accepting to supervise my thesis under the special circumstances for the last months and the effective and enjoyable cooperation within the last four years. The work with Dr. Kornelia Johann and Dr. Lisbeth Harder was exciting and fruitful.
Many thanks go to Prof. Dr. Thomas Heinzel for taking over the mentorship of my thesis and giving me the possibility to graduate at the University of Düsseldorf, where I started my scientific career with a Bachelor in Medical Physics.
I want to thank Carmen Selbach for her ongoing technical support and for teaching me the first steps at the time I started in the working group.
Furthermore, I thank Prof. Dr. Marc Tittgemeyer and Dr. Sharmili Edwin Thanarajah for conceiving and performing the human [11C]raclopride PET study in collaboration with Dr. Heiko Backes.
Special thanks go to Dr. Rachel Lippert for the productive cooperation on the [11C]raclopride PET and voltammetry projects in the chemogenetic mouse model. I appreciate your organizing talent and am thankful for your input and effort.
The great contribution by the group of Prof. Dr. Mark Walton of the University of Oxford, namely Dr. Clio Korn, Dr. Lauren Burgeno and Dr. Thomas Jahans-Price was indispensable for this work. Thank you for performing the ambitious voltammetry experiments and for supporting us in our research objectives also beyond that.

Prof. Dr. Parastoo Hashemi kindly provided 5-HT fast-scan voltammetry data acquired by Alyssa West. Thank you for the straightforward and effective cooperation.

My deepest appreciation goes to Dr. Heiko Backes, who supervised my doctoral work on an every day basis. Thank you for the great scientific education, all the meaningful discussions and for always thinking critical. I truly appreciate your support, sustained patience and constant encouragement. Without you this work would not have been possible.
Last but not least, my sincerest thanks go to my family for supporting me throughout my doctorate period - as always - and for making me to who I am. I am happy to be encouraged by your untiring care, motivation and love.

Curriculum Vitae

Personal Information	
Name:	Anna Lena Cremer
Date of birth:	October 24, 1990 in Bergisch Gladbach, Germany
Email:	anna-lena.cremer@sf.mpg.de or anna.cremer@web.de
Academic Education	
04/2016 – present	PHD GRADUATION Max Planck Institute for Metabolism Research in Cologne, Germany
10/2013 – 10/2015	MASTER OF SCIENCES IN PHYSICS Albert-Ludwigs-University and University Medical Center in Freiburg, Germany
10/2010 – 09/2013	BACHELOR OF SCIENCES IN MEDICAL PHYSICS Heinrich-Heine-University Duesseldorf, Germany
Research Assistance	
10/2014 – 10/2015	RESEARCH ASSISTANT University Medical Center Freiburg, Medical Physics Department in the Hyperpolarization Group
01/2014 – 11/2014	RESEARCH ASSISTANT Fraunhofer Institute for Solar Energy Systems (ISE) Freiburg in the Department for Service Life of Modules and Materials
04/2013 – 06/2013	PHYSICAL LAB COURSE TUTOR FOR MEDICAL STUDENTS Heinrich-Heine-University Duesseldorf
Conferences and Meetings	
Talks	DKE 2019, Goettingen (invited talk); Brain & BrainPET 2017, Berlin (Early Career Investigator Travel Bursary)
Poster Presentations	GRC on Catecholamines 2019, Newry; MMiN 2018, Oxford; EMIM 2017, Cologne; EMIM 2015, Tuebingen (Poster Award)
Participations	From Research to Application 2019, Berlin; Visions in Science 2018, Berlin; Science of Translation 2018, Cologne; Summer School on Hyperpolarization 2014, Marseille
Skills and Qualifications	
Languages	German (native language), English (fluent)
IT	Basic: Python, R, Matlab Intermediate to Advanced: C, IDl, LaTeX, OpenOffice, Linux
Certifications	Radiation Protection Course (2013) Certification for laboratory animal science: FELASA (2016)

List of Publications

05/2020 GLP-1 Receptor Signaling in Astrocytes Regulates Fatty Acid Oxidation, Mitochondrial Integrity, and Function – Cell Metabolism

Authors: Timper, K.; Del Rio-Martin, A.; **Cremer, A.L.**; Bremser, S.; Alber, J.; Giavalisco, P.; Varela, L.; Heilinger, C.; Nolte, H.; Trifunovic, A.; Horvath, T.L.; Kloppenburg, P.; Backes, H.; Brüning J.C.

Abstract: Astrocytes represent central regulators of brain glucose metabolism and neuronal function. They have recently been shown to adapt their function in response to alterations in nutritional state through responding to the energy state-sensing hormones leptin and insulin. Here, we demonstrate that glucagon-like peptide (GLP)-1 inhibits glucose uptake and promotes β-oxidation in cultured astrocytes. Conversely, postnatal GLP-1 receptor (GLP-1R) deletion in glial fibrillary acidic protein (GFAP)-expressing astrocytes impairs astrocyte mitochondrial integrity and activates an integrated stress response with enhanced fibroblast growth factor (FGF)21 production and increased brain glucose uptake. Accordingly, central neutralization of FGF21 or astrocyte-specific FGF21 inactivation abrogates the improvements in glucose tolerance and learning in mice lacking GLP-1R expression in astrocytes. Collectively, these experiments reveal a role for astrocyte GLP-1R signaling in maintaining mitochondrial integrity, and lack of GLP-1R signaling mounts an adaptive stress response resulting in an improvement of systemic glucose homeostasis and memory formation.

04/2020 PNOC^{ARC} Neurons Promote Hyperphagia and Obesity upon High-Fat-Diet Feeding – Neuron

Authors: A. Jais and L. Paeger; T. Sotelo Hitschfeld; S. Bremser; M. Prinzensteiner; P. Klemm; V. Mykytiuk; P. J. M. Widdershooven; A. J. Vesting; K. Grzelka; M. Minère; **A. L. Cremer**; J. Xu; T. Korotkova; B. B. Lowell; H. U. Zeilhofer; H. Backes; H. Fenselau; F. T. Wunderlich; P. Kloppenburg; J. C. Brüning

Abstract: Calorie-rich diets induce hyperphagia and promote obesity, although the underlying mechanisms remain poorly defined. We find that short-term high-fat-diet (HFD) feeding of mice activates prepronociceptin (PNOC)-expressing neurons in the arcuate nucleus of the hypothalamus (ARC). PNOC^{ARC} neurons represent a previously unrecognized GABAergic population of ARC neurons distinct from well-defined feeding regulatory AgRP or POMC neurons. PNOC^{ARC} neurons arborize densely in the ARC and provide inhibitory synaptic input to nearby anorexigenic POMC neurons. Optogenetic activation of PNOC^{ARC} neurons in the ARC and their projections to the bed nucleus of the stria terminalis promotes feeding. Selective ablation of these cells promotes the activation of POMC neurons upon HFD exposure, reduces feeding, and protects from obesity, but it does not affect food intake or body weight under normal chow consumption. We characterize PNOC^{ARC} neurons as a novel ARC neuron population activated upon palatable food consumption to promote hyperphagia.

06/2019 Thyroid-Hormone-Induced Browning of White Adipose Tissue Does Not Contribute to Thermogenesis and Glucose Consumption – Cell Reports

Authors: Johann, K., **Cremer, A. L.**; Fischer, A.; Heine, M.; Rial Pensado E.; Resch, J.; Nock, S.; Virtue, S.; Harder, L.; Oelkrug, R.; Astiz, M., Brabant, G.; Warner, A.; Vidal-Puig, A.; Oster, H.; Boelen, A.; Lopez, M.; Heeren, J.; Dalley, J.W.; Backes, H.; Mittag, J.

Abstract: Regulation of body temperature critically depends on thyroid hormone (TH). Recent studies revealed that TH induces browning of white adipose tissue, possibly contributing to the observed hyperthermia in hyperthyroid patients and potentially providing metabolic benefits. Here, we show that browning by TH requires TH-receptor b and occurs independently of the sympathetic nervous system. The beige fat, however, lacks sufficient adrenergic stimulation and is not metabolically activated despite high levels of uncoupling protein 1 (UCP1). Studies at different environmental temperatures reveal that TH instead causes hyperthermia by actions in skeletal muscle combined with a central body temperature set-point elevation. Consequently, the metabolic and thermogenic effects of systemic hyperthyroidism were maintained in UCP1 knockout mice, demonstrating that neither beige nor brown fat contributes to the TH-induced hyperthermia and elevated glucose consumption, and underlining that the mere presence of UCP1 is insufficient to draw conclusions on the therapeutic potential of browning agents.

01/2019 Time-dependent assessment of stimulus-evoked regional dopamine release – Nature Communications

Authors: Lippert, R. N.* and **Cremer, A. L.***; Edwin Thanarajah, S.; Korn, C.; Jahans-Price, T.; Burgeno, L. M.; Tittgemeyer, M.; Brüning, J. C.; Walton, M. E.; Backes, H.; *equal contribution

Abstract: To date, the spatiotemporal release of specific neurotransmitters at physiological levels in the human brain cannot be detected. Here, we present a method that relates minute-by-minute fluctuations of the positron emission tomography (PET) radioligand [11C]raclopride directly to subsecond dopamine release events. We show theoretically that synaptic dopamine release induces low frequency temporal variations of extrasynaptic extracellular dopamine levels, at time scales of one minute, that can evoke detectable temporal variations in the [11C] raclopride signal. Hence, dopaminergic activity can be monitored via temporal fluctuations in the [11C]raclopride PET signal. We validate this theory using fast-scan cyclic voltammetry and [11C]raclopride PET in mice during chemogenetic activation of dopaminergic neurons. We then apply the method to data from human subjects given a palatable milkshake and discover immediate and - for the first time - delayed food-induced dopamine release. This method enables time-dependent regional monitoring of stimulus-evoked dopamine release at physiological levels.

12/2018 Food Intake Recruits Orosensory and Post-ingestive Dopaminergic Circuits to Affect Eating Desire in Humans – Cell Metabolism
Authors: Edwin Thanarajah, S. and Backes, H.; DiFeliceantonio, A. G.; Albus, K.; **Cremer, A. L.**; Hanssen, R.; Lippert, R. N.; Cornely, O. A.; Small, D. M.; Brüning, J. C.; Tittgemeyer, M.
Abstract: Pleasant taste and nutritional value guide food selection behavior. Here, orosensory features of food may be secondary to its nutritional value in underlying reinforcement, but it is unclear how the brain encodes the reward value of food. Orosensory and peripheral physiological signals may act together on dopaminergic circuits to drive food intake. We combined fMRI and a novel [11C]raclopride PET method to assess systems-level activation and dopamine release in response to palatable food intake in humans. We identified immediate orosensory and delayed post-ingestive dopamine release. Both responses recruit segregated brain regions: specialized integrative pathways and higher cognitive centers. Furthermore, we identified brain areas where dopamine release reflected the subjective desire to eat. Immediate dopamine release in these wanting-related regions was inversely correlated with, and presumably inhibited, post-ingestive release in the dorsal striatum. Our results highlight the role of brain and periphery in interacting to reinforce food intake in humans.

05/2016 Molecular MRI in the Earth's Magnetic Field Using Continuous Hyperpolarization of a Biomolecule in Water. – Journal of Physical Chemistry B
Authors: Rovedo, P.; Knecht, S.; Bäumlisberger, T.; **Cremer, A.L.**; Duckett, S.B.; Mewis, R.E.; Green, G.G.R.; Burns, M.; Rayner, P.J.; Leibfritz, D.; Korvink, J.G.; Hennig, J.; Pütz, G.; Von Elverfeldt, D.; Hövener, J.-B.
Abstract: In this work, we illustrate a method to continuously hyperpolarize a biomolecule, nicotinamide, in water using parahydrogen and signal amplification by reversible exchange (SABRE). Building on the preparation procedure described recently by Truong et al. [J. Phys. Chem. B, 2014, 118, 13882-13889], aqueous solutions of nicotinamide and an Ir-IMes catalyst were prepared for low-field NMR and MRI. The 1H-polarization was continuously renewed and monitored by NMR experiments at 5.9 mT for more than 1000 s. The polarization achieved corresponds to that induced by a 46 T magnet (P = 1.6 x 10-4) or an enhancement of 104. The polarization persisted, although reduced, if cell culture medium (DPBS with Ca2+ and Mg2+) or human cells (HL-60) were added, but was no longer observable after the addition of human blood. Using a portable MRI unit, fast 1H-MRI was enabled by cycling the magnetic field between 5 mT and the Earth's field for hyperpolarization and imaging, respectively. A model describing the underlying spin physics was developed that revealed a polarization pattern depending on both contact time and magnetic field. Furthermore, the model predicts an opposite phase of the dihydrogen and substrate signal after one exchange, which is likely to result in the cancelation of some signal at low field.

Appendix

A.1 Spatiotemporal Assessment of Neurotransmitter Release using PET

A.1.1 FSCV Measurements of Dopamine

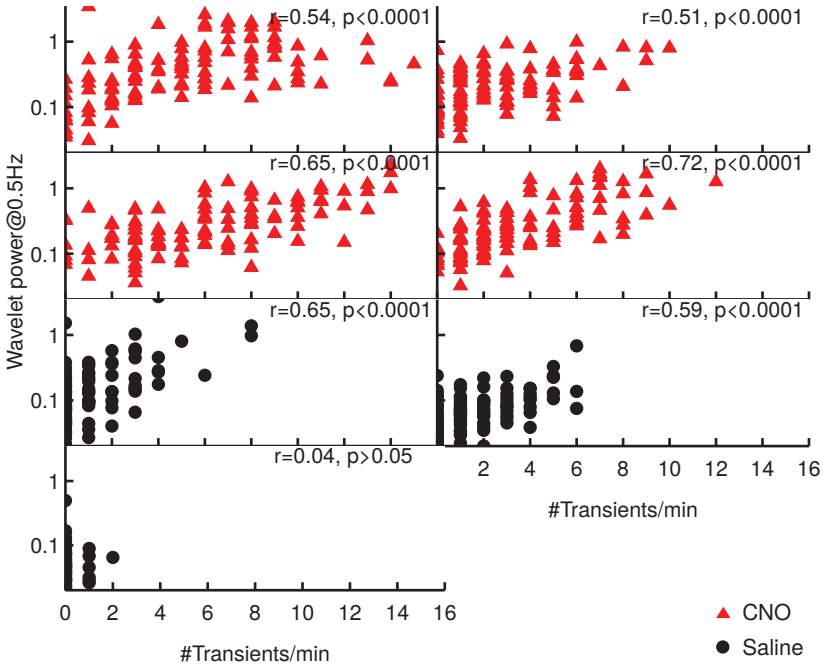

Figure A.1: Correlations between transient rates and wavelet power at 0.5 Hz in individual animals. Wavelet power at 0.5 Hz and transients rates of the individual $hM3D_{Gq}{}^{DAT}$ mice. Wavelet power at 0.5 Hz and transient rates in one-minute intervals correlated significantly with Pearson's product-moment correlation coefficient rgt0.5 with the exception of the last mouse (red triangles=$hM3D_{Gq}{}^{DAT}$+CNO; black circles=$hM3D_{Gq}{}^{DAT}$+Saline). Figure (modified) from Supplemental Information of Lippert and Cremer et al. [86]

A.1.2 FSCV Model Calculations

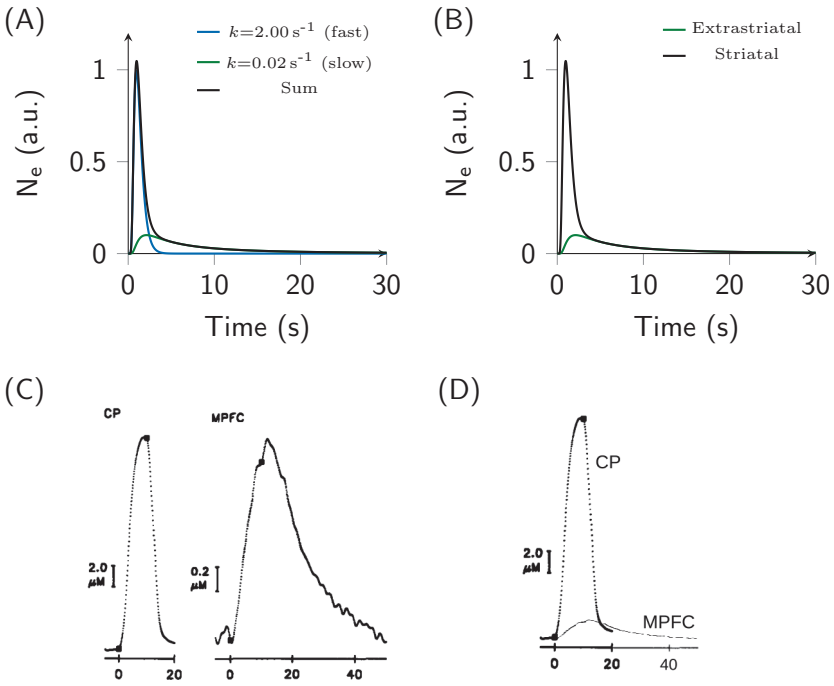

Figure A.2: Extracellular dopamine concentrations after phasic release. (A) Calculated extracellular dopamine concentrations at the location of an FSCV electrode (black) assuming that the signal contains contributions from a fast (blue) with high density of DATs and a slow domain (green) with a low density of DATs. Dopamine is removed from the fast domain at a rate of s^{-1} and from the slow domain at a rate of min^{-1}. Although the overall FSCV signal in the striatum is dominated by the signal from the fast domain, the slow domain determines variations of extracellular dopamine concentration on a minute-by-minute scale. The amplitudes of both, the fast and the slow domain, depend on synaptic dopamine release. (B) The peak amplitude of dopamine transients in extrastriatal regions is lower due to the lower spatial density of dopamine synapses (green). All of the released dopamine is removed at minute time scale due to the lower density of DATs in extrastriatal regions in comparison to the striatum. Consequently the amplitude of minute-by-minute changes in extracellular dopamine concentration is the same in extrastriatal and striatal regions (black). (C) Simultaneous FSCV recordings from the caudate putamen/striatum (CP) and the medial prefrontal cortex (MPFC) in rats after electrical stimulation of the VTA by Garris et al. support this theory [109]. In order to evoke a detectable signal in the MPFC the VTA was stimulated at superphysiological amplitudes. (D) Combination of the CP and MPFC traces in a single graph indicates that the tail representing slowly removed dopamine in the CP is of the same magnitude as the extrastriatal signal. Figure (modified) and description as in Lippert and Cremer et al. [86].

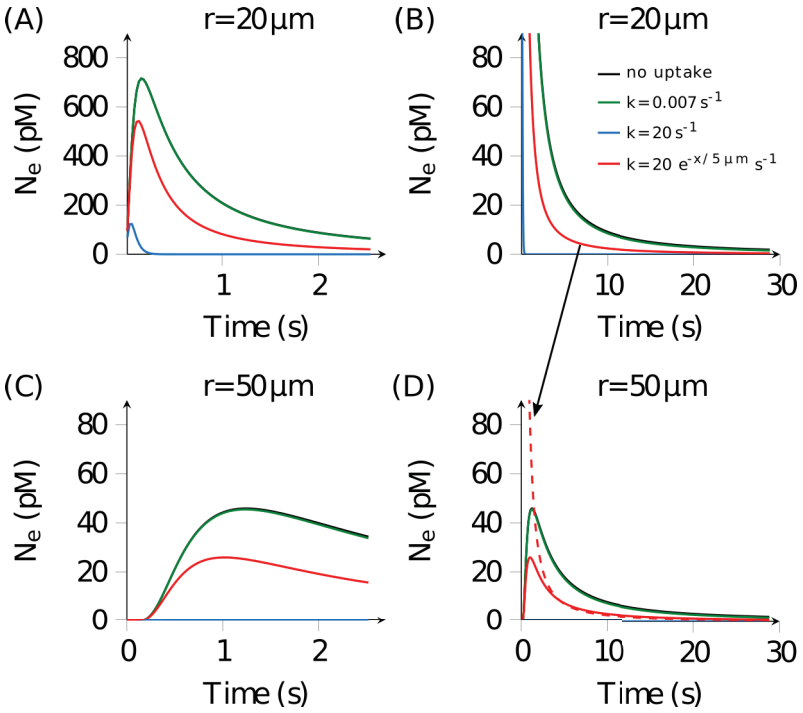

Figure A.3: Dopamine transients after quantal release in tissue with heterogeneous DAT expression. The model for quantal release of 9800 dopamine molecules is identical to that used by Cragg and Rice [99] with the difference that the differential equation is solved numerically instead of using the analytical solution. In this way the model can be calculated for any spatial distribution of DATs. (A) Extracellular dopamine concentration during the first two seconds after quantal release at a distance of 20 μm from the release site. The traces for high (blue) and low (black and green) homogenous DAT expression are identical to those in Figure 1 of Cragg and Rice. Assuming exponential decrease of DAT expression as a function of distance from the release site reduces the peak height (red). (B) Extracellular dopamine concentration during the first 30 seconds after quantal release. If dopamine kinetics is determined by diffusion only (no uptake, black), a noticeable fraction of dopamine is cleared at a minute time scale while at high homogenous DAT expression all dopamine is removed within 0.5 seconds (blue). A small but noticeable minute time scale component is also present at exponential decrease of DAT expression from the release site (red). (C) and (D) show extracellular dopamine concentrations 50 μ from the release site. While the fast component, that determines the peak, critically depends on the distance from the release site, the minute time scale slow component is nearly identical at 20 μ and 50 μ distance. Figure (modified) from Supplemental Information of Lippert and Cremer et al. [86].

A.1.3 Full Publications

Within the framework of this thesis two manuscripts were published, which can be found as full version below.
The first manuscript contains (part of) the model calculations and validation of the introduced novel method for [11C]raclopride PET data analysis:

Title: "Time-dependent assessment of stimulus-evoked regional dopamine release"
Published in: Nature Communications, 2019, Volume 10
Authors: Rachel N. Lippert[1]* and Anna Lena Cremer[1]*,
Sharmili Edwin Thanarajah[1,2], Clio Korn[3,4], Thomas Jahans-Price[4], Lauren M. Burgeno[4], Marc Tittgemeyer[1,5,6], Jens C. Brüning[1,5,7], Mark E. Walton[4,8], Heiko Backes[1]
*Authors contributed equally

[1]Max Planck Institute for Metabolism Research, Cologne, Germany
[2]Department of Neurology, University Hospital of Cologne, Cologne, Germany
[3]Department of Psychiatry, University of Oxford, Warneford Hospital, Oxford, UK
[4]Department of Experimental Psychology, University of Oxford, Oxford, UK
[5]Cologne Cluster of Excellence in Cellular Stress and Aging-Associated Disease (CECAD), Cologne, Germany
[6]Modern Diet and Physiology Research Center, New Haven, CT, USA
[7]Center for Endocrinology, Diabetes and Preventive Medicine (CEPD), University Hospital of Cologne, Cologne, Germany
[8]Wellcome Centre for Integrative Neuroimaging, Department of Experimental Psychology, University of Oxford, Oxford, UK

Contributions: Within this manuscript A. L. Cremer conducted the [11C]raclopride PET measurements in the chemogenetic mouse model. Furthermore, A. L. Cremer analyzed the [11C]raclopride PET data. She programmed the applied computer scripts in IDL and C. Model calculations were performed by A. L. Cremer under supervision of Heiko Backes. The FSCV wavelet data analysis was programmed and conducted by A. L. Cremer. Furthermore, A. L. Cremer visualized the data in form of the Figures in the manuscript (except of Figures 3 and 10). A. L. Cremer reviewed and edited the manuscript.

The second manuscripts contains data of [11C]raclopride PET scans in humans, which is analyzed based on the method developed within the framework of this thesis. The results of this study that are shown within this thesis, are used to demonstrate the power of the novel method. The complete results as well as discussion of the data is published in the manuscript by Sharmili Edwin Thanarajah and Heiko Backes et al.:

Title: "Food Intake Recruits Orosensory and Post-ingestive Dopaminergic Circuits to Affect Eating Desire in Humans"
Published in: Cell Metabolism, 2018, Volume 29
Authors: Sharmili Edwin Thanarajah* and Heiko Backes*, Alexandra G. DiFeliceantonio, Kerstin Albus, Anna Lena Cremer, Ruth Hanssen, Rachel N. Lippert,

Oliver A. Cornely, Dana M. Small, Jens C. Brüning, Marc Tittgemeyer.
*Authors contributed equally
[1]Max Planck Institute for Metabolism Research, Cologne, Germany
[2]Department of Neurology, University Hospital of Cologne, Cologne, Germany
[3]Department of Psychiatry, Yale University School of Medicine, New Haven, CT, USA
[4]Cologne Cluster of Excellence in Cellular Stress and Aging-Associated Disease (CECAD), Cologne, Germany
[5]Department I of Internal Medicine, University Hospital of Cologne, Cologne, Germany
[6]Center for Endocrinology, Diabetes and Preventive Medicine (CEPD), University Hospital of Cologne, Cologne, Germany
[7]Department of Psychology, Yale University, New Haven, CT, USA
[8]Modern Diet and Physiology Research Center, New Haven, CT, USA
[9]Clinical Trials Centre Cologne (ZKS Köln), University of Cologne, Cologne, Germany
[10]Department of Neuroscience, Icahn School of Medicine at Mount Sinai, New York, NY, USA

Contributions: The method applied in this manuscript to analyze the [11C]raclopride PET data was developed by Heiko Backes and A. L. Cremer as presented in the manuscript above. A. L. Cremer contributed to post-processing and visualization of the human [11C]raclopride PET data and reviewed the manuscript.

nature COMMUNICATIONS

ARTICLE

https://doi.org/10.1038/s41467-018-08143-4 OPEN

Time-dependent assessment of stimulus-evoked regional dopamine release

Rachel N. Lippert[1], Anna Lena Cremer[1], Sharmili Edwin Thanarajah[1,2], Clio Korn[3,4], Thomas Jahans-Price[4], Lauren M. Burgeno[4], Marc Tittgemeyer[1,5,6], Jens C. Brüning[1,5,7], Mark E. Walton[4,8] & Heiko Backes[1]

To date, the spatiotemporal release of specific neurotransmitters at physiological levels in the human brain cannot be detected. Here, we present a method that relates minute-by-minute fluctuations of the positron emission tomography (PET) radioligand [11C]raclopride directly to subsecond dopamine release events. We show theoretically that synaptic dopamine release induces low frequency temporal variations of extrasynaptic extracellular dopamine levels, at time scales of one minute, that can evoke detectable temporal variations in the [11C] raclopride signal. Hence, dopaminergic activity can be monitored via temporal fluctuations in the [11C]raclopride PET signal. We validate this theory using fast-scan cyclic voltammetry and [11C]raclopride PET in mice during chemogenetic activation of dopaminergic neurons. We then apply the method to data from human subjects given a palatable milkshake and discover immediate and—for the first time—delayed food-induced dopamine release. This method enables time-dependent regional monitoring of stimulus-evoked dopamine release at physiological levels.

[1] Max Planck Institute for Metabolism Research, Gleueler Str. 50, 50931 Cologne, Germany. [2] Department of Neurology, University Hospital of Cologne, Kerpener Str. 62, 50937 Cologne, Germany. [3] Department of Psychiatry, University of Oxford, Warneford Hospital, Oxford OX3 7JX, UK. [4] Department of Experimental Psychology, University of Oxford, Tinsley Building, Mansfield Road, Oxford OX1 3SR, UK. [5] Cologne Cluster of Excellence in Cellular Stress and Aging-Associated Disease (CECAD), Joseph-Stelzmann-Str. 26, 50931 Cologne, Germany. [6] Modern Diet and Physiology Research Center, 290 Congress Avenue, New Haven, CT 06519, USA. [7] Center for Endocrinology, Diabetes and Preventive Medicine (CEPD), University Hospital of Cologne, Kerpener Str. 62, 50937 Cologne, Germany. [8] Wellcome Centre for Integrative Neuroimaging, Department of Experimental Psychology, University of Oxford, Tinsley Building, Mansfield Road, Oxford OX1 3SR, UK. These authors contributed equally: Rachel N. Lippert, Anna Lena Cremer. Correspondence and requests for materials should be addressed to H.B. (email: backes@sf.mpg.de)

The neurotransmitter dopamine (DA) plays a key role in the control of motor function, motivation, food intake, and reward[1–3]. Malfunctions in the dopaminergic system cause severe symptoms and debilitating diseases (e.g., Parkinson's disease)[4,5]. The dopaminergic system is one of the most extensively studied neurotransmitter systems, nevertheless, it is still far from being fully understood. One reason originates from the basic properties of neurotransmitter signaling: in response to perception of macroscopic stimuli, such as sensory cues, molecules are released into synapses, only 20–30 nm broad, bind within milliseconds to intrasynaptic receptors, diffuse into extracellular space and bind to extrasynaptic receptors, trigger secondary processes, and eventually cause changes in macroscopic behavior. The whole cascade of signal transduction from stimulus to behavior includes a vast range of temporal and spatial scales but the available methods for the analysis of the processes can only address singular aspects of these complex events.

Using positron emission tomography (PET) and the radiotracer [11C]raclopride, we introduce here a method for the in vivo assessment of time-dependent regional dopamine release that makes use of the relation between different time scales in the dopaminergic system and that is—as we also demonstrate here—readily applicable to humans. [11C]raclopride is a well-known antagonist for dopamine type 2 receptors (D2Rs) and to lesser extent dopamine type 3 receptors[6]. Due to its relatively low binding affinity, it has, to date, been predominantly used for the quantitative steady-state assessment of available D2R binding sites in the striatum, the brain region with the highest density of D2Rs. [11C]raclopride competes with endogenous DA for binding to D2Rs and therefore binding events depend on extracellular concentrations of DA. The release of DA, and subsequent binding to the D2R, reduces the amount of free D2Rs available for [11C]raclopride interaction and thereby reduces the amount of bound [11C]raclopride[7]. Based on this principle, several models have been developed that relate task-induced or pharmacological reductions of [11C]raclopride binding to DA release[7–17]. However, given the relatively slow kinetic rate constants of [11C]raclopride, these methods require substantial, pharmacologically enhanced, and long-lasting DA release events. Changes in [11C]raclopride binding are thought to be insensitive to high-frequency transient DA variations.

Here, we propose and validate a novel approach for the analysis of [11C]raclopride data based on theoretically derived predictions of the spatial and temporal consequences of DA release events. We first demonstrate, with the help of a simple model based on fundamental principles, how low-frequency variations of extracellular DA concentrations can be directly linked to synaptic DA release. We then extrapolate how temporal variations of extracellular DA concentrations induce temporal variations of [11C]raclopride binding and derive a parameter that captures temporal variations of the [11C]raclopride signal and can therefore be used as an indirect measure for regional DA dynamics.

To support our theory, we performed [11C]raclopride PET in mice that carry the chemogenetically activatable modified muscarinic receptor ($hM3D_{Gq}$) exclusively in DA neurons. We then compared these [11C]raclopride PET data with sub-second recordings of DA concentrations in the ventral striatum measured in situ using fast-scan cyclic voltammetry (FSCV). We demonstrate that (i) chemogenetic activation of DA neurons in mice increases the rate of spontaneous DA transients detected by FSCV and that (ii) the number of transients is significantly correlated with the logarithm of the power in the frequency band of 0.5 Hz, as calculated by wavelet transform of continuously recorded FSCV data. We further show that (iii) the logarithm of high-frequency power (~0.5 Hz) and transient rates correlate significantly with the logarithm of low-frequency power (~0.01 Hz) and that (iv) these low-frequency variations of extracellular DA concentrations cause detectable variations in the [11C]raclopride PET signal. With the mouse data supporting our theory we conclude that temporal variations of the [11C]raclopride PET signal can be used as a measure of dopaminergic activity.

Finally, we applied our method to healthy human volunteers who received a palatable milkshake during [11C]raclopride PET data acquisition and identified acute and delayed stimulus-related DA release in multiple striatal and extrastriatal brain regions.

Results

Low-frequency variations of extracellular DA. During a synaptic release event, DA concentrations are elevated 10^4-fold within the synaptic cleft for ~1 millisecond[18] (Fig. 1a). Synapses are not leak-proof and due to the high concentration gradient at the border of the synapses part of the released DA diffuses into extracellular space[19]. These changes in extracellular DA concentrations generate the signals detected by FSCV that show stimulus-related transient 10–100-fold increases of extracellular DA levels that last for ~2 s (Fig. 1b). Indeed, shape, magnitude, and duration of FSCV transients can be precisely modeled as integrated DA from synapses surrounding the probe leaking into extracellular space. The extracellular DA concentration D_e is then given by[18]:

$$D_e(r,t) = \sum_{i,j(t>t_{i,j})} \frac{l_s V_s C_s}{\alpha\left(4\pi D\left(t-t_{i,j}\right)\right)^{3/2}} exp\left(\frac{-(r-r_i)^2}{4D\left(t-t_{i,j}\right)}\right) exp\left(-k\left(t-t_{i,j}\right)\right) \quad (1)$$

V_s is the Volume of the synapse, C_s the DA concentration within the synapse, D the apparent diffusion coefficient, α the fraction of extracellular volume, and l_s the fraction of synaptic leakage or spillover (typical values for the striatum: $V_s = 0.02\ \mu m^3$, $C_s = 0.8$ mmol/L, $D = 7.63e{-}6\ cm^2/s$, $\alpha = 0.21$, $l_s = 0.01$)[18,19]. Note that Equation (1) strictly applies to dopamine diffusion in the extracellular space outside the synapse. Within the synapse the narrow space confined by pre- and postsynaptic membranes and the high density of transporters and receptors would require a mathematical description different from Equation (1). However, Equation (1) successfully describes the dopamine concentrations in the extracellular space observed after phasic release. The fraction, l_s, that was able to diffuse out of the synapse, and not the total amount of DA released, should then be inserted into Equation (1). The model includes DA diffusion from the synapses at locations, r_i, and removal from extracellular space by DA transporters (DATs) with an effective removal rate constant of k reflecting the local density of DATs. Reported values range from $k = 0.01\ s^{-1}$ to $20\ s^{-1}$ corresponding to effective lifetimes of 100 to 0.05 s[18,20]. The summation is over all synapses, i, and release times, j, with $t_{i,j}$ being the times of DA release of a synapse at location r_i. See Fig. 2 for DA concentration at the location of an FSCV probe as a function of time after synaptic DA release calculated from Equation 1 assuming that the probe receives input from a fast domain with a high density of DATs ($k = 2\ s^{-1}$) and a slow domain with a low density of DATs ($k = 0.02\ s^{-1}$). The absolute rate of removal in each domain is given by the product of removal rate constant and extracellular DA concentration ($-kD_e$). This means that, depending on the local density of DATs, net changes of extracellular DA concentrations occur at time scales of minutes to seconds and the amplitude of these changes ($dD_e(r,t)/dt$) is proportional to extracellular DA concentration ($D_e(r,t)$) which, by its origin, is directly proportional to synaptic DA release. Thus, the amplitude of low-frequency

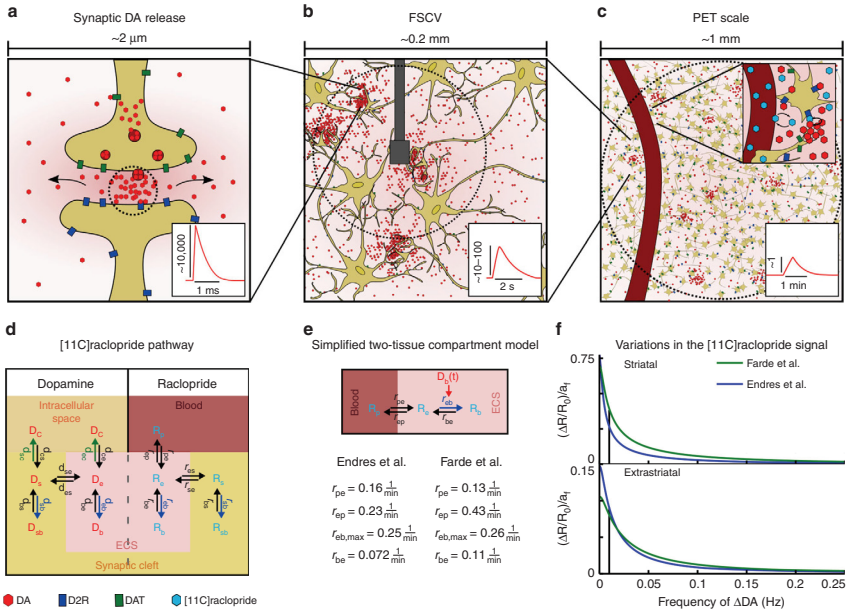

Fig. 1 DA release causes spatiotemporal variations of DA concentrations on multiple scales. **a** DA release increases synaptic DA concentrations by a factor of ~10,000 for ~1 ms. **b** Diffusion-driven outflow of DA from synapses increases DA concentration 10–100-fold in the close vicinity of synapses for ~2 s. These transients can be directly measured using FSCV. **c** DA is cleared from extracellular space by dopamine transporters (DAT). The time scale for clearance depends on the local DAT density. In a volume of 1 µL part of the DA from synaptic release diffuses into regions with low DAT density and accordingly slow clearance rates of ~1 min. In the extracellular space DA competes with [11C]raclopride for binding to D2 receptors. Unbound [11C] raclopride concentration is in equilibrium with [11C]raclopride concentration in the blood (vessel shown in dark red). **d** Synaptic and extracellular tissue compartments are shared by DA and [11C]raclopride, DA is supplied from and cleared into axons (intracellular space), [11C]raclopride from the blood. DA compartments are labeled with D, transfer rate constants with d, [11C]raclopride compartments with R and transfer rate constants with r. Subscripts are c: intracellular space, p: plasma, s: synapse, e: extracellular (extrasynaptic) space, b: bound to D2 in ECS, sb: bound to D2 in synapse. **e** Effectively the [11C] raclopride PET signal is determined by the ECS. Temporal variations of D2-bound extrasynaptic DA modulate the [11C]raclopride binding constant r_{eb}. Reported kinetic rate constants according to Endres et al.[21] and Farde et al.[22]. **f** Periodic changes of D_b cause frequency-dependent periodic variations of the [11C]raclopride PET signal that are proportional to the amplitude a_f of D_b variations using kinetic rate constants from Farde et al. (green line) and from Endres et al. (blue line). a_f can have values between 0 and 1, $a_f = 1$ means that DA occupies 100% of the D2 receptors. Only variations at low frequency are detectable by PET. Extrastriatal variations were calculated assuming a D2R density of 5% of the striatal density

variations of extracellular DA concentrations is directly proportional to (and is therefore a potential measure of) synaptic DA activity (Fig. 1a–c, Fig. 2).

Variations of extracellular DA cause PET signal variations. After intravenous injection, [11C]raclopride is transported to the brain, where blood and brain concentrations in the extracellular fluid equilibrate. Within the brain, [11C]raclopride diffuses through extracellular space which effectively consists of two compartments: the extracellular extrasynaptic compartment covering the fractional volume v_e (referred to as ECS) and the synaptic compartment covering the fractional volume v_s. Within each compartment [11C]raclopride binds to D2R according to its binding affinity which leads to the reaction pathway illustrated in Fig. 1d.

Endogenous DA, released into synapses or directly into the ECS, partially occupies the same compartments as [11C] raclopride. Diffusion of DA between synapses and ECS causes variations of DA concentration in the ECS even in the absence of direct DA release into the ECS. DATs transport DA from ECS and synapses back into the cells (d_{cc} and d_{sc} in Fig. 1d). In the following model, we only take into account DA binding to D2Rs omitting other receptor types due to the specific competition with [11C]raclopride binding. As illustrated in Fig. 1d, DA and [11C] raclopride both occupy ECS and synapses and compete for binding to D2R within these compartments.

The effective binding rates of [11C]raclopride (r_{eb}) and DA (d_{eb}) to D2R in the ECS depend on the amount of unbound D2R:

$$r_{eb} = r_{eb,max}\left(1 - \frac{D_b}{T_e} - \frac{R_b}{T_e}\right) \quad (2)$$

$$d_{eb} = d_{eb,max}\left(1 - \frac{D_b}{T_e} - \frac{R_b}{T_e}\right) \quad (3)$$

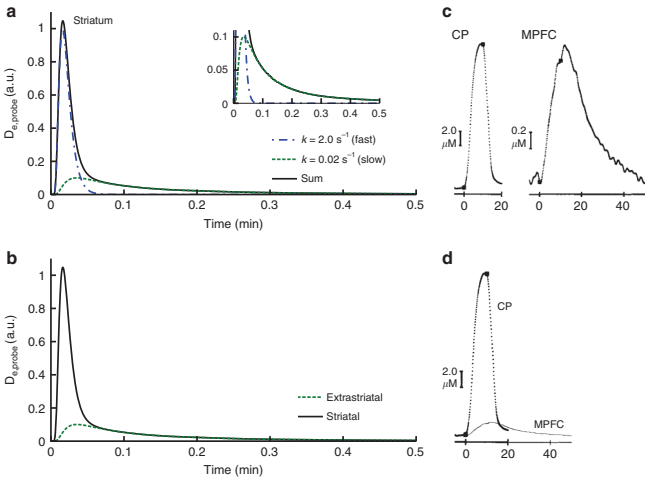

Fig. 2 Extracellular DA after synaptic release. **a** Calculated extracellular DA concentrations at the location of an FSCV electrode (black, solid) assuming that the signal contains contributions from a fast domain (blue, dash-dot) with high density of DA transporters (DATs) and a slow domain (green, dashed) with low density of DATs (Equation 1). DA is removed from the fast domain at a rate of s^{-1} and from the slow domain at a rate of min^{-1}. Although the overall FSCV signal in the striatum is dominated by the signal from the fast domain, the slow domain determines variations of extracellular DA concentration on a minute-by-minute scale. The amplitudes of both, the fast and the slow domain, depend on synaptic DA release. **b** The peak amplitude of dopamine transients in extrastriatal regions is lower due to the lower spatial density of DA synapses (green, dashed). All of the released DA is removed at minute time scale due to the lower density of DATs in extrastriatal regions in comparison to the striatum. Consequently the amplitude of minute-by-minute changes in extracellular DA concentration is the same in extrastriatal and striatal regions (black, solid). **c** Simultaneous FSCV recordings from the striatum (CP) and the medial prefrontal cortex (MPFC) in rats after electrical stimulation of the VTA by Garris et al. support this theory[42]. In order to evoke a detectable signal in the MPFC the VTA was stimulated at superphysiological amplitudes. **d** Combination of the CP and MPFC traces in a single graph indicates that the tail representing slowly removed DA in the CP is of the same magnitude as the extrastriatal signal

T_e is the total (bound plus unbound) amount of D2Rs located on extrasynaptic cellular membranes and thereby accessible by DA and [11C]raclopride in the ECS. D_b and R_b are the concentrations of bound DA and bound [11C]raclopride, respectively. $r_{eb,max}$ and $d_{eb,max}$ are the maximum binding rates of [11C]raclopride and DA when the total amount of D2R is available for binding. The total [11C]raclopride concentration, R, in a certain volume is the sum of all compartments:

$$R = v_P R_P + v_e(R_e + R_b) + v_s(R_s + R_{sb}) \quad (4)$$

R_P is the concentration of [11C]raclopride in plasma, R_e the free concentration in extracellular extrasynaptic space, R_s the free concentration in the synapses, and R_{sb}, the concentration of intrasynaptic bound [11C]raclopride. Since [11C]raclopride does not diffuse into blood cells, the contribution of [11C]raclopride in blood to the volume signal, R, is given by the product of plasma volume fraction v_P and plasma concentration R_P. Given that the free concentrations in tissue are equilibrated, i.e., $R_e = R_s$ and that the amount of bound [11C]raclopride (R_b) is in the order of magnitude of free [11C]raclopride, the contributions of the synaptic [11C]raclopride to the volume signal can be neglected due to the small volume of synapses relative to ECS volume[19]. This leads to a simple two-tissue compartment model illustrated in Fig. 1e. Time-dependent changes of [11C]raclopride concentrations in the free and bound ECS compartment are given by:

$$\frac{dR_e}{dt} = r_{pe}R_p - \left(r_{ep} + r_{eb,max}\left(1 - \frac{D_b}{T_e} - \frac{R_b}{T_e}\right)\right)R_e + r_{be}R_b \quad (5)$$

$$\frac{dR_b}{dt} = r_{eb,max}\left(1 - \frac{D_b}{T_e} - \frac{R_b}{T_e}\right)R_e - r_{be}R_b \quad (6)$$

[Note that for DA, in contrast to [11C]raclopride, the contribution of the synaptic volume would not be negligible because DA concentrations within synapses reach levels 3–4 orders of magnitude higher than in the extracellular space.] Since the [11C]raclopride signal effectively originates from the ECS, it is influenced only by variations of DA binding in the ECS and not in the synapse. For further simplification, we assume that the fraction of D2Rs blocked by [11C]raclopride is negligible in comparison to the total amount of D2Rs. If the amount of D2R-bound DA in the ECS varies in time ($D_b(t)$), the number of D2Rs available to [11C]raclopride changes and the binding parameter of [11C]raclopride (r_{eb}) varies in time by the factor $f_{DA}(t) = (1\text{-}D_b(t)/T_e)$. The effective equations that describe [11C]raclopride kinetics in tissue taking into account DA dynamics are then given

by:

$$\frac{dR_e}{dt} = r_{pe}R_p - \left(r_{ep} + r_{eb,max}f_{DA}(t)\right)R_e + r_{be}R_b \quad (7)$$

$$\frac{dR_b}{dt} = r_{eb,max}f_{DA}(t)R_e - r_{be}R_b \quad (8)$$

If we further assume the contribution of [11C]raclopride in the blood is negligible due to the small fractional volume of this compartment (~3%), the total [11C]raclopride signal in a tissue volume is $R(t) = R_e(t)+R_b(t)$. In order to estimate the impact of temporal variations of DA on the detectable [11C]raclopride signal we decompose $f_{DA}(t)$ as a sum of harmonic oscillations:

$$f_{DA}(t) = \frac{1}{2}\left(1 + \sum_f a_f sin(2\pi ft)\right) \quad (9)$$

We solved Equations 7 and 8 numerically for different frequencies, f, and different amplitudes, a_f, and found the relation between variations of $R(t)$ and the frequency, f, of temporal variations of DA shown in Fig. 1f. This relation informs us that, for example, variations of D_b/T_e with a frequency of 0.25 Hz and an amplitude of 1 (number of D2Rs bound to DA fluctuates from 0% to 100%) will cause negligible relative variations in $\Delta R(t)/R_0$. D_b/T_e variations with the same amplitude but a frequency of 0.01 Hz induce in the striatum variations in $\Delta R(t)/R_0$ of 0.25 if we adopt the [11C]raclopride kinetic parameters from Endres et al. or 0.38 with the parameters taken from Farde et al.[21,22]. [11C] raclopride variations scale linearly with the amplitude a_f of DA variations, i.e., the term $\Delta R(t)/R_0/a_f$ shown in Fig. 1f only depends on the frequency, f, but is independent of the amplitude, a_f, of DA variations. At an amplitude of 0.5 (number of D2R bound to DA changes periodically from 25% to 75%) $\Delta R(t)/R_0$ are 0.125 (Endres et al.) or 0.19 (Farde et al.) at 0.01 Hz. The density of D2Rs in extrastriatal regions is ~2%-8% of the striatal density[23]. Accordingly, extrastriatal DA variations at an amplitude of 1 induce $\Delta R(t)/R_0$ at 0.01 Hz of ~0.08 (Fig. 1f).

Assessment of regional temporal [11C]raclopride variations. Temporal variation of the [11C]raclopride PET signal at time t_n and location i,j,k can be calculated as:

$$rDA \equiv \frac{\Delta R_{ijk}}{R_{0,ijk}}(t_n) = \frac{1}{R_{0,ijk}}\sqrt{\frac{1}{N_{sum}}\sum_{u=i-d_i}^{i+d_i}\sum_{v=j-d_j}^{j+d_j}\sum_{w=k-d_k}^{k+d_k}\left(R_{uvw}(t_n) - R_{uvw}(t_{n-1})\right)^2} \quad (10)$$

$$R_{0,ijk} = \frac{1}{N-ns}\frac{1}{N_{sum}}\sum_{n=ns}^{N}\sum_{u=i-d_i}^{i+d_i}\sum_{v=j-d_j}^{j+d_j}\sum_{w=k-d_k}^{k+d_k}R_{uvw}(t_n) \quad (11)$$

The square root term is a measure of $\Delta R(t_n)$, the average change of the [11C]raclopride signal from time t_{n-1} to time t_n in the box centered at i,j,k (N_{sum}, the number of voxels in the box is $(2d_i+1)(2d_j+1)(2d_k+1)$). R_0 is calculated in Equation 11 as the average signal in the box after the quasi steady state has been reached at $t_{ns} = 20$ min after bolus injection. See Methods section for further details.

In summary, by utilizing the theoretical considerations referenced above, we determined that [11C]raclopride effectively models dynamic variations of DA bound to D2Rs in the ECS at frequencies below 0.05 Hz. The relative amplitude of regional [11C]raclopride variations ($\Delta R(t)/R_0$) is directly proportional to the amplitude, a_f, of variations of DA bound to D2R in the ECS. $\Delta R(t)/R_0$ can be calculated directly from dynamic PET data as a measure of DA release rates.

Dopaminergic activity in the ventral striatum of mice. In the previous sections, we demonstrated theoretically that synaptic DA activity is related to low frequency (~0.01 Hz) variations of extracellular DA which cause detectable temporal variations in the [11C]raclopride PET signal. Here we substantiate the theoretical considerations with data from electrically stimulated wild-type mice and a chemogenetic mouse model, in which dopaminergic cells express a modified muscarinic receptor ($hM3D_{Gq}^{DAT}$) activated by injection of an exogenous synthetic compound, clozapine-*n*-oxide (CNO)[24]. After injection of CNO $hM3D_{Gq}^{DAT}$ mice displayed behavioral changes indicative of dopaminergic activation (Fig. 3; Supplementary Notes).

FSCV data were acquired continuously at a rate of 10 Hz in wild-type mice, where transient DA release was induced by electrical stimulation of the VTA, and in chemogenetically activated ($hM3D_{Gq}^{DAT}$+CNO) and non-activated mice ($hM3D_{Gq}^{DAT}$+Saline). With these data we show that (i) chemogenetic activation of DA neurons increases the rate, but not the magnitude, of spontaneous DA transients measured in the ventral striatum, that (ii) the rate of transients—electrically or chemogenetically induced—is correlated with high frequency (~0.5 Hz) variations in DA levels extracted from the continuous FSCV data, and that (iii) transient rates and high frequency variations are correlated with low frequency variations (~0.01 Hz). We further show that (iv) chemogenetic activation of DA neurons in the $hM3D_{Gq}^{DAT}$ mouse model increases temporal variations in [11C]raclopride PET signal.

i. Activation of DA neurons increases rate of DA transients. We first verified the electrode placement by examining changes in DA levels in the nucleus accumbens evoked by electrical stimulation of the ventral tegmental area (VTA). There were no differences in stimulated DA in the $hM3D_{Gq}^{DAT}$+CNO or Saline-treated animals prior to drug administration (main effect of group: $F(1,4) = 1.33$, $p = 0.31$; group x treatment: $F(4,16) = 1.68$, $p = 0.20$, Two-way ANOVA; note that one mouse of the $hM3D_{Gq}^{DAT}$ CNO group was excluded from this analysis due to a slightly different stimulation protocol). We then determined the spontaneous dopamine transient rate in continuous FSCV data recorded before and after CNO application by correlating the recorded cyclic voltammograms with an evoked dopamine "template" (Fig. 4a; see Methods section). Since transients are directly linked to synaptic DA release, the number of transients per time is a measure of dopaminergic activity. The rate of transients was counted in one-minute intervals of FSCV data of CNO- and Saline-treated $hM3D_{Gq}^{DAT}$ mice. Despite minor differences in spontaneous activity in the first 5 min of baseline recording, the results show a significant increase of the DA transient rate following CNO-treatment that was not present in the Saline-treated mice (main effect of treatment: $F(1,5)_{1st\ hour} = 14.31$, $p = 0.0129$, $F(1,5)_{2nd\ hour} = 6.99$, $p = 0.0458$) (Fig. 4c). Nonetheless, there was no consistent change in the size of the release events in either group over the recording session comparing the pre-drug period with the 1st or 2nd hour after drug administration (period x group interaction: $F(2,8) = 0.946$, $p = 0.428$, Two-way ANOVA; note one saline-treated mouse had no transients in the pre-drug period so was excluded from this analysis), although the transient size recorded in the CNO-treated group was on average marginally higher throughout recording (main effect of group: $F(1,4) = 12.34$, $p = 0.025$) (Fig. 4b). Therefore, while CNO administration increased the transient rate

or probability, it had little effect on the amplitude of each measured release event.

ii. DA transient rate correlates with DA variations at 0.5 Hz. Next, to establish a link between high and low frequency variations of DA concentrations in the ECS and the rate of transients, we extracted a continuous estimate of DA levels from the FSCV signal (Fig. 4a; see Methods section) and decomposed this continuous signal into contributions from different frequencies by performing a wavelet transform[25]. Figure 5 shows the trace of FSCV data continuously recorded in the ventral striatum of a single mouse (Fig. 5a) and the wavelet power spectrum calculated

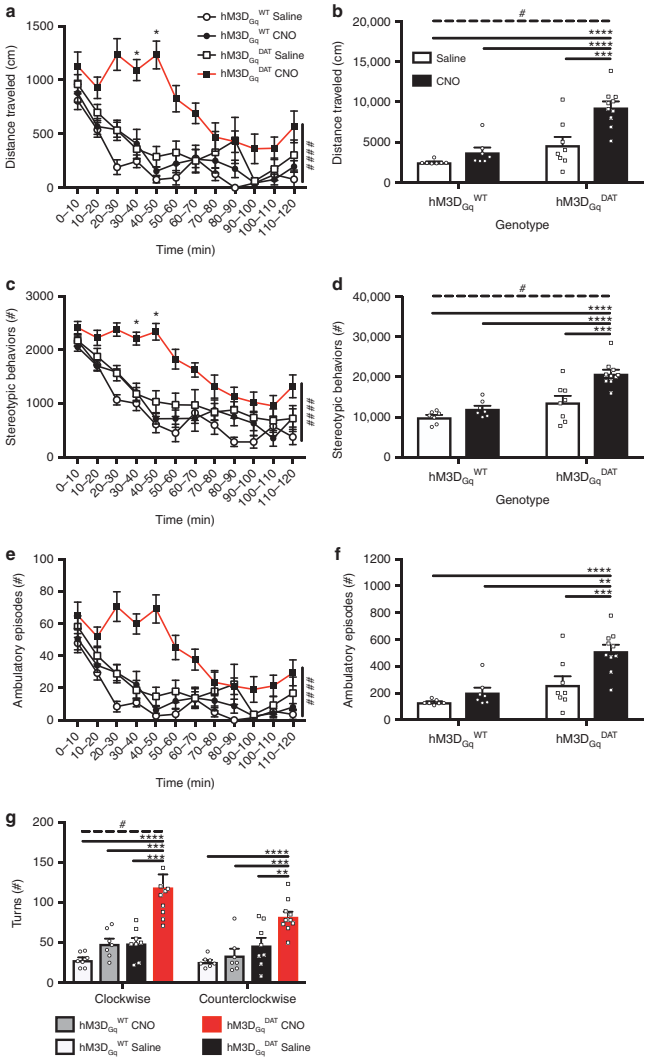

Fig. 3 Locomotor activity in the open field in chemogenetically stimulated mice. **a**, **b** Distance traveled, **c**, **d** stereotypic behaviors and **e**, **f** ambulatory episodes over 120 min (**a**, **c**, **e**) and in total (**b**, **d**, **f**) in $hM3D_{Gq}{}^{DAT}$ and $hM3D_{Gq}{}^{WT}$ mice stimulated with Saline (10 µL/g BW) or CNO (0.3 mg/kg) at $t = 0'$ (open circle = $hM3D_{Gq}{}^{WT}$+Saline ($n = 7$), closed circle = $hM3D_{Gq}{}^{WT}$+CNO ($n = 7$), open square = $hM3D_{Gq}{}^{DAT}$+Saline ($n = 8$), closed square = $hM3D_{Gq}{}^{DAT}$+CNO ($n = 10$)). **g** Rotational behavior in the clockwise or counterclockwise direction throughout the duration of the open field test. Over time data was analyzed via Three-way ANOVA, with a Two-way ANOVA post-hoc analysis at each time point corrected for false discovery rate, * = $p < 0.05$ FDR (5%) corrected, #### = $p < 0.001$ for overall genotype x treatment interaction (**a**, **c**, **e**). Summation data were analyzed via Two-way ANOVA. Treatment and genotype effects were further compared with post-hoc pairwise comparisons via Tukey's multiple comparison test and Bonferroni corrected. All data are represented as mean±SEM. **** = $p < 0.001$, *** = $p < 0.005$, ** = $p < 0.01$, * = $p < 0.05$, # = $p < 0.05$ for overall genotype x treatment interaction (**b**, **d**)

from this trace using a Gaussian mother function of order 3 (Fig. 5b, c).

The typical duration of DA transients in FSCV data is ~2 s (Fig. 4b) causing an expected increase in the power spectrum at a frequency of 0.5 Hz. We tested the relation of transient rates and 0.5 Hz wavelet power in wild-type mice where definite rates of electrically stimulated DA transients were induced. Stimulations were performed at rates of ten per minute or five per minute for one-minute intervals followed by a four-minute (wt-mouse 1) or a nine-minute interval (wt-mouse 2, 3, and 4) without stimulation. The logarithm of the 0.5 Hz wavelet power in each one-minute interval was significantly correlated with the number of transients induced during this interval (Pearson product moment correlation: $r = 0.89$, $p < 10^{-15}$) (Fig. 6).

In agreement with electrically induced DA release in wild-type mice, transients counted in one-minute intervals in chemogenetically activated mice were significantly correlated with the logarithm of the wavelet power of DA variations at frequencies of ~0.5 Hz on group level but also in individual mice (Pearson product moment correlation: $r_{CNO} = 0.64$, $p_{CNO} < 10^{-16}$, $df_{CNO} = 296$, $t_{CNO} = 14.26$, $r_{Saline} = 0.63$, $p_{Saline} < 10^{-16}$, $df_{Saline} = 215$, $t_{Saline} = 11.75$, $r_{combined} = 0.73$, $p_{combined} < 10^{-16}$, $df_{combined} = 513$, $t_{combined} = 24.44$) (Fig. 7, Supplementary Figure 1 and 2). This argues that the power at 0.5 Hz in FSCV data, which can be calculated following a well-defined standard procedure and does not require any thresholds or assumptions on the shape of transients, can be used as a measure of the transient rate. Consequently, activation of DA neurons in mice increases not only the transient rate, but also the wavelet power at 0.5 Hz.

iii. Transient rates and high and low-frequency variations. Decomposition of continuous FSCV data into contributions from different frequencies allows for correlation analysis between high-frequency and low-frequency contributions, which we tested between the logarithm of the FSCV wavelet power at 0.5 Hz (referred to as "high") and 0.01 Hz (referred to as "low"). In electrically stimulated mice we found a significant correlation between the logarithm of high and low frequency power ($r = 0.55$, $p = 0.00012$; Fig. 6e) and also between transient rates and the logarithm of low frequency power (transient rates vs. log(0.01 Hz power), Pearson product moment correlation: $r = 0.44$, $p = 0.0031$).

Furthermore, with chemogenetically activated mice, transient rates and the logarithm of high and low frequency wavelet power correlated significantly within each group and in the combined data (Pearson product moment correlation between logarithmic power at 0.5 Hz and 0.01 Hz: $r_{CNO} = 0.13$, $p_{CNO} = 0.030$, $df_{CNO} = 296$, $t_{CNO} = 2.19$, $r_{Saline} = 0.14$, $p_{Saline} = 0.042$, $df_{Saline} = 215$, $t_{Saline} = 2.05$, $r_{combined} = 0.34$, $p_{combined} < 10^{-14}$, $df_{combined} = 513$, $t_{combined} = 8.17$; correlation between transient rates and logarithmic power at 0.01 Hz: $r_{CNO} = 0.15$, $p_{CNO} = 0.008$, $df_{CNO} = 296$, $t_{CNO} = 2.69$, $r_{Saline} = 0.16$, $p_{Saline} = 0.016$, $df_{Saline} = 215$, $t_{Saline} = 2.43$, $r_{combined} = 0.32$, $p_{combined} < 10^{-12}$, $df_{combined} = 513$, $t_{combined} = 7.63$) (Fig. 5d, Fig. 8a–d). Consistently, activation of DA neurons not only increased temporal fluctuations on a time scale of one second (as measured by the high-frequency wavelet power), but also systematically induced fluctuations at a minute time scale (as measured by the low-frequency wavelet power).

iv. DA release increases temporal variations in PET signal. [11C]raclopride PET emission data were acquired in the same mouse model using the same protocol with respect to $hM3D_{Gq}{}^{DAT}$ activation (Methods section). To rapidly reach a steady state, [11C]raclopride was injected using a bolus + constant infusion method[11]. Temporal variations in the [11C]raclopride signal were calculated using Equation 10. Approximately 10 min after CNO injection a significant increase in the temporal variations was observed in the striatum compared to vehicle-injected mice (paired Student's *t*-test, $n = 6$, $t = 2.858$, $df = 5$, $p = 0.035$) (Fig. 9a, b) with the left ventral striatum having the largest change of temporal variations.

In summary, our data support the theoretically predicted link between DA transient rates and variations of extracellular DA concentrations at high (0.5 Hz) and low (0.01 Hz) frequency. Activation of dopaminergic neurons significantly increases all three components: the rate of DA transients and the power of high and low frequency variations. This finding implies that all three components are measures of in vivo DA activity. While the detection of high frequency variations requires methods with high temporal resolution data acquisition, low frequency variations can be assessed with methods using lower temporal resolution. In particular low frequency variations induce detectable variations in the [11C]raclopride PET signal.

DA release in response to food intake in humans. By application of our method to human subjects who received either milkshake or a tasteless solution during the PET scan we found significant differences at the time of supply in reward-related regions of the DA system (ventral striatum ($p_{FWE,cluster} = 0.003$), habenula ($p_{FWE,cluster} = 0.0007$), substantia nigra/VTA ($p_{FWE,cluster} < 0.0001$), and pons (NTS; $p_{FWE,cluster} = 0.001$; highlighted in red in Fig. 10). Stimulation appears to induce detectable variations in the [11C]raclopride signal even in extrastriatal regions although there is less [11C]raclopride binding. Traditionally in PET analyses, data are integrated over time and each data point includes the history of kinetics from tracer injection up to this time point. In contrast, our method of analyzing signal variations from one-time frame to the next provides variations of [11C] raclopride as a function of time. Taking advantage of this aspect, we found—apart from differences during the time of milkshake/tasteless solution supply—a second-time interval with significant differences in DA activity at 15–20 min post-stimulation (highlighted in green in Fig. 10a, b). Again the pons was part of this

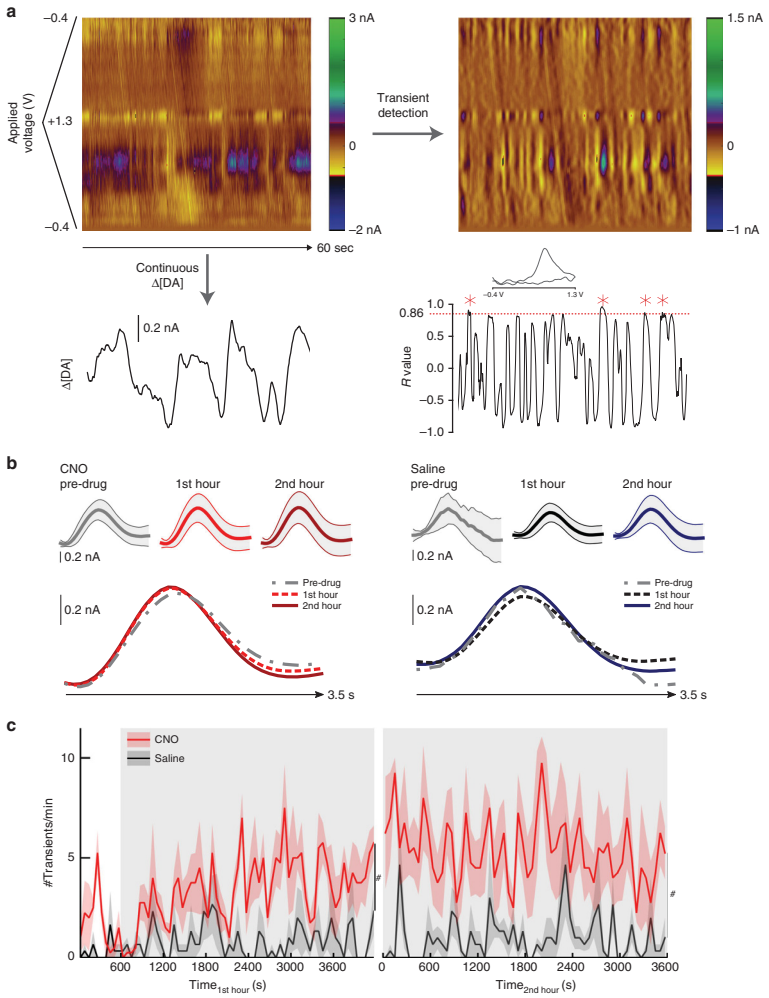

Fig. 4 FSCV recordings of DA transients in mice. **a** Dopamine transients and levels in hM3D$_{Gq}^{DAT}$ mice. Top left panel shows the recorded current x applied voltage in a pseudocolor plot for a representative 60 s period in an hM3D$_{Gq}^{DAT}$ mouse after administration of CNO. Transients were detected by subtracting a moving 1 s window 1.5–0.5 s prior to each cyclic voltammogram (top right panel) and comparing the resulting cyclic voltammogram against an electrically-evoked dopamine template (bottom right panel). Spontaneous transients, identified as dopamine, are marked with a red asterisk; inset shows the average background subtracted cyclic voltammogram for these transients. Continuous dopamine levels were also extracted (bottom left panel) to allow comparisons between rates of transients and changes in dopamine at different timescales. **b** Average transient size (mean ± SD across all recorded transients) during the 15 min before drug administration, during the first hour, and second hour for the hM3D$_{Gq}^{DAT}$ CNO (left, $n = 4$) and hM3D$_{Gq}^{DAT}$ Saline (right, $n = 3$) groups. Transients were aligned on the peak r value and zeroed on the local minimum value in the preceding 1.5 s. **c** Spontaneous transients per minute ± SEM recorded in hM3D$_{Gq}^{DAT}$ mice before (white background) and after (gray background) CNO ($n = 4$) or Saline ($n = 3$) injection. Transients were counted in one-minute intervals. Data were analyzed via Two-way ANOVA, # = $p < 0.05$ for an overall main effect of treatment type

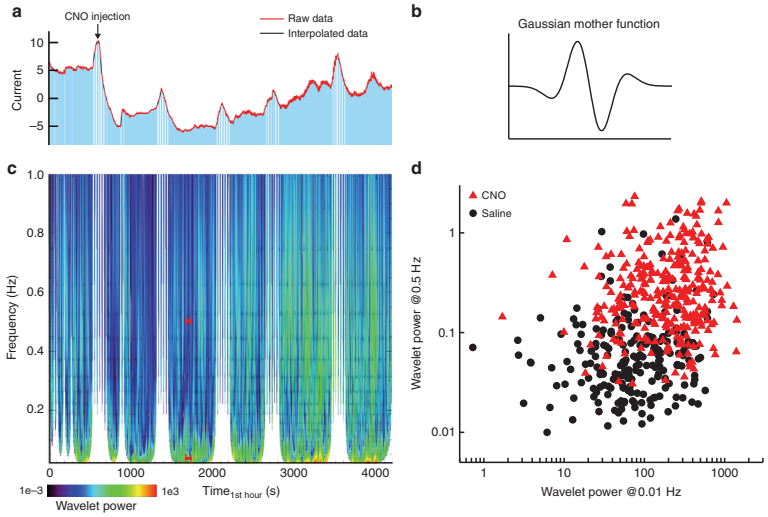

Fig. 5 Wavelet power of continuous FSCV recordings. **a** Continuous FSCV data recorded in the ventral striatum of a single mouse. CNO was injected intraperitoneally at t = 600 s. **b** Gaussian mother function that was applied for the wavelet transform. **c** Contour plot of wavelet power calculated from the FSCV data shown in (**a**). Data gaps were excluded from the analysis together with the corresponding cone of influence (t±2*1/f). The red bars indicate a one-minute interval of low (0.01 Hz) and high frequency (0.5 Hz) power. **d** Power in the high and low-frequency band after CNO administration (red triangles = $hM3D_{Gq}{}^{DAT}$+ CNO, $n_{CNO} = 4$; black circles = $hM3D_{Gq}{}^{DAT}$+ Saline, $n_{Saline} = 3$). Each data point represents a one-minute interval

secondary delayed activation although at a different location ($p_{FWE,cluster}$<0.0001). Neighboring activation sites of the primary activation, also ventral posterior medial nucleus of the thalamus (VPM; $p_{FWE,cluster} = 0.018$) and the dorsal striatum ($p_{FWE,cluster} = 0.0003$) showed delayed secondary response to the milkshake. In rodents it was shown that vagus nerve-transmitted postingestive signals can induce DA response in the brain and that vagal nerve afferent terminals have D2 receptors[26,27]. This mechanism could be the origin of the delayed DA activity that we observe in our data. Note that in contrast to *rDA* the net [11C]raclopride uptake in the corresponding regions did not show any significant differences between milkshake and tasteless condition (Fig. 10c). These results demonstrate the power of our new method for the assessment of dopaminergic activity in humans. Further results of the human study can be found here[28].

Discussion

To date, two main approaches have been introduced to detect DA release using PET. In the first approach, in baseline and stimulated conditions, the binding potential of the PET tracer is determined and differences are attributed to differences in released DA[7,12,29–33]. In the second approach, the kinetic model for the PET tracer was extended to account for dynamic changes of endogenous DA concentrations thereby allowing for transient DA release detection during PET data acquisition[10,11,14,17,34]. However, both approaches have in common that they require robust and long-lasting (> minute time scale) increases of DA concentrations, for example by pharmacological intervention prior to the PET measurement, to significantly reduce net regional tracer binding, leading to detectable DA release events. In our method, we analyze temporal fluctuations instead of net reductions in regional tracer binding. The difference becomes evident when we compare time activity curves (TACs), resulting from net regional tracer binding, with *rDA*, calculated from the temporal PET signal fluctuations using the method described herein (Fig. 10a, c). Despite originating from the identical PET dataset, only *rDA* reveals two distinct time intervals with milkshake-induced activation, while the TACs do not indicate any difference between tasteless and milkshake conditions. Since the two approaches referenced above rely on net differences in the TACs, neither would be capable of detecting DA release. Supporting this observation, our FSCV data recorded in situ indicate that phasic dopamine release induces minute-by-minute fluctuations rather than minute-lasting elevations of DA concentrations implying that temporal PET signal variations are far more sensitive to detect DA release events than the net TAC. Thus, our method, in comparison to the currently utilized non-invasive detection methods, allows for the spatiotemporal assessment of physiologically relevant DA release events.

rDA, calculated as the ratio of local variations to the absolute local [11C]raclopride signal (Equation 10), is region-specific and cannot be compared between different regions, e.g. double *rDA* in the brain stem in comparison to the striatum does not mean that DA release rates in the brain stem are higher than in the striatum. But, as indicated by Fig. 1f, within a region *rDA* is proportional to the amplitude of DA release and can therefore be compared between subjects.

Our method for the detection of DA release is based on three premises: first, the [11C]raclopride signal measured by PET

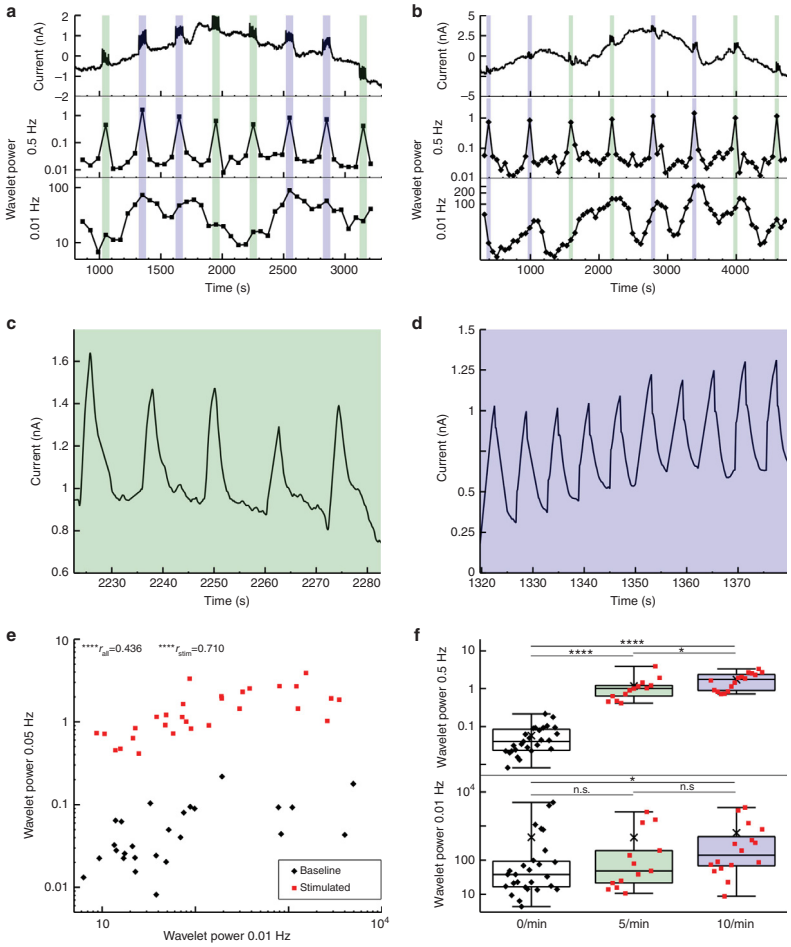

Fig. 6 FSCV recordings of DA transients induced by electrical stimulation. (**a**, **b**, top trace) Continuous FSCV recordings from the ventral striatum of two mice. Five (green interval, **c**) or ten transients per minute (blue interval, **d**) were induced by electrical stimulation of the VTA. (**a** and **b**, mid and bottom trace) resulting wavelet power at 0.5 Hz and 0.01 Hz. **e** Correlation of wavelet power at 0.5 Hz and 0.01 Hz in stimulated one-minute intervals (red squares) and non-stimulated one-minute intervals taken from the center of non-stimulated time intervals (black diamonds, $n = 4$ mice). **f** Wavelet power in one-minute intervals as a function of the number of induced transients (median ± SEM, x = mean, whiskers indicate minimal and maximal values, $n = 4$ mice). Welch two-sample *t*-test: **** = $p < 0.001$, *** = $p < 0.005$, ** = $p < 0.01$, * = $p < 0.05$

originates predominantly from [11C]raclopride binding to extrasynaptic receptors, second, there is noticeable spillover of DA from synapses to the extrasynaptic extracellular space, and third, part of extrasynaptic extracellular DA is removed at a minute time scale. All three premises are well supported by the literature. It has been shown that the majority of D2Rs are located outside and often distant from synapses[35,36]. Together with the fact that the synaptic volume is much smaller than the extrasynaptic extracellular volume, [11C]raclopride binds predominantly to extrasynaptic D2Rs. Spillover of DA from synapses

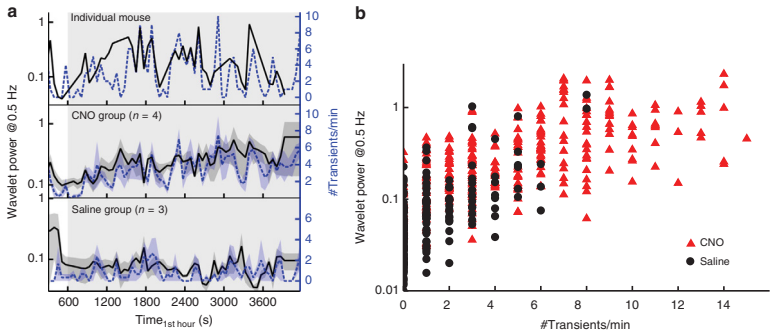

Fig. 7 FSCV wavelet power at 0.5 Hz and transient rates in chemogenetically stimulated mice. **a** Comparison of the number of transients per minute (blue dashed lines) and the wavelet power at 0.5 Hz (black lines) calculated from continuously recorded FSCV data in one individual example mouse and in the CNO and Saline group (mean±SEM). The gray box indicates the time after CNO/ Saline injection. **b** Correlation of transient rate with the logarithm of the wavelet power at 0.5 Hz from all mice (red triangles = $hM3D_{Gq}^{DAT}$+ CNO, $n_{CNO} = 4$; black circles = $hM3D_{Gq}^{DAT}$+ Saline, $n_{Saline} = 3$; Pearson product moment correlations: $r_{CNO} = 0.64$, $p_{CNO}<10^{-16}$, $df_{CNO} = 296$, $t_{CNO} = 14.26$, $r_{Saline} = 0.63$, $p_{Saline}<10^{-16}$, $df_{Saline} = 215$, $t_{Saline} = 11.75$, $r_{combined} = 0.73$, $p_{combined}<10^{-16}$, $df_{combined} = 513$, $t_{combined} = 24.44$)

is the reason that DA transients can be reliably detected by FSCV although the electrodes cannot be positioned within the synaptic cleft. The concept of diffusive loss of DA from synapses has been elaborately discussed and is well established[18]. Moreover, minute time scale removal rates are often present in FSCV transient recordings – sometimes referred to as "hang-up". As discussed by A. Michael and colleagues "Evoked responses … with hang-up are absolutely commonplace."[20,37] Although in vitro experiments showed that part of the "hang-up" could be caused by adsorption of DA molecules on the electrode surface and could thereby be a methodological artifact, not all of the minute time scale DA clearance rates observed in vivo can be explained by this effect[38–40]. DA adsorption is related to exposure of the probe to high DA concentrations: the higher the peak and duration of DA concentration, the higher the DA adsorption. However, several observations show minute time scale DA clearance rates without the presence of a secondtime scale DA peak, which can accordingly not be caused by adsorption[41,42].

A potential mechanism that could explain the slow minute time scale component in the FSCV data could be the heterogeneous subcellular distribution of DATs. A fraction of the released DA diffuses into subcellular regions with low DAT expression and accordingly slow removal rates (Figure 2).[43,44] In order to show that heterogeneous expression of DATs can cause minute time scale DA clearance rates, we performed model calculations that describe diffusion of DA through tissue with heterogeneous DAT expression. When we assumed homogenous DAT expression our model provided identical results to Cragg and Rice (Supplementary Figure 4A)[19]. Heterogeneous DAT expression, however, produced prolonged DA clearance rates (Supplementary Figure 4B). Furthermore, our calculations show that the contribution of the minute time scale component of a measured transient critically depends on the distance from the release site. Further away from the release site the slow component is more pronounced relative to the peak, while close to the release site the contribution of the slow component appears negligible relative to the peak in accordance with in vivo observations (Supplementary Figure 4C and D)[41]. Our model replicates another aspect of these in vivo data: when we compare the minute time scale component recorded close to the release site with that recorded further distant, both are approximately identical (Supplementary Figure 4D). The accordance of our model results with in vivo observations indicates that transport and not diffusion determine the minute time scale dynamics and—given that DAT staining confirms the heterogeneous spatial distribution of DATs[44]—that heterogeneous DAT expression could be a potential mechanism to explain the minute time scale removal rates. Thus, the three prerequisites are in line with the current data on dopaminergic signal transduction.

Although the density of D2Rs in extrastriatal regions is much lower than in the striatum we were able to identify significant extrastriatal DA release. Several aspects promote the sensitivity of our method for detection of extrastriatal DA release. First, temporal variations in the signal relative to the total signal were analyzed instead of the absolute [11C]raclopride uptake, which makes the method more sensitive for the detection of variations in regions with low [11C]raclopride uptake. Second, although less DA is released in extrastriatal regions due the lower density of DA synapses, the major fraction of released DA is removed at a minute time scale due to the lower density of DATs. Therefore, the amplitudes of release-induced minute-by-minute variations in extracellular DA concentrations are of the same order of magnitude extrastriatally and in the striatum despite the difference in total amount of released DA (Figure 2).[42] A detailed discussion of this topic can be found in the Supplementary Discussion.

We found with continuous FSCV recordings that CNO-treated $hM3D_{Gq}^{DAT}$ mice increased the rate of transients – although a low rate of spontaneous transients was detectable in non-activated mice. Typically, FSCV is applied to recording of transient phasic neurotransmitter release that is time-locked to direct stimulation of an upstream brain region or to a release-inducing behavioral task[41,45,46]. With continuous recording, spontaneous transients were identified by application of a DA template. Interestingly, we could show that wavelet power at 0.5 Hz strongly correlates with the transient rate. This means that transient rates can be derived from continuous FSCV data by application of a wavelet transform, which, in contrast to template application, does not require any assumptions or thresholds and

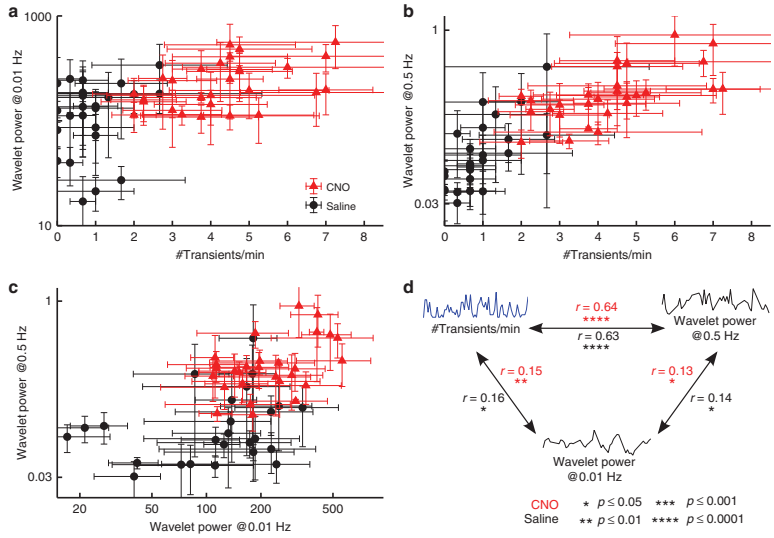

Fig. 8 Correlations between transient rates and high as well as low-frequency power. **a**–**c** Correlations of the logarithm of low-frequency power (0.01 Hz) with transient rate (**a**), the logarithm of high-frequency power and transient rate (**b**), and the logarithm of low and high-frequency power (**c**). Data points are shown for each one-minute time interval as mean ± SEM for each group (red triangles = $hM3D_{Gq}{}^{DAT}$+ CNO, $n_{CNO} = 4$; black circles = $hM3D_{Gq}{}^{DAT}$+ Saline, $n_{Saline} = 3$). **d** Pearson product moment correlation coefficients, r, were calculated within each group (in red for the $hM3D_{Gq}{}^{DAT}$+ CNO group: df = 296, * = $p \leq 0.05$ ($t > 1.97$), ** = $p \leq 0.01$ ($t > 2.59$), *** = $p \leq 0.001$ ($t > 3.32$), **** = $p \leq 0.0001$ ($t > 3.94$); in black for the $hM3D_{Gq}{}^{DAT}$+ Saline group: df = 215, * = $p \leq 0.05$ ($t > 1.97$), ** = $p \leq 0.01$ ($t > 2.60$), *** = $p \leq 0.001$ ($t > 3.34$), **** = $p \leq 0.0001$ ($t > 3.96$)). All correlations were statistically significant

can therefore be applied more easily. Thus, wavelet transform is a powerful tool to extract changes of DA levels from continuous FSCV data.

Moreover, we found correlations between high and low-frequency wavelet power within the continuous data indicating that minute-by-minute DA levels might be causally linked to second-by-second levels. This finding agrees with another experimental FSCV study where DA levels were continuously recorded in the nucleus accumbens. The authors conclude that extracellular DA largely arises from phasic DA release[47]. The causal link between minute-by-minute and second-by-second DA levels potentially challenges functional segregation of the two processes: If minute-by-minute levels are just a consequence of second-by-second release, evoked functions are presumably related to each other. In other words: if phasic DA release determines the tonic DA level, the functional consequences of both might also be related[48]. (For further discussion see Berke[49]).

The relation of synaptic release and low-frequency variations of extracellular concentrations is based on fundamental principles (diffusion, transport)[18] and should theoretically not be limited to dopamine but should also apply to other neurotransmitters. However, whether conditions are suitable (signal to noise ratio, life time, etc.) to produce detectable signals of neurotransmitter activity, will have to be evaluated individually for each neurotransmitter system. Nevertheless, the method provided here not only opens novel avenues to study temporal and local dynamics of dopaminergic transmission in human, but potentially for a whole range of other neurotransmitters

Methods

Ethical approval. All animal procedures were conducted in compliance with protocols approved by local governmental authorities (Bezirksregierung Köln) and were also in accordance with NIH guidelines for animal research. FSCV experiments were conducted under the auspices of the UK Home Office laws for the treatment of animals under scientific procedures and of the University of Oxford ethical review board.

All subjects included in the human PET study gave written informed consent prior to study, which was approved by the local ethics committee of the Medical Faculty of the University of Cologne (Cologne, Germany).

Genetic mouse models. The Rosa26CAGSloxSTOPloxhM3D$_{Gq}$ and dopamine transporter-Cre recombinase (DAT-Cre) expressing mice are described elsewhere[50,51]. All animal lines were maintained on C57BL/6N backgrounds. To generate the experimental model, homozygous Rosa26CAGSloxSTOPloxhM3D$_{Gq}$ (hM3D$_{Gq}$) females were crossed to DAT-Cre males, to generate mice with heterozygous expression of the hM3D$_{Gq}$ specifically in dopamine neurons. Non-transgenic littermate controls were used in the behavioral experiments (referred to as $hM3D_{Gq}{}^{WT}$). In all other experiments Cre positive animals were used (referred to as $hM3D_{Gq}{}^{DAT}$). Mice were housed at 22 °C-24 °C with a 12 h light/12 h dark cycle. Animals had *ad libitum* access to food and water in the home cage at all times. All experiments were performed in adult male mice (age: 13–37 weeks, body weight: 24.6–47.9 g).

CNO administration. Clozapine-*n*-oxide (CNO) was purchased from Sigma (Cat. No. C0832–5MG). A 5 mg/mL stock solution was made using DMSO (Sigma). 32 µL aliquots were stored at −20 °C, and on individual test days, a working solution of 0.03 mg/mL was generated using sterile saline (0.9%; Aquapharm). All injections were made intraperitoneally. Sterile Saline was used for vehicle injection in all experiments unless otherwise stated. The vehicle control consisted of 0.6% DMSO in saline.

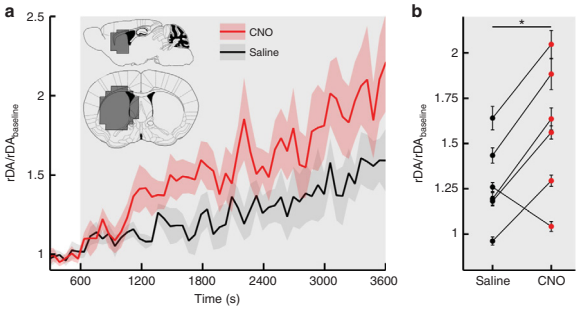

Fig. 9 Dopamine release assessed by [11C]raclopride-PET in hM3D$_{Gq}^{DAT}$ mice. **a** Dopaminergic activity changes temporal variations of the [11C]raclopride signal (*rDA*, mean±SEM). In $n = 6$ mice *rDA* was increased in the left striatum after chemogenetic activation with CNO (red line) in comparison to Saline injection (black line) at $t = 600$ s. The gray background indicates the time after injection. **b** Average *rDA* (mean ± SEM) after $t = 600$ s in each mouse after saline and CNO injection. (Paired Student's *t*-test: $n = 6$, $t = 2.858$, df = 5, $^* = p = 0.035$)

Open field test. hM3D$_{Gq}^{DAT}$ and hM3D$_{Gq}^{WT}$ mice were acclimated for 5 days to daily injections prior to the test day. On the test day, animals received an injection of CNO (0.3 mg/kg, Sigma) or sterile saline (10 µl/g BW) and were placed immediately into open field chambers (27.3 cm × 27.3 cm × 20.3 cm; Med Associates, VT). The animals were monitored for 120 min in the chambers using infrared beam breaks in the X, Y and Z planes and data was collected in 10-minute bins. Post analysis of locomotor and rotational behaviors were assessed using MedActivity Software (Med Associates, VT).

Electrode implantation surgery. Mice were anesthetized using isoflurane (3–4% for induction and 1.0–1.5 % for maintenance) and given 5 mg/kg meloxicam (Metacam) and 0.7 ml glucosesaline (0.5 % in 0.9 % saline; Aquapharm) subcutaneously (note, no opioid analgesic was given to avoid any potential interactions with dopamine systems). After induction, the head was shaved and secured in a stereotaxic frame. Body temperature was maintained at 36–37 °C with the use of a homeothermic heating blanket. Corneal dehydration was prevented with application of ophthalmic ointment (Lacri-Lube, Allergan, UK). The head was then cleaned with dilute Hibiscrub and Reprochem (diluted 1:20 in water), and a local anesthetic, bupivacaine (2 mg/kg; AstraZeneca), was administered under the scalp. The skull was then exposed and holes were drilled for an Ag/AgCl reference electrode, an anchoring screw, a recording electrode and a stimulating electrode. After the reference electrode was secured in place using dental cement (Kemdent, Swindon, UK), a custom-made carbon fiber microelectrode was attached to a voltammetric amplifier and lowered toward the dorsal nucleus accumbens (NAc) core (AP: +1.4, ML: 0.75, DV: −3.5 to −4.25 from skull) followed by a 2-channel untwisted stimulating electrode (PlasticsOne) to the ipsilateral ventral tegmental area (VTA) (AP: −3.5, ML: 0.35, DV: −4.0 to −4.55 from brain), and the recording process commenced (see below). The reference electrode and anchoring screw were positioned contralateral to the carbon fiber and stimulating electrodes. The mouse was given additional boluses of 0.7 ml glucosesaline ~every 3 h for the rest of the surgery.

Fast-scan cyclic voltammetry recordings. Recordings of in vivo nucleus accumbens (NAc) core dopamine levels were made under anesthesia using FSCV. The potential applied to the carbon fiber was ramped from −0.4 V (vs Ag/AgCl) to +1.3 V and back at a rate of 400 V/s during a voltammetric scan and held at −0.4 V between scans. This happened at a frequency of 60 Hz for an initial 20-minute period in order to condition the electrode, after which scan rate was reduced to 10 Hz for the rest of the experiment and dopamine detection commenced. Electrical stimulation was applied using an isolated current stimulator (DS3, Digitimer). Stimuli were generated and recordings collected using Tarheel CV (National Instruments). The positions of the recording and stimulating electrodes were optimized by moving them to find the maximal changes in dopamine that could be detected after stimulation (50 × 2 ms monophasic pulses, 200 µA current, at 50 Hz).

Once this was achieved, the main experiment was started to determine the effect of chemogenetic activation of dopamine neurons on patterns of NAc core dopamine release. This consisted of two situations: (1) monitoring spontaneous changes in dopamine levels in the absence of external stimulation, and (2) examining evoked dopamine release after electrical stimulation of the VTA. For the latter, we used 5 different stimulation parameters (2 recordings with each, 3 min between stimulations): (i) 20 pulses 100 µA, (ii) 30 pulses 100 µA, (iii) 30 pulses 150 µA, (iv) 40 pulses 150 µA, and (v) 50 pulses 200 µA. This was performed 3 times: before mice were given an intraperitoneal injection of either CNO (0.3 mg/kg body weight) or vehicle (0.6% DMSO in sterile saline), 1 h after injection, and at the end of the experiment (~145 min after injection). For the middle set of stimulations, only parameters (ii), (iv) and (v) were used. With the exception of the first mouse that had a slightly different set of stimulation parameters the protocol described was used for all mice.

To examine spontaneous changes in dopamine, we continuously monitored dopamine levels under anesthesia, first for 10 min prior to injection of either CNO or vehicle, then for 60 min after injection, and then finally for a further 60 min after the middle set of electrical stimulations.

Additional continuous FSCV recordings were performed in the ventral striatum of four wild-type mice. In one-minute time intervals DA release was induced by electrical stimulation of the VTA at a rate of either 5 or 10 transients per minute followed by a resting time interval of either 4 min (mouse 1) or 9 min (mouse 2, 3, and 4). The parameters of the electrical stimulation were adjusted to 50 Hz, 4–7 pulses, and 100–200 µA in order to obtain transients with an average amplitude of ~1–2 nA. Recordings of mouse 3 and 4 displayed periods where the chemometric model failed. Affected time intervals were excluded from the analysis. Note, that all reported significances remain significant if these intervals are included in the analysis.

Voltammetry data analysis. Voltammetric analysis was carried out using custom-written scripts in Matlab. All data were low-pass filtered at 2 kHz. In order to characterize the rate of spontaneous dopamine transients in each mouse, we first subtracted the average current recorded between 1.5–0.5 s before the target cyclic voltammogram to account for large changes in capacitance current. We then looked for periods when the cyclic voltammograms recorded over the course of the experiment correlated with a correlation coefficient of $R \geq 0.86$ with a dopamine "template" derived by electrically stimulating the VTA before the experiment began (Daberkow, 2013; Cheer, 2004). The numbers of transients per minute before and after either CNO or vehicle injections were then compared.

To extract an estimate of changes in dopamine levels over time across the session, a principal component analysis was performed using a standard training set of stimulated dopamine release detected by chronically implanted electrodes, with dopamine treated as the first principal component among other unrelated electrochemical fluctuations such as changes in pH. For this analysis, we divided the data into non-overlapping 30 s bins and, for each, subtracted the average current recorded over the initial 1 s in each bin. Given that it is only possible to derive a relative and not an absolute measurement of dopamine levels using FSCV, the extracted dopamine in each bin were combined by assuming that the first recorded value in bin N+1 continued relative to the last time point in bin N.

Wavelet transform of continuous FSCV data. A wavelet transform decomposes the signal into harmonic functions of different frequencies but in contrast to the Fourier transform these harmonic functions have a finite duration. Thereby, a wavelet transform does not lose the temporal information of the signal[25]. The wavelet power calculated as the square of the wavelet coefficients gives the power in variations of extracellular DA levels as a function of frequency and time.

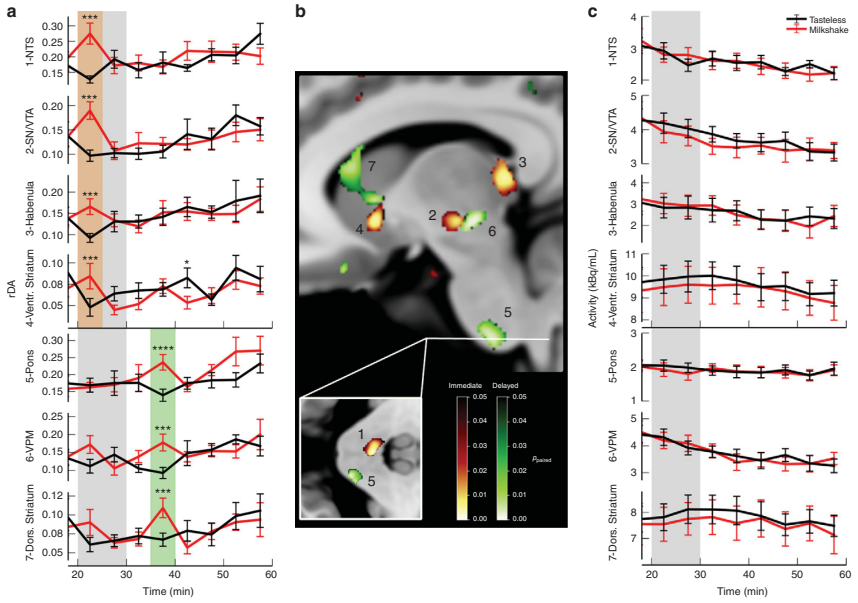

Fig. 10 Food-induced DA release in humans. During two separate PET imaging sessions human volunteers ($n = 10$) received either a tasty milkshake or a tasteless solution starting 20 min after [11C]raclopride injection for 10 min. **a** Time course of *rDA* in regions with significant differences between milkshake (red) and tasteless (black) condition in the 20–25 min (orange box) or 35–40 min (green box) time interval. The gray box indicates the time of milkshake/tasteless solution administration. **b** Locations of regions with significant differences of *rDA* between milkshake and tasteless condition in the 20–25 min (red color scale) or 35–40 min (green color scale) time interval. **c** Time activity curves in the regions indicated in (**b**) showing no detectable differences between the tasteless and milkshake condition. Identified regions are 1: nucleus of the solitary tract (NTS), 2: substantia nigra/VTA, 3: habenula, 4: ventral striatum, 5: pons, 6: ventral posterior medial nucleus of the thalamus (VPM), and 7: dorsal striatum. All data are represented as mean±SEM, paired Student's *t*-test: df = 9, **** = $p < 0.001$ ($t > 4.78$), *** = $p < 0.005$ ($t > 3.69$), * = $p < 0.05$ ($t > 2.26$) (uncorrected)

For the analysis of high and low-frequency variations in the FSCV data a wavelet transform with a Gaussian mother function (3. order) was applied. Since continuous data is needed for the wavelet transform missing points in the data were interpolated. Using a cone of influence the wavelet data of these segments were removed from the resulting spectra ($t \pm 2*1/f$). Additionally, to avoid edge effects the borders of the wavelet transform were also removed ($t_{min}+4*1/f$ and $t_{max}-4*1/f$). The power in the wavelet spectrum at 0.01 and 0.5 Hz was averaged in windows of 1 min to yield time courses of wavelet power at 0.01 Hz and at 0.5 Hz for each animal. Correlation analyses were restricted to time intervals that contained continuous data in all three parameters (#transients/minute, wavelet power at 0.01 Hz and at 0.5 Hz).

Synthesis of [11C]raclopride. [11C]-O-methylraclopride was prepared according to Langer et al.[52] with the following modifications: (1) 2–2.5 mg precursor des-methylraclopride•HBr was used instead of free base, (2) 350 µl DMSO together with 6 µl 5N NaOH was used instead of acetone as reaction solvent, (3) the reaction mixture was heated at 80 °C for 4 min, (4) the eluent was removed after semi-preparative HPLC separation by solid phase extraction with a Waters OASIS MCX 1cc cartridge, eluted with 500–700 µl ethanol 96%/NH3 (95:5) and 2 ml 0.9% NaCl solution, and (5) formulation by adding another 6.5 ml 0.9% NaCl solution and 1 ml 125 mM sodium phosphate buffer, resulting in a solution with pH 5–7. The specific activity at time of injection was 22.8 ± 9.0 GBq/µmol.

Mouse PET data acquisition. Dynamic PET data were acquired using a combined preclinical PET/CT scanner (Inveon, Siemens). For each scan session of 60 min two animals were placed on a water-heated mouse carrier with stereo-tactic holders (Medres). During the procedure mice were anesthetized with ~2 % isoflurane vaporized in 1.0 L/min of oxygen-nitrogen gas (30 % O_2 / 70 % N_2). At the start of the PET data acquisition the animals received a bolus-plus-constant-infusion injection of 10.5 ± 2.6 MBq of [11C]raclopride via the tail vein: a bolus of 80 µl was injected in one minute, followed by additional 120 µl injected via constant infusion until the end of data acquisition using programmable syringe pumps („Genie" Kent, Kent Scientific Corp., Torrington, CT). 10 min after the start of the PET scan the mice either received CNO (0.3 mg/kg body weight) or sterile saline (10 µl/kg body weight) intraperitoneally. Each animal was measured twice in a randomized order once receiving CNO and once saline. Following the PET scan the animals were automatically moved into the CT gantry and a CT scan was performed (180 projections/360°, 200 ms, 80 kV, 500 µA). CT data were used for attenuation correction of the PET data and the CT image of the skull was used for image co-registration.

Mouse PET data processing. PET data were histogrammed in 60 time frames of 1 min, Fourier rebinned and after correction for attenuation and decay, images were reconstructed using the MAP-SP algorithm provided by the manufacturer. The images were co-registered to a reference mouse brain CT by rigid body transformation using the imaging software VINCI[53]. Parametric images were calculated using Equation 10 (see detailed description below, procedures written in IDL and C).

Using a 3D mouse atlas constructed from a 2D mouse brain atlas[54], an anatomical volume of interest (VOI) of the left striatum was drawn. This region was analyzed since FSCV data were acquired from this region.

Human PET. Although invasive methods such as FSCV have been applied to measure task-related neurotransmitter release in the human brain[55–57], PET measurements are non-invasive and therefore much more readily translatable to humans. In contrast to mice, human subjects do not require anesthesia during the PET scan and natural non-pharmacological types of stimulation, such as food, can be applied as a stimulus to induce DA release. In order to analyze food-related reward signaling, we applied the method to healthy human volunteers who received a milkshake during [11C]raclopride-PET data acquisition. Human subjects ($n = 10$) were monitored in two different conditions: in one session they received a palatable milkshake and in the other session a tasteless solution. Following the method introduced here, maps of DA activity were calculated in time intervals of five minutes. Voxelwise statistical testing was performed (paired Student's t-test) between the two conditions to identify locations with stimulation-induced changes in dopaminergic activity. Here we discuss only exemplary aspects of that data as a proof of principle and to demonstrate the power of the new approach. The full-length results of this study can be found here[28].

Subjects were ten healthy, male, normal-weight (BMI: 25.73 ± 2.67, age: 57.1 ± 10.55) and non-smoking volunteers recruited from a preexisting database of Max Planck Institute for Metabolism Research. No history of neurological, psychiatric or eating disorders were present. Further exclusion criteria were special diets, lactose intolerance, diabetes, the participation in a previous PET study and a score higher than 12 in the Beck Depression Inventory (BDI II)[58].

Human PET data acquisition. Two PET scans were performed in a randomized order with the subjects receiving either milkshakes or a tasteless and non-nutritive solution (potassium chloride/sodium bicarbonate) during the scan. A HRRT Siemens PET gantry with a spatial resolution of ~2.5 mm FWHM was used. The head of the subjects was fixed by an inflatable helmet to prevent motion during data acquisition. Data for attenuation correction was acquired by performing a ten-minute transmission scan using a rotating germanium-68/gallium-68 source. Afterwards, [11C]raclopride injection started and emission data were acquired for the following 60 min 70 % of the [11C]raclopride (220–370 MBq) was applied as bolus within a minute and 30 % was constantly infused during the remaining 59 min using a programmable syringe pump (Perfusor compact, Braun, Melsungen). The food stimulus started 20 min after the start of the data acquisition, when steady-state conditions were reached, and lasted for 10 min During this time either milkshake or tasteless solution was delivered to the tongue tip of the subjects via a teflon mouthpiece that was attached to the gantry. For further details see ref. [28].

Human PET data processing. The acquired emission data were corrected for attenuation and scatter. PET images were reconstructed in 12-time frames of 5 min duration using three-dimensional ordinary Poisson ordered subset expectation maximization (OP-3D-OSEM) including the modeling of the system's point spread function (PSF). The resulting images were smoothed using a 10 mm Gaussian filter using the imaging software VINCI[53]. The smoothed PET images were co-registered to an additionally acquired individual anatomical T1-weighted scan by rigid body transformation. The MR scans were normalized into the Montreal Neurological Institute (MNI) stereotactic space using a non-linear transformation algorithm (VINCI). The obtained transformation matrix from this step was subsequently applied to the coregistered PET images to transform them into the MNI-152 standard space.

Parameter for measuring temporal dynamics of [11C]raclopride. From the [11C]raclopride PET images parametric maps were calculated. In the manuscript we have shown that variations of the [11C]raclopride signal are related to variations of D2R-bound DA in the ECS. Part of the temporal variations in the [11C] raclopride signal is due to noise. However, since the noise level does not abruptly change during the measurement, short-term changes in the temporal variations are presumably caused by changes in DA activity. Temporal variation of the [11C] raclopride signal at time t_n and location (image voxel) i,j,k can be calculated as:

$$rDA \equiv \frac{\Delta R_{ijk}}{R_{0,ijk}}(t_n) = \frac{1}{R_{0,ijk}}\sqrt{\frac{1}{N_{sum}}\sum_{u=i-d_i}^{i+d_i}\sum_{v=j-d_j}^{j+d_j}\sum_{w=k-d_k}^{k+d_k}\left(R_{uvw}(t_n) - R_{uvw}(t_{n-1})\right)^2} \quad (10)$$

$$R_{0,ijk} = \frac{1}{N - ns}\frac{1}{N_{sum}}\sum_{n=ns}^{N}\sum_{u=i-d_i}^{i+d_i}\sum_{v=j-d_j}^{j+d_j}\sum_{w=k-d_k}^{k+d_k} R_{uvw}(t_n) \quad (11)$$

In order to reduce noise in the parameter for temporal variations of the tissue [11C]raclopride signal we here calculate the average of the absolute difference between the signal at time t_n and t_{n-1} in a region that includes the box $i-d_i,i+d_i,j-d_j,j+d_j,k-d_k,k+d_k$. The square root term is a measure for $\Delta R(t_n)$ the average change from time t_{n-1} to time t_n of the [11C]raclopride signal in the box centered at i,j,k (N_{sum} is the number of voxels in the box). R_0 is calculated in Equation 11 as the average signal in the box after the quasi steady state has been reached at t_{ns} = 20 min after bolus injection. The size of d reduces the spatial resolution but also reduces spatial noise in the parameter. The choice of d depends on the system used for data acquisition and on the quality of the data. For mouse data acquired we used $d_i = d_j = 2$ and $d_k = 1$ (asymmetric voxel size), for the human data we used $d_i = d_j = d_k = 2$.

It is important that $rDA = \Delta R(t)/R_0$ is calculated from the square root of the sum-of-squares and not just from the sum of differences (Equation 10). From theory, the absolute value of temporal changes but not the direction of change (increase or decrease) is a measure for DA activity.

$\Delta R(t_n)$ is calculated from the difference in [11C]raclopride signal at time t_n and time t_{n-1} and therefore depends on the duration of time frames ($\Delta t = t_n - t_{n-1}$) of the PET data. Although shorter time frames provide higher temporal resolution, Fig. 1f indicates that shorter time frames (i.e. higher frequencies) are less sensitive to variations of DA and apart from that include more noise inherent in the measurement procedure. For the mouse data we used $\Delta t = 1$ min, for humans we used $\Delta t = 5$ min

rDA is a measure for local temporal variations of the [11C]raclopride signal (ΔR) relative to total local [11C]raclopride signal (R_0). rDA is thereby a measure for local DA activity and is thus comparable between subjects but it cannot be compared between regions. Since D2R density in extrastriatal regions is lower than in the striatum there is consequently less total [11C]raclopride binding. Higher rDA in an extrastriatal region than in the striatum does not necessarily mean that more DA was released in the extrastriatal region. But following the time course of rDA within a region indicates temporal variations of DA activity.

Statistical testing. For behavioral studies, Three-Way ANOVA analysis of data collected over time was conducted using JASP Version 0.8.3.1 (University of Amsterdam), followed by Two-way ANOVA post-hoc analysis at individual time points corrected for false discovery rate using GraphPad Prism version 7.0c for Mac OS X, (GraphPad Software, California, USA, www.graphpad.com). Two-way ANOVA followed by Bonferroni post-hoc analysis of locomotor behavior totals and rotational behavior was performed using GraphPad Prism version 7.0c. P-values<0.0.5 were considered significant. For FSCV analyses, Pearson product moment correlations were calculated using R. For testing differences between groups unpaired Student's t-test was performed. P-values <0.05 were considered significant. In mouse PET studies differences between activation and baseline were determined by performing a paired Student's t-test. P-values <0.05 were considered significant. In the human PET study voxel-wise independent paired Student's t-tests of parametric images were performed between milkshake and tasteless scans for each time frame. Clusters with statistically significant differences (p-value <0.05) were corrected for multiple comparisons by calculating family-wise error rates on cluster level[59]. All statistical tests in this work were two-sided.

Code availability. Custom computer code used to generate the results of this study is available from the corresponding author upon reasonable request.

Reporting summary. Further information on experimental design is available in the Nature Research Reporting Summary linked to this article.

Data availability

The data that support the findings of this study are available from the corresponding author upon reasonable request.

Received: 9 April 2018 Accepted: 18 December 2018
Published online: 18 January 2019

References

1. Wise, R. A. Dopamine, learning and motivation. *Nat. Rev. Neurosci.* **5**, 483–494 (2004).
2. Smillie, L. D. & Wacker, J. Dopaminergic foundations of personality and individual differences. *Front. Hum. Neurosci.* **8**, 874 (2014).
3. Land, B. B. et al. Medial prefrontal D1 dopamine neurons control food intake. *Nat. Neurosci.* **17**, 248–253 (2014).
4. Palmiter, R. D. Dopamine signaling as a neural correlate of consciousness. *Neuroscience* **198**, 213–220 (2011).
5. Dauer, W. & Przedborski, S. Parkinson's disease: mechanisms and models. *Neuron* **39**, 889–909 (2003).
6. Farde, L., Hall, H., Ehrin, E. & Sedvall, G. Quantitative analysis of D2 dopamine receptor binding in the living human brain by. *Pet. Sci. (New Y., NY)* **231**, 258–261 (1986).
7. Dewey, S. L. et al. Striatal binding of the PET ligand11C-raclopride is altered by drugs that modify synaptic dopamine levels. *Synap. (New Y., NY)* **13**, 350–356 (1993).

8. Volkow, N. D. et al. Decreased striatal dopaminergic responsiveness in detoxified cocaine-dependent subjects. *Nature* **386**, 830–833 (1997).
9. Morris, E. D. et al. Creating dynamic images of short-lived dopamine fluctuations with lp-ntPET: dopamine movies of cigarette smoking. *J. Vis. Exp.* e50358–e50358 (2013).
10. Breier, A. et al. Schizophrenia is associated with elevated amphetamine-induced synaptic dopamine concentrations: evidence from a novel positron emission tomography method. *Proc. Natl. Acad. Sci. U. S. A.* **94**, 2569–2574 (1997).
11. Carson, R. E. et al. Quantification of amphetamine-induced changes in [11C] raclopride binding with continuous infusion. *J. Cereb. Blood Flow. Metab.* **17**, 437–447 (1997).
12. Laruelle, M. Imaging synaptic neurotransmission with in vivo binding competition techniques: a critical review. *J. Cereb. Blood Flow. Metab.* **20**, 423–451 (2000).
13. Badgaiyan, R. D., Fischman, A. J. & Alpert, N. M. Striatal dopamine release during unrewarded motor task in human volunteers. *Neuroreport* **14**, 1421–1424 (2003).
14. Alpert, N. M., Badgaiyan, R. D., Livni, E. & Fischman, A. J. A novel method for noninvasive detection of neuromodulatory changes in specific neurotransmitter systems. *Neuroimage* **19**, 1049–1060 (2003).
15. Badgaiyan, R. D., Fischman, A. J. & Alpert, N. M. Striatal dopamine release in sequential learning. *Neuroimage* **38**, 549–556 (2007).
16. Badgaiyan, R. D., Fischman, A. J. & Alpert, N. M. Dopamine release during human emotional processing. *Neuroimage* **47**, 2041–2045 (2009).
17. Normandin, M. D., Schiffer, W. K. & Morris, E. D. A linear model for estimation of neurotransmitter response profiles from dynamic PET data. *Neuroimage* **59**, 2689–2699 (2012).
18. Rice, M. E. & Cragg, S. J. Dopamine spillover after quantal release: rethinking dopamine transmission in the nigrostriatal pathway. *Brain. Res. Rev.* **58**, 303–313 (2008).
19. Cragg, S. J. & Rice, M. E. DAncing past the DAT at a DA synapse. *Trends Neurosci.* **27**, 270–277 (2004).
20. Taylor, I. M. et al. Kinetic diversity of dopamine transmission in the dorsal striatum. *J. Neurochem.* **133**, 522–531 (2015).
21. Endres, C. J. et al. Kinetic modeling of [11C]raclopride: combined PET-microdialysis studies. *J. Cereb. Blood Flow. Metab.* **17**, 932–942 (1997).
22. Farde, L., Eriksson, L., Blomquist, G. & Halldin, C. Kinetic analysis of central [11C]raclopride binding to D2-dopamine receptors studied by PET--a comparison to the equilibrium analysis. *J. Cereb. Blood Flow. Metab.* **9**, 696–708 (1989).
23. Suhara, T. et al. Extrastriatal dopamine D2 receptor density and affinity in the human brain measured by 3D PET. *Int. J. Neuropsychopharmacol.* **2**, 73–82 (1999).
24. Armbruster, B. N., Li, X., Pausch, M. H., Herlitze, S. & Roth, B. L. Evolving the lock to fit the key to create a family of G protein-coupled receptors potently activated by an inert ligand. *Proc. Natl. Acad. Sci. U. S. A.* **104**, 5163–5168 (2007).
25. Goupillaud, P., Grossmann, A. & Morlet, J. Cycle-Octave and Related Transforms in Seismic Signal Analysis. *Geoexploration* **23**, 85–102 (1984).
26. Tellez, L. A. et al. A gut lipid messenger links excess dietary fat to dopamine deficiency. *Sci. (New Y., NY)* **341**, 800–802 (2013).
27. Lawrence, A. J., Krstew, E. & Jarrott, B. Functional dopamine D2 receptors on rat vagal afferent neurones. *Br. J. Pharmacol.* **114**, 1329–1334 (1995).
28. Thanarajah, S. E. et al. Food intake recruits orosensory and post-ingestive dopaminergic circuits to affect eating desire in humans. *Cell. Metab.* **29**, 1–12 (2019).
29. Logan, J. et al. Graphical analysis of reversible radioligand binding from time-activity measurements applied to [N-11C-methyl]-(-)-cocaine PET studies in human subjects. *J. Cereb. Blood Flow. Metab.* **10**, 740–747 (1990).
30. Gunn, R. N., Lammertsma, A. A., Hume, S. P. & Cunningham, V. J. Parametric imaging of ligand-receptor binding in PET using a simplified reference region model. *Neuroimage* **6**, 279–287 (1997).
31. Wang, G.-J. et al. BMI modulates calorie-dependent dopamine changes in accumbens from glucose intake. *PLoS. One.* **9**, e101585 (2014).
32. Slifstein, M. et al. Striatal and extrastriatal dopamine release measured with PET and [(18)F] fallypride. *Synap. (New Y., NY)* **64**, 350–362 (2010).
33. Narendran, R. et al. Positron emission tomography imaging of amphetamine-induced dopamine release in the human cortex: a comparative evaluation of the high affinity dopamine D2/3 radiotracers [11C]FLB 457 and [11C] fallypride. *Synap. (New Y., NY)* **63**, 447–461 (2009).
34. Pappata, S. et al. In vivo detection of striatal dopamine release during reward: a PET study with [(11)C]raclopride and a single dynamic scan approach. *Neuroimage* **16**, 1015–1027 (2002).
35. Sulzer, D., Cragg, S. J. & Rice, M. E. Striatal dopamine neurotransmission: regulation of release and uptake. *Basal Ganglia* **6**, 123–148 (2016).
36. Egerton, A. et al. The dopaminergic basis of human behaviors: A review of molecular imaging studies. *Neurosci. Biobehav. Rev.* **33**, 1109–1132 (2009).
37. Walters, S. H., Taylor, I. M., Shu, Z. & Michael, A. C. A novel restricted diffusion model of evoked dopamine. *ACS Chem. Neurosci.* **5**, 776–783 (2014).
38. Bath, B. D. et al. Subsecond adsorption and desorption of dopamine at carbon-fiber microelectrodes. *Anal. Chem.* **72**, 5994–6002 (2000).
39. Taylor, I. M. et al. Kinetic diversity of dopamine transmission in the dorsal striatum. *J. Neurochem.* **133**, 522–531 (2015).
40. Walters, S. H., Robbins, E. M. & Michael, A. C. Modeling the kinetic diversity of dopamine in the dorsal striatum. *ACS Chem. Neurosci.* **6**, 1468–1475 (2015).
41. Robinson, D. L., Venton, B. J., Heien, M. L. A. V. & Wightman, R. M. Detecting subsecond dopamine release with fast-scan cyclic voltammetry in vivo. *Clin. Chem.* **49**, 1763–1773 (2003).
42. Garris, P. A., Collins, L. B., Jones, S. R. & Wightman, R. M. Evoked extracellular dopamine in vivo in the medial prefrontal cortex. *J. Neurochem.* **61**, 637–647 (2006).
43. Kaya, C. et al. Heterogeneities in axonal structure and transporter distribution lower dopamine reuptake efficiency. *eNeuro* **5**, ENEURO.0298–17.2017 (2018).
44. Block, E. R. et al. Brain region-specific trafficking of the dopamine transporter. *J. Neurosci.* **35**, 12845–12858 (2015).
45. Wassum, K. M. & Phillips, P. E. M. Probing the neurochemical correlates of motivation and decision making. *ACS Chem. Neurosci.* **6**, 11–13 (2015).
46. Papageorgiou, G. K., Baudonnat, M., Cucca, F. & Walton, M. E. Mesolimbic dopamine encodes prediction errors in a state-dependent manner. *Cell Rep.* **15**, 221–228 (2016).
47. Owesson-White, C. A. et al. Sources contributing to the average extracellular concentration of dopamine in the nucleus accumbens. *J. Neurochem.* **121**, 252–262 (2012).
48. Hamid, A. A. et al. Mesolimbic dopamine signals the value of work. *Nat. Neurosci.* **19**, 117–126 (2016).
49. Berke, J. D. What does dopamine mean? *Nat. Neurosci.* **21**, 787–793 (2018).
50. Steculorum, S. M. et al. AgRP neurons control systemic insulin sensitivity via myostatin expression in brown adipose tissue. *Tissue Cell* **165**, 125–138 (2016).
51. Ekstrand, M. I. et al. Progressive parkinsonism in mice with respiratory-chain-deficient dopamine neurons. *Proc. Natl Acad. Sci. USA.* **104**, 1325–1330 (2007).
52. Langer, O. et al. Precursor synthesis and radiolabelling of the dopamine D2 receptor ligand [11C]raclopride from [11C]methyl triflate. *J. Label. Compd. Radiopharm.* **42**, 1183–1193 (1999).
53. Cizek, J. et al. Fast and robust registration of PET and MR images of human brain. *Neuroimage* **22**, 434–442 (2004).
54. Franklin, K. B. J. & Paxinos, G. *The mouse brain in stereotaxic coordinates*. (Boston, 2008).
55. Kishida, K. T. et al. Subsecond dopamine fluctuations in human striatum encode superposed error signals about actual and counterfactual reward. *Proc. Natl Acad. Sci. USA* **113**, 200–205 (2016).
56. Lohrenz, T., Kishida, K. T. & Montague, P. R. BOLD and its connection to dopamine release in human striatum: a cross-cohort comparison. *Philos. Trans. R. Soc. Lond. B. Biol. Sci.* **371**, 20150352 (2016).
57. Moran, R. J. et al. The Protective Action Encoding of Serotonin Transients in the Human Brain. *Neuropsychopharmacology* **43**, 1425–1435 (2018).
58. Beck, A. T., Steer, R. A. & Brown, G. K. *Manual for the Beck Depression Inventory-II. Manual* (San Antonio, TX: Psychological Corporation, 1996).
59. Friston, K. J., Worsley, K. J., Frackowiak, R. S., Mazziotta, J. C. & Evans, A. C. Assessing the significance of focal activations using their spatial extent. *Hum. Brain. Mapp.* **1**, 210–220 (1994).

Acknowledgements

M.E.W. and C.K. were supported through a Wellcome Trust Senior Research Fellowship to M.E.W. (202831/Z/16/Z). H.B., M.T. and J.C.B were supported by of the German Research Foundation in the Transregional Collaborative Research Center 134. M.T. and J.C.B were supported by the German Centre for Diabetes Research. [11C]raclopride was provided by the radiochemistry lab of Prof. Dr. Bernd Neumaier. We kindly thank N.G. Larsson (Max Planck Institute for Biology of Ageing, Cologne, Germany) for providing Dat-Cre mice.

Author contributions

Conceptualization, R.L. and H.B.; Methodology, R.L., A.L.C. and H.B.; Software, A.L.C., T.J.P. and H.B.; Validation, H.B., R.L., A.L.C., and M.W.; Formal analysis, R.L., A.L.C., C. K., T.J.P., L.M.B., and H.B.; Investigation, H.B., R.L., A.L.C., M.W., C.K., L.M.B., and S.E.

T.; Writing—Original Draft, H.B.; Writing—Review & Editing, R.L., A.L.C., and H.B.; Visualization, H.B., A.L.C., and R.L.; Supervision, M.T., J.C.B., M.W., and H.B.

Additional information

Supplementary Information accompanies this paper at https://doi.org/10.1038/s41467-018-08143-4.

Competing interests: The authors declare no competing interests.

Reprints and permission information is available online at http://npg.nature.com/reprintsandpermissions/

Publisher's note: Springer Nature remains neutral with regard to jurisdictional claims in published maps and institutional affiliations.

Article

Cell Metabolism

Food Intake Recruits Orosensory and Post-ingestive Dopaminergic Circuits to Affect Eating Desire in Humans

Graphical Abstract

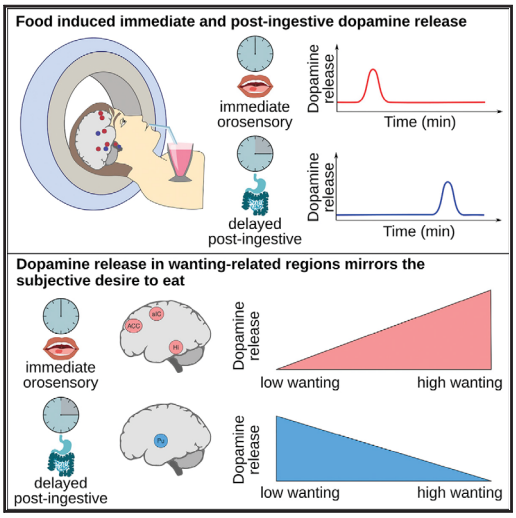

Highlights

- Food intake induces orosensory and post-ingestive dopamine release in humans
- Both recruit distinct pathways: orosensory integrative and higher cognitive centers
- Dopamine release in "wanting"-associated regions mirrors subjective desire to eat
- Post-ingestive dopamine release in the putamen is inversely correlated to "wanting"

Authors

Sharmili Edwin Thanarajah, Heiko Backes, Alexandra G. DiFeliceantonio, ..., Dana M. Small, Jens C. Brüning, Marc Tittgemeyer

Correspondence

backes@sf.mpg.de

In Brief

Thanarajah et al. combined fMRI and PET to assess the brain's response to food intake and discovered immediate and delayed dopamine release in distinct areas of the human brain. In addition, they identified areas where dopamine release reflected subjective wanting to eat, shedding light on how the brain transforms energetic signals into the desire to eat.

Thanarajah et al., 2019, Cell Metabolism 29, 695–706
March 5, 2019
https://doi.org/10.1016/j.cmet.2018.12.006

CellPress

Cell Metabolism
Article

Food Intake Recruits Orosensory and Post-ingestive Dopaminergic Circuits to Affect Eating Desire in Humans

Sharmili Edwin Thanarajah,[1,2,11] Heiko Backes,[1,11,12,*] Alexandra G. DiFeliceantonio,[1,3,8,10] Kerstin Albus,[4] Anna Lena Cremer,[1] Ruth Hanssen,[1,6] Rachel N. Lippert,[1] Oliver A. Cornely,[4,5,9] Dana M. Small,[3,7,8] Jens C. Brüning,[1,4,6] and Marc Tittgemeyer[1,4,8]

[1]Max Planck Institute for Metabolism Research, Cologne, Germany
[2]Department of Neurology, University Hospital of Cologne, Cologne, Germany
[3]Department of Psychiatry, Yale University School of Medicine, New Haven, CT, USA
[4]Cologne Cluster of Excellence in Cellular Stress and Aging-Associated Disease (CECAD), Cologne, Germany
[5]Department I of Internal Medicine, University Hospital of Cologne, Cologne, Germany
[6]Center for Endocrinology, Diabetes and Preventive Medicine (CEPD), University Hospital of Cologne, Cologne, Germany
[7]Department of Psychology, Yale University, New Haven, CT, USA
[8]Modern Diet and Physiology Research Center, New Haven, CT, USA
[9]Clinical Trials Centre Cologne (ZKS Köln), University of Cologne, Cologne, Germany
[10]Department of Neuroscience, Icahn School of Medicine at Mount Sinai, New York, NY, USA
[11]These authors contributed equally
[12]Lead Contact
*Correspondence: backes@sf.mpg.de
https://doi.org/10.1016/j.cmet.2018.12.006

SUMMARY

Pleasant taste and nutritional value guide food selection behavior. Here, orosensory features of food may be secondary to its nutritional value in underlying reinforcement, but it is unclear how the brain encodes the reward value of food. Orosensory and peripheral physiological signals may act together on dopaminergic circuits to drive food intake. We combined fMRI and a novel [11C]raclopride PET method to assess systems-level activation and dopamine release in response to palatable food intake in humans. We identified immediate orosensory and delayed post-ingestive dopamine release. Both responses recruit segregated brain regions: specialized integrative pathways and higher cognitive centers. Furthermore, we identified brain areas where dopamine release reflected the subjective desire to eat. Immediate dopamine release in these wanting-related regions was inversely correlated with, and presumably inhibited, post-ingestive release in the dorsal striatum. Our results highlight the role of brain and periphery in interacting to reinforce food intake in humans.

INTRODUCTION

Recent evidence from animal models indicates that both the pleasant taste and the nutritional value of food act as reinforcers in food selection behavior (de Araujo, 2016). Highly desired food items, in turn, can enhance food intake and may lead to over-eating and obesity (Mela, 2006). In the light of the recent obesity epidemic, a growing number of studies have investigated brain signaling mechanisms underlying food intake and their modulation by the desire to eat. However, the physiological mechanisms still remain poorly understood.

Observations in rodent models of dopamine (DA) release during active feeding (Taber and Fibiger, 1997) identified the brain's dopaminergic system as a critical mediator for the neurobiological control of food intake (Palmiter, 2007). The reinforcing properties of food seemingly arise from a complex interplay between orosensory and nutritive signals. To that end, orosensory stimulation has been demonstrated to evoke striatal DA release mediating the rewarding effect of sucrose to promote food intake in rats (Hajnal et al., 2004; Schneider, 1989; Smith, 2004). In mice, the nutritive value of food, on the other hand, is signaled post-ingestively by DA independently of taste (Tellez et al., 2013, 2016) and has the capacity to override the homeostatic control of eating (Andrews and Horvath, 2008).

For example, direct nutrient infusion into the mouse gut evokes calorie-dependent striatal DA release (Ferreira et al., 2012). Moreover, mice genetically modified to lack taste receptor signaling can develop, following repeated exposures, a similar magnitude of DA release in the ventral striatum upon sucrose ingestion as wild-type mice, reflecting nutrient association learning (de Araujo et al., 2008). Similarly, the parallel presentation of a flavor and a high-calorie gut infusion consistently induces long-lasting flavor preference (Sclafani and Ackroff, 2012) and cue-associated learning in mice (Han et al., 2016; Lucas and Sclafani, 1989). This flavor-nutrient conditioning also occurs in humans at a behavioral (Yeomans et al., 2008) and neural level (de Araujo et al., 2013). These findings suggest that orosensory features of food are secondary to its nutritional value in underlying reinforcement (de Araujo, 2016).

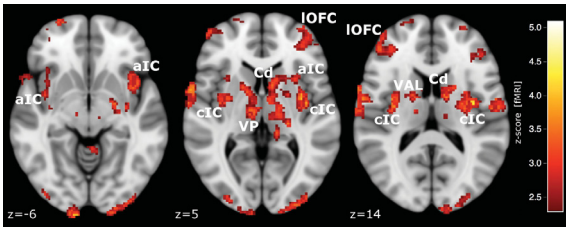

Figure 1. BOLD Activation in Response to Milkshake Intake

Compared to tasteless condition, milkshake intake elicited BOLD activation bilaterally in the anterior (aIC) as well as central insular cortex (cIC), lateral orbital frontal cortex (lOFC), ventral posterior complex of the thalamus (VP), lateral ventral anterior nucleus of the thalamus (VAL), and caudate nucleus (Cd).

To facilitate distinct orosensory and post-ingestive influences on reinforcement, segregated dopaminergic pathways are likely recruited within discrete temporal windows of action: an early window reflecting orosensation upon consumption and a second window reflecting the generation of post-ingestive signals. The latter is thought to unfold over minutes in mice (Beutler et al., 2017; Su et al., 2017) and is dependent on nutrients reaching the enteroendocrine cells in the intestine (Kaelberer et al., 2018; Tolhurst et al., 2012). Accordingly, analysis of the temporal dynamics of the blood oxygen level-dependent (BOLD) signal following glucose consumption also supports the existence of an immediate and delayed neural response (Liu et al., 2000).

Identification and discrimination of these circuits may furnish our understanding of physiological control, but also of pathophysiological dysregulation of food intake. Highly processed food with added fat and sugar is known to induce higher food wanting and overconsumption (DiFeliceantonio et al., 2018; Polk et al., 2017; Veldhuizen et al., 2017). Notably, in rodents the desire to eat (food wanting) is closely related to brain DA signaling. DA depletion in the striatum (Sotak et al., 2005) and administration of DA antagonists reduce food wanting and diminish food approach (Hsiao and Smith, 1995; Wise et al., 1978). However, as dopaminergic neuromodulation differentially impacts motor behavior and reward association (Howe and Dombeck, 2016; Volkow et al., 2017), animal studies on motivational signals that determine food intake have been debated (Baldo et al., 2002; Kelley et al., 2005), especially as the behavioral readout is always conflicted by locomotion. In humans, conversely, very little is understood about the interplay between food intake, desire to eat, and brain dopamine signaling.

The majority of studies addressing food-related DA release in humans have used functional magnetic resonance imaging (fMRI; e.g., Babbs et al., 2013; O'Doherty et al., 2002; Rothemund et al., 2007; Stice et al., 2008b; Stoeckel et al., 2008). While fMRI is advantageous in capturing brain function effectively and at a considerable spatial and temporal resolution, the respective BOLD signal is not directly related to specific neurotransmitter systems. Positron emission tomography (PET) represents a suitable technique to specifically address the dopaminergic system *in vivo*, but the application was limited by the fact that conventional analysis approaches did not allow the examination of temporal dynamics of food-induced DA release (Cosgrove et al., 2015; Small et al., 2003b; Volkow et al., 2002).

To overcome this limitation, we applied a novel method for the analysis of continuous [11C]raclopride PET data that enabled us to assess time-dependent regional DA response during and after food intake. PET as well as fMRI data were acquired in human volunteers who received a palatable milkshake during data acquisition. With our approach, we demonstrate immediate orosensory and, for the first time, post-ingestive DA release in humans and at brain systems level. Orosensory and post-ingestive signaling recruit segregated neural circuits after food intake. We further identified brain areas where the immediate DA response was related to the desire to eat and negatively associated with post-ingestive DA release in the dorsal striatum. This suggests the existence of distinct DA mechanisms that interact over time to integrate orosensory information with post-ingestive signals regarding the nutritive value of foods. Taken together, these findings suggest a mechanism to explain how the brain transforms energetic signals into the desire to eat.

RESULTS

To investigate brain signaling during food intake we performed fMRI in 12 male, normal-weight volunteers (age, 56 ± 9.5 years; BMI, 25.57 ± 2.41 kg/m^2). Ten of these participants (age, 57 ± 10.6 years; BMI, 25.73 ± 2.67 kg/m^2) underwent two additional [11C]raclopride PET acquisitions to characterize spatiotemporal DA release.

We acquired fMRI data during milkshake and tasteless consumption using the gustometer setup as introduced by Small et al. (2003a) and Veldhuizen et al. (2007). In line with these previous reports (*cf.* also de Araujo et al., 2012, for a review on orosensory-responsive brain areas), the taste of milkshake elicited activation in the anterior and central insular cortex, ventral posterior complex of the thalamus, caudate nucleus, and lateral orbitofrontal cortex, among others (Figure 1).

However, the BOLD signal is not related to a specific neurotransmitter system. Hence, we performed PET imaging with the radiolabeled D2-receptor antagonist [11C]raclopride to investigate dopamine release with the same gustometer setup providing either milkshake or tasteless solution on separate testing days. To detect any putative post-ingestive DA signaling, we continued PET acquisition for 30 min after milkshake or tasteless delivery was completed (Figure S1). Subsequently, we calculate the regional DA release rate (rDA) from [11C]raclopride data. Milkshake-induced DA release was assessed by performing a voxel-wise paired t test between rDA in response to milkshake and tasteless consumption for each 5-min time interval.

We first determined time intervals with increased DA release related to milkshake consumption by plotting the number of

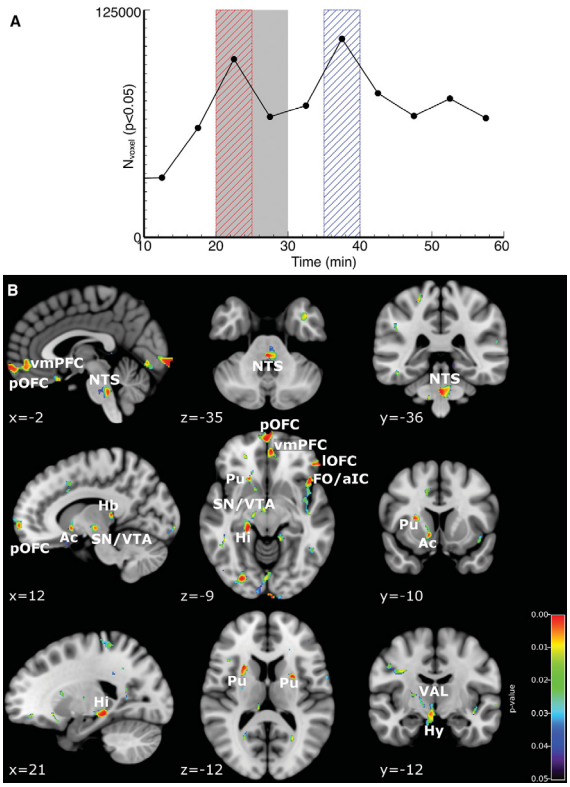

Figure 2. DA Response to Milkshake Intake

(A) Time intervals of food-induced DA response. Number of voxels with significantly increased rDA in milkshake versus tasteless condition. The data indicate an immediate (20–25 min, red box) and a delayed (35–40 min, blue box) time interval of food-induced dopaminergic activation. The gray box indicates the time of milkshake/tasteless solution supply.

(B) Immediate DA response. Immediately after milkshake delivery was initiated, rDA increased in the polar (pOFC) and lateral (lOFC) orbitofrontal cortex, nucleus of the solitary tract (NTS), nucleus accumbens (Ac), putamen (Pu), substantia nigra/ventral tegmental area (SN/VTA), lateral ventral anterior nucleus of the thalamus (VAL), habenular complex (Hb), frontal operculum/anterior insular cortex (FO/aIC), hippocampus (Hi), ventromedial prefrontal cortex (vmPFC), and hypothalamus (Hy) (Table 1). The maps are thresholded at $p < 0.05$ (whole-brain analysis; time interval, 20–25 min).

significantly increased voxels over time following a temporal clustering method introduced by Liu et al. (2000). Corresponding to Liu et al. (2000), we identified two time intervals of neural response: the first immediately after application of milkshake or tasteless solution (20–25 min); the second 15–20 min after onset and accordingly 5–10 min after offset of milkshake or tasteless solution intake (35–40 min; Figure 2A).

In a whole-brain analysis, we next focused on these two time intervals to identify brain circuitries involved in the immediate and delayed DA release (15–20 min after food intake). With onset of milkshake delivery, DA release was increased in the lateral hypothalamus and dorsal striatum (bilateral putamen) as well as in orosensory pathways (including the frontal operculum/anterior insular cortex, nucleus of the solitary tract), mesolimbic DA system (nucleus accumbens, substantia nigra/ventral tegmental area [SN/VTA] complex), areas involved in reward value signaling (ventromedial prefrontal cortex, lateral orbitofrontal cortex), memory (hippocampus), and inhibitory control (lateral ventral anterior nucleus of the thalamus, habenula; Figure 2B; Table 1). However, 15–20 min after milkshake consumption, DA release occurred in a distinct brain circuit including the anterior insula, ventral posterior medial nucleus of the thalamus, caudate nucleus, pallidum (external segment), amygdala (basolateral complex), parietal operculum, dorsomedial prefrontal cortex, anterior prefrontal cortex, and lateral caudal pontine nuclei (Figure 3; Table 2).

To analyze the interaction between immediate and delayed DA release, we performed a pairwise correlation analysis between immediate and delayed responding regions. Immediate DA release in the nucleus accumbens predicted later DA release in the caudate nucleus ($p = 0.037$, $r = 0.66$; Figure 3B).

To identify BOLD activation related to DA release, we compared group statistics of immediate DA release with the corresponding fMRI response (milkshake-tasteless). We found an overlap of activations for both modalities in the anterior insular cortex, SN/VTA complex, and occipital cortex. Interestingly, a widespread network of brain areas showed activation in the fMRI data without overlapping PET response, possibly due to the engagement of other neurotransmitter systems: lateral ventral anterior and ventral posterior medial nucleus of the thalamus, claustrum, and anterior prefrontal cortex (Figure 4).

To elucidate whether measures of eating desire were related to immediate and late DA release, we performed a voxel-wise correlation analysis between the wanting score and difference between rDA after milkshake and tasteless solution intake (⊿rDA). The wanting score was highly correlated with the immediate ⊿rDA in the anterior insular cortex ($p = 0.0002$, $r = 0.94$),

Table 1. Areas Showing DA Release Immediately after Milkshake Intake

Area	Hemisphere	x	y	z	Number of Voxels	Mean rDA (Tasteless)		Mean rDA (Milkshake)		% Increase	P_{uncorr} (min)	P_{FWE} (min)	P_{uncorr} (Cluster)	P_{FWE} (Cluster)
Ventromedial prefrontal cortex (vmPFC)	left	−1	48	−10	555	0.0842	± 0.0426	0.1432	± 0.0596	70.0	0.00027	0.00048[a]	0.00001	0.00000[a]
Orbitofrontal cortex (polar part, pOFC)	right	4	58	−14	612	0.0974	± 0.0565	0.1819	± 0.0842	86.8	0.00018	0.00005[a]	0.00030	0.00000[a]
Cingulate gyrus (CG)	right	11	18	39	280	0.0852	± 0.0341	0.1369	± 0.0599	60.7	0.01147	1.00000	0.00391	0.00933[a]
Dorsomedial prefrontal cortex (dmPFC)	left	−8	51	21	407	0.0736	± 0.0372	0.1220	± 0.0588	65.7	0.00232	0.50764	0.00198	0.00007[a]
Anterior insular cortex (aIC)	left	−44	18	−9	490	0.0964	± 0.0491	0.1821	± 0.0742	88.8	0.00018	0.00005[a]	0.00018	0.00000[a]
	right	39	20	8	305	0.0777	± 0.0430	0.1253	± 0.0482	61.2	0.00037	0.00159[a]	0.00208	0.00042[a]
Central insular cortex (cIC)	left	−39	2	−9	66	0.0954	± 0.0495	0.1466	± 0.0530	53.6	0.01135	1.00000	0.00684	0.66303
Hypothalamus (Hy)	right	6	−11	−12	245	0.1041	± 0.0623	0.2064	± 0.1087	98.3	0.00229	0.49845	0.00318	0.00651[a]
Substantia nigra/ventral tegmental area (SN/VTA)	right	11	−15	−5	270	0.0989	± 0.0498	0.1843	± 0.0773	86.3	0.00327	1.00000	0.00120	0.00005[a]
Lateral orbitofrontal cortex (lOFC)	left	−49	38	−7	302	0.0974	± 0.0425	0.1662	± 0.0655	70.7	0.00061	0.00885[a]	0.00252	0.00107[a]
Nucleus accumbens (Ac)	right	11	8	−7	215	0.0489	± 0.0322	0.0831	± 0.0443	70.1	0.00180	0.26544	0.00234	0.00292[a]
Putamen (Pu)	right	26	10	12	259	0.0714	± 0.0382	0.1134	± 0.0316	58.9	0.00027	0.00042[a]	0.00040	0.00000[a]
	left	−24	4	13	275	0.0467	± 0.0200	0.0863	± 0.0407	84.8	0.00037	0.00123[a]	0.00050	0.00000[a]
Hippocampus (Hi)	right	21	−31	−7	260	0.0996	± 0.0505	0.1877	± 0.0709	88.4	0.00003	0.00000[a]	0.00019	0.00000[a]
Parahippocampal gyrus (PHG)	right	2	−81	−5	100	0.0846	± 0.0512	0.1716	± 0.0728	102.9	0.00024	0.00021[a]	0.00024	0.00000[a]
Habenula (Hb)	right	11	−30	7	284	0.1021	± 0.0453	0.1668	± 0.0754	63.4	0.00186	0.29509	0.00215	0.00068[a]
Nucleus of the solitary tract (NTS)	left	−2	−35	−35	339	0.1272	± 0.0543	0.2807	± 0.1347	120.6	0.00021	0.00014[a]	0.00283	0.00110[a]
Fusiform gyrus (middle part, FuG)	right	46	−44	−16	370	0.0879	± 0.0360	0.1558	± 0.0740	77.3	0.00015	0.00004[a]	0.00054	0.00000[a]
	left	−49	−44	−15	51	0.0792	± 0.0282	0.1193	± 0.0376	50.5	0.00229	0.49002	0.00329	0.18747
Precentral gyrus (PrG)	right	42	−7	30	275	0.0693	± 0.0259	0.1273	± 0.0694	83.7	0.00650	1.00000	0.00924	0.18901
Ventral anterior nucleus of the thalamus (VAL)	right	22	−11	7	52	0.0820	± 0.0343	0.1256	± 0.0499	53.3	0.01199	1.00000	0.00120	0.00005[a]

[a]$p < 0.05$

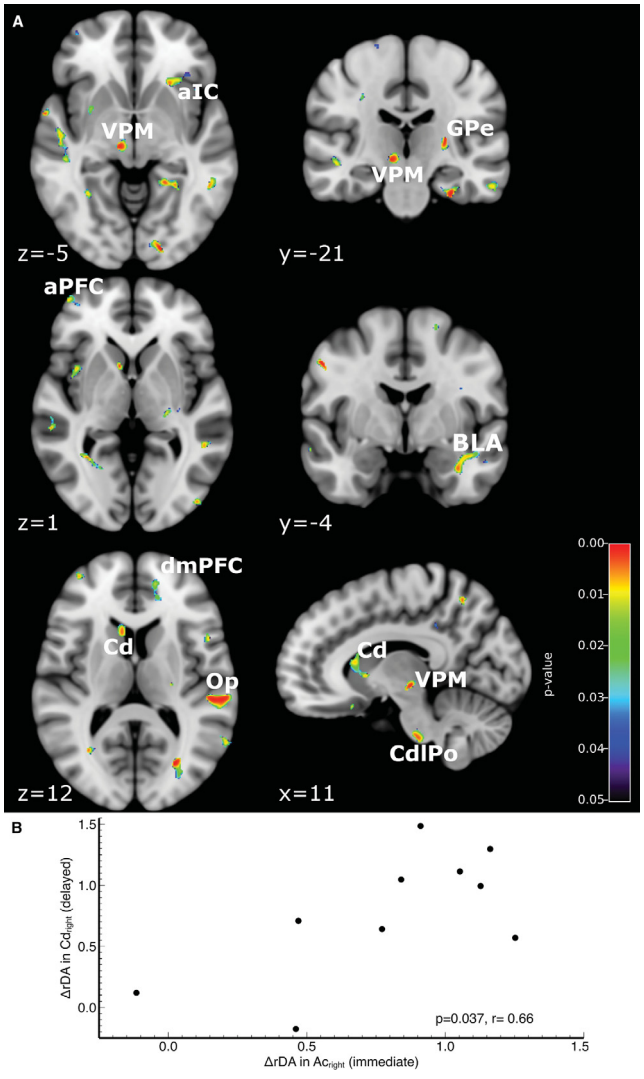

(legend on next page)

hippocampus (p = 0.0002, r = 0.94), and anterior cingulate cortex (ACC; p = 0.0006, r = 0.91; Figure 5A). The correlation with the delayed signal showed an opposite effect. Here, the wanting score predicted diminished ⊿rDA in the putamen (p = 0.00005, r = −0.96; Figure 5B). Consequently, there was also a negative correlation between combined early ⊿rDA in the anterior insula cortex, hippocampus, and ACC as well as the late ⊿rDA in the putamen (p = 0.0001, r = −0.93), although this analysis included additional PET data from one subject who did not perform the wanting rating.

Next, we tested the correlation between dopaminergic activity in the areas associating with food wanting (anterior insular cortex, hippocampus, ACC) at the time of food intake—milkshake or tasteless solution—and the post-ingestive dopaminergic activity in the putamen (Figure 5D). Independent of the stimulus (tasteless or milkshake) the immediate DA release in the wanting-related regions was negatively correlated with the post-ingestive DA release in the putamen (milkshake, p = 0.008, r = −0.78; tasteless solution, p = 0.007, r = −0.78).

To control for differences in the internal states between testing days and time points, we instructed the participants to rate hunger, satiety, and tiredness. The ratings in baseline condition and the repeated measures after PET or fMRI acquisition did not show a difference between testing days or time points (pre- and post-scan).

To ensure adherence to overnight fast and to control for putative metabolic influences, we acquired insulin and glucose level in the baseline conditions of both fMRI and PET scans. None of the parameters showed a significant difference between the testing days. Moreover, the glucose level acquired before and after the gustometer task did not differ on all three testing days.

DISCUSSION

It is generally assumed that both taste and nutritional value influence food-related DA signaling, but the underlying mechanisms and functional consequences remained unclear. By applying a novel method for the analysis of [11C]raclopride PET data, we provide evidence for an immediate and delayed DA release in segregated brain areas after food intake in humans.

The sensation of pleasant taste immediately elicited DA release in the orosensory pathway comprising the nucleus of the solitary tract, lateral ventral anterior nucleus of the thalamus, and frontal operculum/anterior insular cortex. These findings extend previous human and animal work on orosensory perception (Chen et al., 2011; de Araujo and Simon, 2009), and provide evidence that the BOLD activation of the insular cortex reported in previous studies indeed relates to DA release (Frank et al., 2016; Small et al., 2003a; Veldhuizen et al., 2011). The frontal operculum/anterior insular cortex is the primary gustatory cortex, and the DA release that straddles the entire ventral agranular insula (Evrard et al., 2014) integrates multi-sensory information and motivation-related circuitry (de Araujo et al., 2012; Maffei et al., 2012; Small et al., 2004). Congruent with these assumptions, our data revealed DA release in key regions of motivated behavior, reward valuation, and inhibitory control, such as the SN/VTA complex, nucleus accumbens, putamen, ventromedial prefrontal cortex, orbitofronatal cortex, hippocampus, and habenula (Assar et al., 2016; Baker et al., 2016; Berridge and Robinson, 1998; Kenny, 2011; Palmiter, 2007). Moreover, we found a strong DA release in the hypothalamus, tentatively in the lateral hypothalamus. This is interesting in the context of recent studies highlighting the role of lateral hypothalamus in integrating reward and feeding-specific circuits (Stuber and Wise, 2016) and disseminating information about reward-predictive cues (Sharpe et al., 2017). The fact that release was observed in the early "sensory" phase is also consistent with findings in mice showing that sensory detection of food activates agouti-related protein (AgRP) and proopioimelanocortin (POMC) hypothalamic neurons even before food is consumed (Chen et al., 2015). Collectively, this pattern of activation suggests that the immediate DA signals orosensory, homeostatic, and reinforcing features of food perceived in the oral cavity and highlights a role for the hypothalamus in responding to the sensory properties of foods.

Fifteen to twenty minutes after milkshake intake, we discovered a delayed DA release in a different circuit including the caudate head, pallidum, basolateral amygdala, ventral posterior medial thalamus, anterior insula, anterior and dorsomedial prefrontal cortex, and lateral caudate pontine nucleus. The temporal delay suggests that the second peak is mediated by post-ingestive signaling. Our finding thereby supports the current view based on rodent studies that the nutritional value of food primarily affects feeding by modulating dopaminergic pathways through gut-derived signals also in humans. According to previous microdialysis data in mice showing calorie-dependent DA release in the dorsal striatum after gastric infusion (Tellez et al., 2013), we identified a strong DA signal in the caudate head after milkshake consumption. In our data, DA release was also evident in areas representing interoceptive signaling from throughout the body as well as state-specific biased processing of motivationally relevant cues (insular cortex, ventral posterior medial thalamus, and basolateral amygdala; *cf.* Livneh et al., 2017), corticopontine pathways concerned with multiple domains of higher-order processing (dorsomedial and anterior prefrontal cortex, lateral caudate pontine nucleus; see Schmahmann and Pandya, 1997), and areas associated with goal-directed behavior and affective processing (dorsal caudate, pallidum; Balleine et al., 2007; Delgado et al., 2004).

Collectively, these findings provide first evidence for post-ingestive DA release in humans and stress the relevance of higher cognitive centers in control of food intake. Furthermore, our data support the concept that brain DA circuits serve as a nutritional sensor and guide food control by reinforcing highly nutritive food stimuli (Pignatelli and Bonci, 2015). In light of the

Figure 3. Delayed DA Release

(A) Twenty minutes after milkshake consumption, rDA release raised in the caudate nucleus (Cd), pallidum (external segment; GPe), anterior insular cortex (aIC), ventral posterior medial nucleus of the thalamus (VPM), amygdala (basolateral complex; BLA), parietal operculum (Op), anterior and dorsomedial prefrontal cortex (aPFC and dmPFC), and lateral caudal pontine nucleus (CdlPo). The maps are thresholded at $p < 0.05$ (whole brain; time interval, 40–45 min) (Table 2).

(B) Correlation between the immediate difference between rDA in the milkshake and the tasteless condition (⊿rDA) in nucleus accumbens (Ac) correlates with delayed ⊿rDA in the caudate nucleus (Cd).

Table 2. Areas Showing DA Release 20 min after Milkshake Intake

Area	Hemisphere	x	y	z	Number of Voxels	Mean rDA (Tasteless)		Mean rDA (Milkshake)		% Increase	p_{uncorr} (min)	p_{FWE} (min)	p_{uncorr} (Cluster)	p_{FWE} (Cluster)
Anterior insular cortex (aIC)	left	−25	23	−5	140	0.0633	± 0.0307	0.1159	± 0.0544	83.1	0.00214	0.41236	0.00233	0.01048[a]
	right	31	18	−11	256	0.0865	± 0.0418	0.1659	± 0.0756	91.8	0.00052	0.00488[a]	0.00038	0.00000[a]
Caudate nucleus (Cd)	right	11	18	9	361	0.0697	± 0.0298	0.1232	± 0.0540	76.7	0.00122	0.08886	0.00231	0.00031[a]
Operculum (Op)	left	−52	−29	10	759	0.0836	± 0.0354	0.1607	± 0.0729	92.1	0.00012	0.00002[a]	0.00008	0.00000[a]
Subthalamic nucleus (STh)	right	10	−20	−4	252	0.0983	± 0.0543	0.1719	± 0.0785	74.8	0.00113	0.06832	0.00433	0.01952[a]
Nucleus accumbens (Ac)	right	10	11	0	23	0.0674	± 0.0294	0.1093	± 0.0430	62.2	0.00122	0.08886	0.00175	0.06889
Amygdala (basolateral portion; Amg)	left	−34	−5	−24	379	0.0866	± 0.0328	0.1566	± 0.0642	80.9	0.00204	0.36735	0.00029	0.00000[a]
Anterior prefrontal cortex/frontal pole (aPFC)	right	41	58	−1	303	0.0639	± 0.0247	0.1118	± 0.0467	74.9	0.00040	0.00205[a]	0.00076	0.00000[a]
Dorsomedial prefrontal cortex (dmPFC)	left	−9	50	23	232	0.0676	± 0.0333	0.1202	± 0.0542	77.8	0.00217	0.42912	0.00296	0.00588[a]
Precentral gyrus (PrG)	left	−46	24	28	247	0.0857	± 0.0427	0.1501	± 0.0729	75.1	0.00137	0.12594	0.00171	0.00042[a]
Central insular cortex (cIC)	right	37	5	1	174	0.0831	± 0.0376	0.1482	± 0.0717	78.4	0.00610	1.00000	0.00623	0.16587
Substantia nigra/ventral tegmental area (SN/VTA)	right	10	−16	−9	134	0.0950	± 0.0543	0.1763	± 0.0787	85.5	0.00113	0.06832	0.00270	0.02017[a]
Pallidum (external segment, GPe)	left	−25	−17	8	203	0.0734	± 0.0352	0.1190	± 0.0553	62.0	0.00003	0.00000[a]	0.00147	0.00046[a]
Hippocampus (Hi)	right	39	−26	−17	308	0.0945	± 0.0381	0.1647	± 0.0619	74.3	0.00018	0.00005[a]	0.00011	0.00000[a]
	left	−39	−26	−10	302	0.0960	± 0.0350	0.1591	± 0.0674	65.6	0.00174	0.24616	0.00224	0.00062[a]
Thalamus (ventral posteriomedial nucleus, VPM)	right	9	−23	−3	221	0.0978	± 0.0541	0.1731	± 0.0786	77.0	0.00113	0.06832	0.00381	0.01825[a]
Lateral caudate pontine nucleus (CdlPo)	right	13	−27	−38	307	0.1405	± 0.0652	0.2314	± 0.0953	64.7	0.00107	0.06109	0.00102	0.00001[a]

[a] $p < 0.05$

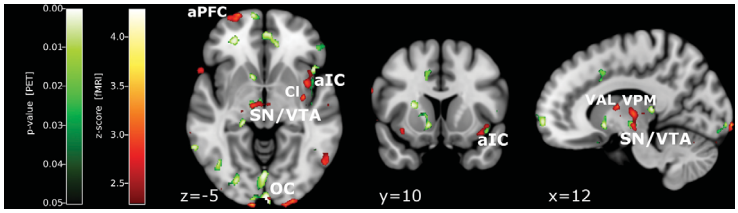

Figure 4. Combined fMRI and PET Analysis

The fMRI-BOLD activation (red scale) overlapped with DA release (green scale) in the anterior insular cortex (aIC), substantia nigra/ventral tegmental area (SN/VTA), and occipital cortex (OC). BOLD activation in the fMRI data occurs without overlapping primarily in the claustrum (Cl) and in the ventroanterior (VAL) and ventral posterior medial nucleus (VPM) of the thalamus as well as in the anterior prefrontal cortex. Both maps were derived from group statistics for the contrast milkshake-tasteless. The DA release was assessed in the early time interval (20–25 min), thresholded at $p < 0.05$. The fMRI map was derived from z-statics at group level and thresholded for $z > 2.3$.

literature we review in the introduction, it is interesting that immediate and post-ingestive response recruit anatomically segregated structures in the striatum, highlighting different roles in action-reward associations in decision-making and reward dependence to continue previously rewarded behavior (Balleine et al., 2007; Cohen et al., 2009). This mechanism is further substantiated through a correlation between delayed activation in the caudate head and immediate activation in the nucleus accumbens, suggesting a stronger brain response to the taste of milkshake depending on its learned nutritional value.

The desire to eat has a strong impact on food selection and the amount of food that we eat even beyond metabolic demands. We identified a set of brain regions in which DA release was strongly correlated with the subjective desire to eat. Higher wanting scores predicted enhanced orosensory DA release in motivation-associated areas comprising the ACC, hippocampus, and insular cortices (Murdaugh et al., 2012; Robinson et al., 2016) and diminished post-ingestive DA release in the putamen. Surprisingly, even irrespective of milkshake or tasteless solution intake, DA release in the regions related to wanting score at food intake was inversely correlated with post-ingestive DA release in the putamen (Figure 5D). Therefore, high desire to eat and thus high DA release in wanting-related areas presumably inhibits post-ingestive DA release in the putamen—a scenario illustrated in Figure 5E. A potential interpretation for this mechanism is that wanting suppresses satiety-related signaling, which would then lead to overconsumption of highly desired food. This hypothesis, however, requires further investigation.

The current findings also have high relevance for understanding the obesity epidemic. Prolonged high-fat diet and compulsive eating as well as weakened impulse control are associated with D2-receptor downregulation in rodents (Adams et al., 2015; Johnson and Kenny, 2010; van de Giessen et al., 2013) and reduced striatal activation in response to food consumption in humans (Babbs et al., 2013; Stice et al., 2008a; Volkow et al., 2017). Nutrient sensing in DA circuits is critical for learned food preferences and directly involved in the initiation of feeding motor programs (Tellez et al., 2016). Hence, post-ingestive DA deficiency in obesity has behavioral consequences. In rodents, it was associated with reduced motivated food-seeking behavior and increased preference for high caloric food (Tellez et al., 2013). The behavioral consequences of wanting-dependent DA release reported in our study have to be investigated in future studies.

In conclusion, we demonstrate evidence for immediate orosensory and delayed post-ingestive DA release in separate neural circuits after food intake in humans at a brain systems level. While the immediate DA response recruits specialized orosensory integrative pathways, post-ingestive DA signaling acts on higher cognitive centers and mediates their modulation by the internal state of the body, stressing therefore their central role in food intake regulation. Furthermore, we showed that DA release in wanting-related areas at food intake mirrored subjective desire to eat and presumably inhibited post-ingestive DA release in the putamen.

Limitations of Study

Given that the density of D2 receptors in extrastriatal regions is only <10% of the density in the striatum, it may be questionable if low-affinity tracers such as [11C]raclopride are able to detect DA release outside of the striatum. However, there are two factors that promote detection of extrastriatal DA release with the novel method. First, the method relates relative variations of the [11C] raclopride signal and not the absolute signal to DA release events. By comparison of intra- and extrastriatal [11C]raclopride kinetics and its responsiveness to minute-by-minute temporal variations of extracellular DA concentrations, we could show, with the help of model calculations, that although the D2 density is more than a factor of 10 lower outside of the striatum, the amplitude of temporal variations of [11C]raclopride is only a factor of 5 lower in these regions (Lippert et al., 2018). Second, [11C]raclopride solely responds to slow variations of extracellular DA concentrations. *In situ* voltammetric recordings in the striatum of rodents indeed show that part of the DA that diffuses into extracellular space after phasic release is removed at a minute timescale. We hypothesized that this slow removal rate originates from subcellular compartments in the extracellular space with low density of DA transporters. Extrastriatal regions have a lower density not only of DA synapses and DA receptors but also of DA transporters.

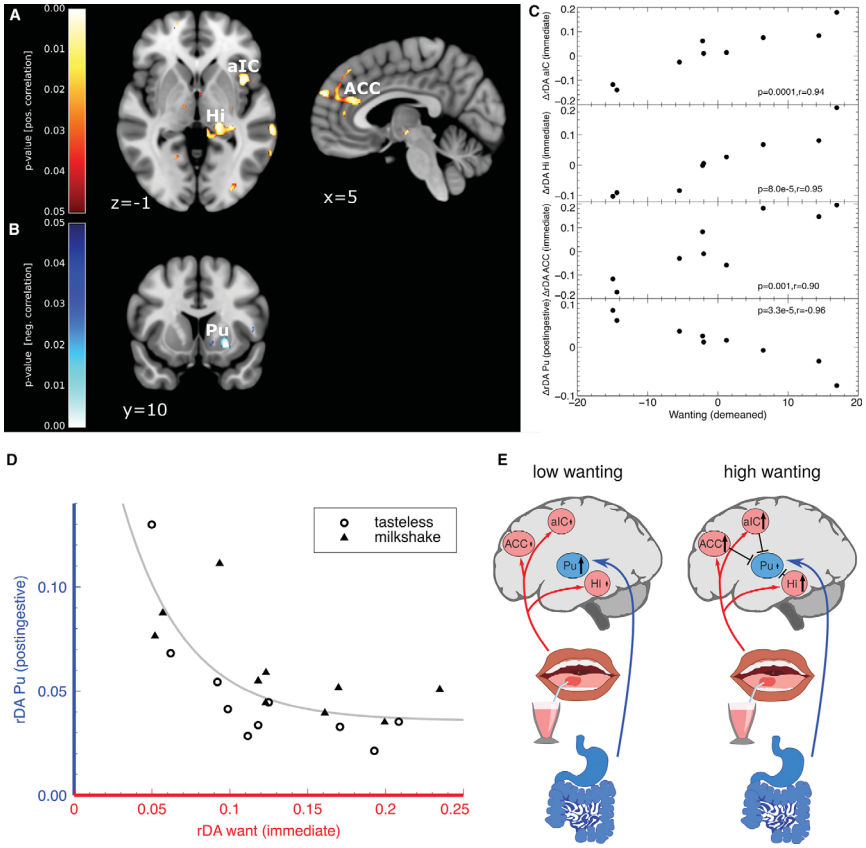

Figure 5. Measures of Wanting and DA Response

(A) Correlation between wanting ratings and the difference between immediate DA release after milkshake and tasteless solution intake (⊿rDA; 20–25 min) in the anterior insular cortex (aIC), hippocampus (Hi), and anterior cingulate cortex (ACC; red; voxel-wise correlation with a threshold of $p < 0.05$).

(B) Correlation of the difference between delayed DA release after milkshake and tasteless solution intake (rDA; 35–40 min) in the putamen (Pu) with the wanting score (blue; voxel-wise correlation with a threshold of $p < 0.05$).

(C) Post hoc analysis revealing correlations between wanting scores and ⊿rDA in aIC, Hi, ACC, and Pu.

(D) Correlation between DA release in wanting-associated areas at stimulus delivery with post-ingestive DA release in the putamen. The correlation was significant in both milkshake (triangle; $p = 0.008$, $r = -0.78$) and tasteless (circle; $p = 0.007$, $r = -0.78$) condition.

(E) Desire to eat is potentially linked to DA release in motivation-associated brain areas. Post-ingestive DA release in the putamen presumably inhibits desire to eat and hence DA release in wanting-related areas.

Therefore, although the amount of released DA is lower in extrastriatal regions, the major fraction is removed slowly and thereby contributes to variations in [11C]raclopride binding. Simultaneous voltammetry recordings of evoked striatal and cortical DA release in rats clearly show this effect: the amplitudes of release-induced minute-by-minute variations in extracellular DA concentrations are of the same order of magnitude in extrastriatal regions as in the striatum despite the difference in total amount of released

DA (Garris et al., 1993). This could explain the extrastriatal food-induced changes of rDA that we observed here.

In the present study, a novel method for the analysis of [11C]raclopride was applied to assess stimulus-induced DA release in humans. The method introduces the parameter rDA, which is directly calculated from temporal variations in the [11C]raclopride signal, as a measure for regional DA release. In the methodological paper we could demonstrate, with the help of voltammetry recordings in mice, that phasic DA release systematically induces minute-by-minute variations in extracellular DA concentrations, that these variations induce detectable variations in the [11C]raclopride signal (as measured by rDA), and that the amplitude of these variations is proportional to the rates of phasic DA release (Lippert et al., 2018). In order to compare regional rDA values between subjects, it is imperative that the PET data were acquired under similar conditions (same scanner, specific activity of the tracer, etc.). Regarding the data shown in Figure 5, it appears that the determination of rDA is strikingly robust: each data point in Figure 5B indicates the difference between rDA during milkshake and tasteless solution condition in the same region for each individual subject (9 data points, one subject did not fill out the "wanting" data sheet). There was at minimum 1 week between the two PET sessions. In the four regions displayed, we found high correlations between the individual wanting scores and the individual difference of rDA. Each data point in Figure 5D displays rDA in the wanting-related regions (immediate) and in the putamen (post-ingestive) for each individual PET session (10 subjects * 2 sessions = 20 data points; the subject who did not fill out the "wanting" data sheet is also included here). These data indicate that post-ingestive rDA is only high if immediate rDA in wanting-related regions is low. Without providing solid proof, these results do indicate that rDA is reproducible. However, further studies are necessary to substantiate the utility of the method for the detection of DA release.

STAR★METHODS

Detailed methods are provided in the online version of this paper and include the following:

- KEY RESOURCES TABLE
- CONTACT FOR REAGENT AND RESOURCE SHARING
- EXPERIMENTAL MODEL AND SUBJECT DETAILS
- METHOD DETAILS
  - Experimental Design
  - Gustometer Setup
  - fMRI Data Acquisition
  - PET Data Collection
- QUANTIFICATION AND STATISTICAL ANALYSIS
  - fMRI Analysis
  - PET Analysis
  - Combined fMRI and PET Analysis
  - Reporting of Brain Areas
  - Other Statistical Analyses

SUPPLEMENTAL INFORMATION

Supplemental Information includes one figure and can be found with this article online at https://doi.org/10.1016/j.cmet.2018.12.006.

ACKNOWLEDGMENTS

The authors are especially grateful to Ivan de Araujo for his comments on an earlier version of the manuscript, to Henning Fenselau for providing his insight into gastric signaling, and to Henry Evrard for discussions on insular anatomy and its relevance in this work. Hendrik Nolte assisted with statistical analysis, Sonja Blum provided excellent technical assistance, and Bernd Neumaier together with the former Radiochemistry Lab at the Max Planck Institute for Neurological Research provided the PET tracer. H.B., M.T., and J.C.B. were supported by the German Research Foundation in the Transregional Collaborative Research Center 134. M.T. and J.C.B. are further supported by the German Centre for Diabetes Research.

AUTHOR CONTRIBUTIONS

S.E.T., J.C.B., D.M.S., and M.T. conceived the study; S.E.T. performed all experiments. S.E.T. and H.B. analyzed the data. A.G.D. provided support to establish the gustometer setup and A.L.C. as well as R.N.L. supported validation of the analysis technique. K.A., O.A.C., and R.H. contributed to participant recruitment as well as data acquisition. S.E.T., H.B., and M.T. wrote the manuscript. All authors agreed on the final version of the manuscript.

DECLARATION OF INTERESTS

The authors declare no competing interests.

Received: February 1, 2018
Revised: May 18, 2018
Accepted: December 4, 2018
Published: December 27, 2018

REFERENCES

Adams, W.K., Sussman, J.L., Kaur, S., D'souza, A.M., Kieffer, T.J., and Winstanley, C.A. (2015). Long-term, calorie-restricted intake of a high-fat diet in rats reduces impulse control and ventral striatal D2 receptor signalling - two markers of addiction vulnerability. Eur. J. Neurosci. *42*, 3095–3104.

Andersson, J.L.R., Skare, S., and Ashburner, J. (2003). How to correct susceptibility distortions in spin-echo echo-planar images: application to diffusion tensor imaging. Neuroimage *20*, 870–888.

Andrews, Z.B., and Horvath, T.L. (2008). Tasteless food reward. Neuron *57*, 806–808.

Assar, N., Mahmoudi, D., Farhoudian, A., Farhadi, M.H., Fatahi, Z., and Haghparast, A. (2016). D1- and D2-like dopamine receptors in the CA1 region of the hippocampus are involved in the acquisition and reinstatement of morphine-induced conditioned place preference. Behav. Brain Res. *312*, 394–404.

Babbs, R.K., Sun, X., Felsted, J., Chouinard-Decorte, F., Veldhuizen, M.G., and Small, D.M. (2013). Decreased caudate response to milkshake is associated with higher body mass index and greater impulsivity. Physiol. Behav. *121*, 103–111.

Baker, P.M., Jhou, T., Li, B., Matsumoto, M., Mizumori, S.J.Y., Stephenson-Jones, M., and Vicentic, A. (2016). The lateral habenula circuitry: reward processing and cognitive control. J. Neurosci. *36*, 11482–11488.

Baldo, B.A., Sadeghian, K., Basso, A.M., and Kelley, A.E. (2002). Effects of selective dopamine D1 or D2 receptor blockade within nucleus accumbens subregions on ingestive behavior and associated motor activity. Behav. Brain Res. *137*, 165–177.

Balleine, B.W., Delgado, M.R., and Hikosaka, O. (2007). The role of the dorsal striatum in reward and decision-making. J. Neurosci. *27*, 8161–8165.

Bartoshuk, L.M., Duffy, V.B., Green, B.G., Hoffman, H.J., Ko, C.W., Lucchina, L.A., Marks, L.E., Snyder, D.J., and Weiffenbach, J.M. (2004). Valid across-group comparisons with labeled scales: the gLMS versus magnitude matching. Physiol. Behav. *82*, 109–114.

Beck, A.T., Steer, R.A., and Brown, G.K. (1996). Manual for the Beck Depression Inventory-II (Psychological Corporation).

Berridge, K.C., and Robinson, T.E. (1998). What is the role of dopamine in reward: hedonic impact, reward learning, or incentive salience? Brain Res. Brain Res. Rev. *28*, 309–369.

Beutler, L.R., Chen, Y., Ahn, J.S., Lin, Y.C., Essner, R.A., and Knight, Z.A. (2017). Dynamics of gut-brain communication underlying hunger. Neuron *96*, 461–475.e5.

Brainard, D.H. (1997). The Psychophysics Toolbox. Spat. Vis. *10*, 433–436.

Chen, X., Gabitto, M., Peng, Y., Ryba, N.J.P., and Zuker, C.S. (2011). A gustotopic map of taste qualities in the mammalian brain. Science *333*, 1262–1266.

Chen, Y., Lin, Y.-C., Kuo, T.-W., and Knight, Z.A. (2015). Sensory detection of food rapidly modulates arcuate feeding circuits. Cell *160*, 829–841.

Cízek, J., Herholz, K., Vollmar, S., Schrader, R., Klein, J., and Heiss, W.-D. (2004). Fast and robust registration of PET and MR images of human brain. Neuroimage *22*, 434–442.

Cohen, M.X., Schoene-Bake, J.C., Elger, C.E., and Weber, B. (2009). Connectivity-based segregation of the human striatum predicts personality characteristics. Nat. Neurosci. *12*, 32–34.

Cosgrove, K.P., Veldhuizen, M.G., Sandiego, C.M., Morris, E.D., and Small, D.M. (2015). Opposing relationships of BMI with BOLD and dopamine D2/3 receptor binding potential in the dorsal striatum. Synapse *69*, 195–202.

de Araujo, I.E. (2016). Circuit organization of sugar reinforcement. Physiol. Behav. *164* (Pt B), 473–477.

de Araujo, I.E., and Simon, S.A. (2009). The gustatory cortex and multisensory integration. Int. J. Obes. *33* (*Suppl 2*), S34–S43.

de Araujo, I.E., Oliveira-Maia, A.J., Sotnikova, T.D., Gainetdinov, R.R., Caron, M.G., Nicolelis, M.A., and Simon, S.A. (2008). Food reward in the absence of taste receptor signaling. Neuron *57*, 930–941.

de Araujo, I.E., Geha, P., and Small, D.M. (2012). Orosensory and homeostatic functions of the insular taste cortex. Chemosens. Percept. *5*, 64–79.

de Araujo, I.E., Lin, T., Veldhuizen, M.G., and Small, D.M. (2013). Metabolic regulation of brain response to food cues. Curr. Biol. *23*, 878–883.

Delgado, M.R., Stenger, V.A., and Fiez, J.A. (2004). Motivation-dependent responses in the human caudate nucleus. Cereb. Cortex *14*, 1022–1030.

DiFeliceantonio, A.G., Coppin, G., Rigoux, L., Edwin Thanarajah, S., Dagher, A., Tittgemeyer, M., and Small, D.M. (2018). Supra-additive effects of combining fat and carbohydrate on food reward. Cell Metab. *28*, 33–44.e3.

Evrard, H.C., Logothetis, N.K., and Craig, A.D. (2014). Modular architectonic organization of the insula in the macaque monkey. J. Comp. Neurol. *522*, 64–97.

Ferreira, J.G., Tellez, L.A., Ren, X., Yeckel, C.W., and de Araujo, I.E. (2012). Regulation of fat intake in the absence of flavour signalling. J. Physiol. *590*, 953–972.

Frank, S., Veit, R., Sauer, H., Enck, P., Friederich, H.C., Unholzer, T., Bauer, U.M., Linder, K., Heni, M., Fritsche, A., and Preissl, H. (2016). Dopamine depletion reduces food-related reward activity independent of BMI. Neuropsychopharmacology *41*, 1551–1559.

Friston, K.J., Worsley, K.J., Frackowiak, R.S., Mazziotta, J.C., and Evans, A.C. (1994). Assessing the significance of focal activations using their spatial extent. Hum. Brain Mapp. *1*, 210–220.

Garris, P.A., Collins, L.B., Jones, S.R., and Wightman, R.M. (1993). Evoked extracellular dopamine in vivo in the medial prefrontal cortex. J. Neurochem. *61*, 637–647.

Green, B.G., Dalton, P., Cowart, B., Shaffer, G., Rankin, K., and Higgins, J. (1996). Evaluating the 'Labeled Magnitude Scale' for measuring sensations of taste and smell. Chem. Senses *21*, 323–334.

Hajnal, A., Smith, G.P., and Norgren, R. (2004). Oral sucrose stimulation increases accumbens dopamine in the rat. Am. J. Physiol. Regul. Integr. Comp. Physiol. *286*, R31–R37.

Han, W., Tellez, L.A., Niu, J., Medina, S., Ferreira, T.L., Zhang, X., Su, J., Tong, J., Schwartz, G.J., van den Pol, A., and de Araujo, I.E. (2016). Striatal dopamine links gastrointestinal rerouting to altered sweet appetite. Cell Metab. *23*, 103–112.

Howe, M.W., and Dombeck, D.A. (2016). Rapid signalling in distinct dopaminergic axons during locomotion and reward. Nature *535*, 505–510.

Hsiao, S., and Smith, G.P. (1995). Raclopride reduces sucrose preference in rats. Pharmacol. Biochem. Behav. *50*, 121–125.

Jenkinson, M., Bannister, P., Brady, M., and Smith, S. (2002). Improved optimization for the robust and accurate linear registration and motion correction of brain images. Neuroimage *17*, 825–841.

Johnson, P.M., and Kenny, P.J. (2010). Dopamine D2 receptors in addiction-like reward dysfunction and compulsive eating in obese rats. Nat. Neurosci. *13*, 635–641.

Kaelberer, M.M., Buchanan, K.L., Klein, M.E., Barth, B.B., Montoya, M.M., Shen, X., and Bohórquez, D.V. (2018). A gut-brain neural circuit for nutrient sensory transduction. Science *361*, eaat5236.

Kelley, A.E., Baldo, B.A., Pratt, W.E., and Will, M.J. (2005). Corticostriatal-hypothalamic circuitry and food motivation: integration of energy, action and reward. Physiol. Behav. *86*, 773–795.

Kenny, P.J. (2011). Reward mechanisms in obesity: new insights and future directions. Neuron *69*, 664–679.

Laruelle, M. (2000). Imaging synaptic neurotransmission with in vivo binding competition techniques: a critical review. J. Cereb. Blood Flow Metab. *20*, 423–451.

Lim, J., Wood, A., and Green, B.G. (2009). Derivation and evaluation of a labeled hedonic scale. Chem. Senses *34*, 739–751.

Lippert, R.N., Cremer, A.L., Thanarajah, S.E., Korn, C., Jahans-Price, T., Burgeno, L., Tittgemeyer, M., Brüning, J.C., Walton, M.E., and Backes, H. (2018). Time-dependent assessment of stimulus-evoked regional dopamine release. Nat. Commun. Published online December 27, 2018. https://doi.org/10.1038/s41467-018-8143-4.

Liu, Y., Gao, J.H., Liu, H.L., and Fox, P.T. (2000). The temporal response of the brain after eating revealed by functional MRI. Nature *405*, 1058–1062.

Livneh, Y., Ramesh, R.N., Burgess, C.R., Levandowski, K.M., Madara, J.C., Fenselau, H., Goldey, G.J., Diaz, V.E., Jikomes, N., Resch, J.M., et al. (2017). Homeostatic circuits selectively gate food cue responses in insular cortex. Nature *546*, 611–616.

Lucas, F., and Sclafani, A. (1989). Flavor preferences conditioned by intragastric fat infusions in rats. Physiol. Behav. *46*, 403–412.

Maffei, A., Haley, M., and Fontanini, A. (2012). Neural processing of gustatory information in insular circuits. Curr. Opin. Neurobiol. *22*, 709–716.

Mai, J.K., Majtanik, M., and Paxinos, G. (2015). Atlas of the Human Brain (Academic Press).

Mela, D.J. (2006). Eating for pleasure or just wanting to eat? Reconsidering sensory hedonic responses as a driver of obesity. Appetite *47*, 10–17.

Murdaugh, D.L., Cox, J.E., Cook, E.W., 3rd, and Weller, R.E. (2012). fMRI reactivity to high-calorie food pictures predicts short- and long-term outcome in a weight-loss program. Neuroimage *59*, 2709–2721.

Nichols, T., and Hayasaka, S. (2003). Controlling the familywise error rate in functional neuroimaging: a comparative review. Stat. Methods Med. Res. *12*, 419–446.

O'Doherty, J.P., Deichmann, R., Critchley, H.D., and Dolan, R.J. (2002). Neural responses during anticipation of a primary taste reward. Neuron *33*, 815–826.

Palmiter, R.D. (2007). Is dopamine a physiologically relevant mediator of feeding behavior? Trends Neurosci. *30*, 375–381.

Pignatelli, M., and Bonci, A. (2015). Role of dopamine neurons in reward and aversion: a synaptic plasticity perspective. Neuron *86*, 1145–1157.

Polk, S.E., Schulte, E.M., Furman, C.R., and Gearhardt, A.N. (2017). Wanting and liking: Separable components in problematic eating behavior? Appetite *115*, 45–53.

Robinson, M.J., Fischer, A.M., Ahuja, A., Lesser, E.N., and Maniates, H. (2016). Roles of "wanting" and "liking" in motivating behavior: gambling, food, and drug addictions. Curr. Top. Behav. Neurosci. *27*, 105–136.

Rothemund, Y., Preuschhof, C., Bohner, G., Bauknecht, H.C., Klingebiel, R., Flor, H., and Klapp, B.F. (2007). Differential activation of the dorsal striatum

by high-calorie visual food stimuli in obese individuals. Neuroimage *37*, 410–421.

Schmahmann, J.D., and Pandya, D.N. (1997). Anatomic organization of the basilar pontine projections from prefrontal cortices in rhesus monkey. J. Neurosci. *17*, 438–458.

Schneider, L.H. (1989). Orosensory self-stimulation by sucrose involves brain dopaminergic mechanisms. Ann. N Y Acad. Sci. *575*, 307–319, discussion 319–320.

Sclafani, A., and Ackroff, K. (2012). Role of gut nutrient sensing in stimulating appetite and conditioning food preferences. Am. J. Physiol. Regul. Integr. Comp. Physiol. *302*, R1119–R1133.

Sharpe, M.J., Marchant, N.J., Whitaker, L.R., Richie, C.T., Zhang, Y.J., Campbell, E.J., Koivula, P.P., Necarsulmer, J.C., Mejias-Aponte, C., Morales, M., et al. (2017). Lateral hypothalamic GABAergic neurons encode reward predictions that are relayed to the ventral tegmental area to regulate learning. Curr. Biol. *27*, 2089–2100.e5.

Small, D.M., Gregory, M.D., Mak, Y.E., Gitelman, D., Mesulam, M.M., and Parrish, T. (2003a). Dissociation of neural representation of intensity and affective valuation in human gustation. Neuron *39*, 701–711.

Small, D.M., Jones-Gotman, M., and Dagher, A. (2003b). Feeding-induced dopamine release in dorsal striatum correlates with meal pleasantness ratings in healthy human volunteers. Neuroimage *19*, 1709–1715.

Small, D.M., Voss, J., Mak, Y.E., Simmons, K.B., Parrish, T., and Gitelman, D. (2004). Experience-dependent neural integration of taste and smell in the human brain. J. Neurophysiol. *92*, 1892–1903.

Smith, S.M. (2002). Fast robust automated brain extraction. Hum. Brain Mapp. *17*, 143–155.

Smith, G.P. (2004). Accumbens dopamine mediates the rewarding effect of orosensory stimulation by sucrose. Appetite *43*, 11–13.

Sotak, B.N., Hnasko, T.S., Robinson, S., Kremer, E.J., and Palmiter, R.D. (2005). Dysregulation of dopamine signaling in the dorsal striatum inhibits feeding. Brain Res. *1061*, 88–96.

Stice, E., Spoor, S., Bohon, C., and Small, D.M. (2008a). Relation between obesity and blunted striatal response to food is moderated by TaqIA A1 allele. Science *322*, 449–452.

Stice, E., Spoor, S., Bohon, C., Veldhuizen, M.G., and Small, D.M. (2008b). Relation of reward from food intake and anticipated food intake to obesity: a functional magnetic resonance imaging study. J. Abnorm. Psychol. *117*, 924–935.

Stoeckel, L.E., Weller, R.E., Cook, E.W., 3rd, Twieg, D.B., Knowlton, R.C., and Cox, J.E. (2008). Widespread reward-system activation in obese women in response to pictures of high-calorie foods. Neuroimage *41*, 636–647.

Stuber, G.D., and Wise, R.A. (2016). Lateral hypothalamic circuits for feeding and reward. Nat. Neurosci. *19*, 198–205.

Su, Z., Alhadeff, A.L., and Betley, J.N. (2017). Nutritive, post-ingestive signals are the primary regulators of AgRP neuron activity. Cell Rep. *21*, 2724–2736.

Taber, M.T., and Fibiger, H.C. (1997). Activation of the mesocortical dopamine system by feeding: lack of a selective response to stress. Neuroscience *77*, 295–298.

Tellez, L.A., Medina, S., Han, W., Ferreira, J.G., Licona-Limón, P., Ren, X., Lam, T.T., Schwartz, G.J., and de Araujo, I.E. (2013). A gut lipid messenger links excess dietary fat to dopamine deficiency. Science *341*, 800–802.

Tellez, L.A., Han, W., Zhang, X., Ferreira, T.L., Perez, I.O., Shammah-Lagnado, S.J., van den Pol, A.N., and de Araujo, I.E. (2016). Separate circuitries encode the hedonic and nutritional values of sugar. Nat. Neurosci. *19*, 465–470.

Tolhurst, G., Reimann, F., and Gribble, F.M. (2012). Intestinal sensing of nutrients. Handb. Exp. Pharmacol. (209), 309–335.

van de Giessen, E., la Fleur, S.E., Eggels, L., de Bruin, K., van den Brink, W., and Booij, J. (2013). High fat/carbohydrate ratio but not total energy intake induces lower striatal dopamine D2/3 receptor availability in diet-induced obesity. Int. J. Obes. *37*, 754–757.

Veldhuizen, M.G., Bender, G., Constable, R.T., and Small, D.M. (2007). Trying to detect taste in a tasteless solution: modulation of early gustatory cortex by attention to taste. Chem. Senses *32*, 569–581.

Veldhuizen, M.G., Douglas, D., Aschenbrenner, K., Gitelman, D.R., and Small, D.M. (2011). The anterior insular cortex represents breaches of taste identity expectation. J. Neurosci. *31*, 14735–14744.

Veldhuizen, M.G., Babbs, R.K., Patel, B., Fobbs, W., Kroemer, N.B., Garcia, E., Yeomans, M.R., and Small, D.M. (2017). Integration of sweet taste and metabolism determines carbohydrate reward. Curr. Biol. *27*, 2476–2485.e6.

Volkow, N.D., Wang, G.J., Fowler, J.S., Logan, J., Jayne, M., Franceschi, D., Wong, C., Gatley, S.J., Gifford, A.N., Ding, Y.S., and Pappas, N. (2002). "Nonhedonic" food motivation in humans involves dopamine in the dorsal striatum and methylphenidate amplifies this effect. Synapse *44*, 175–180.

Volkow, N.D., Wise, R.A., and Baler, R. (2017). The dopamine motive system: implications for drug and food addiction. Nat. Rev. Neurosci. *18*, 741–752.

Wise, R.A., Spindler, J., deWit, H., and Gerberg, G.J. (1978). Neuroleptic-induced "anhedonia" in rats: pimozide blocks reward quality of food. Science *201*, 262–264.

Woolrich, M.W., Jbabdi, S., Patenaude, B., Chappell, M., Makni, S., Behrens, T., Beckmann, C., Jenkinson, M., and Smith, S.M. (2009). Bayesian analysis of neuroimaging data in FSL. Neuroimage *45* (1, Suppl), S173–S186.

Yeomans, M.R., Leitch, M., Gould, N.J., and Mobini, S. (2008). Differential hedonic, sensory and behavioral changes associated with flavor-nutrient and flavor-flavor learning. Physiol. Behav. *93*, 798–806.

STAR★METHODS

KEY RESOURCES TABLE

REAGENT or RESOURCE	SOURCE	IDENTIFIER
Chemicals, Peptides, and Recombinant Proteins		
[11C]Raclopride	Radio Chemistry Lab, Max Planck Institute for Neurological Research	N/A
Software and Algorithms		
GraphPad Prism 7.0d	GraphPad Software	https://www.graphpad.com/scientific-software/prism/
MATLAB 2014	MathWorks	https://de.mathworks.com/products/matlab.html
FSL 5.0	FMRIB Software Library	https://fsl.fmrib.ox.ac.uk/fsl/fslwiki
VINCI 4.9	Max Planck Institute for Metabolism Research	http://vinci.sf.mpg.de/
IDL 8.5.1	Exelis Visual Information Solutions	https://www.harrisgeospatial.com/Software-Technology/IDL
Gcc 4.8.4	Free Software Foundation	https://www.gnu.org/software/gcc/
Numerical Recipes in C, 3rd edition	Cambridge University Press	http://numerical.recipes/
Veusz 1.18	Jeremy Sanders and contributors	https://veusz.github.io/

CONTACT FOR REAGENT AND RESOURCE SHARING

Further information and requests for resources should be directed to and will be fulfilled by the Lead Contact, Heiko Backes (backes@sf.mpg.de).

EXPERIMENTAL MODEL AND SUBJECT DETAILS

Thirteen healthy volunteers of normal weight (BMI 25.57 ± 2.41 kg/m^2) participated in the study. All participants were recruited from a preexisting database maintained at the Max Planck Institute for Metabolism Research. To follow regulations of the German radiation protection authorities (BfS) only male participants between 40 and 70 years (age: 56 ± 9.5 years) were included in the study; also, to fulfill legal requirements, these participants had not participated in any previous PET study. Furthermore, all participants were non-smokers without any history of neurological, psychiatric, metabolic or eating disorders. We excluded volunteers on special diets, showing gluten or lactose intolerance as well as those scoring on the Beck Depression Inventory (BDI II; Beck et al., 1996) higher than 12. All volunteers participated in the fMRI part of the study. Out of these, 10 (age: 57.1 ± 10.55 years, BMI 25.73 ± 2.67 km/m^2) additionally underwent two PET-measurements. In the course of the data analysis, one subject had to be excluded from the fMRI-analysis due to incomplete data-acquisition. All subjects gave written informed consent to participate in the experiment, which was approved by the local ethics committee of the Medical Faculty of the University of Cologne (Cologne, Germany; No. 16-320).

METHOD DETAILS

Experimental Design

The study was carried out in a controlled, randomized, crossover design (Figure S1). Each volunteer participated on three testing days starting around the same time on the testing day (either 8 a.m. or 9 a.m.). On each testing day, participants arrived fasted with the last meal before 10 p.m. of the previous day. At the beginning of each day an intravenous catheter was inserted in the right forearm vein. Adherence to overnight fast was controlled by sampling blood glucose and insulin level in baseline condition. To assess metabolic changes by milkshake consumption glucose sampling was repeated after each scan. In addition, we acquired triglycerides, cholesterol, cortisol as well as HbA1c levels on the first testing day in order to rule out metabolic diseases. After each blood draw, the participants were asked to rate their hunger, satiety, thirst, tiredness as well as their wish to eat on a 100 mm visual analog scale (0 = "not hungry/sated/tired at all" and 100 = "very hungry/sated/tired").

On the first day, participants received training for using different rating scales with imagined stimuli. For the control condition, a solution was finally selected that the subjects indicated as tasteless during the test. Here, four different dilutions (100%, 75%,

50% and 25%) of the original solution (25 mM potassium chloride and 2.5 mM sodium bicarbonate) were presented pairwise. The solution selected in two successive comparisons was finally picked. Next, participants were presented four different milkshake flavors (vanilla, strawberry, banana, and chocolate). Here, the two milkshakes that were rated highest on liking and wanting were finally picked. Overall stimulus intensity as well as sweetness intensity were tested with the general labeled magnitude scale (gLMS; Bartoshuk et al., 2004; Green et al., 1996). Liking was rated on a vertical labeled hedonic scale (Lim et al., 2009; upper anchor point = "most liked," lower anchor point = "most disliked") and wanting was rated on a 100 mm visual analog scale (upper anchor point = "I don't want to drink the solution at all," lower anchor point = "I want to drink the solution very much"). After each tasting, participants were instructed to rinse their mouth with a glass of water and wait one minute for the next trial. Only participants that at least moderately liked and wanted the milkshake were included in the study.

Subsequently, on the first testing day each chosen participant underwent fMRI acquisition. On the second and third testing day PET Scans were performed in a randomized order with participants either receiving the chosen milkshakes or tasteless solution during the scan.

Gustometer Setup

All participants were fitted with a custom designed Teflon mouth-piece for fluid delivery to the tongue tip that was attached to the head-coil (64-channel head coil; Siemens, Erlangen, Germany) or to PET gantry. The gustometer consisted of four programmable syringe pumps (LA-100, HLL Landgraf Laborsysteme, Langenhagen, Germany), each with a 50 mL syringe (Braun, Melsungen, Germany) that contained either one of the two selected milkshakes, tasteless solution or water. The syringes were connected to the mouth-piece via a silicon beverage tubing (Lindemann GmbH, Helmstedt) with an inside diameter of 2 mm. The syringe pumps were controlled by scripts written in MATLAB (The Mathworks, MATLAB version 2014b) using the psychophysics toolbox extension (version 3.0.11; Brainard, 1997). In two 8.37 min long sessions, participants received tasteless solution and both milkshakes in a randomized order. Each milkshake supply was followed by a water rinse. Moreover, 80% of the stimuli were predictable by an auditory cue and 20% of the supplies appeared unpredicted. The interval between cue and stimulus was programmed with a random exponential jitter of, on average, two seconds. Either a high tone (600 Hz) or a low tone (300 Hz) predicted the milkshake or the tasteless solution. The association between cue and stimulus remained constant across sessions; participants were informed about the tone-delivery association in the beginning of the scan through a standardized instruction.

fMRI Data Acquisition

The imaging was performed on a 3T MRI system (Siemens Magnetom Prisma, Erlangen, Germany) using a 64-channel head-coil. Two 8.37 min sessions were acquired of each subject. Gradient echo-planar images (EPI) with 34 slices (voxel size: 2.8x2.8x2.8 mm^3, field of view: 220 mm, 2100 ms repetition time (TR), 30 ms echo time (TE), no distance factor) were acquired parallel to the commissural line (AC-PC) in a descending order from top to bottom. In addition, we acquired 2 short EPI-scans with 3 volumes each in opposing phase encoding directions (Anterior-Posterior, Posterior-Anterior) for later use in distortion correction. After each fMRI block a short anatomical scan was acquired (MPRAGE: 30 slices, voxel size: 2x2x2 mm^3, field of view: 192x192 mm, TR = 250 ms, TE = 2,86 ms, no distance factor) for the purpose of registration to standard space (MNI). High-resolution T1-weighted images were acquired using a 12-channel array head coil with 128 sagittal slices and whole brain coverage on a different day (MDEFT3D: TR = 1930 ms, TI = 650 ms, TE = 5.8 ms, resolution 1x1x1.25 mm^3, flip angle 18°).

PET Data Collection

PET imaging was acquired on a brain dedicated HRRT Siemens PET scanner. Each scan lasted 60 min. Participants were instructed not to sleep and to lie still. We injected 220-370 MBq [11C]raclopride using a programmable syringe pump (Perfusor compact, Braun, Melsungen): 70% was applied in a bolus within the first minute, 30% was constantly infused during the remaining 59 min. To ensure steady state and acquire dynamic PET-data, the gustometer task started 20 min after the onset of data collection and lasted 10 min. The PET scan was continued for 30 min after task completion. Since we wanted to analyze time-dependent DA release following food intake we performed two different PET imaging sessions with either milkshake or tasteless solution in a randomized order. Each milkshake or tasteless supply was followed by a rinse of water.

QUANTIFICATION AND STATISTICAL ANALYSIS

fMRI Analysis

The individual datasets were preprocessed before running statistical analyses using tools form the FMRIB software Library (FSL version 5.0.8, https://fsl.fmrib.ox.ac.uk/fsl/fslwiki): time series were first re-aligned to correct for small head movements using MCFLIRT (Jenkinson et al., 2002). Non-brain tissues were removed using an automated brain extraction tool (BET; Smith, 2002). For distortion correction, we collected pairs of images with distortions going in opposite phase encoding directions. From these pairs, the susceptibility-induced off-resonance field was estimated using the topup tool as implemented in FSL (Andersson et al., 2003). The FEAT package within FSL was used for single- and group level analysis. Slice time correction, Gaussian smoothing with a 6 mm FWHM kernel and high pass temporal filtering (FWHM = 120 s) was performed for each session. The EPI-images were first

registered to the individual anatomical T1-weighted scan and subsequently to the MNI-152 standard brain. Additionally, we extracted time series of white matter in both hemispheres, and the ventricle to account for possible confounds. Since stimuli were presented repeatedly in blocks, a block-related model was used in the GLM analysis. Predicted and unpredicted trials were collapsed. A boxcar convolved with a double gamma hemodynamic response function (HRF) was used to model the data. To detect areas that responded to milkshake we obtained the contrast "milkshake-tasteless" for each session. In the second level analysis, both sessions of each subject were included and analyzed with a fixed effect model. On group level, we performed a mixed effect model analysis with Bayesian estimation techniques using FLAME (FMRIB's Local Analysis of Mixed Effects; Woolrich et al., 2009) stage 1 and 2 to test for the average effect across the group. Age and BMI were included as covariates after demeaning. Gaussian random field theory was applied for cluster-based correction for multiple comparisons resulting in thresholded z-score maps. Note that we only report data that survived cluster level correction (z-threshold = 2.3, cluster significance p-threshold = 0.05, corrected) in whole brain analysis.

PET Analysis

After correcting for attenuation and scatter, PET images were reconstructed in 12 time intervals of 5 min duration using three-dimensional ordinary Poisson ordered subset expectation maximization (OP-3D-OSEM) including the modeling of the system's point spread function (PSF). Individual PET images were smoothed by application of a 10 mm Gaussian filter and co-registered with respective T1-weighted MR image using the imaging software VINCI (Cízek et al., 2004). The individual MR images were then non-linearly transformed into the stereotaxic Montreal Neurological Institute (MNI) space and the transformation matrix was applied to the corresponding multiframe PET images (VINCI). [11C]raclopride PET data were analyzed following a newly developed approach. Details of the method are published in a separate methodological paper (Lippert et al., 2019). In brief, [11C]raclopride predominantly binds to extrasynaptic extracellular D2 receptors and thereby competes with endogenous extracellular DA levels. We have shown that activation of DA neurons not only induces synaptic DA transmission and corresponding extracellular DA transients (timescale ~1 s), but also induces low frequency variations of DA levels in extracellular space. We further showed that the amplitude of low and high frequency variations of DA are linearly correlated. Low frequency variations of extracellular DA cause variations of the amount of D2 receptor-bound DA levels, which interact with the binding of [11C]raclopride. Therefore low frequency (~minutes) variations of [11C]raclopride in tissue are related to low frequency variations of DA (and also to the correlated high frequency variations) and can be used as a quantitative measure for dopaminergic activity. The parameter rDA, which has been shown to be a measure for transient dopamine release rates, is calculated from the [11C]raclopride PET data as

$$rDA_{ijk}(t_n) = \frac{1}{R_{0,ijk}} \sqrt{\frac{1}{125} \sum_{u=i-2}^{i+2} \sum_{v=j-2}^{j+2} \sum_{w=k-2}^{k+2} \left(R_{uvw}(t_n) - R_{uvw}(t_{n-1})\right)^2}$$

$$R_{0,ijk} = \frac{1}{8} \frac{1}{125} \sum_{n=5}^{12} \sum_{u=i-2}^{i+2} \sum_{v=j-2}^{j+2} \sum_{w=k-2}^{k+2} R_{uvw}(t_n)$$

with $R_{ijk}(t_n)$ the [11C]raclopride PET signal in voxel i,j,k at time t_n (Lippert et al., 2019). Calculation of dopaminergic activity (rDA) from the [11C]raclopride data requires quasi-steady state conditions. To fulfill this prerequisite, we inject [11C]raclopride by a bolus plus infusion method. A quasi-steady state is then reached after ~15 min. After this time, the new method provides spatio-temporal maps of rDA at a temporal resolution of 5 min and a spatial resolution of ~1 mL. Note, that PET tracer delivery by a bolus plus constant infusion method has the merit of making the PET signal insensitive to variations in blood flow (Laruelle, 2000). We can therefore rule out that the observed alterations in the [11C]raclopride PET signal could have been caused by changes in blood flow.

In order to identify regions with differences in rDA depending on food intake (tasteless solution or milkshake) we performed voxel-wise paired t tests and found clusters of contiguous voxels with p(uncorrected)<0.05. Random field theory-based correction for multiple comparisons was performed by calculating the family-wise error-corrected p value for the most significant voxel for each cluster with the whole brain as search volume (Nichols and Hayasaka, 2003). Additionally we performed family-wise error correction taking into account the cluster extent (Friston et al., 1994).

To identify regions where rDA depends on the subjective desire to eat we performed a voxel-wise correlation analysis (Pearson) between the change in rDA after milkshake versus tasteless solution intake (ΔrDA) and the wanting score. From this, clusters of contiguous voxels with $p < 0.05$ were identified. The Pearson correlation coefficients and p values were then calculated for each cluster.

Combined fMRI and PET Analysis

To identify brain areas that showed both a BOLD signal and DA release we extracted the z-statistics of group level fMRI analysis for the contrast "milkshake-tasteless" and constructed an overlap map with the group statistics of DA release. For this comparison, only the early time interval (0-5 min) in the PET data was selected that corresponds to the immediate response to milkshake consumption acquired in fMRI.

Reporting of Brain Areas

Coordinates of all brain areas that have been annotated in figures and reported in tables as results of our analysis have been carefully compared to the atlas provided by Mai et al. (2015).

Other Statistical Analyses

The analyses of biochemical data and ratings were performed using GraphPad Prism (vers. 6.0h, GraphPad Software, San Diego California USA, https://www.graphpad.com/).